Deglacial to Holocene Changes in Eastern Equatorial Pacific Upper-Ocean Dynamics – Indications from Foraminiferal (Isotope) Geochemistry

DISSERTATION

zur Erlangung des Doktorgrades Dr. rer. nat.

an der Mathematisch-Naturwissenschaftlichen Fakultät

der Christian-Albrechts-Universität zu Kiel

vorgelegt von

Tebke Böschen

Kiel, 2013

Referent: Prof. Dr. Dirk Nürnberg

Koreferent: Prof. Dr. Ralph Schneider

Tag der mündlichen Prüfung: 22.10.2013

Zum Druck genehmigt: 25.04.2014

gez. (Prof. Dr. Wolfgang J. Duschl, Dekan):

Eidesstattliche Erklärung

Hiermit versichere ich an Eides statt, dass die vorliegende Dissertation von mir eigenständig und nur mit Hilfe der angegebenen Quellen sowie der wissenschaftlichen Beratung durch meine Betreuer verfasst wurde. Ferner versichere ich, dass der Inhalt der Dissertation weder in dieser, noch in veränderter Form, einer anderen Prüfungsbehörde vorliegt. Die Arbeit ist unter Einhaltung der Regeln guter wissenschaftlicher Praxis der Deutschen Forschungsgemeinschaft entstanden.

Kiel, den 30. Juli 2013

(Tebke Böschen)

Abstract

Oxygen Minimum Zones (OMZs) in the ocean represent key regions for the interaction between atmosphere and ocean waters and can be a sink or source for atmospheric CO_2. Hence, they play a major role with respect to anthropogenic induced global warming. Biological productivity is very high in these areas and resulting degradation processes consume substantial amounts of dissolved oxygen from the water column, leaving certain water depths almost oxygen-free. One of the largest and most distinctive OMZs world-wide stretches along the west coast of South America offshore Ecuador, Peru and Chile. This OMZ is associated with intense coastal upwelling, which is most pronounced between ~5°S and ~25°S. The intensity of the upwelling varies seasonally, being propelled mainly by external forcing mechanisms like the position of the Intertropical Convergence Zone (ITCZ), the strength of trade winds and modulations of the El Niño Southern Oscillation (ENSO).

This hydrographically complex ocean area affords different approaches to study its characteristics. Sediment surface samples and corresponding seawater samples from the Eastern Equatorial Pacific (EEP), ranging from a water depth of 60 to 2,000 m and covering a large latitudinal range from the equator to 17°S, were investigated. Apparent calcification depths (ACDs) were calculated by combined analyses of stable oxygen isotopes ($\delta^{18}O$) in planktonic foraminifers from these samples and from water samples (Chapter 4). Investigations of ACDs for species *G. ruber* (white, morphotype sensu stricto) and *N. dutertrei* (dextral) show clear differences between both species within the EEP. Surface dweller *G. ruber* constantly inhabits the upper 16 meters of the water column; contrary *N. dutertrei* favors different habitat depths in dependence on the surrounding water masses. On average, the ACDs for *N. dutertrei* indicate a calcification depth of ~200m in the northern part of the study area (the equator to 5°S) and ~70m in the southern region (7° to 13°S). The shallower habitat depth in the south is probably related to the more intense upwelling, which results in the rise of cooler water masses and thus similar temperatures (~15°C) are reached in shallower depths. Additionally, lower oxygen concentrations in the southern part of the study area are likely to force *N. dutertrei* to shallower habitat depths. The correct estimation of ACDs in the EEP provides a more detailed view on the vertical

habitat of *N. dutertrei*, which is particularly important for the following paleo-interpretations in Chapter 5.

Two piston cores from the Gulf of Guayaquil at 3.5°S in the EEP were studied, covering time spans of ~13,000 years (core 056; temporal resolution ~60 years) and of ~18,000 years (core 059; temporal resolution ~80 years), respectively (Chapter 5). Surface and subsurface temperatures were reconstructed for the past 18,000 years using alkenone-thermometry as well as foraminiferal Mg/Ca-based approaches for surface (*Globigerinoides ruber*, white) and for subsurface depths (~200 m; *Neogloboquadrina dutertrei*). Salinity approximations ($\delta^{18}O_{ivf\text{-}sw}$) for surface and subsurface depths were generated to corroborate the high-resolution temperature records. In the study area the deglaciation was characterized by much warmer temperatures (~3°C) and higher salinities than nowadays, in surface as well as in subsurface depths. Surface dweller *G. ruber* and alkenone records show almost identical temperatures prior to ~10 ka BP, indicating that both proxy carriers recorded a similar habitat and seasonality during this time. After ~10 ka BP both proxies divert markedly, which was possibly caused by a shift of alkenone-synthesizing coccolithophores from annual mean temperatures during the deglaciation to austral summer temperatures during the Holocene. The cooling in *G. ruber* records by ~2°C in both cores during the Holocene implies a strengthened influence of cooler water masses. The surface records lag the subsurface records of *N. dutertrei* by ~1-2 kyrs, implying that different mechanisms control the surface and subsurface hydrography. The temperature decrease and freshening trends during the Holocene coincide with an enhanced marine productivity, indicating that cooler (EUC-sourced) water masses and strengthened upwelling intensity transported more nutrients into the EEP.

A newly developed species-specific transfer function for benthic Mg/Ca ratios based on *Uvigerina peregrina* data from the EEP is presented in Chapter 6 and completes the foraminiferal investigations. The sediment surface data set of endobenthic species *U. peregrina* shows a clear correlation between water depth and $\delta^{18}O$ as well as Mg/Ca ratios, thus supporting the use of this species as a reliable temperature proxy. The reconstruction of bottom water temperatures is important to understand the complex, local hydrography. The effect of bottom water $\Delta[CO_3^{2-}]$ on Mg/Ca ratios in *U. peregrina* is apparently small and does not influence the temperature signal. A compilation of data from the EEP and literature data results in a transfer function covering a temperature range between 5

and 20°C; the resulting function (R^2= 0.77) estimates temperatures with a precision of ±1.6°C. This new transfer function provides a more precise estimation of Mg/Ca-derived temperatures in the EEP for endobenthic species *U. peregrina* than previous approaches.

Zusammenfassung

Sauerstoff-Minimum-Zonen (SMZ) im Ozean sind Schlüssel-Regionen für die Interaktion zwischen Atmosphäre und Ozean und können ein Speicher oder eine Quelle für atmosphärisches CO_2 sein, daher sind sie im Zusammenhang mit der anthropogen verursachten globalen Erwärmung wichtig. Die biologische Produktivität ist in diesen Regionen sehr hoch und die daraus resultierenden Abbauprozesse verbrauchen große Mengen von gelöstem Sauerstoff aus der Wassersäule. Zusätzlich reduziert eine träge Zirkulation den Sauerstoffgehalt weiter und sorgt in bestimmten Wassertiefen für beinahe sauerstofffreie Zonen. Eine der weltweit größten und markantesten SMZ erstreckt sich entlang der Westküste von Südamerika vor den Küsten von Ecuador, Peru und Chile. Diese SMZ ist durch intensiven, küstennahen Auftrieb gekennzeichnet, der zwischen ~5°S und ~25°S am stärksten ausgeprägt ist. Die Intensität des Auftriebs variiert saisonal und wird vor allem durch externe Faktoren wie die Position der Intertropischen Konvergenz Zone (ITCZ), die Stärke der Passatwinde sowie durch Veränderungen der El Niño Southern Oscillation (ENSO) bestimmt.

Dieses hydrographisch komplexe Meeresgebiet erfordert verschiedene methodische Ansätze, um seine Charakteristiken zu verstehen. Sediment-Oberflächenproben und dazugehörige Wasserproben aus dem Äquatorialen Ost-Pazifik (EEP) aus Wassertiefen zwischen 60 und 2.000 m und Breitengraden vom Äquator bis 17°S wurden untersucht. Durchschnittliche Kalzifizierungs-Tiefen (ACDs) wurden aus der kombinierten Analyse von stabilen Sauerstoffisotopen ($\delta^{18}O$) in planktischen Foraminiferen aus Sediment-Oberflächenproben und aus Wasserproben bestimmt (Kapitel 4). Berechnungen der ACDs für die Arten *G. ruber* (weiß, Morphotyp sensu stricto) und *N. dutertrei* (dextral) zeigen deutliche Unterschiede zwischen beiden Arten im EEP. Während die oberflächennahe Art *G. ruber* die obersten 16 m der Wassersäule bewohnt, bevorzugt *N. dutertrei*, in Abhängigkeit von den umgebenden Wassermassen, andere Tiefen. Die ACDs für *N. dutertrei* deuten auf eine Tiefe von ~200 m im nördlichen Arbeitsgebiet hin (Äquator bis ~5°S). Im Gegensatz dazu zeigen die Proben aus dem südlichen Arbeitsgebiet (7° bis 13°S) flachere ACDs von ~70 m. Das flachere Habitat im Süden steht wahrscheinlich in Zusammenhang mit dem küstennahen Auftrieb, welcher das Aufsteigen von kalten Wassermassen bedingt und folglich werden ähnliche Temperaturen (~15°C) im Süden in geringeren Tiefen er-

reicht als im Norden. Zusätzlich zwingen niedrigere Sauerstoff-Konzentrationen im südlichen Arbeitsgebiet *N. dutertrei* wahrscheinlich in geringere Wassertiefen. Die präzise Abschätzung von ACDs im EEP liefert einen detaillierteren Blick auf das vertikale Habitat von *N. dutertrei* als bisher und erlaubt daher eine genauere Interpretation von Veränderungen der Wassertemperaturen und Salzgehalte in den Paläo-Rekonstruktionen in Kapitel 5.

Außerdem wurden bei 3.5°S zwei Kolbenlot-Kerne aus dem Golf von Guayaquil entnommen (Kapitel 5); die untersuchten Kerne umfassen die letzten ~13.000 Jahre (Kern 056; zeitliche Auflösung ~60 Jahre) beziehungsweise ~18.000 Jahre (Kern 059; zeitliche Auflösung ~80 Jahre). Oberflächen- und Zwischenwasser-Temperaturen für die vergangenen 18.000 Jahre wurden mit Hilfe von Alkenonen sowie Mg/Ca-Verhältnissen in Foraminiferen für Oberflächen-Tiefen (*Globigerinoides ruber*, weiß) und Zwischenwasser-Tiefen (~200 m; *Neogloboquadrina dutertrei*) rekonstruiert. Zusätzlich wurden Abschätzungen der Salinität ($\delta^{18}O_{ivf\text{-}sw}$) für Oberflächen- und Zwischenwassertiefen gemacht um die hochauflösenden Temperatur-Rekonstruktionen zu unterstützen. Die Deglaziation war im oberflächennahen und Zwischenwasser-Bereich durch deutlich wärmere Temperaturen (~3°C) und salzhaltigere Bedingungen gekennzeichnet als heutzutage. Die Oberflächen-Art *G. ruber* und die Alkenone zeigen bis vor ~10.000 Jahren fast identische Temperaturen, was andeutet dass beide Proxies während dieser Zeit ein ähnliches Habitat und eine ähnliche Saison aufgezeichnet haben. Seit ~10.000 Jahren vor heute divergieren beide Proxies deutlich, was möglicherweise durch eine Veränderung der durch Coccolithophoriden produzierten Alkenone von Jahresmitteltemperaturen während der Deglaziation zu Südhemisphären-Sommertemperaturen während des Holozäns liegt. Die Abkühlung in den *G. ruber* Datensätzen beider Kernen von ~2°C während des Holozäns deutet auf einen verstärkten Einfluss kühlerer Wassermassen hin. Die Verzögerung der Oberflächen-Datensätze von etwa 1.000-2.000 Jahren im Vergleich zu den Zwischenwasser-Datensätzen von *N. dutertrei* deutet darauf hin, dass unterschiedliche Mechanismen die Oberflächenwasser und Zwischenwasser-Hydrographie kontrollieren. Die Abkühlungen sowie die geringeren Salinitäten im Verlauf des Holozäns fallen mit einer erhöhten marinen Produktivität zusammen was darauf hindeutet, dass kühlere Wassermassen innerhalb des Äquatorialen Unterstroms (EUC) verstärkt in den EEP transportiert wurden und mehr Nährstoffe verfügbar waren.

Eine neu entwickelte Art-spezifische Transferfunktion für benthische Mg/Ca Verhältnisse basierend auf *Uvigerina peregrina* Daten aus dem EEP wird in Kapitel 6 vorgestellt und vervollständigt die Untersuchungen an Foraminiferen. Der Datensatz aus Sediment-Oberflächenproben der endobenthischen Art *U. peregrina* zeigt eine starke Korrelation zwischen Wassertiefe und $\delta^{18}O$ sowie Mg/Ca Verhältnissen und unterstützt daher die Zuverlässigkeit dieser Art für Temperatur-Rekonstruktionen. Die Rekonstruktion von Bodenwasser Temperaturen ist wichtig um die komplexe, lokale Hydrographie zu verstehen. Die Auswirkungen von Bodenwasser $\Delta[CO_3^{2-}]$ auf die Mg/Ca Verhältnisse von *U. peregrina* sind offensichtlich gering und beeinflussen das Temperatursignal nicht. Eine Zusammenstellung von Daten aus dem EEP und der entsprechenden Fachliteratur resultieren in einer Transferfunktion, die den Temperaturbereich zwischen 5 und 20°C abdeckt; die daraus entwickelte Gleichung (R^2=0,77) berechnet Temperaturen mit einer Genauigkeit von ±1.6°C. Diese neue Transferfunktion ermöglicht eine präzisere Abschätzung von Mg/Ca-basierten Temperaturen für die endobenthische Art *U. peregrina* im EEP als bisherige Ansätze.

Contents

List of abbreviations

AAIW – Antarctic Intermediate Water

ACD – Apparent Calcification Depth

ADCP – Acoustic Doppler Current Profiler

AR – Accumulation Rates

B/A – Bølling/ Allerød

BP – Before Present, before A.D. 1950

C/N – ratio of (atomic) carbon to (atomic) nitrogen

CO_2 – Carbon Dioxide

$\delta^{13}C$ – stable carbon isotope ratio

$\delta^{18}O$ – stable oxygen isotope ratio

$\delta^{18}O_{sw}$ – ratio of stable oxygen isotopes in sea water

$\delta^{18}O_{ivf\text{-}sw}$ – ratio of stable oxygen isotopes in sea water, ice-volume corrected

EEP – Eastern Equatorial Pacific

EF – Equatorial Front

ENSO – El Niño Southern Oscillation

EqPIW – Equatorial Pacific Intermediate Water

ESSW – Equatorial Sub-Surface Water

ESW – Equatorial Surface Water

EUC – Equatorial Under Current

H1 – Heinrich Event 1

HC – Humboldt Current

ICP-AES – Inductively Coupled Plasma-Atomic Emission Spectrometer

ICP-OES – Inductively Coupled Plasma-Optical Emission Spectrometer

ITCZ – Inter Tropical Convergence Zone

ka – kilo annum

kyrs – kilo years

LGM – Last Glacial Maximum

LSR – Linear Sedimentation Rates

Mg/Ca – ratio of magnesium to calcium

MUC – Multi Corer

NPIW – North Pacific Intermediate Water

OMZ – Oxygen Minimum Zone

PC – Piston Corer

PCC – Peru Chile Current

PCCC – Peru Chile Counter Current

PCUC – Peru Chile Undercurrent

PP – Primary Production

ppm – parts per million

SAMW – Subantarctic Mode Water

SEC – South Equatorial Current

SSCC – Southern Subsurface Counter Current

SST – Sea Surface Temperature

$SST_{UK'37}$ – Sea Surface Temperature, derived from the alkenone unsaturation index

$SST_{Mg/Ca}$ – Sea Surface Temperature, derived from Mg/Ca ratios of foraminifers

subSST – Subsurface Temperature

TN – Total Nitrogen

TC – Total Carbon

TOC – Total Organic Carbon

$U^{K'}_{37}$ – alkenone unsaturation index

WOA 2009 – World Ocean Atlas 2009

WOCE – World Ocean Circulation Experiment

XRF – X-Ray Fraction

YD – Younger Dryas

List of Figures and Tables

Chapter 1: Introduction

1.1: Motivation and Major Objectives of this Thesis

One of the largest and most distinctive Oxygen Minimum Zones (OMZs) worldwide stretches in the Eastern Equatorial Pacific (EEP) along the west coast of South America offshore Ecuador, Peru and Chile. This OMZ is well known for intense coastal upwelling, which is most pronounced between ~5°S and ~25°S. The intensity of the upwelling varies seasonally, being driven mainly by external forcing mechanisms like insolation intensity, the position of the ITCZ and the strength of trade winds. Additionally, modulations of the El Niño Southern Oscillation (ENSO) interfere with the local hydrography on inter-annual time scales.

This PhD thesis was incorporated into the DFG-funded Collaborative Research Centre "Climate – Biogeochemistry Interactions in the Tropical Ocean" (SFB 754). The SFB 754 aims to investigate OMZs in the tropics, which are key regions regarding low oxygen concentrations in today's climate. Circulation processes spread the effects of oxygen-dependent nutrient cycles taking place within OMZs into the ocean. Consequently, OMZs influence nutrient cycles, biological productivity and CO_2-fixation of the ocean. Knowledge of past oxygenation levels can help to understand how, for example, a rise in atmospheric CO_2 concentrations will influence the intensity and expansion of OMZs in the future.

This PhD thesis aims to reconstruct changes in the upper-ocean stratification and circulation in the area of the low-latitude OMZ offshore Ecuador and Peru for the Holocene and the last Deglaciation. External control factors, which controlled and actively shaped the local hydrography within the last ~18,000 years, are the focus of the investigations. Benthic and especially planktonic foraminifers serve as a widely used tool in paleoceanography to reconstruct past ocean conditions; hence, they are the most important proxy carriers within this PhD thesis. This PhD thesis aims to investigate past changes in the stratification and circulation from surface to subsurface depths on centennial to millennial time scales, and thus to contribute important information for the SFB 754 for an overall better understanding of OMZs worldwide and in the EEP in particular.

1.2: Structure of this PhD thesis

This thesis is divided into six chapters:

Chapter 1 provides the introduction and contains the motivation as well as major objectives of this thesis. Furthermore, a summary of previously performed paleoceanographic studies in the area is given.

Chapter 2 describes the local hydrography including the Oxygen Minimum Zone and the El Niño Southern Oscillation.

Chapter 3 gives an overview of the sedimentology in the study area and provides detailed information about the selected piston cores as well as the analyzed sediment surface samples. Furthermore, the geochemical proxies applied within this thesis (foraminiferal-based and bulk sediment) are introduced. The stratigraphy for both cores, based on a combination of AMS^{14}C datings and stable oxygen isotopes, is also introduced in this chapter.

Chapters 4 to 6 represent manuscripts, which the author of this thesis prepared as the principal author. In Chapter 4, apparent calcification depths (ACDs) for planktonic species *Globigerinoides ruber* (white) and *Neogloboquadrina dutertrei* (dextral) are investigated based on δ^{18}O analyses. The results of Chapter 4 were the basis for the following chapter, since it is crucial to know the habitat depth of planktonic foraminifers for the following paleo-applications as precise as possible. Chapter 5 focuses on the evolution of temperatures in surface and subsurface water depths based on ratios of magnesium to calcium (Mg/Ca) of different foraminiferal species as well as alkenone analyses during deglaciation and Holocene. It investigates changes in the local water mass structure and aims to clarify which mechanisms might have caused the observed changes. Besides two planktonic species, a benthic species was also investigated to track changes in the local bottom water composition. Thus, in Chapter 6 a newly evolved calibration function is introduced to calculate bottom water temperatures (BWTs) based on Mg/Ca ratios of *U. peregrina* from the EEP.

Chapter 7 summarizes the main conclusions of this PhD thesis. Furthermore, an outlook and perspectives for future research regarding the topic are presented. Additional information on the studied sediment cores, particularly about nutrient cycles, can be obtained from the PhD thesis of *Mollier-Vogel* [2012].

The data set of this PhD thesis has been completed by accompanying PhD and Diploma Theses. The $\delta^{18}O$ analyses of water samples used in Chapter 4 were performed within the frame work of a Diploma thesis by *Klostermann* [2011]. For Chapter 5 downcore Mg/Ca and $\delta^{18}O$ records of *G. ruber* were included into the thesis presented here, which are based on the work conducted within the frame work of a Diploma Thesis [*Doering,* 2012]. The accompanying PhD thesis by *Mollier-Vogel* [2012] contributed alkenone-based sea surface temperatures for core M772-059-1, which are presented in Chapter 5 of this thesis. Furthermore, the TOC and TN analyses of core M772-056-5 (Chapter 5) were taken from the PhD thesis of *Mollier-Vogel* [2012].

1.3: Background Information

1.3.1: Knowledge of Calcification Depths

For the correct interpretation of paleo-data it is crucial to know the calcification depth of the analyzed foraminiferal species as exactly as possible. Planktonic foraminifers inhabit a wide range of depths, from surface waters down to ~800 m [*Hemleben et al.*, 1989]. The intensity of upwelling in the EEP might drive the foraminifers to lesser or greater habitat depths and might also be related to the presence or absence of certain foraminiferal species. Additionally, ocean tunnels influence the local hydrography since they represent a connection between subtropical waters and those water masses being upwelled off Peru and Ecuador [*Sun et al.*, 2004].

The habitat depth of planktonic species *N. dutertrei* is difficult to specify, as views on its vertical occurrence in the water column deviate largely. However, many authors associate its habitat with the thermocline or adjacent depths [*Ravelo and Fairbanks*, 1992]; the habitat of *N. dutertrei* is associated with the deep chlorophyll maximum [*Fairbanks and Wiebe*, 1980; *Fairbanks et al.*, 1982; *Bé et al.*, 1985]. The deep chlorophyll maximum is found in roughly 50 m water depth; the chlorophyll concentration in this water depth is ~0.75 mg/m³ compared to ~3 mg/m³ in surface waters [*Pennington et al.*, 2006]. A core top study from the EEP indicates a calcification depth for *N. dutertrei* of ~110 m [*Faul et al.*, 2000]. This is in agreement with *Regenberg et al.* [2009], who calculated calcification depths for *N. dutertrei* based on $\delta^{18}O$ values to be ~80-190 m in the tropical Atlantic and Caribbean. In the tropics, *N. dutertrei* favors no particular season [*Tedesco and Thunell*,

2003], but *Thunell et al.* [1983] observed maximum abundance for *N. dutertrei* in the Panama Basin during the upwelling season (winter to spring). Based on the findings of *Faul et al.* [2000], who studied habitat depths in vicinity of the sites studied within this thesis, a preliminary habitat depth of ~110 for *N. dutertrei* is assumed.

Globigerinoides ruber is a surface dweller [*Deuser et al.*, 1981; *Bé et al.*, 1985; *Dekens et al.*, 2002], and hence serves as an archive to record seawater temperatures of the top ~30 m. These findings are consistent with the results of *Faul et al.* [2000], who report that *G. ruber* as a photosynthesizing species is restricted to the upper water column, where light levels but not necessary nutrients or chlorophyll levels are highest. *Deuser et al.* [1981] indicate a year-round presence of *G. ruber*, thus making it a suitable archive for annual SST. Investigation of surface Mg/Ca ratios in *G. ruber* are in best accordance with summer temperatures of the WOA 2009 data set, hence leading to the conclusion that *G. ruber* seems to be a reliable recorder of summer temperatures in the EEP. Species selection of *G. ruber* was restricted to the morphotype sensu stricto (*G. ruber* s.s.), as *Wang* [2000], *Kuroyanagi and Kawahata* [2004] and *Steinke et al.* [2005] revealed pronounced differences in the habitat among different morphotypes of *G. ruber*. According to the findings by *Wang* [2000] morphotype sensu stricto (s.s.) calcifies in shallower water depths than sensu lato (s.l.) and is restricted to the upper ~30 m of the water column (based on $\delta^{18}O$ signatures of the species), it thus represents ocean surface conditions. Additional investigations of Mg/Ca ratios in both morphotypes revealed similar results, with *G. ruber* s.s. indicating warmer and thus shallower habitat depth [*Steinke et al.*, 2005]. The correct species selection for paleoceanographic investigations is of fundamental importance. Any mixture between the two morphotypes would result in an underestimation of the reconstructed temperatures as proportions of morphotype s.l. would indicate lower temperatures due to its greater habitat depth [*Steinke et al.*, 2005].

1.3.2: Hydrography in the EEP during Deglaciation and Holocene

A number of previous studies have used Mg/Ca and $\delta^{18}O$ ratios of planktonic foraminifers or alkenone-based reconstructions to estimate the evolution of the SST in the EEP from deglacial to Holocene times. The reasons for temperature changes remain partly unclear and are debated controversially. Planktonic Mg/Ca records of *G. ruber* indicate that SSTs

in the EEP experienced differences of up to 5°C during glacial/ interglacial periods, with the Last Glacial Maximum (LGM) being ~3°C colder than present-day SSTs in the area [*Lea et al.*, 2000]. The concurrence between northern hemisphere cold spells and temperature drops in the EEP (alkenone-based) has been linked to the oceans thermohaline circulation, even though this connection might be amplified in the tropical ocean by ocean-atmosphere interactions [*Kienast et al.*, 2006]. Besides changes in temperatures in the EEP, the ENSO also plays an important role for the local hydrography. A northward-displaced ITCZ during the Middle Holocene and a related attenuation of the ENSO frequency of up to 50% indicates a strong interaction between both features [*Koutavas et al.*, 2006]. Modulations in ENSO variability have also been linked to changes in the Earth orbit, namely to modulations in precession and obliquity [*Clement et al.*, 2000; *Pena et al.*, 2008a]. The onset of modern ENSO conditions in the EEP has been described to start between ~7 and 5 ka BP [*Loubere et al.*, 2003; *Ehlert et al.*, 2013]; this is related to changes in the thermocline structure and mixed layer depth in the area, implying that especially the thermocline developments controls ENSO frequencies [*Loubere et al.*, 2003]. The same authors observed a thermocline cooling for the Late Holocene, accompanied by higher nutrient concentrations and a resulting increase of the biological productivity.

1.3.3: Bottom Water Temperatures in the EEP

Physical properties like water temperatures are key mechanisms to evaluate changes in ocean circulation and thus the extension of OMZs. The reconstruction of past bottom water temperatures (BWT) is an essential and powerful tool to monitor intermediate to deep water formation and circulation. The tight correlation between water temperatures and Mg/Ca ratios in benthic foraminifers are a commonly applied approach to investigate this issue. An important factor influencing the reconstructed BWT is the habitat of the benthic species. Depending on the habitat depth (epifaunal to infaunal), the estimated temperatures represent either bottom waters or pore water conditions. Most approaches focus on epifaunal species like *Cibicides wuellerstorfi*, which is known to live either on the sediment or shallow infaunal in soft sediments [*McCorkle et al.*, 1997; *Jorissen*, 1999]. A transfer function evolved for samples from the EEP is based on *C. wuellerstorfi* and aims to

reconstruct deep water formation [*Martin et al.*, 2002]. Several approaches use the shallow infaunal species *Uvigerina spp.* from various regions worldwide [*Elderfield et al.*, 2006; *Bryan and Marchitto*, 2008; *Yu and Elderfield*, 2008; *Elderfield et al.*, 2010], but for the EEP no linear transfer function for this species is yet existing.

Chapter 2: Study Area: Eastern Equatorial Pacific

The hydrographic setting in the EEP (Figs. 2-1 and 2-2) is complex and has been described in several publications [*Fiedler and Talley*, 2006; *Kessler*, 2006; *Montes et al.*, 2010]. Persistent southeast trade winds, which are parallel to the coast, result in an offshore transport of surface waters [*Ekman*, 1905], which is balanced by equatorial upwelling [*Kessler*, 2006]. This allows colder, nutritious water masses from subsurface depths to stream into the area. Wind and upwelling intensity vary in the course of the year due to changes of the position of the Intertropical Convergence Zone (ITCZ); the upwelling seems to extend far into the thermocline and below [*Kessler*, 2006]. The upwelling is strongest during austral winter (July to September) when the ITCZ moves from ~5°N to ~10°N [*Karstensen and Ulloa*, 2008]. However, currents in the Eastern Tropical Pacific are in general not very pronounced and thus short term alterations like wind events and eddies strongly influence the movement of water masses [*Czeschel et al.*, 2011]. Figure 2-1 depicts the main oceanographic currents and important water masses in the study area.

2.1: Local Water Mass Structure

Modern surface water masses in the EEP are [*Wyrtki*, 1966; *Fiedler and Talley*, 2006]: Tropical Surface Water (TSW) located north of the equator, with temperatures exceeding 25°C and a salinity below 34 (practical salinity unit – psu); Equatorial Surface Water (ESW) is dominant along the equator with temperatures below 25°C and a salinity exceeding 34. Both water masses are separated by the Equatorial Front (EF), a sharp hydrographic barrier in the study area. Subtropical Surface Water (STSW) is characterized by a salinity of 35 or above; it is most influential in the north and south Pacific central gyres, which are located northwest and southwest of the Eastern Tropical Pacific [*Fiedler and Talley*, 2006]. Cold Coastal Water (CCW) dominates surface depths at ~12-15°S, with temperatures between 14-18°C and a salinity of ~35 [*Ayón et al.*, 2008]. This pronounced cool surface water mass probably originates from a mixture of subantarctic water masses, being transported northwards, and water being upwelled offshore Peru.

Important water masses in subsurface depths are: The Equatorial Undercurrent (EUC), whose source waters originate in subantarctic regions of the south-western Pacific [*Strub*

et al., 1998], and which flows in water depths of roughly 100 – 250 m eastwards along the equator [*Kessler*, 2006]. The EUC picks up speed when travelling eastwards, while the over-lying South Equatorial Current (SEC) slows down west of ~85°W. In the far East Tropical Pacific the EUC as well as the thermocline rise much closer to the surface, resulting in the mixing of several water masses in a very thin layer of water. The eastern EUC shoals when local easterly winds weaken during March and August. Characteristic of the EUC are the high salinity and the highly oxygenated waters, which can be traced back to the coasts of Ecuador and Peru [*Toggweiler et al.*, 1991], thus implying that the deepest layers of this stream travel this far into the east Pacific. The EUC is split by the Galápagos Islands, which separate it into a weaker northern and a stronger southern branch [*Lukas*, 1986]. The southern branch of the EUC is feeding the Peru Chile Undercurrent (PCUC) and consequently supports the upwelling offshore Peru [*Brink et al.*, 1983], even though recent studies [*Montes et al.*, 2010] revealed that it still remains unclear to what extent the EUC influences the upwelling. The northern branch of the EUC ultimately feeds the Equatorial Subsurface Water (ESSW), which is characterized by high nutrient contents but low oxygen levels. It is transported pole wards, merging with the PCUC and consequently forms the core of the OMZ [*Hormazábal et al.*, 2006]. The EUC and in particular the ESSW are the main contributors in subsurface depths at the down core study sites in the Gulf of Guayaquil (Chapter 5).

The EUC as well as the Southern Subsurface Counter Current (SSCC) originate in the central Pacific [*Toggweiler et al.*, 1991]; the source waters of the EUC even originate from subantarctic regions in the South-Western Pacific. The SSCC flows westwards in subsurface depths and turns southwards when getting closer to the continental shelf. Roughly 75% of the water masses in the SSCC reach the Peruvian coast, feeding into the PCUC and consequently support upwelling in the area [*Montes et al.*, 2010]. In the northern part of the OMZ, close to the continental slope, the PCUC reaches water depths of 150 to 200 m [*Czeschel et al.*, 2011]. Contrary, *Karstensen and Ulloa* [2008] found the PCUC to be in water depths of 50 to 150 m. This water mass transports waters with relatively low oxygen saturation originating from the EUC pole wards and deepens its extension when extending down to ~700 m further south [*Czeschel et al.*, 2011]. Brink *et al.* [1983] found the PCUC to be in shallower depths of 50-100 m with temperatures of 13-16°C.

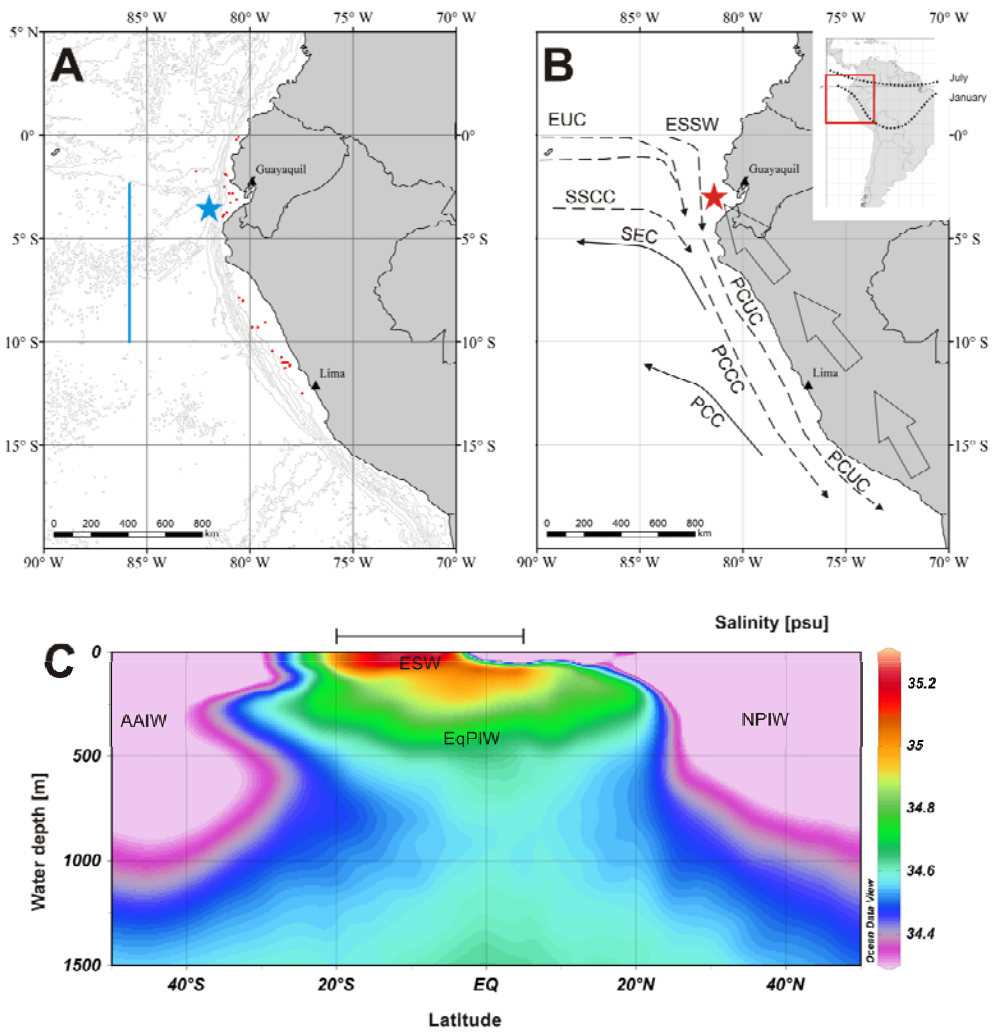

Figure 2-1: Maps of the study area and salinity cross-section along the American coast

A: Red dots mark the positions of multi corer (MUC) surface samples (Table 1). Blue line is track P19C from the World Ocean Circulation Experiment (WOCE; Fig. 2-2; [*Rubin et al.*, 1998]). The blue star indicates World Ocean Atlas Station #21835, which is referred to as reference site within this thesis. Gray lines are 1,000 m depth contours, indicating the steepness of the continental slope.

B: Sediment core location (red star) offshore Ecuador. Inlet provides larger view of South America with dashed lines indicating ITCZ position for January and July [*van Breukelen et al.*, 2008]. Open block arrows show main wind direction [*Kessler*, 2006]. Thin arrows indicate the main oceanographic currents offshore Ecuador and Peru after [*Brink et al.*, 1983; *Strub et al.*, 1998; *Fiedler and Talley*, 2006; *Kessler*, 2006; *Silva et al.*, 2009; *Bostock et al.*, 2010]. Surface currents (solid lines): SEC (South Equatorial Current), PCC (Peru Chile Current); subsurface currents (dashed lines): EUC (Equatorial Under Current), ESSW (Equatorial Subsurface Water), SSCC (Southern Subsurface Counter Current), PCUC (Peru Chile Under Current) and PCCC (Peru Chile Counter Current); data source for both upper maps is ESRI®.

C: Salinity section for September from 50°S to 50°N along the American coast [*Antonov et al.*, 2010]; ODV was used to generate the plot [*Schlitzer*, 2010]; black bar across section indicates latitudinal range from upper map. Water masses indicated are AAIW (Antarctic Intermediate Water), ESW (Equatorial Surface Water), EqPIW (Equatorial Pacific Intermediate Water) and NPIW (North Pacific Intermediate Water).

Another subsurface current, the Peru Chile Counter Current (PCCC), is located further offshore than the PCUC. The PCCC is flowing roughly 100 to 300 km offshore Chile and Peru; it originates at approximately 7°S and extends to 35-40°S [*Strub et al.*, 1995]. In the north a connection between the PCCC and the EUC is obvious, thus making the PCCC an important water mass in the Eastern Pacific. The northward directed Peru Chile Current (PCC; sometimes also referred to as Humboldt Current/ HC) merges with the PCUC at ~14°S.

The thermocline in the EEP is most pronounced between 5°S and 15°N; its density structure is caused by sharp gradients of temperature superimposed by a halocline [*Fiedler and Talley*, 2006]. The distinctive thermocline is also a sharp nutricline; the relation between temperature and nutrients has been investigated globally [*Kamykowski and Zentara*, 1986] and for the Eastern Tropical Pacific in particular [*Chavez et al.*, 1996]. The depth of the thermocline controls supply of macro nutrients (nitrate, phosphate) and thus biological productivity in surface waters [*Pennington et al.*, 2006]. Although at this low latitude the sun is at its peak at the equator twice a year, only an annual cycle can be observed in Sea Surface Temperatures (SST) which are coldest in September. The entire thermocline rises roughly 20 m between June and September, thus bringing colder water within reach of stronger winds, causing a mixing of water masses during this time of the year [*Kessler*, 2006]. At the core locations offshore Peru the thermocline deepens to ~25 m during austral summer compared to austral winter.

According to *Fiedler and Talley* [2006] the Mixed Layer Depth (MLD) shows a similar pattern regarding the spatial and seasonal structure as the thermocline. On average, the MLD is located 10-20 m below the thermocline. In the upwelling region offshore Peru the MLD is usually less than 20 m during summer and autumn, but it can descend to ~50 m during El Niño events [*Brink et al.*, 1983].

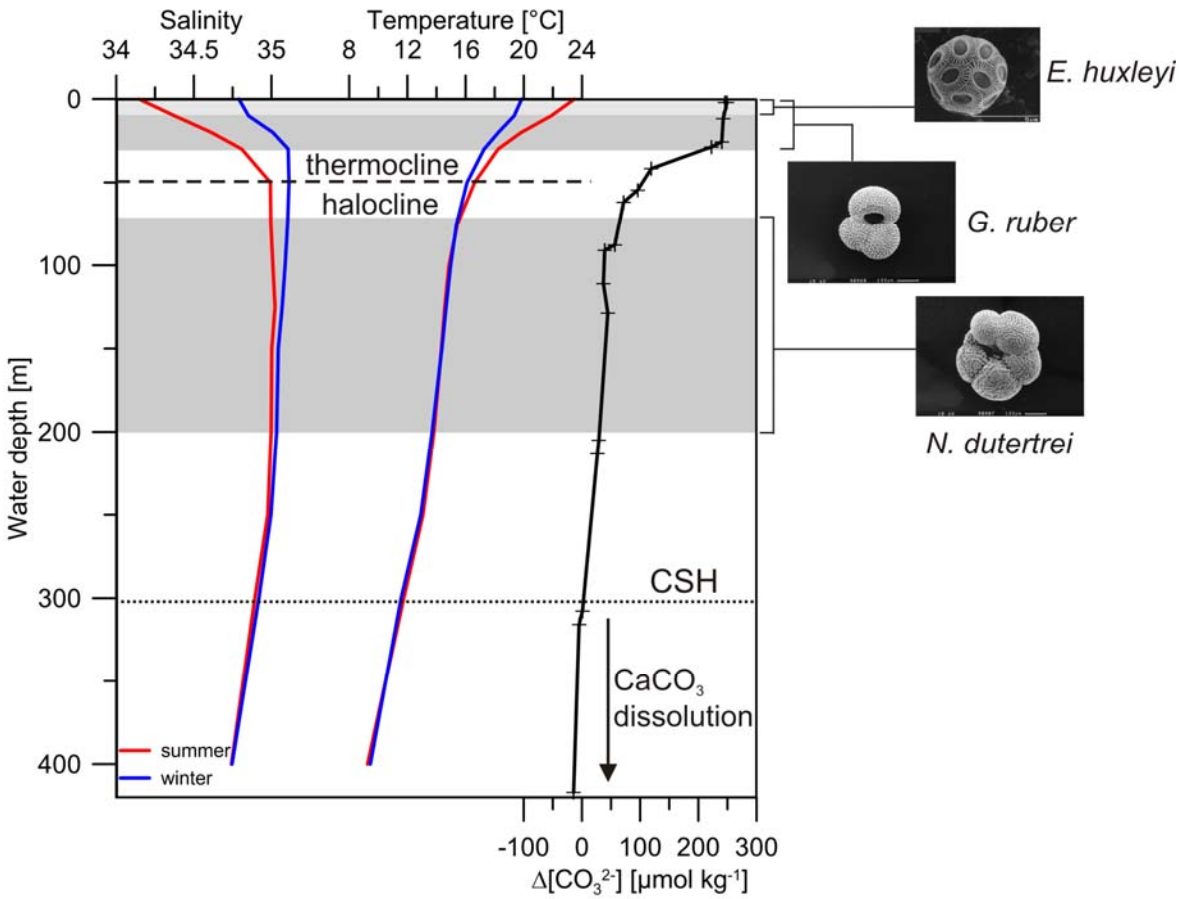

Figure 2-2: Seasonal T/S profiles, $\Delta[CO_3^{2-}]$ and habitat depths of proxy carriers

Seasonal profiles of salinity and temperature extracted from the WOA 2009, station 21835 at 3.5°S/ 81.5°W [*Antonov et al.*, 2010; *Locarnini et al.*, 2010] and the $\Delta[CO_3^{2-}]$ profile from line P19C (WOCE). Calcite dissolution is assumed to start below ~300 m. The WOA 2009 data indicates warmer and fresher conditions during the summer (red line) and cooler and more saline conditions during the winter (blue line). The thermocline/ halocline is situated in approximately 50 m water depth. Alkenone producing coccolithophores inhabit the upper ocean in ~0-10 m water depth (picture of *Emiliania huxleyi*; available at the Electronic Microfossil Image Database System, http://www.emidas.org/). Slightly deeper in ~0-30 m water depths planktonic foraminifer *Globigerinoides ruber* (white, morphotype senso stricto) is dwelling. Hydrographic changes in subsurface depths are mirrored by planktonic foraminifer *Neogloboquadrina dutertrei* (dextral), which is assumed to inhabit depths varying between ~70 and 200 m in the EEP (details on calcification depths in Chapter 4).

Low salinity water between 500 and 1000 m can be either Antarctic Intermediate Water (AAIW) or North Pacific Intermediate Water (NPIW; [*Bostock et al.*, 2010]). The AAIW in this region is subducted Antarctic Mode Water (AAMW); the AAMW has been formed from the deep winter mixed layer north of the Subantarctic Front in the southeast Pacific [*Hanawa and Talley*, 2001]. The AAIW bottom waters enter the Peru basin from the south through the Chile basin; typically for these water masses are a salinity of ~34.5 and temperatures ranging from 3.5 to 10°C [*Tsuchiya and Talley*, 1996]. The oxygen concentration

is higher but nutrients are lower in these abyssal water masses compared to the overlying deep waters; the composition of the AAIW changes from south to north, indicating an aging of the bottom water masses [*Fiedler and Talley*, 2006]. The AAIW can be found in water depths between 600 and 1300 m offshore Chile [*Bostock et al.*, 2010]. The NPIW is entering the area offshore Peru from the central North Pacific; north of the equator it can be found in depths of 400 to 800 m. In this water mass the salinity is low (~34) as well as the oxygen concentration. Both water masses, the AAIW as well as the NPIW, can not be found undiluted in the study area because they mix and form another water mass, the Equatorial Pacific Intermediate Waters (EqPIW; [*Bostock et al.*, 2010]). This water mass is characterized by relatively low salinity and oxygen concentrations as well as cool temperatures; offshore Peru it is located in water depths of ~300-700 m.

2.2: Oxygen Minimum Zones

Regions with high levels of primary production and resulting decomposition processes leave certain water depths lacking oxygen; these areas with extremely low oxygen concentrations are referred to as OMZs. These zones are sensitive to decadal as well as long-term climate changes [*Deutsch et al.*, 2011]. Recent studies have shown that the oxygen content of the ocean is decreasing and OMZs are expanding [*Stramma et al.*, 2010]; both processes are probably influencing marine ecosystems [*Keeling et al.*, 2010]. The currently observed global warming is closely related to the expansion of the OMZs, because the ability of the ocean to exchange gases with the atmosphere is closely connected to temperatures [*Broecker and Peng*, 1974]. The studied OMZ in the Pacific offshore South-America is currently a source of atmospheric CO_2 [*Friederich et al.*, 2008]; its extension would result in even greater CO_2 out-gassing on a local scale which could possibly also influence the global climate. Anthropogenic warming and climate change will likely influence global circulation patterns and thus the spreading and extension of OMZs worldwide; these are urgent reasons to improve our understanding of OMZ scenarios.

The worlds largest OMZ stretches the western coast of South America, with its center being located between the equator and ~25°S in water depths ranging from ~50 to 700 m (Fig. 2-3. In this case OMZ is defined as O_2<20 µmol kg^{-1} [*Fuenzalida et al.*, 2009]. The upper boundary of this OMZ may be as shallow as 50 m [*Morales et al.*, 1999] and deepens

to ~200 m during strong El Niño events [*Levin et al.*, 2002]. Coastal upwelling of cold and nutritious water is the essential process for the formation of this OMZ. Resulting high Primary Production (PP) leads to degradation processes, which leave certain water depths almost oxygen free (O_2<20 µmol kg^{-1}). The upwelling and overall shape and spreading of the OMZ are controlled by changes in insolation intensity and thus shifts of the ITCZ position. The ITCZ position furthermore provides control on the position of the Equatorial Front (EF), a sharp hydrographic barrier in the EEP.

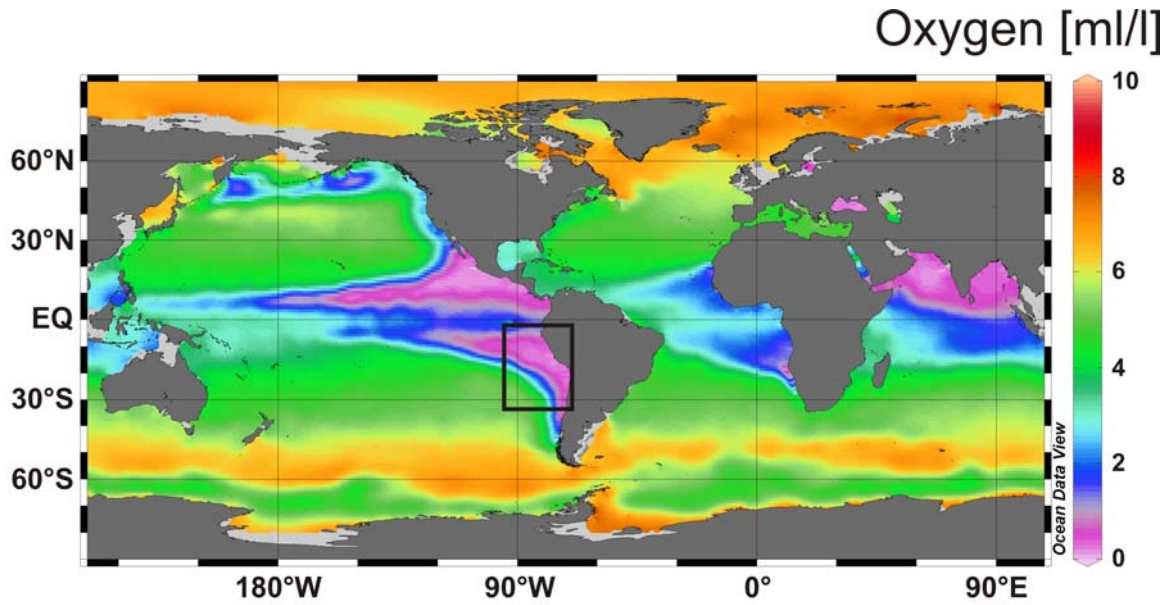

Figure 2-3: Oxygen saturation in 200 m water depth

Oxygen saturation (ml/l; annual mean) in 200 m water depth extracted from the WOA 2009 [*Garcia et al.*, 2010]. Most striking OMZs span the west coast of South America, offshore Namibia and in the Arabian Sea. The rectangle marks the study area offshore Ecuador and Peru.

The Peruvian upwelling system is one of the most productive marine ecosystems worldwide [*Strub et al.*, 1998; *Carr et al.*, 2002]. Even though the high PP rates in the EEP indicate this area might be a net sink for carbon burial (CO_2), the EEP is regarded as a source for CO_2 and the amount of released CO_2 is directly linked to the upwelling intensity [*Friederich et al.*, 2008].

2.3: El Niño Southern Oscillation

The oceanic structure in the EEP has varied in the past on seasonal, inter-annual and long-term scales. During the early months of the year the waters off Ecuador and Peru usually

experience a warming, which is related to the seasonal weakening of the trade winds associated with a southward displaced ITCZ [*Philander*, 1999]. On inter-annual time scales of two to ten years [*Philander*, 1983], this warming is particularly intense and persistent, resulting in an El Niño event (Fig. 2-4). Even though this phenomenon is most strongly evolved in the EEP it is more than a local, coastal event because all El Niño events influence circulation in the entire tropical Pacific Ocean [*Philander*, 1999]. The Southern Oscillation, consisting of warm El Niño and cold La Niña phases (Fig. 2-4), is often described as a see-saw effect between the South-East-Pacific High Pressure Zone and the North Australian-Indonesian Low Pressure Zone [*Philander*, 1983; *McPhaden et al.*, 1998]. Consequently, the Southern Oscillation has the potential to influence the global atmospheric circulation, in particular exchange processes between the atmosphere and the ocean.

Within the EEP El Niño events reduce the **u**pwelling intensity, resulting in a temperature anomaly that in turn causes warmer surface waters. Moreover, Westerlies flatten the equatorial thermocline and at the same time weaken the SEC. During times of particularly strong El Niño events the influential Equatorial Under Current (EUC) might even disappear temporarily [*Philander*, 1999]. The counter part of these events is La Niña, which causes very intense upwelling activity in the area and consequently unusually cold surface waters. The thermocline deepens down to ~150 m during warm El Niño events and is much shallower during cold La Niña conditions. Additionally, La Niña increases the nutrient supply in the EEP through stronger upwelling and hence intensifies marine primary production. Both extremes, El Niño as well as La Niña, are an interplay of the heat-flux interaction between atmosphere and ocean, occurring on time scales of two to ten years [*Philander*, 1983]. The full range of El Niño and La Niña events is called El Niño Southern Oscillation (ENSO; [*McPhaden et al.*, 1998]. El Niño events seriously affect the regional fishing industry because the unusual warm surface waters and the lower nutrient availability result in an increased mortality of commercial fish stocks [*Barber and Chavez*, 1983]; understanding the mechanisms creating this phenomenon are thus also of great economic interest.

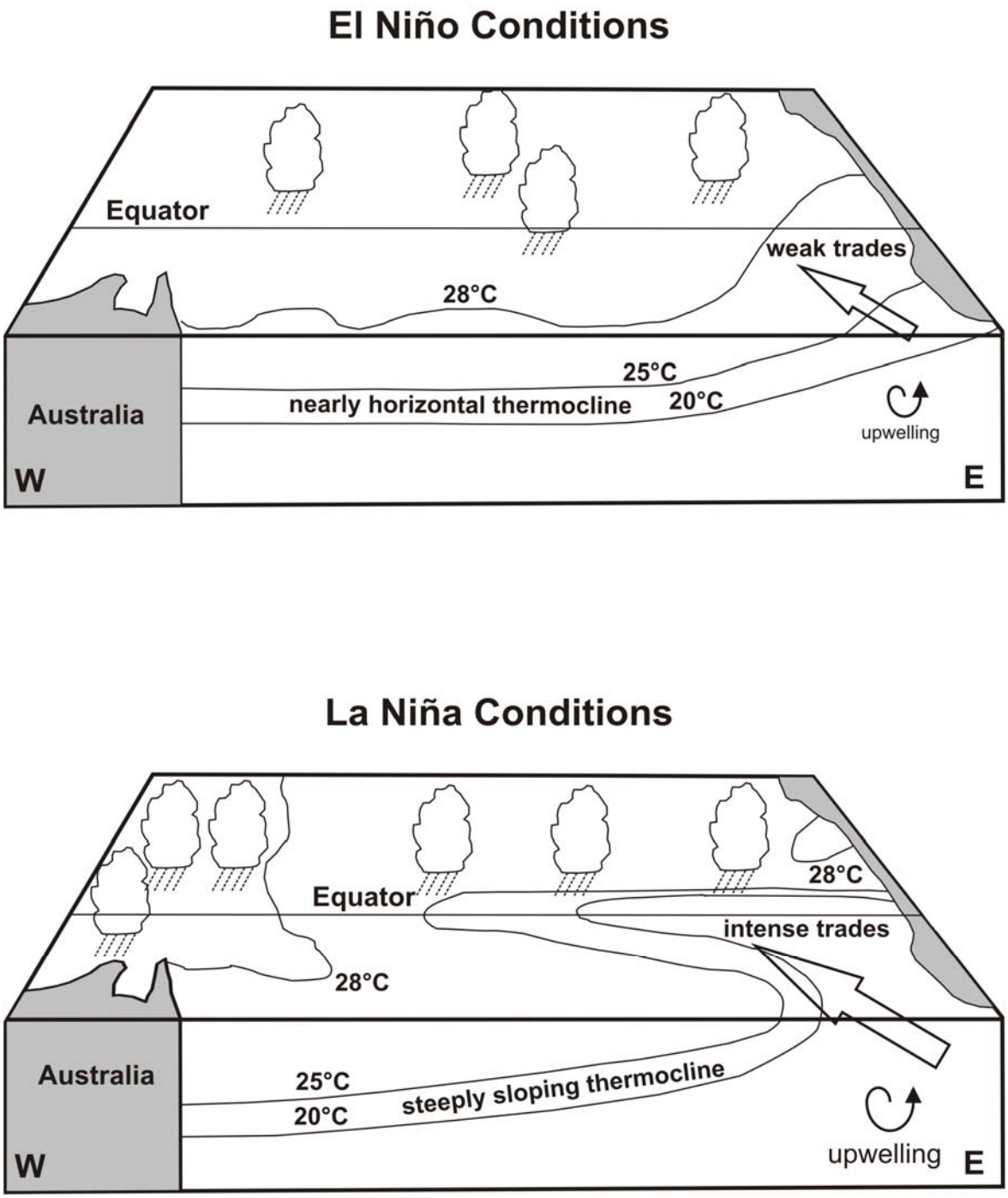

Figure 2-4: El Niño and La Niña conditions

Weaker trade winds result in a decreased upwelling intensity, which causes warmer surface waters to remain in the EEP during El Niño events (upper panel). The water column is characterized by a nearly horizontal thermocline during these events. On the contrary, La Niña (lower panel) is caused by intensified trade winds, which result in a particular strong upwelling. As a consequence, the thermocline is very steep and surface temperatures in the EEP are particularly cool. *Modified after Philander [1999].*

Chapter 3: Material and Methods

3.1: Sedimentology and Core Selection

Sediments offshore Ecuador and Peru are different from outside and inside the OMZ: The cores recovered from outside the OMZ are dominated by varying amounts of dark olive to gray clays and silts, containing different quantities of foraminifers and shell fragments. Also they are partly bioturbated and sometimes sedimentation is disturbed by slumps. In opposition to this, cores taken directly within the OMZ are characterized by fine laminations and higher amounts of diatoms, sometimes containing hardly any foraminifers. The PP off Ecuador and Peru is dominated by diatoms; foraminifers contribute to a much smaller extent to it. As planktonic foraminifers are extremely rare directly within the OMZ, this thesis focuses on piston cores which were recovered at the northern rim of this zone and contained enough foraminifers to perform Mg/Ca and δ^{18}O analyses. Sediment surface samples allowed the analysis of planktonic Mg/Ca and δ^{18}O within and outside the OMZ; benthic foraminifer content was overall sufficient for analyses.

Selection of the core locations was accomplished by extensive bathymetric surveying and sediment-echosounder profiling. The studied sediment cores are piston cores (PC); they were retrieved during a cruise with RV Meteor (Leg 2; Nov-Dec 2008) in the Gulf of Guayaquil (Fig. 2-1). Piston core M772-056-5 (03°44.99' S; 81°07.48' W, recovery 10.58 m) was retrieved from 355 m water depth. Approximately 16 nautical miles further offshore, piston core M772-059-1 (03°57.01' S; 81°19.23' W, recovery 13.59 m) was retrieved from 997 m water depth. The MUC sediment surface samples were collected at 47 stations, spanning a latitudinal transect from the Equator to 17°S and covering a wide depth range from 60 down to 2,600 m (Table 1).

Table 3-1: Multi-corer sediment surface samples

Multi-corer sediment surface samples from the study area in the Eastern Equatorial Pacific. Samples listed here have been used to generate the data for Chapters 4 and 5 (planktonic foraminifers) and Chapter 6 (benthic foraminifers), respectively.

Station number	Latitude (°S)	Longititude (°W)	Water Depth (m)
M771-398	-17.4675	-71.8740	496
M771-408	-17.5728	-71.9333	790

Station number	Latitude (°S)	Longitude (°W)	Water Depth (m)
M771-409	-17.6393	-71.9708	920
M771-411	-17.7450	-72.7450	2167
M771-420	-15.1892	-75.5813	516
M771-450	-11.0002	-78.1662	319
M771-457	-11.0000	-78.3205	467
M771-458	-11.0020	-78.4265	698
M771-462	-10.9998	-78.7450	2020
M771-469	-11.0010	-77.9433	145
M771-471	-11.0001	-78.1656	316.5
M771-482	-11.0003	-78.2362	375
M771-488	-11.0003	-78.3863	580
M771-519	-11.0002	-78.2715	410
M771-554	-10.4397	-78.9117	522
M771-581	-11.1870	-78.1353	352
M771-582	-11.1617	-78.0810	299
M771-583	-11.1143	-78.0518	247
M771-590	-11.2517	-78.2737	547
M771-602	-11.2672	-78.3063	618
M771-608	-12.5417	-77.5083	584
M771-611	-12.4912	-77.4660	417
M771-615	-12.4263	-77.4143	290
M771-623	-12.6333	-77.5932	1085
M772-005-5	-12.0943	-77.6783	214
M772-026-3	-10.7522	-78.4738	424
M772-028-1	-9.2948	-79.8977	1105
M772-029-5	-9.2950	-79.6185	437
M772-031-2	-9.0495	-79.2600	114
M772-045-3	-7.9998	-80.3418	359
M772-047-3	-7.8668	-80.5227	625
M772-050-1	-8.0173	-80.5022	1013
M772-052-3	-5.4835	-81.4502	1252
M772-053-1	-5.4823	-81.5672	2607
M772-056-1	-3.7503	-81.1210	350
M772-059-2	-3.9492	-81.3193	995
M772-060-1	-3.8515	-81.2582	701
M772-062-2	-2.5002	-81.2452	1678
M772-064-1	-1.8915	-81.1958	529
M772-065-2	-1.9502	-81.1205	206
M772-067-2	-1.7523	-82.6245	2075
M772-069-2	-3.2670	-80.9478	339
M772-070-2	-3.1167	-80.6473	59
M772-071-1	-2.8165	-80.8453	100
M772-072-2	-2.8167	-81.0088	425
M772-075-2	-0.2167	-80.6573	1314
M772-076-2	-0.0908	-80.5567	290

3.2: Foraminifers as Temperature Proxy

The ratio of ^{18}O to ^{16}O in the shells of foraminifers can be used as a temperature proxy, because thermodynamic fractionation occurs when oxygen is incorporated into the shells [*Urey*, 1947; *McCrea*, 1950; *Epstein et al.*, 1953; *Craig and Gordon*, 1965; *O'Neil et al.*, 1969; *Shackleton*, 1974; *Kim and O'Neil*, 1997]. Local $\delta^{18}O$ signatures in seawater are controlled mainly by advection and mixing of water masses from different sources, additionally influenced by local evaporation, precipitation and river input. Equilibrium fractionation processes between water and the different carbonate species depict an important temperature influence on the $\delta^{18}O$ signature in foraminiferal calcite [*Rohling and Cooke*, 1999]. Biological fractionation processes ('vital effects') might occur in both, benthic [*Duplessy et al.*, 1970; *Wefer and Berger*, 1991] and planktonic foraminifers [*Fairbanks and Wiebe*, 1980; *Duplessy et al.*, 1981]. The reasons for disequilibrium between seawater and carbonates are various; five main reasons have been identified [*Rohling and Cooke*, 1999]: the ontogenetic effect, the symbiont photosynthesis effect, the respiration effect, the gametogenic effect, and the effect of changes in $[CO_3^{2-}]$. The gametogenic effect in planktonic foraminifers is connected with the vertical migration of the specimen during its life cycle and thus a mixture of different $\delta^{18}O$ signatures from shallower and deeper water masses. The various disequilibrium effects can occur simultaneously and can also mask each other. Some disequilibrium effects occur enhanced amongst planktonic species, but benthic foraminifers might also be affected by them [*Rohling and Cooke*, 1999].

Past ocean temperatures can also be reconstructed via the ratios of magnesium to calcium (Mg/Ca) in the tests of benthic and particularly planktonic foraminifers. These two elements are incorporated into the shells in dependence on the surrounding water temperature [*Nürnberg et al.*, 1996; *Elderfield and Ganssen*, 2000; *Dekens et al.*, 2002; *Anand et al.*, 2003; *Regenberg et al.*, 2009]. The correlation between measured in-situ temperatures and analyzed Mg/Ca ratios from sediment traps, plankton nets or sediment surface samples allows calculating the relationship between both parameters. Some calibration functions are also based on studies of laboratory-based cultures. These transfer functions allow the reconstruction of paleo-temperatures with a precession of approximately ±1°C [e.g. *Regenberg et al.*, 2009].

There is a number of functions for species *G. ruber* and *N. dutertrei* to transfer measured Mg/Ca ratios into temperatures. Table 3-1 gives a brief summary of commonly used transfer functions.

Table 3-2: Summary of different transfer functions for Mg/Ca-based temperature reconstructions Cleaning methods refer to oxidative cleaning (O) or reductive and oxidative cleaning (R/O).

Species	Location	Sampling	Mg/Ca =	Cleaning	Reference
G. ruber, white 240-350 nm	Equatorial Pacific	Core tops	$0.3 * \exp(0.089*T_C)$	R/O	*Lea et al.*, 2000
G. ruber	Multiple	Core tops	$0.38 * \exp(0.09*T_C)$	R/O	*Dekens et al.*, 2002
G. ruber, white 250-350 nm	Sargasso Sea	Sediment traps	$0.34 * \exp(0.102*T_C)$	O	*Anand et al.*, 2003
G. ruber, white 355-400 nm	Atlantic and Caribbean	Core tops	$0.4 * \exp(0.094*T_C)$	O	*Regenberg et al.*, 2009
Warm multispecies 355-400 nm	Atlantic and Caribbean	Core tops	$0.22 * \exp(0.113*T_C)$	O	*Regenberg et al.*, 2009
N. dutertrei 355-400 nm	Atlantic and Caribbean	Core tops	$0.65 * \exp(0.065*T_C)$	O	*Regenberg et al.*, 2009

One crucial issue when using planktonic foraminifers as a temperature archive is the correct assignment of their main habitat depth. Due to vertical migration in the water column the reconstructed temperatures always represent an averaged habitat depth. Investigated species within this thesis are surface dweller *G. ruber* and thermocline dweller *N. dutertrei*. Estimated habitat depths and corresponding seasonal salinity and temperature profiles from the WOA 2009 are displayed in Fig. 2-2. *G. ruber* is assumed to live in the upper ~0-30 m of the water column, while *N. dutertrei* inhabits varying depths of ~70 to ~200 m in the EEP (detailed discussion in Chapter 4).

Under saturation of water masses with respect to calcite ion concentrations can bias the initial Mg/Ca ratio in the foraminiferal tests. Several studies demonstrated a relationship

between low calcite ion concentrations in the water column and changes in the foraminifers test structure [*Dekens et al.*, 2002; *Regenberg et al.*, 2006]. Correction for this dissolution effect, which results in the preferential removal of Mg ions out of the tests and thus a lowering of the originally recorded temperatures, requires either a depth-dependent correction or a correction based on the in-situ carbonate ion concentration. None of the named mechanisms were applied to the data presented in this study. Even though calcite dissolution indeed matters in the EEP today (Fig. 2-2) the equivalence between core top samples and WOA 2009 data set was so good that it can be assumed that dissolution of Mg did not have a major influence on the analyzed samples.

3.3: Foraminiferal Based Analyses

3.3.1: Sample Preparation

Many foraminifers build their tests out of calcium carbonate ($CaCO_3$), including the benthic and planktonic species which were used for different analyses within this thesis. These included radiocarbon datings, stable carbon isotopes ($\delta^{13}C$) and stable oxygen isotopes ($\delta^{18}O$) measurements as well as Mg/Ca based thermometry. The results of benthic $\delta^{18}O$ analyses and radiocarbon datings were used to establish the age models (Chapter 3.5.). The results of planktonic $\delta^{18}O$ from sediment surface samples and analyses of the same proxy in water samples were used to calculate apparent calcification depths for two planktonic species (Chapter 4). The down core measurements of Mg/Ca ratios were combined with alkenone-based thermometry and marine productivity proxies to investigate changes in the local water masses from the deglaciation into the Holocene (Chapter 5). The Mg/Ca ratios from multi corer (MUC) sediment surface samples were combined with CTD-casted temperature profiles to develop a benthic transfer function for the EEP (Chapter 6).

Piston core sub-samples were taken by syringes and contained roughly 10 cm^{-3} of sediment. Parallel series of samples were taken for foraminiferal-based and for bulk sediment analyses. The volume of the syringe samples was noted as well as their wet weight. All samples were freeze-dried and weighed afterwards to calculate the amount of pore water, which evaporated during the drying procedure. The upper ~4m of both cores (056

and 059) were additionally sampled with 1 cm thick slices; this was necessary since the generally lower amount of foraminifers in these core sections demanded that a greater amount of sediment material was needed. Subsequently, the sediment samples were washed over a 63 µm wide sieve, transferred with de-ionized water and dried at ~50°C. The remaining coarse or sand fraction was weighed to calculate the weight percent (on average 1-3%). Dried samples were sieved into six different size categories (63-125 µm, 125-250 µm, 250-315 µm, 315-355 µm, 355-400 µm, >400 µm). The surface samples are

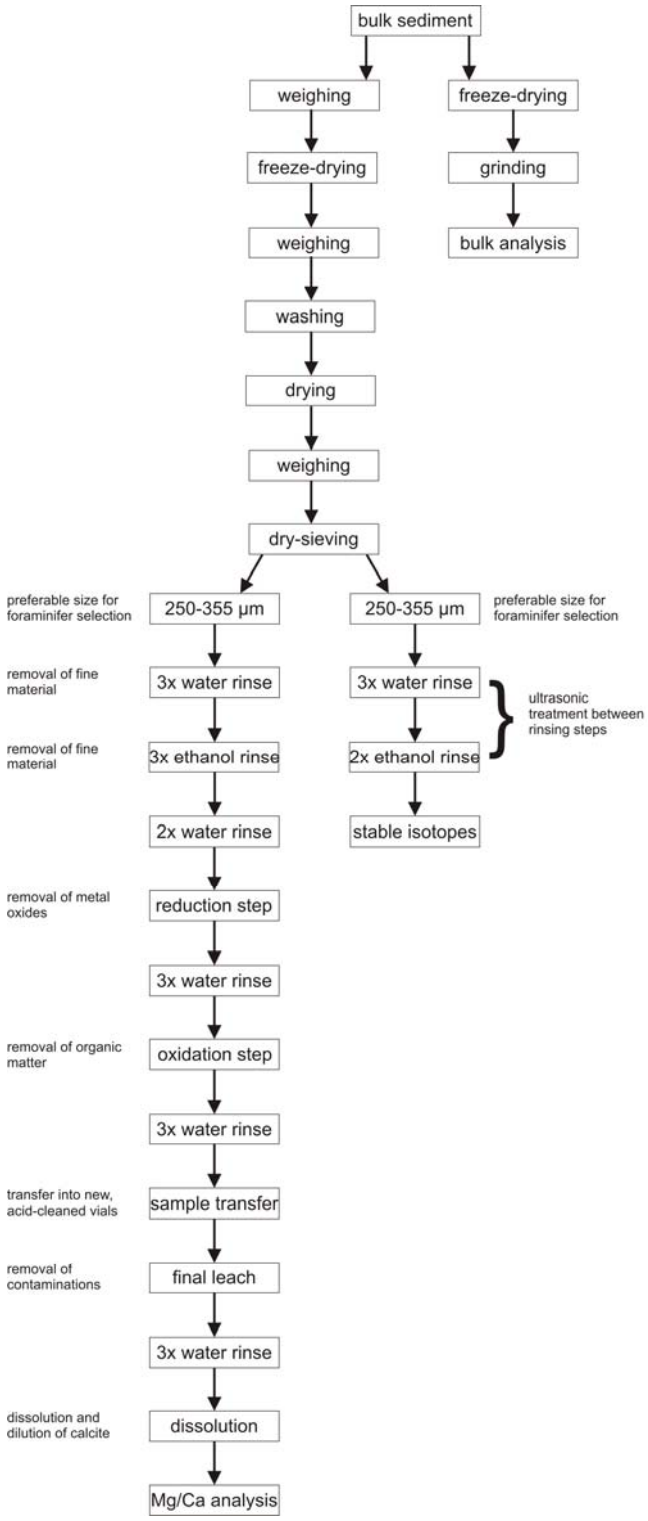

Figure 3-1: Standardized scheme of sample processing for Mg/Ca, stable isotopes and bulk sediment

Standardized scheme of sample processing as performed for Mg/Ca, stable isotopes and bulk sediment analyses. All three investigated foraminiferal species were treated as described in the above scheme with respect to Mg/Ca and stable isotope analyses.

derived from MUCs from legs 1 and 2 of the same Meteor cruise. MUC surface samples consist of the uppermost ~0-1 cm of the sediment, only if the foraminifer content was considered too low this range was widened to ~0-2 cm sediment depth. The MUC samples were prepared in the same way for foraminiferal analyses as the PCs, the only difference being that the MUC samples were washed wet and that freeze-drying was skipped.

3.3.2: AMS Radiocarbon Dating

Accelerator Mass Spectrometry (AMS) was used to provide absolute age control for the studied sediment cores via radiocarbon (^{14}C) dating. Mono-specific samples of subsurface dweller *Neogloboquadrina dutertrei* (Fig. 3-2) were analyzed at the Leibniz-Laboratory for Radiometric Dating and Isotope Research, University of Kiel. Approximately 300 calcite tests from size fractions >250 µm were selected to achieve sample weights of ~8-10 mg. The $CaCO_3$ concentrations in the samples were varying between ~1 and ~8%. A detailed discussion of the age models and the resulting stratigraphy is given in Chapter 3.5..

3.3.3: Stable Carbon and Oxygen Isotopes

Stable carbon ($\delta^{13}C$) and oxygen isotope ratios ($\delta^{18}O$) were measured in calcite tests of both, benthic and planktonic species. The ratios are given in the common δ-notation ($\delta = (R_{sample}/ R_{standard} - 1) \times 1000$, where R is the ratio between the heavy and the light isotope). Benthic foraminifers can experience a size-related bias with respect to the stable isotope signal [*Lutze et al.*, 1979]. Hence, for stable isotope analyses two to three specimens of the endobenthic species *Uvigerina peregrina* (Fig. 3-2) were selected from a narrow size range (250-355 µm) to avoid any size-related bias. A change in the stable isotope ratio of foraminifers due to tests of differently sized individuals is also referred to as 'ontogenetic effect'. $\delta^{18}O$ ratios in sea water change due to the amount of globally fixed ice volume, which removes ^{16}O from the global oxygen budget [*Rohling and Cooke*, 1999]. Thus, $\delta^{18}O$ values do not only contain information about temperature changes, but can also be used for stratigraphic purposes as they indicate changes between glacial and interglacial times [*Lisiecki and Raymo*, 2005].

For combined stable isotope and Mg/Ca analyses samples of ~25 clean specimen of dextral coiling *N. dutertrei* and ~30 specimens of *G. ruber* (Fig. 3-2) were picked from size fractions 250-355 µm. The samples were picked from this narrow size range to avoid size-related intraspecific elemental variations [*Elderfield et al.*, 2002]. The planktonic foraminifer content was lower in the upper 4 m of both cores than in the remaining parts; the size range was expanded during picking if necessary to gain enough material for the analyses. This was particularly the case for *G. ruber*, as its occurrence was strongly reduced in the top part of the cores. Consequently, *G. ruber* samples for the upper 4 m were picked from the 125-400 µm size fractions for both cores. All specimens were individually picked and identified using the planktonic foraminifers species concepts by *Kennett and Srinivasan* [1983] and *Hemleben et al.* [1989]. The selection of *N. dutertrei* was limited to individuals, which had a tooth at their final chamber since this characteristic enables a definite species classification. From those MUC surface samples, which were analyzed for benthic stable isotopes and Mg/Ca, ~20 specimen of *U. peregrina* were selected from the 250-355 µm size fractions. The samples were gently crushed between two glass plates to open the chambers for following cleaning procedures; the samples were homogenized and split for stable isotope (~$^1/_3$) and Mg/Ca analyses (~$^2/_3$ of total sample) and transferred into acid-cleaned vials (Fig. 3-1). Subsamples for stable isotope analyses were rinsed three times with ultrapure water (MilliQ 18.2 MΩ), twice with ethanol and sonicated in between each rinse to remove clay particles.

Measurements were conducted with a ThermoScientific MAT 253 mass spectrometer, equipped with an automated CARBO Kiel IV carbonate preparation device (GEOMAR, Kiel). The calcite was dissolved with phosphoric acid at 70°C, releasing CO_2 which was subsequently analyzed. Manually detrended results were calibrated versus NBS19 (National Bureau of Standard and reported in per mill relative to the Vienna Pee Dee Belemnite (‰ VPDB). The in-house standard used was the “Standard Bremen” (Solnhofen limestone), which indicates an analytical long-term precision (n > 1000) of ±0.03‰ for $\delta^{13}C$ and ±0.06‰ for $\delta^{18}O$.

3.3.4: Foraminiferal Mg/Ca Analyses

Samples for Mg/Ca measurements were cleaned following the protocol of *Barker et al*. [2003], but adding a reductive step [*Martin and Lea*, 2002]. The initial cleaning for Mg/Ca analyses followed the protocol for stable isotopes (Fig. 3-1). The last rinse with ethanol was followed by two rinses with ultrapure water to remove any remaining ethanol. A reductive step was performed to remove metal oxides from the shells. 375 µl of hydrazine were mixed with 15 ml of ammonium citrate; 100 µl of this solution was added to each sample. The samples were put into a 92°C hot water bath and carefully agitated every five minutes to release any gaseous build-up. The samples were rinsed three times with ultrapure water, followed by an oxidation step. Here, 250 µl of an 80 µl H_2O_2 to 15 ml sodium hydroxide mixture were added to each sample. Again a 10 minutes treatment in a hot water bath was carried out, including agitation to prevent too much gaseous pressure, followed by three rinsing cycles. Afterwards, samples were transferred into new vials and a final leaching with 0.001 molar HNO_3 was performed. The samples were dissolved in 2 ml of 0.075 molar HNO_3 (thermally distilled, “supra acid”) prior to measurement. The samples of core M772-059-1 were dissolved in 0.075 molar HNO_3 and diluted with 2.5 ml yttrium water (made by adding 1 ml dissolved yttrium to 1 l of 0.075 molar suprapure HNO_3, which equals a concentration of 1 ppm yttrium). The Yttrium was added to detect a possible machine drift.

Mg/Ca analyses of core M772-056-5 (*N. dutertrei*) and MUC surface samples (*N. dutertrei*) were carried out with a simultaneous, radial-viewing Inductively Coupled Plasma – Atomic Emission Spectrometer (ICP-AES; SPECTRO *Ciros^{CCD} SOP*) at the University of Kiel. Spectral lines used were 279.553 for Mg and 370.603 for Ca. All remaining samples were analyzed with a simultaneous, axial-viewing Inductively Coupled Plasma – Optical Emission Spectrometer (ICP-OES; Varian 720) at GEOMAR. Spectral lines used were 279.553 for Mg and 370.602 for Ca. The measurements at both machines involved the analysis of standards and blanks to assure analytical quality control. The data from the ICP-AES was manually drift-corrected; a software automatically corrected samples from the ICP-OES for analytical drift (detrending). All results were manually normalized to the ECRM 752-1 standard (Mg/Ca = 3.761 mmol mol^{-1}; [*Greaves et al.*, 2008]), which was used as internal consistency standard. The quality standard ECRM 752-1 was run on both machines to track pos-

sible offsets between machines; average values for Mg/Ca were 3.86 ±0.09 mmol mol^{-1} (*SPECTRO Ciros*, Kiel University) and 3.80 ±0.06 mmol mol^{-1} (Varian, GEOMAR), respectively. Analytical precision, with respect to the Mg/Ca ratio of the ECRM standard, was ~0.1 mmol mol^{-1} (2 σ). Replicate measurements of selected samples were performed for eight samples on both machines (ICP-AES and ICP-OES). The correlation between both data sets was high (R^2=0.9), indicating a strong consistency in ICP analyses additionally to the ECRM quality control.

To exclude clay contamination and post-depositional Mn-rich carbonate coatings, which can have strong control on Mg/Ca ratios [*Rosenthal et al.*, 2000], Fe/Ca, Al/Ca and Mn/Ca ratios of the samples were analyzed. Al/Ca and Mn/Ca ratios were below the detection limit of the ICP within the data sets. Previous studies have shown that Mn is already reduced in the water column offshore Peru and thus only minor amounts of particulate-bound Mn are available at the bottom of the sea [*Böning et al.*, 2004; *Scholz et al.*, 2011; *Glock et al.*, 2012]. Fe/Ca ratios were on average 4.08 mmol mol^{-1}. A correlation between high Fe/Ca ratios and outliers within the Mg/Ca data set was not observed, hence leading to the conclusion that the measured high Fe/Ca ratios did not affect the Mg/Ca signal.

Mg/Ca-based subsurface sea temperatures ($subSST_{Mg/Ca}$) were reconstructed by applying the 'warm water' multispecies calibration of *Regenberg et al.* [2009]:

$$Mg/Ca = 0.22 * \exp(0.113 * T_c) \quad (1)$$

Mg/Ca ratios of planktonic *G. ruber* were converted into temperatures ($SST_{Mg/Ca}$) by using the 'species specific' calibration for *G. ruber* of *Regenberg et al.* [2009]:

$$Mg/Ca = 0.4 * \exp(0.094 * T_c) \quad (2)$$

Analytical precision for Mg/Ca translates into an uncertainty for the paleo-temperature estimations of ±1°C.

Paleo salinities were approximated from the ice-volume corrected $\delta^{18}O$ of seawater ($\delta^{18}O_{ivf\text{-}sw}$). The $\delta^{18}O$ signal in foraminiferal tests is a function of temperature and the isotopic composition of the surrounding seawater ($\delta^{18}O_{sw}$, reported in ‰ Vienna Standard Mean Ocean Water). The $\delta^{18}O_{sw}$ is influenced by regional variations in hydrology and by global ice volume changes [*Schmidt et al.*, 2004]. The $\delta^{18}O_{ivf\text{-}sw}$ was calculated by using the equation by *Thunell et al.* [1999]:

$$T = 14.9 - 4.80 (\delta^{18}O_{calcite} - \delta^{18}O_{sw}) \quad (3)$$

To generate the regional $\delta^{18}O_{ivf\text{-}sw}$, we accounted for changes in global $\delta^{18}O_{sw}$ due to continental ice volume variability using the relative sea level curve of *Waelbroeck et al*. [2002].

The foraminiferal Mg/Ca signal can be affected by several processes: Re-crystallization of calcite crystals might distort the original information of the tests, thus resulting in a misinterpretation of Mg/Ca ratios. Diagenetic alteration might further influence the test structure; within the EEP this process is mainly occurring in the form of metal oxides, which form under anoxic conditions inside the deposited foraminiferal tests. The most severe problem when working with foraminifers is the potential dissolution of their tests. Dissolution primarily removes the Mg out of the tests, resulting in a lowering of the Mg/Ca ratio; it is thus essential to evaluate in particular the influence of dissolution onto our samples. A correction of the initially measured Mg/Ca ratios was not applied, even though most samples were recovered from below the critical depth for selective Mg-removal (~250 m; according to *Regenberg et al.*, 2006) and also from below the Calcite Saturation Horizon (CSH; ~300 m; Fig. 2-2). The reason for this was the good fit between initially measured Mg/Ca ratios and the reconstructed temperatures and data from WOA 2009 ([*Locarnini et al.*, 2010]; see supplementary of Chapter 5 for more details).

3.3.5: Characteristics of Foraminifers

3.3.5.1: Benthic Species *Uvigerina peregrina*

The preferred habitat of *U. peregrina* (Fig. 3-2) are the uppermost centimeters of the sediment, although it may migrate as deep as 10 cm into the sediment [*McCorkle et al.*, 1997]. The habitat depth changes under the influence of bottom water oxygen concentrations and is shallower if oxygen concentrations are low and *vice versa* [*Sen Gupta and Machain-Castillo*, 1993; *Loubere et al.*, 1995]. *U. peregrina* is widely used for $\delta^{18}O$ analyses since *Shackleton* [1974] described the species to be a reliable recorder of the bottom water $\delta^{18}O$ signature. Although the species lives infaunal, the Mg/Ca ratio reliably reflects Bottom Water Temperatures (BWT; [*Elderfield et al.*, 2010]).

A recent study from the Peruvian OMZ [*Mallon*, 2011] indicates that the presence of *U. peregrina* is restricted by bottom water oxygen concentrations. Between 10°S and 15°S, where the OMZ is most intense, *U. peregrina* was not found in stations above 520 m. The

species was partly present in the OMZ, but its main occurrence was below the OMZ, where oxygen concentrations exceeded 4.8 µmol kg-1. In areas in the EEP where *U. peregrina* was present, its habitat was located within the upper 0-2 cm of the sediment [*Mallon*, 2011]. Consequently, *U. peregrina* is regarded as a reliable proxy to display changes in bottom water conditions within the Peruvian OMZ.

3.3.5.2: Planktonic Species *G. ruber* and *N. dutertrei*

Planktonic foraminifers live worldwide in a great range of habitats, from surface waters down to depths of up to 800 m [*Hemleben et al.*, 1989]. Their good fossilization potential and their broad occurrence make them a favorable proxy in paleoceanography to reconstruct changes in ocean conditions. However, as planktonic foraminifers experience significant vertical migration throughout their ontogenetic life cycle, information gained from their tests will thus display a mixture of different depths. The cause for these differences might depend on temperature and salinity concentrations as well as differing nutrient concentrations. Calcification depths derived from stable oxygen analyses ($\delta^{18}O$) thus represent an average depth, which the foraminifer inhabited during its life cycle. Geochemical analyses for this thesis were performed on the surface dwelling species *Globigerinoides ruber* white; ~0-30 m WD (morpho type sensu stricto; [*Wang*, 2000; *Steinke et al.*, 2005]) and on the subsurface dwelling species *Neogloboquadrina dutertrei* (dextral coiling; ~70-200 m WD), which are depicted in Figure 3-2.

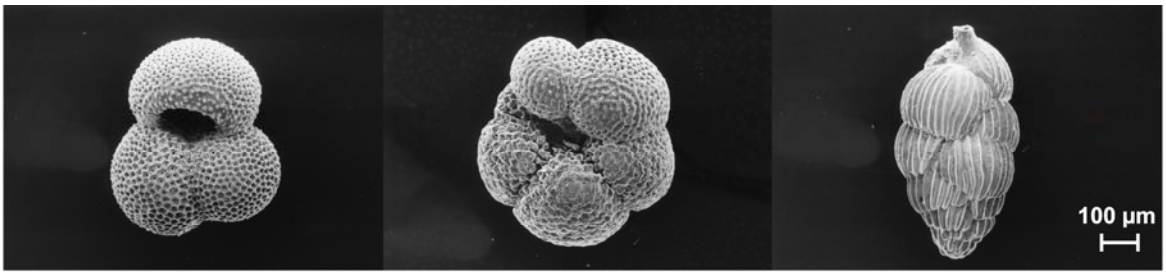

Figure 3-2: Scanning electron microscope images of all investigated foraminiferal species

From left to right pictures show planktonic species *G. ruber* white (morphotype sensu stricto), *N. dutertrei* (dextral coiling) and benthic species *U. peregrina*. All specimens were selected from two piston cores in the study area (M772-056-5 and -059-1, respectively). Scale bar is 100 µm for all pictures; applied voltage was 15 kV.

3.3.5.3: $\delta^{13}C$ in Foraminifers

$\delta^{13}C$ can widely be used as a proxy for multiple purposes, since it is influenced by a number of factors. Photosynthesis processes in the surface ocean preferably remove the lighter ^{12}C from the ocean, leaving the upper layers enriched in ^{13}C which is incorporated in the carbonates formed in these water depths. Re-mineralization processes in greater depths release not only ^{13}C depleted CO_2, but they also provide nutrients [*Rohling and Cooke*, 1999]. Furthermore, lateral gradients in $\delta^{13}C$ in deep water can be used to trace the source of these water masses, sometimes also referred to as 'aging' of the water masses. The $\delta^{13}C$ signature provides information on the time of exposure to organic matter decay and the amount of organic matter decayed within the deep water [*Rohling and Cooke*, 1999]; it is an essential tool for the reconstruction of ocean circulation processes. Additionally, the $\delta^{13}C$ in the ocean is also influenced by the interaction between atmosphere and the ocean, with the latter one representing a much larger reservoir than the atmosphere.

Deviation from equilibrium values in the $\delta^{13}C$ ratios of benthic and planktonic foraminifers might be caused by: (1) utilization of metabolic CO_2 during shell formation, (2) photosynthesis activity of symbionts, (3) growth rate, and (4) variation in carbonate ion concentration in ambient waters [*Rohling and Cooke*, 1999]. In particular the uptake of respiratory CO_2, which is often referred to as 'vital effect', is difficult to evaluate. The 'vital effect' magnitude is proportional to the amount of metabolic CO_2 within the organism's internal CO_2 pool, which reflects the organism's ability for gas exchange with ambient water [*Rohling and Cooke*, 1999]. Organisms from OMZs worldwide show little influence of 'vital effects', indicating that they are especially adapted to an efficient gas-exchange with the ambient water [*Leutenegger and Hansen*, 1979; *Grossman*, 1984; 1987]. Recent studies have also used $\delta^{13}C$ as a water mass tracer, to differentiate between water masses of (sub) tropical and (sub) polar origin [*Euler and Ninnemann*, 2010]

3.4: Bulk Sediment Analyses

Bulk sediment samples were used to determine total organic carbon (TOC), total nitrogen, biogenic opal and to perform quantitative XRF and $U^{K'}_{37}$ (alkenones) analyses. Cores 056

and 059 were sampled as described in Chapter 3.2.1. The samples were freeze-dried, ground and homogenized; the samples for the total organic carbon (TOC) and total nitrogen (TN) analyses were homogenized in a planetary mill to ensure an extremely regular sample composition. The samples for biogenic opal analyses were homogenized manually, using an agate mortar to ensure a coarse-grained structure.

3.4.1: Alkenone Unsaturation Index ($U^{K'}_{37}$)

Besides foraminiferal analyses, SSTs were also derived from the alkenone unsaturation index ($U^{K'}_{37}$). The alkenone analyses were carried out within the frame work of the complementary PhD thesis by *Mollier-Vogel* [2012]. Alkenones are synthesized mainly by coccolithophorids (e.g. *Emiliania huxleyi*), which live in the uppermost ~10 m of the water column within the photic zone (Fig. 2-2). The concentration of long-chain ketones varies in the sedimentary record, depending on the water temperatures in which the coccolithophorids lived. The analytical method for the $U^{K'}_{37}$ record of core 059 (Chapter 5) is described in detail in the complementary PhD thesis of *Mollier-Vogel* [2012].

3.4.2: Total Organic Carbon and Total Nitrogen

The total organic carbon (TOC, wt %) and total nitrogen (TN, wt %) were measured in bulk sediment to assess changes in paleo-productivity. The TOC content for core 056 was determined by a LECO C-S analyser with a precision for repeated measurements of ±0.5% (2 σ; University of Bordeaux, France). The TN of the sediment samples from core 056 was measured with a CARLO ERBA CN analyser 2500 at University of Bordeaux, France (precision ±0.5%, 2 σ values). The TOC, TN and total carbon (TC, wt %) for sediment samples of core 059 were analyzed with CARLO ERBA Model NA 1500 Elemental Analyzer at GEOMAR, Kiel (Germany), where replicate analysis of an internal standard was 0.15% for TN and TC, and 0.2% for TOC (2 σ; n=10). The TC and TN were measured in bulk sediment samples whereas the TOC was measured in decalcified samples (HCl, 0.25 M). The ratio of atomic organic carbon to atomic nitrogen was calculated, which will be hereafter referred to as C/N ratio. C/N ratios of bulk sediment are an indicator of the source of organic matter in the sediment. Typically, marine organic matter exhibits C/N ratios of 5-8 close to

the Redfield ratio (C/N ~7) of marine phytoplankton [*Redfield et al.*, 1963], while terrestrial organic matter shows ratios between 20 and 200 [*Hedges et al.*, 1986].

3.4.3: XRF Core Scanning

The split halves of both cores were analyzed in a non-destructive way with the Avaatech XRF Core Scanner (University of Kiel). These analyses were carried out within the frame work of the complementary PhD thesis by *Mollier-Vogel* [2012]. The cores were scanned with a spatial resolution of 1 cm applying a basic voltage of 10 kV, which covers the elements aluminium (Al) to iron (Fe). Filters of 30 and 50 kV were used to reduce the background for certain elements. Prior to the analysis, the core halves were covered with SPEX Ultralene® foil to prevent contamination of the instrument sensor and desiccation of the core during the measurement. According to *Tjallingii et al*. [2007], the observed elements remain relatively unaffected by changing physical properties, i.e. water content. Data quality was ensured by monitoring the "dead time", which was constantly below the critical value of 40% [*Tjallingii*, 2006]. The element intensities are given in counts per second (cps) and are used to estimate elemental concentrations. However, log ratios for elemental ratios were partly calculated as these do surely exclude any matrix effects which might have been caused by the scanning process [*Tjallingii et al.*, 2010].

3.5: Age Models and Stratigraphy

The age models for both cores are primarily based on AMS^{14}C datings of the planktonic foraminifer *N. dutertrei*, supported by benthic δ^{18}O records. AMS-^{14}C ages were converted into 2 σ calendar ages using the CALIB 6.0 software [*Reimer et al.*, 2009]. Calendar ages are reported in BP (= before present, i.e. before 1950 AD). Ages are expressed in kilo annum (ka) BP when referring to a point in time and in kilo years (kyrs) when referring to a time span. A constant reservoir effect (ΔR) of 200 ±50 years was applied which is based on values from the Marine Reservoir Correction Database (http://calib.qub.ac.uk/marine/). The ΔR is based on a mean value from sites located closest to the study sites. The selected regional ΔR is in agreement with a duplicate-dating performed on a benthic and a planktonic foraminifer sample from a multi corer

station (station M772-056-1; 03°45.01' S, 81°07.29' W, 350 m WD). The planktonic sample revealed an (uncorrected) age of recent origin, whereas the benthic sample was dated at 660 ± 30 years. Subtracting 400 years from the 660 years, which is the basic setting for the worldwide reservoir correction in the CALIB program, a local reservoir effect of ~200 years is assumed. This value is in agreement with the ΔR from the Marine Reservoir Correction Database.

A recent publication [*Ortlieb et al.*, 2011] suggests a varying reservoir effect during the Holocene for the region in the Eastern Pacific spanning 14-24°S. This approach was tested for the age models, but the resulting calendar ages were implausible for the shown data records. The correlation between the benthic δ^{18}O records and a global stack record for further stratigraphic control [*Lisiecki and Raymo*, 2005] were less conclusive when the reservoir ages by *Ortlieb et al.* [2011] were applied. Consequently, the averaged reservoir age calculated from samples out of the Marine Reservoir Correction Database seems to be the more precise approach to convert ^{14}C ages into calendar ages. No tuning of our records to other data sets was performed. Benthic δ^{18}O records were compared graphically with a globally stacked δ^{18}O record [*Lisiecki and Raymo*, 2005].

Linear sedimentation rates (LSR) were calculated between age control points as the thickness of a sediment interval divided by the time interval of its deposition (Fig. 3-3). The LSR for core 059 peak during the Bølling/Allerød (B/A; 14.7-12.9 ka BP; [*Blockley et al.*, 2012]) with values of max. 150 cm kyr^{-1} and are much lower before and after this episode (LSR ~80-90 cm kyr^{-1}). Towards the Late Holocene LSR for core 059 are decreasing down to values of ~50 cm kyr^{-1}. The LSR for the shallower core 056 are on average higher (~90-110 cm kyr^{-1}), and also decrease during Middle and Late Holocene towards ~60-80 cm kyr^{-1}.

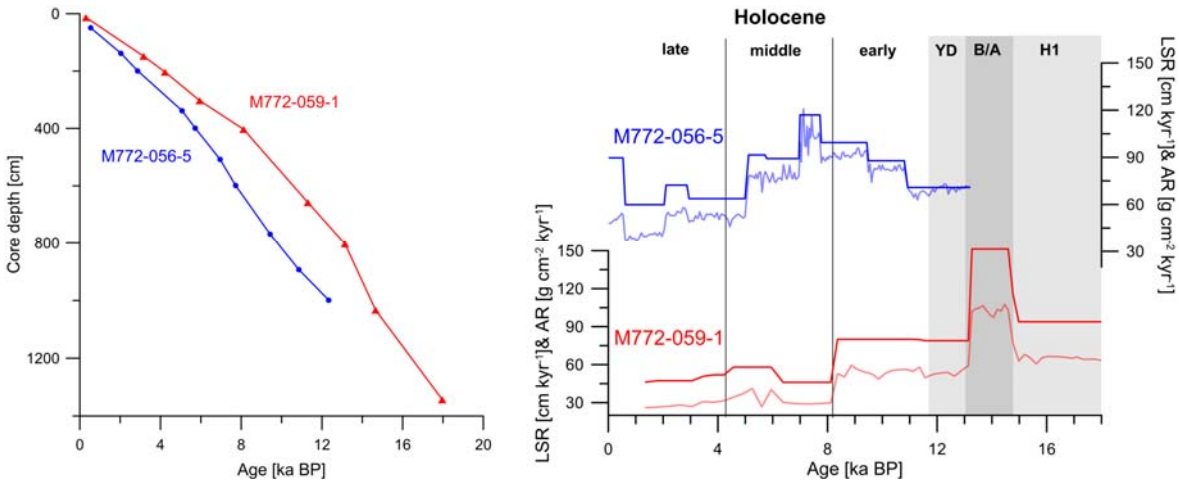

Figure 3-3: Age-depth relation for cores 056 and 059; AR and LSR for cores 056 and 059

Left panel shows relationship between core depth and AMS^{14}C-dated age control points for cores 056 (blue) and 059 (red).

Right panel shows linear sedimentation rates (LSR; solid lines) and bulk sediment accumulation rates (AR; transparent lines), which are plotted on the same scale. LSR and AR peak during the B/A interval in core 059 and during the Middle Holocene in core 056. LSR values average to ~70-90 cm kyr^{-1} for core 059 and to ~80-100 cm kyr^{-1} for the shallower core 056, respectively.

Core 056 has an average temporal resolution of ~60 years for the geochemical analyses and up to 10 years for the XRF-scanned data. The temporal resolution of core 059 is slightly lower, averaging ~80 years (geochemical analyses) and ~25 years (XRF-scanned data), respectively. The paleo-flux of bulk sediment as well as sediment components is expressed by accumulation rates (AR in g cm^{-2} kyr^{-1}). AR were computed following the approach of *van Andel et al*. [1975]: AR_{bulk} = LSR * D_{bulk}, where LSR is the linear sedimentation rate (cm kyr^{-1}) and D_{bulk} is the dry bulk density (g cm^{-3}). In general, the shallower core 056 has higher AR (85 to 60 g cm^{-2} kyr^{-1}) than the deeper core 059 further offshore (~50 to <30 g cm^{-2} kyr^{-1}; Fig. 3-3). Both cores show relatively high AR, thus providing an excellent temporal resolution.

Chapter 4:

Calcification Depths of Planktonic Foraminifers *Globigerinoides ruber* and *Neogloboquadrina dutertrei* in and outside the Peruvian Upwelling

Tebke Böschen[1*], Dirk Nürnberg[1], Kristin Doering[2], Lars Klostermann[3] and Christian Dullo[1]

[1] Helmholtz Centre for Ocean Research Kiel (GEOMAR)
Wischhofstrasse 1-3, 24148 Kiel, Germany

[2] Institute of Geosciences, University of Kiel
Ludewig-Meyn-Str. 10, 24118 Kiel, Germany

[3]Institute of Geosciences, Goethe University
Altenhöferallee 1, 60438 Frankfurt am Main, Germany

Keywords: planktonic foraminifers, calcification depth, $\delta^{18}O$, EEP, upwelling

Prepared for submission to *Biogeosciences*

Abstract

The reliable estimation of calcification depths for planktonic foraminiferal species remains a challenge, mainly due to the fact that available information is sparse and regional as well as seasonal differences occur. While *Globigerinoides ruber* is broadly accepted to dwell at surface depths, the subsurface-dwelling species *Neogloboquadrina dutertrei* is often associated with the thermocline. This depth assignment remains vague and not all studies agree upon this view. In this study we present stable oxygen isotope data ($\delta^{18}O$) of *N. dutertrei* (dextral) and *Globigerinoides ruber* (white, sensu stricto), samples taken in the Eastern Equatorial Pacific (EEP) along the Ecuadorian and Peruvian continental margin from the equator to 11°S. Respective calcification depths for both species were calculated by using $\delta^{18}O$ measurements of water samples from the same ocean area. $\delta^{18}O$ values of *N. dutertrei* are in good agreement with $\delta^{18}O_{seawater}$ values, while $\delta^{18}O_{G.\ ruber}$ shows stronger isotopic fractionation towards lighter values. The calculated calcification depth of *G. ruber* implies sea surface conditions as the predominant living depth, while *N. dutertrei* appears to change calcification depth in relation to the oceanographic setting (varying from 25 to 310 m). The calcification depth of *N. dutertrei* is on average ~200 m in the northern part of our study area and shoals to ~70 m due to the influence of the upwelling center off Peru; hence, changes in the apparent calcification depth of *N. dutertrei* seem to be closely correlated with the local hydrography, in particular with the oxygen concentrations in subsurface depths.

4.1: Introduction

Defining the habitat depth of planktonic foraminifers remains a challenge since their habitat changes throughout their life cycle [*Hemleben et al.*, 1989]. For the correct interpretation of paleo-data it is crucial to know the calcification depth of the analyzed foraminiferal species as exactly as possible. Planktonic foraminifers inhabit a wide range of depths, from surface waters down to ~800 m [*Hemleben et al.*, 1989]. Many species are known to sink to greater water depths when they reach their gametogenic stadium. Consequently, the reconstructed habitat depth of any planktonic foraminifer will always represent different water depths and thus should be referred to as apparent calcification depth (ACD).

This investigation focuses on the planktonic species *G. ruber* (white) and *N. dutertrei*. As a photosynthesizing species *G. ruber* is a surface dweller [*Deuser et al.*, 1981; *Bé et al.*, 1985; *Dekens et al.*, 2002], being restricted to the top ~30 m of the water column where its symbionts catch enough light. *Deuser et al.* [1981] indicate a year-round presence of *G. ruber*, thus making it suitable for reconstructing annual sea surface temperature (SST). *N. dutertrei* is often referred to as 'thermocline dweller', implying that the preferred habitat of this species is the thermocline and adjacent areas (~50-150 m; [*Fairbanks et al.*, 1982; *Hemleben et al.*, 1989; *Loubere*, 2001]). However, the depth of the thermocline varies strongly between different ocean basins and might furthermore change in the course of a year. A core top study from the EEP indicates a calcification depth for *N. dutertrei* of ~110 m [*Faul et al.*, 2000]. The intensity of upwelling in the EEP is changing throughout the year, thus providing an extremely variable environment for planktonic foraminifers. Upwelling is strongest during austral winter (July to September), when the depth of the thermocline shoals [*Kessler*, 2006].

In this study we present a combined set of sediment surface and water samples from the EEP, covering a wide range of latitudes and water depths. We aim to improve already existing calcification depth estimates for species *G. ruber* and *N. dutertrei* within and outside the upwelling system in the EEP. Combined analysis of calcite $\delta^{18}O$ values and $\delta^{18}O$ in water samples taken during the same cruise allows to estimate ACDs within the upwelling area off Ecuador and Peru. Additionally, $\delta^{13}C$ and phosphate data from the water column locate the active upwelling center south of ~5°S. The results confirm the previous knowledge of *G. ruber* being restricted to the surface of the ocean. *N. dutertrei* calcifies in much

greater water depth in the northern part of the study area (~200 m) than in the southern part (~70 m). A possible cause for this is the expansion of cooler and oxygen-lacking water masses towards the water surface due to enhanced upwelling in the southern area.

4.2: Hydrography

The complex hydrographic setting in the EEP (Fig. 4-1) has been described in several studies, e.g. *Kessler* [2006], *Fiedler and Talley* [2006], *Montes et al.* [2010]. Persistent easterly trade winds result in an offshore Ekman transport of surface waters, which is balanced by equatorial upwelling [*Kessler*, 2006], thus allowing colder, nutrient-rich water masses from subsurface depths to enter the EEP. Lateral extension of the upwelling can be identified by different proxies measured in the water column, e.g. $\delta^{13}C$, phosphate or dissolved oxygen (Fig. 4-2). Wind and upwelling intensity vary throughout the year due to changes of the position of the ITCZ; coastal upwelling is shallow offshore Ecuador and Peru, reaching to a depth of ~75-100 m [*Huyer*, 1980; *Huyer et al.*, 1987; *Kessler*, 2006]. The thermocline is located in ~50-70 m water depth, being shallower south of ~5°S due to enhanced upwelling [*Locarnini et al.*, 2010]. Upwelling is strongest during austral winter (July to September), when the ITCZ moves from ~5°N to ~10°N [*Karstensen and Ulloa*, 2008].

Equatorial Subsurface Water (ESSW) forms the dominant water mass for the OMZ; characteristic are its high nutrient contents but low oxygen concentrations. It flows southward, merging with the Peru Chile Undercurrent (PCUC) around 5°S and consequently constitutes the core of the OMZ [*Hormazábal et al.*, 2006]. In contrast, Tropical Surface Water (TSW), located north of the ESSW, is warmer and less saline than the ESSW (T>25°C, S<34 [*Zuta and Guillén*, 1970; *Gutiérrez et al.*, 2005]). Subsurface depths are dominated by the Equatorial Undercurrent (EUC), which flows eastwards, originating west of the Galápagos Islands where it is situated in water depths of roughly 100–250 m [*Kessler*, 2006]. The high salinity and the highly oxygenated waters [*Toggweiler et al.*, 1991] of the EUC can be traced all the way to the coasts of Ecuador and Peru, implying that its deepest layers are being transported far into the east Pacific.

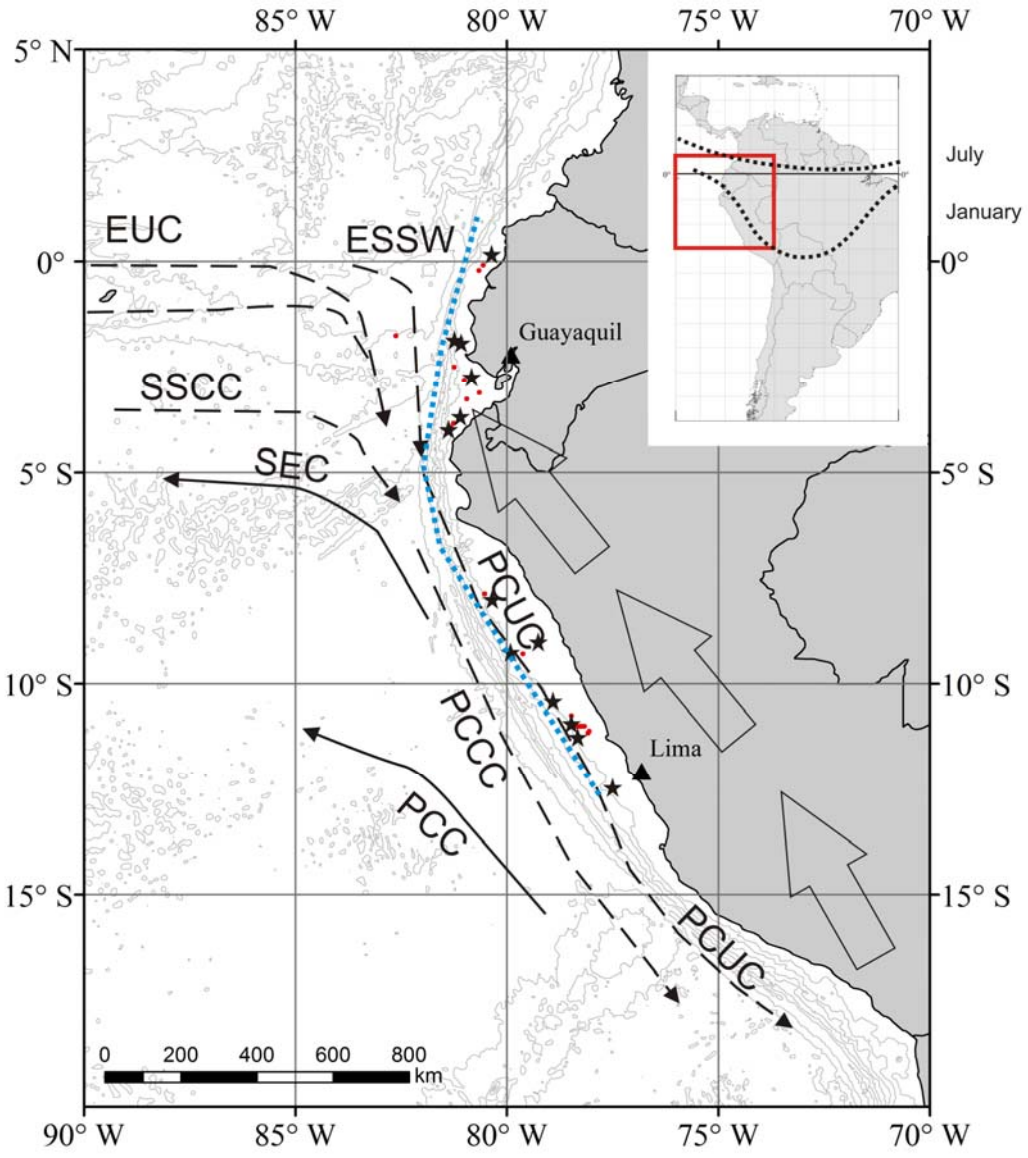

Figure 4-1: Sample locations, WOA 2009 profile line and oceanographic currents off Peru and Ecuador

Sample locations off Ecuador and Peru (surface sediments: red dots and water samples: black stars). Positions with multiple samples (11°S transect) are labelled with one symbol only. Dotted blue line is the WOA 2009 profile line shown in the following figures. Gray lines are 1,000 m bathymetric depth contours, indicating the steepness of the continental slope. Reference sites are located between ~2°N-5°S/ 83°-103°W [*Faul et al.*, 2000] and ~7°N-13°S/ 76°-102°W [*Rincón-Martínez et al.*, 2011], respectively. Inlet provides larger view of South America with red rectangle indicating study area and dotted lines indicating ITCZ positions for austral winter (July) and austral summer (January; [*van Breukelen et al.*, 2008]). Open block arrows show main wind direction [*Kessler*, 2006]. Thin arrows indicate the main oceanographic currents offshore Ecuador and Peru after [*Brink et al.*, 1983; *Fiedler and Talley*, 2006; *Hormazábal et al.*, 2006; *Kessler*, 2006; *Ayón et al.*, 2008; *Bostock et al.*, 2010]. Surface currents (solid lines): SEC (South Equatorial Current) and PCC (Peru Chile Current); subsurface currents (dashed lines): EUC (Equatorial Under Current), ESSW (Equatorial Subsurface Water), SSCC (Southern Subsurface Counter Current), PCUC (Peru Chile Under Current) and PCCC (Peru Chile Counter Current); data source for the map is ESRI®.

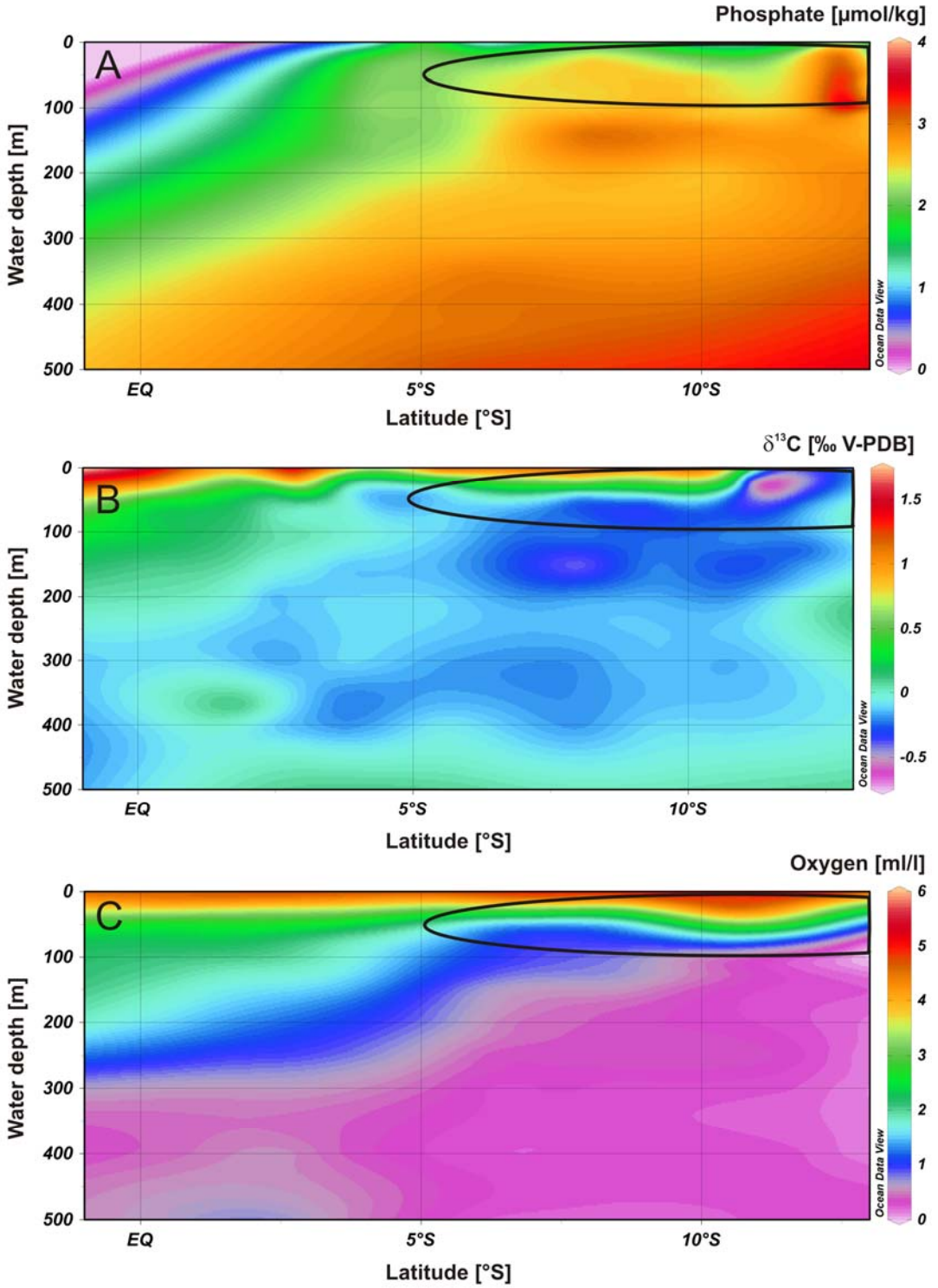

Figure 4-2: Lateral extension of the upwelling center indicated by different proxies

Sections from 1°N to 13°S for the upper 500 m of the water column, showing different proxies indicating the lateral extension of the upwelling center/ the OMZ: (A) phosphate [*Kalvelage et al.*, 2013], (B) $\delta^{13}C$ [*Klostermann*, 2011], and (C) oxygen (annual mean; [*Garcia et al.*, 2010]). Samples for water column analysis were sampled during cruises M77-2 ($\delta^{13}C$; Nov-Dec 2008) and M77-3 and -4 (phosphate; Dec 2008-Feb 2009), respectively. Legends on the right depict scales for each proxy. Black ovals in upper right corner of each panel indicate lateral extension of shallow coastal upwelling (until ~100 m depth), starting at ~5°S and stretching southwards.

The thermocline in the eastern tropical Pacific is most strongly developed between 5°S and 15°N; its density structure is shaped by extremely sharp temperature gradients superimposed by a halocline [*Fiedler and Talley*, 2006]. The strongly revealed thermocline is also a sharp nutricline; the relationship between temperature and nutrients has been demonstrated globally [*Kamykowski and Zentara*, 1986] and in particular for the Eastern Tropical Pacific [*Chavez et al.*, 1996]. Thermocline depth controls nutrient supply and thus biological production in surface waters [*Pennington et al.*, 2006]. The thermocline rises up to ~20 m water depth between June and September, thus bringing colder water into the range of stronger winds and thus enabling enhanced mixing during this time of the year [*Kessler*, 2006].

4.3: Material & Methods

4.3.1: Sample Selection

This study is based on samples collected during Meteor cruise M77 (legs 1 and 2; Fig. 4-1). We investigated 164 water samples derived from 15 stations for their $\delta^{18}O$ signature as well as 32 multicorer surface samples, which provided the material for foraminiferal analyses. To ensure that our sediment surface samples represent recently deposited specimen, we performed an AMS-^{14}C dating on one sample from a MUC station at the northern rim of the OMZ (M772-056-1; 3°45 S, 81°07 W; 350 m WD). This station is located outside the active upwelling region and thus, in comparison, situated in a relatively well oxygenated area. The dating was based on the analysis of ~300 specimens of species *N. dutertrei* from size fractions >250 µm (Table 4-1). The sample revealed an age >1954 A.D. indicating that it contained bomb shell ^{14}C, thus confirming the assumption that sediment surfaces were recently deposited.

Table 4-1: AMS^{14}C-dated MUC surface sample of species *N. dutertrei*

Station number	Core depth	KIA number	Radiocarbon age [1 σ]	Analyzed species
M772-056-1	0 – 2 cm	KIA 41847	> 1954 A.D.	*N. dutertrei*

4.3.2: Water Samples for Stable Isotope Analysis

At all multicorer stations additional CTD deployments were performed, which revealed local temperature and oxygen saturation profiles. Furthermore, the CTD was equipped with 10 l Niskin bottles, which were used to sample the water column in different depths. On average, the uppermost 100 m were sampled with approximately 9 bottles and below this depth the distance between samples was stepwise increased (Fig. 4-3A). Water samples were taken at 15 stations with a total of 164 samples covering a depth range from 60 m on the shelf down to 455 m. Water was sampled from the Niskin bottles with a tube and filled into 115 ml glass bottles on board. 0.2 ml saturated mercury chloride ($HgCl_2$) were added to the samples to prevent further degradation or oxidation. The glass bottles were closed with a rubber cap, crimped with an aluminium cap and subsequently stored at ~4°C.

All water samples were analyzed for ratios of stable oxygen ($\delta^{18}O$) and carbon isotopes ($\delta^{13}C$) within the frame work of a Diploma thesis [*Klostermann*, 2011]. The samples were measured using a Finnigan Delta E mass spectrometer with a dual inlet-equipment at the Leibniz-Laboratory for Radiometric Dating and Isotope Research (Kiel University, Germany). The mass spectrometer was connected with an equilibration bath (Equi) to measure the ratios of oxygen isotopes ($^{18}O/^{16}O$). The results are reported in the common δ-notation in ‰ relative to a standard material (Vienna Standard Mean Ocean Water, VSMOW). Duplicate measurements were performed to detect possible offsets; precision for $\delta^{18}O$ was <0.08‰ (2 σ) and for $\delta^{13}C$ <0.2‰ (2 σ).

4.3.3: Analysis of Stable Isotopes in Foraminiferal Shells

For all multicorer stations the uppermost 0-1 cm were sampled; if foraminiferal content was very low this fraction was enlarged to the uppermost 0-2 cm. Species *G. ruber* was only sampled at 12 stations due to its limited occurrence within the study area. The dominant species in all surface samples was *N. dutertrei*, which amounts to ~70% of the total planktonic foraminifer assemblage in the study area. The wet sediment samples were washed over a 63 µm wide sieve. Afterwards, the samples were dried in an oven at ~50°C and sieved into six different size classes (63–125, 125–250, 250-315, 315-355, 355-

400 and >400 µm). Roughly 25 individuals of *N. dutertrei* (dextral coiling) and ~30 of *G. ruber* (white, morphotype s.s.) were picked from size fractions 250-355 µm. In case foraminiferal content was too low in this fraction, the size range was widened to gain enough material for the analysis (maximum to 125-400 µm). This was particularly the case for *G. ruber* since its occurrence was in general lower within all samples than for species *N. dutertrei*. The identification of both species followed the taxonomic concepts of *Kennett and Srinivasan* [1983] *and Hemleben et al.* [1989].

All picked samples were carefully crushed between two glass plates and homogenized. The samples were split afterwards and about $^1/_3$ of the total sample was used for stable oxygen and carbon isotope analysis. The remaining sample material was used for Mg/Ca analysis (data not shown here). Prior to measurement all samples were rinsed three times with ultrapure water with ultrasonic treatment between each rinse, followed by two rinses with methanol. Stable oxygen and carbon isotope measurements were performed with a ThermoScientific MAT 253 mass spectrometer equipped with an automated CARBO Kiel IV carbonate preparation device (GEOMAR, Germany). The isotopic values were calibrated versus NBS 19 (National Bureau of Standards); the internal reference standard used was the "Standard Bremen" (Solnhofen limestone). The isotope values are reported in ‰ relative to the VPDB (Vienna Pee Dee Belemnite) scale. Long term precision of the in-house standard is ±0.09‰ for $\delta^{18}O$ (2 σ) and ±0.052‰ for $\delta^{13}C$ (2 σ). The $\delta^{18}O$ ratio in foraminiferal shells will be referred to $\delta^{18}O_{calcite}$ hereafter.

4.3.4: Calculation of $\delta^{18}O$ Values in Equilibrium

$\delta^{18}O$ values, which are in equilibrium with the surrounding water ('theoretical $\delta^{18}O$ values'), were calculated based on the analyzed $\delta^{18}O$ ratios of seawater. The values were converted from VSMOW to VPDB standard by applying a factor of -0.27‰ [*Hut*, 1987]. The equilibrium values were calculated with equation (1) by *Kim and O'Neil* [1997], revised by *Wilke et al.* [2006]:

$$\delta^{18}O_{eq} = 25.778 - 3.333 * (43.704 + T)^{0.5} + \delta^{18}O_{sw} \quad (1)$$

Foraminifers can show an isotopic offset between $\delta^{18}O$ values in equilibrium and the actually measured $\delta^{18}O$ of their tests, which is referred to as 'vital effect' [*Erez and Honjo*, 1981; *Spero and Williams*, 1989; *Spero et al.*, 1991]. This 'vital effect' is caused by meta-

bolic effects, which results in either enrichment or depletion of $\delta^{18}O$ within the foraminifers tests. The observed $\delta^{18}O$ disequilibrium effect for *G. ruber* and *N. dutertrei* deviates largely from other studies, possibly depending on the presence of symbionts or on the studied locations. There is no trend in *G. ruber* with respect to its ontogeny, indicating that its habitat is in surface waters during its entire life cycle [*Kroon and Darling*, 1995]. Fractionation of the $\delta^{18}O$ ratio is thus likely due to the symbionts, which might be responsible for the offset between the tests and surrounding waters. The 'vital effect' for *G. ruber* (white) varies between 0 and -1‰ [*Fairbanks et al.*, 1982; *Deuser*, 1987; *Niebler et al.*, 1999]; an average value of -0.5‰ for *G. ruber* thus seems to be reliable, implying that the $\delta^{18}O$ values of its shells will be lighter compared to the expected equilibrium value. We have taken a value of -0.5‰ into account when we calculated ACDs for species *G. ruber*, consequently subtracting this value from the $\delta^{18}O$ calcite ratios.

N. dutertrei is known to fractionate the $\delta^{18}O$ of seawater to a smaller amount than *G. ruber* [*Fairbanks et al.*, 1982]. The 'vital effect' for *N. dutertrei* ranges between 0 and -0.53‰ [*Niebler et al.*, 1999] and 0‰ [*Kemle-von Mücke and Oberhänsli*, 1999]. Since the reported 'vital effect' for *N. dutertrei* is rather small, we neglected correcting for this effect within our data set. The advantages and disadvantages of this decision will be discussed in more detail in Chapter 4.5.3.. To summarize, the symbiont-bearing species (*G. ruber*) seems to be strongly influenced by 'vital effects'; the partly symbiontic species *N. dutertrei* seems to be less influenced by the isotopic disequilibrium effects.

Besides deviations from isotopic equilibrium due to the 'vital effect', ontogenetic effects can also influence the $\delta^{18}O$ signal of the tests, depending on the size fraction which is used for analysis. Proxy carrier *N. dutertrei* is known to calcify in shallower water depths during its pre-gametogenic stage and thus has (during this life stage) $\delta^{18}O$ values similar to those of surface-dweller *G. ruber*. During its life cycle, *N. dutertrei* sinks down to subsurface depths and consequently its $\delta^{18}O$ signature will become more positive. It is suspected that *N. dutertrei* is pre-gametogenic in size classes <270 µm [*Kroon and Darling*, 1995]. Consequently, our sampled range (250-315 µm) should mainly represent subsurface conditions for *N. dutertrei*.

ACDs were calculated based on the $\delta^{18}O$ values in equilibrium with the ambient seawater. After subtracting the 'vital effect' from the $\delta^{18}O$ shell values (performed only for *G. ruber*),

we sorted them to the depth where they were according to their $\delta^{18}O$ equilibrium value. We assigned the ACDs to each sample and plotted them according to the newly established depth as overlay on the WOA 2009 temperature data set [*Locarnini et al.*, 2010] and oxygen concentration data set [*Garcia et al.*, 2010], respectively. The oxygen concentrations were used as comparative data because the ACDs seem to arrange along oxygen gradients rather than along temperature gradients (for details see discussion in Chapter 4.5.3. and Fig. 4-6).

4.3.5: Habitat Depths: An Overview

The depth that *N. dutertrei* inhabits is difficult to specify as views on its vertical occurrence in the water column deviate largely. The thermocline or adjacent depths have been associated as its habitat [*Ravelo and Fairbanks*, 1992]. A habitat in depths of ~50 to 150 m depth was initially suggested by *Hemleben et al.* [1989]; *Loubere* [2001], *Dekens et al.* [2002] and *Schmuker and Schiebel* [2002] defined the habitat depth of *N. dutertrei* shallower to ~50 m water depth for study sites in the EEP, multiple locations and the Caribbean, respectively. According to *Fairbanks et al.* [1982], *N. dutertrei* lives preferably within the tropic to subtropic thermocline; its habitat is associated with the deep chlorophyll maximum [*Fairbanks and Wiebe*, 1980; *Fairbanks et al.*, 1982; *Bé et al.*, 1985]. Several studies suggest that *N. dutertrei* occurs over a wide range of vertical temperature gradients [*Hilbrecht*, 1997]. However, in upwelling zones its habitat can also shift from the thermocline to surface waters in case of particularly strong upwelling [*Hilbrecht*, 1997; *Loubere*, 2001]. A core top study from the EEP indicates a calcification depth for *N. dutertrei* of ~110 m [*Faul et al.*, 2000]. This is in agreement with *Regenberg et al.* [2009], who calculated calcification depths for *N. dutertrei* based on $\delta^{18}O$ values of ~80-190 m in the tropical Atlantic and Caribbean. In the tropics, *N. dutertrei* favors no particular season [*Tedesco and Thunell*, 2003], but *Thunell et al.* [1983] observed the largest quantities of *N. dutertrei* in the Panama Basin during the upwelling season (winter to spring). Based on the findings of *Faul et al.* [2000], who studied habitat depths in the vicinity to our study sites, a first order approximation of ~110 m habitat depth for *N. dutertrei* seems to be reliable. As intra-annual variations of temperatures in this water depth are miniscule (~1°C; (WOA 2009)) we disregarded seasonal effects on the $\delta^{18}O$ signature of *N. dutertrei*.

Only samples from the northern study area, located close to the Gulf of Guayaquil, might be influenced in their $\delta^{18}O$ signature by the discharge of the Guayas River. However, it seems unlikely that the river influences subsurface depths since its discharge is rather small (max. 1,400 m³/s; [*Twilley et al.*, 2001]). Since there are no other rivers in Ecuador and Peru close to our sample locations, the remaining samples are unlikely to have been effected by riverine input.

G. ruber is a surface dweller [*Deuser et al.*, 1981; *Bé et al.*, 1985; *Dekens et al.*, 2002], and hence serves to reconstruct seawater temperatures of the top ~25 m. These findings are consistent with the results of *Faul et al.* [2000], who report that *G. ruber* as a photosynthesizing species is restricted to the upper water column, where light levels are highest but levels of necessary nutrients or chlorophyll are not at their peak. *Deuser et al.* [1981] indicate a year-round presence of *G. ruber*, thus reinforcing the argument of it being a suitable archive for annual SSTs. Investigations of surface Mg/Ca ratios in *G. ruber* from our data set showed best accordance with summer temperatures of the WOA 2009 data set, hence leading to the conclusion that *G. ruber* seems to be a reliable recorder of summer temperatures in the EEP (data not shown here).

Species selection of *G. ruber* was restricted to the morphotype sensu stricto (*G. ruber* s.s.), as *Wang* [2000], *Kuroyanagi and Kawahata* [2004] and *Steinke et al.* [2005] revealed pronounced differences in the habitat of different morphotypes of *G. ruber*. Morphotype sensu stricto (s.s.) is restricted to the upper ~30 m of the water column [*Wang*, 2000], thus representing ocean surface conditions. *Kuroyanagi and Kawahata* [2004] found *G. ruber* s.s. predominately in surface waters, whereas morphotype sensu lato (s.l.) lives in greater depths. The authors relate the dominant presence of morphotype s.s. in surface waters to its greater dependence on symbionts and thus light. Additional investigations of Mg/Ca ratios in both morphotypes revealed similar results, with *G. ruber* s.s. indicating warmer and thus shallower habitat depth [*Steinke et al.*, 2005]. This morphotype is characterized by spherical chambers sitting symmetrically over previous structures and by a wide-opened aperture over the suture [*Wang*, 2000]. *Steinke et al.* [2005] emphasize the fundamental importance of the correct species selection for paleoceanographic investigations. Any mixture between the two morphotypes would result in an underestimation of the reconstructed temperatures as proportions of morphotype s.l. would indicate lower temperatures due to its deeper habitat.

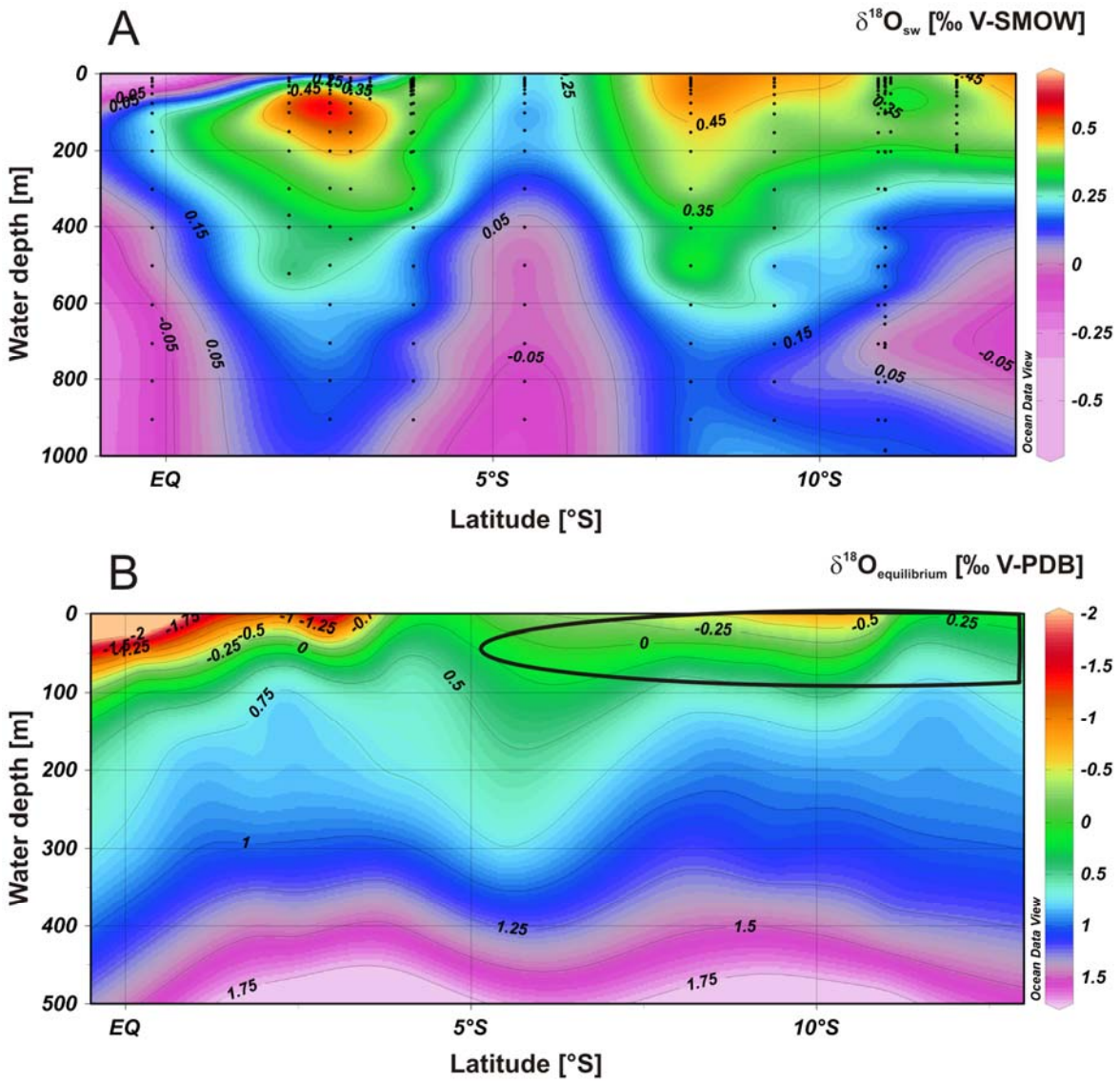

Figure 4-3: Stable isotopes ($\delta^{18}O$) in the water column and resulting $\delta^{18}O_{equilibrium}$ values

A: $\delta^{18}O_{seawater}$ values from Meteor cruise 77 (legs 1 and 2) along a section from 1°N to 13°S for the upper 1,000 m of the water column. Black dots indicate positions of water samples taken for $\delta^{18}O$ analyses and simultaneously profiled CTD casts. Contour lines and numbers show measured $\delta^{18}O_{seawater}$ values (Klostermann, 2011); legend to the right depicts $\delta^{18}O_{seawater}$ values in ‰ V-SMOW.

B: Calculated $\delta^{18}O_{equilibrium}$ values according to equation (1) by *Kim and O'Neil* (1997) based on the measured $\delta^{18}O_{seawater}$ values depicted in Fig. 4-3A. Contour lines and numbers provide detailed information about the $\delta^{18}O_{equilibrium}$ distribution. Legend to the right indicates $\delta^{18}O_{equilibrium}$ values in ‰ V-PDB across the latitudinal section from 1°N to 13°S. Water depth was restricted to 500 m as calcification depths for both species do not exceed this range. Black ovals in upper right corner of each panel indicate lateral extension of shallow coastal upwelling (until ~100 m depth), starting at ~5°S and stretching southwards.

4.4: Results

4.4.1: $\delta^{18}O$ Values of Seawater

Results of the analysis ($\delta^{18}O_{seawater}$) are shown in Fig. 4-3A. Ocean Data View (ODV; [*Schlitzer*, 2010]) was used to create the plot and the option "DIVA gridding" to create a two-dimensional picture of the water column. The $\delta^{18}O_{seawater}$ values vary from -0.25‰ to 0.58‰, generally decreasing with rising water depth (average of all values is 0.33‰). Exceptions of this trend are the tropical water masses, in particular the TSW, which show relatively light values of ~0.05‰. In surface to subsurface depths (~0-200 m WD) between 2° and 3°S as well as between 7° and 10°S distinct spots with heavier $\delta^{18}O_{seawater}$ values of ~0.45‰ are apparent. In water depths greater than 600 m three areas with lighter $\delta^{18}O_{seawater}$ can be identified: At the equator, around 5°S and south of 11°S, where $\delta^{18}O_{seawater}$ values range from 0 to -0.5‰.

4.4.2: Stable Isotopes in Planktonic Foraminifers

The $\delta^{13}C$ and $\delta^{18}O$ values of species *G. ruber* and *N. dutertrei* are plotted in Figs. 4-4 and 4-5, with species *N. dutertrei* having been measured at all 32 stations and species *G. ruber*, due to its lower presence, at only 12 stations. The $\delta^{18}O_{calcite}$ varies between *N. dutertrei* and *G. ruber* due to their different calcification depths. $\delta^{18}O_{calcite}$ values of *G. ruber* are relatively light (-2.0‰ on average) with the whole data set ranging from -1.25 to -2.33‰. The values for $\delta^{18}O_{calcite}$ of *N. dutertrei* range from 0.22 to 1.69‰, with an overall average of 0.57‰. Three samples within the *N. dutertrei* sample set seem to be outliers; they are marked accordingly in the figures and were excluded from calculating the average. The $\delta^{18}O_{calcite}$ values of both species remain relatively uniform along a latitudinal section from the equator to 13°S (Fig. 4-5). Our data sets are compared with two reference data sets from the EEP based on the same species (Fig. 4-5). The reference data sets are from areas located to the north and north-west of our study area [*Faul et al.*, 2000] and from ~7°N to ~13°S ([*Rincón-Martínez et al.*, 2011]; Fig. 4-1), respectively. All data was plotted according to their latitude, longitudinal differences between the study sites were neglected. Data sets are located between 83°W and 103°W [*Faul et al.*, 2000] and 76°W and 102°W [*Rincón-Martínez et al.*, 2011], respectively.

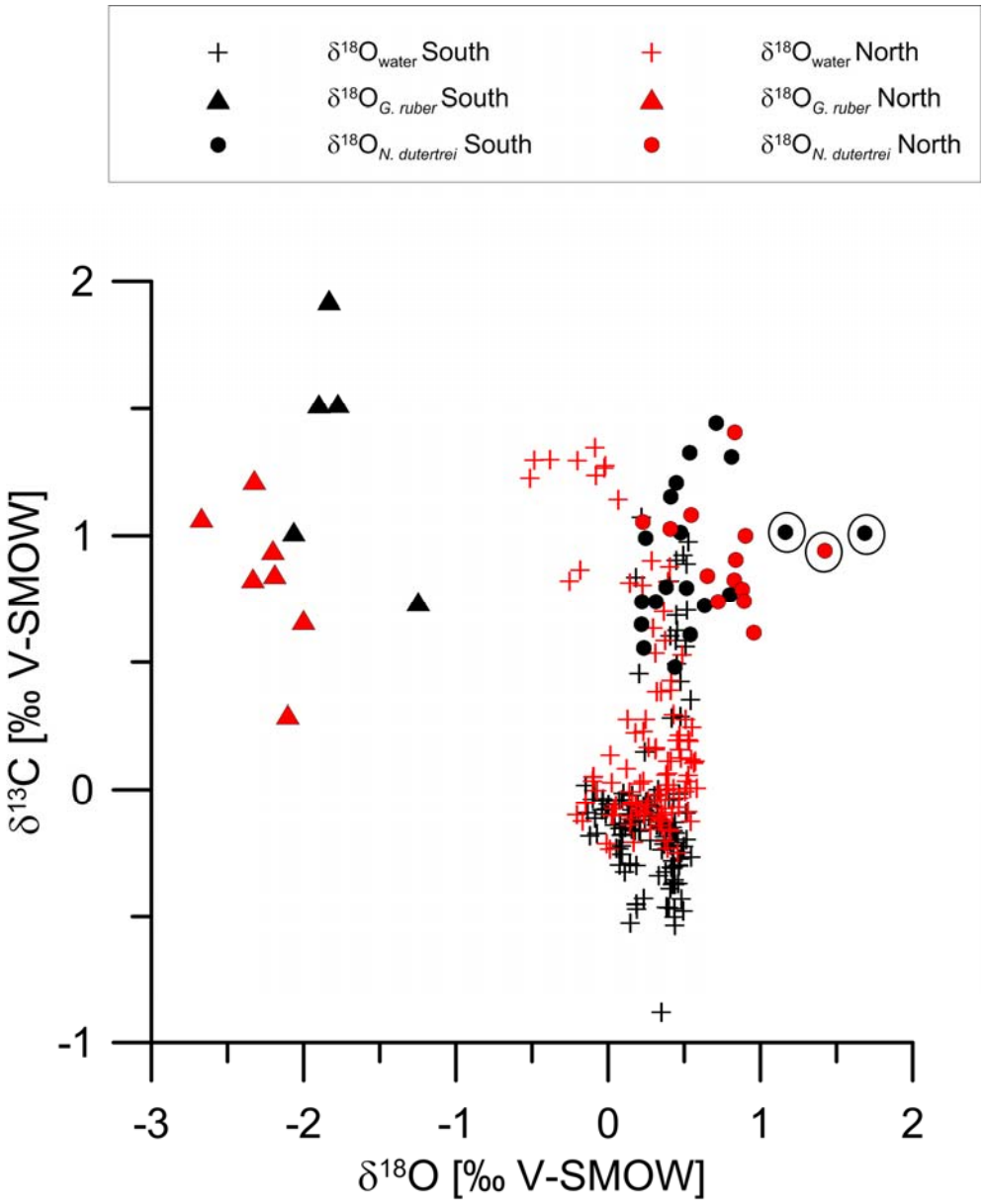

Figure 4-4: $\delta^{13}C$ *versus* $\delta^{18}O$ values for water samples and planktonic foraminifers

$\delta^{13}C$ *versus* $\delta^{18}O$ values for water samples and planktonic foraminifers (*G. ruber* and *N. dutertrei*) for our sample set from the EEP. Water samples were analyzed within the frame work of a Diploma thesis [*Klostermann*, 2011]. All black symbols indicate lateral positions of 5°S or further south, all red symbols indicate samples from north of 5°S. Water samples (crosses), *G. ruber* samples (triangles) and *N. dutertrei* samples (dots) differ markedly: All samples exhibit a rather large range in $\delta^{13}C$, compared to a relatively small range in $\delta^{18}O$. Water samples and *N. dutertrei* samples are similar in their $\delta^{18}O$ signature, but show large variations in their $\delta^{13}C$ signature. The *G. ruber* samples show a large offset in their $\delta^{18}O$ ratios compared to the water samples, implying that strong fractionation took place when the $\delta^{18}O$ signal was recorded in their tests. Circled data points are defined as outliers, which were excluded from average calculations for *N. dutertrei*.

The $\delta^{13}C$ ratios vary less strongly between both species than compared to the $\delta^{18}O$ ratios (Fig. 4-4). The water samples show a great diversity of their $\delta^{13}C$ ratios in contrast to the rather uniform $\delta^{18}O$ data set. The larger variety of the $\delta^{13}C$ ratios in water samples is

partly mirrored in the foraminiferal data sets of *G. ruber* and *N. dutertrei*. Both species show a range in $\delta^{13}C$ of ~1‰ (*N. dutertrei*) and ~1.5‰ (*G. ruber*), which is slightly smaller than the observed $\delta^{13}C$ range in the water samples (~2‰).

4.4.3: Equilibrium Values for Foraminiferal Calcite

Calculated $\delta^{18}O$ equilibrium values ($\delta^{18}O_{equilibrium}$) for our study area (Fig. 4-3B) reveal slightly negative values in the tropical surface ocean: From 1°N until ~3°S, values range from -0.5‰ in the South to slightly below -2‰ in the North. At surface depths south of 3°S the $\delta^{18}O_{equilibrium}$ values are around 0‰ with slightly more negative values at 10°S. At subsurface depths between 100 and 300 m they vary between 1 and 0.5‰. Water depths greater than 300 m are characterized by rather uniform values of approximately 1 to 1.75‰ over the whole latitudinal transect.

ACDs for *G. ruber* (Fig. 4-6) show a great consistency over the whole transect, most of them are located at the sea surface (0 m). Three values exceed this range slightly, being located at 7 and 16 m, respectively. The results for the northern and southern part of our study area are very similar. Corresponding surface temperatures for habitat depths of *G. ruber* s.s. from the WOA 2009 data set indicate temperatures of ~21-22°C for the southern and of ~22-24°C for the northern part of our study area.

Results for ACDs (Fig. 4-6) of subsurface dweller *N. dutertrei* vary from 10 to 310 m, being on average 120 m. The values indicate strong differences between the northern and southern part of our study area. Calcification depths in the north range from 45 to 310 m, with an average value of 197 m. Contrary, the southern sample set varies between 10 and 170 m at the deepest station with values averaging 68 m. The offset between the northern and southern area with respect to the average ACDs is ~130 m.

4.5: Discussion

4.5.1: $\delta^{18}O$ Values of Seawater

The $\delta^{18}O_{seawater}$ ratios within the tropical surface waters at the equator range from -0.25 to 0.25‰ (Fig. 4-3A) and are in good agreement with values from the Panama Bight [*Benway and Mix*, 2004]. This implies that tropical surface waters off Ecuador and Peru

experience a strong control from the Panama Bight region. The $\delta^{18}O$ signature in surface waters in the Panama Bight is a mixture between local precipitation sources and $\delta^{18}O$-depleted moisture sources from the Caribbean [*Benway and Mix*, 2004]. Local $\delta^{18}O$ signatures are strongly influenced on short time scales by evaporation and precipitation rates as well as river runoffs. Thus we assume that the $\delta^{18}O_{seawater}$ values in the northern part of our study area are additionally influenced by the Guayas River. This river discharges into the Gulf of Guayaquil, which is close to the sampling area. River runoffs can be strongly depleted with respect to $\delta^{18}O$ [*Craig and Gordon*, 1965]; discharge of the Guayas River might have an influence on the $\delta^{18}O$ signature of near-surface waters off Ecuador and Peru, further adding to the influence of surface waters from the Panama Bight. The influence of the inflow of $\delta^{18}O$-depleted and low saline waters from the Guayas River via the Gulf of Guayaquil can however not be observed in our data set (Fig. 4-3A) nor in the CTD data from the respective Meteor cruise [*Pfannkuche et al.*, 2011].

Subsurface $\delta^{18}O_{seawater}$ values (Fig. 4-3A) show two distinct features at ~3°S and ~8°S with values around 0.5‰, in accordance with the data analyzed by *Benway and Mix* [2004], who report average values of 0.35‰ for the Panama Basin. Deeper water masses in our study area show relatively consistent $\delta^{18}O_{seawater}$ values between 0.05 and -0.05‰. These values can be attributed to Antarctic Intermediate Water (AAIW; [*Benway and Mix*, 2004]).

4.5.2: $\delta^{18}O$ in Planktonic Foraminifers

The $\delta^{18}O$ versus $\delta^{13}C$ plot (Fig. 4-4) clearly depicts a relatively large range of $\delta^{18}O$ ratios for both species. The ratios for *G. ruber* seem to be lighter in the northern study area, whereas the results for *N. dutertrei* imply heavier ratios in the northern study area. Additionally to 'vital effects' and ontogenetic effects, the highly variable local water mass structure (Chapter 2) might cause differing $\delta^{18}O$ and $\delta^{13}C$ signatures. A reference data set from the EEP [*Faul et al.*, 2000] agrees largely on the amplitude of $\delta^{18}O$ calcite values with respect to species *G. ruber* from our data set, but compared to the reference data set our data experiences a higher variance in absolute values (-1.25 to -2.33‰; Fig. 4-5). This range of values matches those of another data set from the EEP, where *G. ruber* values scatter between -0.7 and -3‰ [*Rincón-Martínez et al.*, 2011]. The larger variability within

our *G. ruber* $\delta^{18}O$ data set probably results from the differences in surface water characteristics between north of the equator and 13°S, which are more prominent than the differences in subsurface depths. Surface depths are influenced by a number of factors, e.g. precipitation, evaporation, riverine input and marine productivity; thus surface water masses often show different characteristics on short spatial scales. The lighter $\delta^{18}O$ calcite values of *G. ruber* compared to *N. dutertrei* are caused by the much shallower habitat depth of surface dwelling *G. ruber*. The tendency towards slightly heavier $\delta^{18}O$ calcite in the southern part of our study area might be related to stronger upwelling conditions and consequently cooler water masses, which biased the foraminifers $\delta^{18}O$ values towards heavier values.

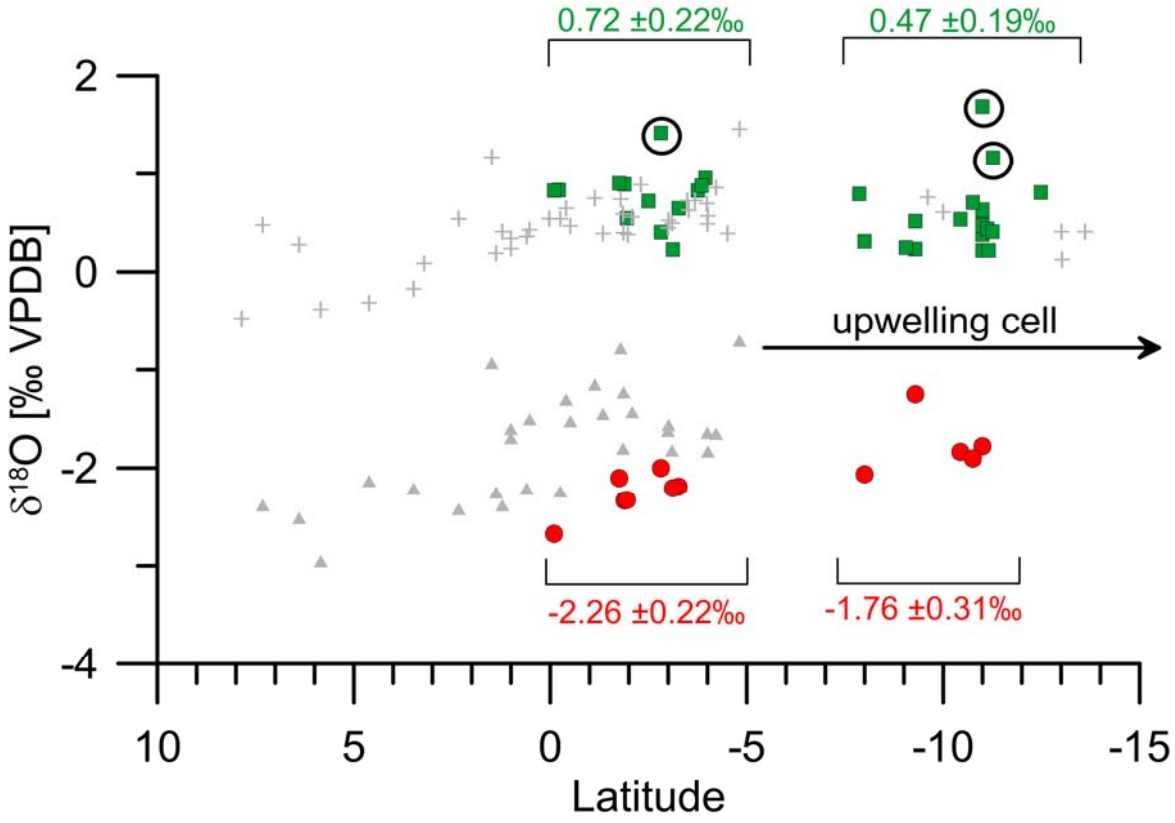

Figure 4-5: $\delta^{18}O_{foram}$ values of this study and reference data sets from the EEP

$\delta^{18}O_{foram}$ values from multicorer sediment surface samples in the EEP (this study) and reference data sets. Green squares identify species *N. dutertrei* (this study), gray crosses are data from the same species from reference sites [*Faul et al.*, 2000; *Rincón-Martínez et al.*, 2011]. Red dots indicate species *G. ruber* (this study), gray triangles are *G. ruber* values from reference data sets [*Faul et al.*, 2000; *Rincón-Martínez et al.,* 2011]. Circled squares are defined as outliers, which were excluded from the average $\delta^{18}O_{foram}$ calculation for *N. dutertrei*. Average $\delta^{18}O_{foram}$ values for both species (own data set only) are indicated for the northern and southern study area in green (*N. dutertrei*) and red (*G. ruber*), respectively. Average $\delta^{18}O_{foram}$ values for entire own data set are -2.05 ±0.35‰ (*G. ruber*) and 0.57 ±0.24‰ (*N. dutertrei*), respectively. The lateral extension of the upwelling center, starting at ~5°S and stretching southwards, is indicated by the arrow.

The $\delta^{18}O_{calcite}$ values from all *N. dutertrei* samples were on average 0.653‰; this is in good agreement with the $\delta^{18}O_{equilibrium}$ for calcite (average 0.824‰) and hence supporting the notion of a negligible 'vital effect' for this species. The $\delta^{18}O_{calcite}$ values of *N. dutertrei* are in good accordance with the two reference data sets from the EEP (Fig. 4-5; [*Faul et al.*, 2000; *Rincón-Martínez et al.*, 2011]). The $\delta^{18}O_{calcite}$ of *N. dutertrei* ranges from 0.22 to 1.69‰ in our data set, thus being slightly heavier than the range between -0.38 and 1.59‰ suggested by *Rincón-Martínez et al.* (2011). Furthermore, *Rincón-Martínez et al.* report a statistically obvious N-S gradient with respect to $\delta^{18}O_{calcite}$ signatures, which we did not observe in our data set. Even though several authors proposed that *N. dutertrei* inhabits thermocline and adjacent depths we did not find a correlation between $\delta^{18}O_{calcite}$ values and latitudinal trends. The thermocline is located in shallower water depths in the southern part of the OMZ due to intensified upwelling, but this fact is not evident in our foraminiferal $\delta^{18}O$ data set. We thus conclude that other factors than hydrographic features might have influenced subsurface dweller *N. dutertrei* in our study area, possibly oxygen concentrations or food/ nutrient availability.

Faul et al. [2000] conclude from their study, which divided the data set into three different regional areas, that calcification depths and temperatures for each species are not constant throughout the EEP. Both can change depending on vertical hydrographic features as well as food/ nutrient availability. The $\delta^{13}C$ ratios, measured in water samples and both foraminiferal species, show distinct differences throughout the data set (Fig. 4-4). $\delta^{13}C$ ratios can depict nutrient availability [*Rohling and Cooke*, 1999], thus implying that changes in the foraminifers habitat might be related to nutrient/ food availability. Based on our $\delta^{18}O_{calcite}$ data set from *G. ruber* we propose that hydrographic differences in surface waters between the northern and southern part of our study area have caused the trend towards heavier $\delta^{18}O_{calcite}$ values in the southern region. South of ~5°S the hydrography is additionally influenced by the OMZ off Peru. Consequently, upwelling is much stronger in this area compared to the tropical surface waters. No north-south gradient is evident in our subsurface proxy carrier *N. dutertrei*; we suspect it to be relatively unaffected by latitudinal changes in hydrography.

4.5.3: $\delta^{18}O_{equilibrium}$ and Assorted Calcification Depths

The average value for $\delta^{18}O_{equilibrium}$ in surface waters in our study area is ~-0.44‰, the mean of all surface samples of *G. ruber* results in a $\delta^{18}O_{calcite}$ value of -2‰. Consequently, our results from the EEP indicate a 'vital effect' for *G. ruber* of ~-1.5‰; this would indicate a stronger isotopic fractionation for *G. ruber* than the previously reported of 0 to -1.0‰ [*Fairbanks et al.*, 1982; *Niebler et al.*, 1999]. The comparison of 'vital effects' observed in different studies also needs to take the ontogenetic effect into account; this effect refers to test size- related changes in the foraminifers $\delta^{18}O$ signature during its life cycle [*Elderfield et al.*, 2002]. Our sampled size range for *G. ruber* (250-355 µm) is similar to the one used by *Niebler et al.* ([1999]; 200-400 µm), thus resulting 'vital effects' are comparable. Another study reported that there is no trend in *G. ruber* $\delta^{18}O$ signal with respect to its ontogeny, indicating that its habitat is consistently in surface waters during its entire life cycle [*Kroon and Darling*, 1995].

The $\delta^{18}O_{calcite}$ values of *G. ruber* [*Faul et al.*, 2000] indicate calcification in the surface ocean or just above the thermocline. When taking a 'vital effect' of -0.5‰ into account, the resulting ACDs for *G. ruber* in the EEP based on our data set range from 0 to 16 m, with most values being close to 0 m. These findings are similar to other studies highlighting *G. ruber* as a surface dweller restricted to the uppermost ~30 m of the water column [*Deuser et al.*, 1981; *Faul et al.*, 2000; *Dekens et al.*, 2002; *Anand et al.*, 2003]. The comparison of our *G. ruber* data set to the corresponding $\delta^{18}O_{equilibrium}$ values indicates a more pronounced 'vital effect' than the one described by *Fairbanks et al.* [1982] of ~-0.5‰. The offset between the average value for $\delta^{18}O_{calcite}$ in *G. ruber* (-2‰) and the mean value for $\delta^{18}O_{equilibrium}$ for the surface ocean in our study area (~-0.44‰) is ~1.5‰. We consider this value to more accurately approximate the 'vital effect' in the EEP for species *G. ruber* than the previously assumed value of ~-0.5‰. When applying this 'vital effect' of ~1.5‰ to our measured $\delta^{18}O$ ratios the resulting estimates decrease strongly and consequently our ACDs are located in greater water depths. Only the values from the northern part of our study area (20- 30 m WD), still match previously reported habitat depths of *G. ruber* [*Deuser et al.*, 1981; *Dekens et al.*, 2002]. However, our indicated ACDs for *G. ruber* in the northern EEP are slightly deeper than the <20 m suggested by *Faul et al.* [2000]. Our values agree with the results of *Schmuker and Schiebel* [2002], who found an average habitat

depth for *G. ruber* (white) in the Caribbean of 39 m. The assorted ACDs for *G. ruber* (Fig. 4-6) refer to an average 'vital effect' of ~-0.5‰ based on literature data [*Niebler et al.*, 1999]. Consequently, our observed 'vital effect' of ~-1.5‰ is markedly larger; it thus affords further validation, e.g. through a larger data set.

Our sampled size range for *N. dutertrei* (250-355 µm) is smaller than the one used by *Niebler et al.* ([1999]; >350µm). *N. dutertrei* is known to calcify in shallower water depths during its pre-gametogenic stage and sink down to subsurface depths during later life stages. It is suspected that *N. dutertrei* is pre-gametogenic in size classes <270 µm [*Kroon and Darling*, 1995]. Consequently, our sampled range and the reference data set [*Niebler et al.*, 1999] should mainly represent subsurface conditions for *N. dutertrei*, since both data sets include mainly pre-gametogenic individuals. The $\delta^{18}O_{calcite}$ values for subsurface species *N. dutertrei* are in good accordance with the $\delta^{18}O_{equilibrium}$ values, which are based on the analysis of $\delta^{18}O_{seawater}$ in the local water column (Fig. 4-4). Consequently, we did not observe an isotopic fractionation effect or 'vital effect' with respect to species *N. dutertrei*. Our findings agree with other studies, which report a negligible 'vital effect' for *N. dutertrei* [*Fairbanks*, 1982; *Niebler et al.*, 1999; *Kemle-von Mücke and Oberhänsli*, 1999]. We thus refrain from using a 'vital effect' correction for *N. dutertrei* in the following.

The resulting ACDs for *N. dutertrei* show a great range of depths, varying between 25 and 310 m (Fig. 4-6), indicating pronounced differences for the northern and southern part of our study area. Overall, *N. dutertrei* calcifies in greater water depths in the northern part of our study area (~200 m), which stretches from ~5°S northwards to the equator. Further south the ACDs appear to be much shallower (~70 m). Particularly the northern region values are in line with those values found within a core top study by *Faul et al.* [2000]. The authors investigated *N. dutertrei* in the EEP and concluded an average habitat depth of 75-160 m for the area east to south-east of the Galápagos Islands. *Faul et al.* [2000] partitioned their study area into three regional subareas, defined by the amount of organic carbon being buried in the sediment: 1) region with lowest organic carbon accumulation, located furthest offshore; 2) region with medium accumulation; 3) region with highest accumulation closest to the coast. The ACDs for region 2 (located slightly north of the equator) is ~130 m. The values for region 3, which is located between 1 and 5°S, average at ~160 m and are consequently similar to our ACD of ~200 m for the northern part of

our study area (equator to 5°S). A plankton net study from the Panama Basin indicates growth of *N. dutertrei* in thermocline waters based on $\delta^{18}O$ analysis of its tests [*Fairbanks et al.*, 1982]. Several authors indicated a presence and consequently a habitat depth of *N. dutertrei* along the 15°C isotherm [*Faul et al.*, 2000; *Dekens et al.*, 2002]. Contrary observations were made by *Schmuker and Schiebel* [2002], who defined the average habitat depth for *N. dutertrei* to be 39 m based on plankton tow studies in the Caribbean. Due to apparent hydrographic discrepancies between the EEP and the Caribbean we neglected the habitat depth estimation by *Schmuker and Schiebel* [2002] for comparison with our ACDs.

Rincón-Martínez et al. [2011] concluded from their surface study in the EEP that habitat depths for *N. dutertrei* do not change strongly throughout the study area. They observed no latitudinal trends with respect to the $\delta^{18}O_{calcite}$ ratios and thus suggest a uniform calcification depth of ~50 to 250 m for *N. dutertrei* in the EEP. Our $\delta^{18}O_{calcite}$ results also show relatively uniform values for both species, *G. ruber* and *N. dutertrei*, along our N-S transect. However, when taking into account the $\delta^{18}O_{equilibrium}$ values, which are based on the analyses of local $\delta^{18}O_{seawater}$ samples, we detect distinct trends within our data set. The pronounced differences for ACDs of *N. dutertrei* in the northern (~200 m) compared to the southern part of the study area (~70 m) indicate different settings at the northern rim of the OMZ and within the present-day OMZ. We suspect the lack of latitudinal gradients in the data set by *Rincón-Martínez et al.* [2011] to have been caused by a different and less precise approach than the one we have performed. Approximation of $\delta^{18}O$ ratios in the water column via salinity data are likely to show less accuracy than $\delta^{18}O$ values analyzed directly from water samples as we performed in our study. We thus strongly suggest that our combined analysis of $\delta^{18}O$ in water samples and planktonic foraminifers from the EEP represents a more precise approach to estimate ACDs for planktonic foraminifers.

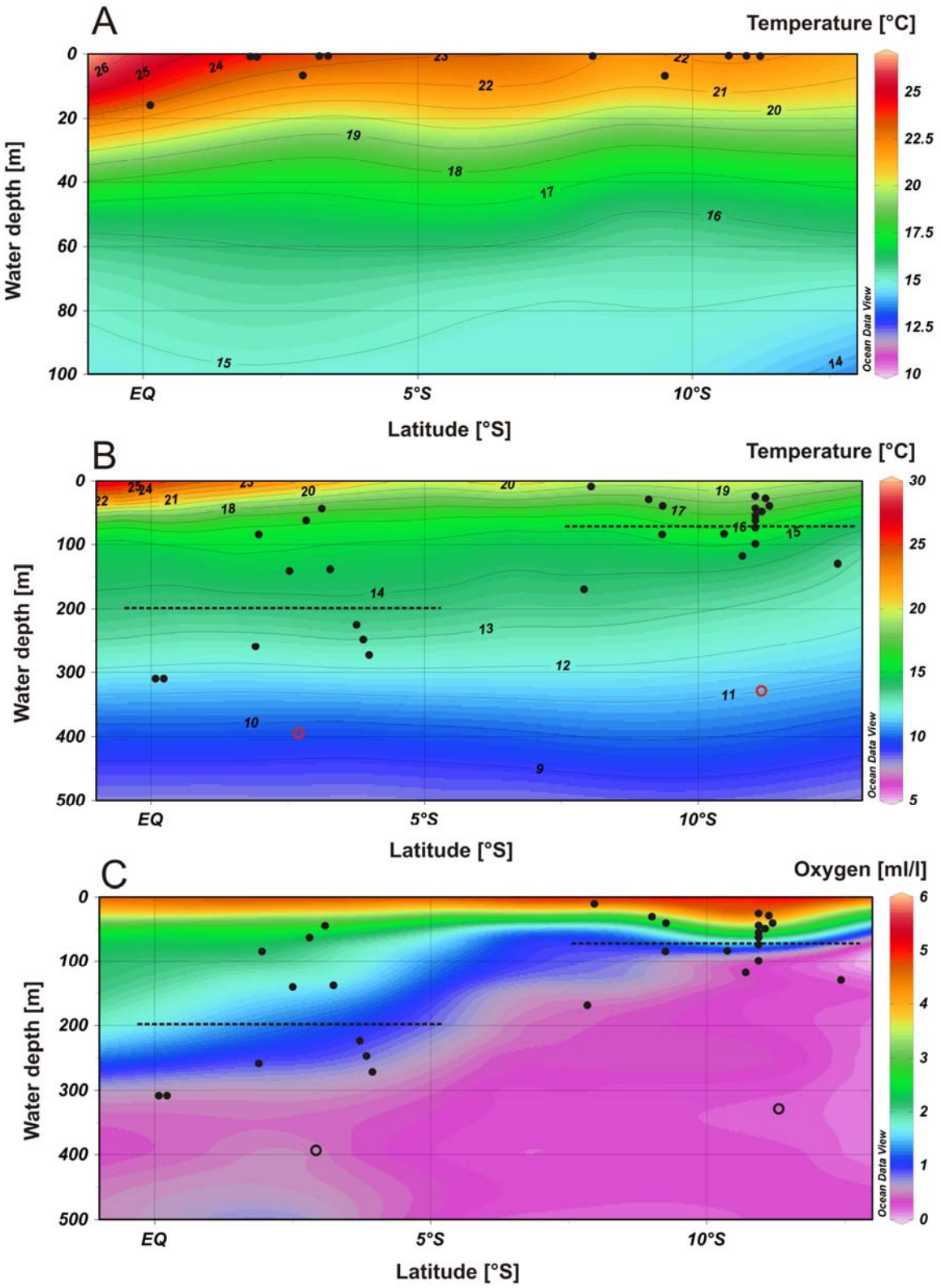

Figure 4-6: ACDs for species *G. ruber* and *N. dutertrei* from 1°N to 13°S off Ecuador and Peru

The $\delta^{18}O_{equilibrium}$ values are based on $\delta^{18}O$ ratios of analyzed water samples [*Klostermann*, 2011] from the study area. (A) calculated ACDs of *G. ruber* s.s. (black dots) in comparison to the WOA 2009 Jan-Mar temperatures [*Locarnini et al.*, 2010] for the upper 100 m of the water column, implying that *G. ruber* s.s. calcifies in the uppermost 16 m. (B) and (C) depict calculated ACDs for *N. dutertrei* plotted on top of WOA 2009 annual mean temperatures and annual mean oxygen concentrations [*Garcia et al.*, 2010], respectively.

Legends to the right indicate respective temperatures and oxygen concentrations; contour lines and numbers provide further details. ACDs reveal a much larger spreading with values ranging from greater water depths north of 5°S (on average ~200 m) to shallower depths south of 5°S (on average ~70 m); averaged ACDs are indicated by horizontal, dotted lines. Three $\delta^{18}O_{calcite}$ values exceeded the observed ACDs, they were excluded from average calculations. Two of them are marked by open circles in the plots; the third value was located below 500 m water depth and is not depicted in the figure.

Our calculated shallower ACDs for *N. dutertrei* in the southern study area are probably related to more intense upwelling in this region; this is closely connected with an enhanced marine productivity in the southern study area, resulting in the formation of the strongly evolved OMZ. Consequently, the OMZ extends further to the water surface in the south compared to the north and under-saturation with respect to oxygen starts in shallower water depths in the south (Figs. 4-2C and 4-6C). This might provide an important explanation for the shallower habitat of *N. dutertrei* in the south, since not only cooler water masses but also lower oxygen conditions in the water might force this species closer to the sea surface. The different ACDs in the northern and southern part of the study area are in line with similar oxygen concentrations (~1-3 ml/l; [*Garcia et al.*, 2010]) in the respective water depths. Oxygen concentrations [*Garcia et al.*, 2010] are much lower in ~200 m in the south of our study area compared to the northern part (Figs. 4-2C and 4-6C). This limitation of oxygen probably pushes *N. dutertrei* to shallower depths, because south of ~5°S concentrations in ~200 m might be too low for this species. The oxygen tolerance of planktonic foraminifers has been investigated and species seem to tolerate oxygen concentration >0.7 mg l^{-1} [*Kuroyanagi et al.*, 2013]. The oxygen concentrations in the core of the investigated OMZ in the EEP are <20 µmol kg^{-1} [*Fuenzalida et al.*, 2009], and thus markedly lower than the observed oxygen tolerance of planktonic foraminifers. It seems thus likely that lower oxygen concentrations in the core of the OMZ (=southern part of our study area) force *N. dutertrei* to inhabit shallower habitat depths. The gradual shoaling of the ACDs for *N. dutertrei* from the equator southwards is a genuine trend and implies a noticeable influence of the local hydrography on the species habitat depth. To sum it up, the habitat depth of *N. dutertrei* is very likely controlled by the oxygen concentration of the water column in close relation with the extension and strength of the OMZ offshore Ecuador and Peru.

4.6: Conclusions

Our surface data set of planktonic foraminifers *G. ruber* (white, sensu stricto) and *N. dutertrei* (dextral) from the EEP reveals a close correlation between the $\delta^{18}O_{calcite}$ values and the corresponding $\delta^{18}O_{equilibrium}$ values. The $\delta^{18}O$ analyses of water samples were the basis for calculating the $\delta^{18}O$ values in equilibrium with the surrounding water masses. The $\delta^{18}O_{calcite}$ values in species *G. ruber* show a larger 'vital effect' than reported previously for this species (~-0.5‰), being approximately -1.5‰ with respect to $\delta^{18}O$ in the EEP. Intense upwelling activity seems to exhibit strong control on the habitat depth of *G. ruber* and is thus likely to play a major role in areas with sharp, vertical hydrographic gradients like the EEP. The ACDs for *G. ruber* indicate a preferred habitat depth in the uppermost surface ocean (referring to the uppermost 16 m of the water column) and are in accordance with previous studies.

A 'vital effect' with respect to the subsurface dwelling species *N. dutertrei* was not observed in our data set. The resulting ACDs show strong differences between the northern and southern part of our study area. On average, *N. dutertrei* calcifies in markedly greater water depths in the northern (~200 m) than in the southern area (~70 m); we relate this to the occurrence of stronger upwelling in the southern part and a resulting shallower thermocline. Species *N. dutertrei* seems to change its habitat depth depending on external, hydrographic factors like the occurrence of pronounced upwelling. Additionally, the generally lower oxygen concentrations in the water column in the southern study area might provide a further explanation for the shallower habitat depth of *N. dutertrei*. Depths of ~200 m in the southern study area are characterized by much lower oxygen concentrations than comparable depths in the northern part, thus likely pushing *N. dutertrei* to shallower depths in the south.

Acknowledgements:

This work is a contribution of the DFG Collaborative Research Project "Climate – Biogeochemistry interactions in the Tropical Ocean" (SFB 754). We acknowledged technical support from N. Gehre, L. Haxhiaj (GEOMAR) and Bianca Willié (Kiel University). $\delta^{18}O$ analyses of water samples and AMS^{14}C-measurements were provided by the Leibniz-Laboratory for Radiometric Dating and Isotope Research, Kiel University.

Chapter 5:
Deglacial to Holocene Upper Ocean Dynamics in the Eastern Equatorial Pacific

Tebke Böschen[1*], Dirk Nürnberg[1], Elfi Mollier-Vogel[2], Kristin Doering[2], Ralph Schneider[2] and Christian Dullo[1]

[1] Helmholtz Centre for Ocean Research Kiel (GEOMAR)
Wischhofstrasse 1-3, 24148 Kiel, Germany

[2] Institute of Geosciences, University of Kiel
Ludewig-Meyn-Str. 10, 24118 Kiel, Germany

Keywords: foraminiferal Mg/Ca, alkenones, salinity, EUC, EEP

Submitted to *Paleoceanography*

Abstract

We present high resolution paleotemperature records from two marine sediment cores in the hydrographically complex Eastern Equatorial Pacific (EEP) off northern Peru. Temperature reconstructions cover surface and subsurface depths using the alkenone unsaturation index $U^{K'}_{37}$ and foraminiferal Mg/Ca of shallow-dwelling *Globigerinoides ruber* and thermocline-dwelling *Neogloboquadrina dutertrei*, which mirror changes in upper ocean stratification during the last 18,000 years. For all depths relatively warm temperatures are recorded from the deglaciation into the Early Holocene, indicating a strong influence of tropical water masses during this time period. From Early to Late Holocene, foraminiferal-based sea surface temperatures ($SST_{Mg/Ca}$) and in particular subsurface temperatures ($subSST_{Mg/Ca}$) indicate cooling of the upper ocean; the magnitude of cooling is larger in subsurface depths. The $SST_{Mg/Ca}$ lags the $subSST_{Mg/Ca}$ by ~1-2 kyrs, indicating that SST development is considerably influenced by subSST evolution. These observations indicate the invasion of cooler water masses in the EEP, probably the enhanced admixture of the Equatorial Under Current (EUC), while tropical surface waters are pushed towards the equator. Cooling trends are accompanied by freshening of surface and subsurface water masses, indicated by decreasing $\delta^{18}O$ values of seawater. Freshening is accompanied by a pronounced increase in the temperature gradient between surface ($SST_{UK'37}$) and subsurface ($subSST_{Mg/Ca}$) waters from ~5°C during the deglaciation to ~8°C during the Late Holocene, pointing to the shoaling of the thermocline. Cooling and freshening trends coincide with the gradually and continuously increasing marine productivity during the Holocene, indicating that the enhanced admixture of the nutrient-rich EUC fueled marine productivity from below.

5.1: Introduction

The large, northward flowing Humboldt Current (HC) transports cold and nutrient rich surface and subsurface water masses into the EEP, making this area to a key region for circulation processes within the Pacific. The HC converges with warm and nutrient-depleted equatorial surface waters in the North of the EEP. This tropical region is characterized by permanent or seasonal upwelling along the coast of Peru [*Kessler*, 2006], which transports cool subsurface waters with high nutrient contents to the ocean surface, resulting in the highest primary production (PP) in the World (3.6 g C m^{-2} d^{-1} [*Pennington et al.*, 2006]). The combination of extremely high rates of PP and oxygen consumption through organic matter remineralization creates one of the most pronounced oxygen minimum zones (OMZs) worldwide [*Karstensen and Ulloa*, 2008; *Fuenzalida et al.*, 2009]. Oxygen concentration is also controlled through oceanic currents, mainly through the EUC, which supplies oxygen to the OMZ. Changes in the EUC contribution or the extension of the OMZ are fundamental for the PP and related degradation processes. On interannual time scales, the El Niño Southern Oscillation (ENSO) causes large variations in the chemical, physical and biological conditions of this sensitive system [*Philander*, 1983; *McPhaden et al.*, 1998]. Furthermore, changes in the position of the Intertropical Convergence Zone (ITCZ) result in a modification of hydrographic features like the Equatorial Front (EF) and are thus important control factors for the local hydrography [*Palacios*, 2004; *Fiedler and Talley*, 2006].

A number of previous studies have used Mg/Ca and $\delta^{18}O$ ratios of planktonic foraminifers or alkenone-based reconstructions to estimate the SST evolution in the area, modulation in ENSO activity, warming since the Last Glacial Maximum, and past changes in the position of ITCZ and EF [*Lea et al.*, 2000; *Loubere et al.*, 2003; *Kienast et al.*, 2006; *Koutavas et al.*, 2006; *Koutavas and Sachs*, 2008; *Pena et al.*, 2008a; *Dubois et al.*, 2009; *Leduc et al.*, 2009]. Mg/Ca ratios of foraminiferal tests serve as a widely-used proxy in paleoceanography to assess past ocean temperatures [*Nürnberg et al.*, 1996; *Nürnberg*, 2000]. The combined analysis of Mg/Ca and $\delta^{18}O$ ensures the recording of the same seasonality and/or habitat effects that may occur when proxy data from different faunal groups are compared. Most advantageous, such approach allows to extract the $\delta^{18}O$ record of past

ocean water, and hence approximation of salinity variations [*Nürnberg*, 2000; *Schmidt et al.*, 2004; *Pahnke and Zahn*, 2005].

Main focus of this study is to reconstruct the external forcing mechanisms, which affected the spatial and temporal extension of the local hydrography. Here, we present high resolution time series of surface and subsurface temperatures covering the last ~18 kyrs from cores M772-056-5 and 059-1 off the Peruvian margin. Surface temperatures are based on the analyses of alkenones as well as Mg/Ca of shallow dwelling foraminifers; subsurface temperature records are based on Mg/Ca of deeper-dwelling foraminifers. Our records show the gradual shoaling of the thermocline during the Holocene, probably resulting from an enhanced admixture of cooler EUC waters in subsurface depths.

5.2: Hydrography

The hydrographic setting of the EEP [*Fiedler and Talley*, 2006; *Kessler*, 2006; *Montes et al.*, 2010] is characterized by permanent or seasonal upwelling along the coasts of Chile and Peru. Persistent south-easterly trade winds result in an Ekman transport of surface waters, which is balanced by coastal upwelling of cold, nutrient-rich water masses from subsurface depths [*Kessler*, 2006]. During austral winter (Jul-Sep), the more northern position of the ITCZ causes an intensification of the southeast trades [*Wyrtki and Meyers*, 1976; *Strub et al.*, 1998], leading to stronger upwelling of the subsurface waters along the Peruvian margin [*Karstensen and Ulloa*, 2008]. In contrast to this, the austral summer (Jan-Mar) is characterized through a warm and relatively stratified water column in the EEP.

Surface depths at ~12-15°S are characterized by a relatively cool water mass, which shows temperatures of 14-18°C and a salinity of ~35 [*Ayón et al.*, 2008]. This water mass is Cold Coastal Water (CCW) and it can be clearly identified in surface temperature plots (Fig. 5-1). It contains a mixture of northward travelling currents and waters upwelled along the coasts of Chile and Peru. South of the equator, Equatorial Surface Water (ESW) is characterized by moderate to warm temperatures ranging from 20 to 25°C and low salinities between 33.8 and 34.8 (Fig. 5-1; [*Wyrtki*, 1966; *Fiedler and Talley*, 2006]). North of the ESW, Tropical Surface Water (TSW) is warmer than ESW while showing a similar salinity (T>25°C, S<34). TSW and ESW are separated by a steep thermal gradient, the EF [*Wyrtki*, 1966; *Palacios*, 2004; *Fiedler and Talley*, 2006; *Rincón-Martínez et al.*, 2010]; it is

a clear surface feature, limited to the upper ~100 m of the water column [*Pak and Zanefeld*, 1974]. The position of the EF is controlled by seasonal migrations of the ITCZ and varies from an equatorial location during austral summer (Jan-Mar) to ~3°N during austral winter (Jul-Sep; [*Palacios*, 2004]). The position of the EF is further influenced by the El Niño Southern Oscillation (ENSO; [*Kessler*, 2006; *Lea et al.*, 2006]), which effectively shapes the local hydrography. In particular, El Niño events cause a strong reduction in the southeast trades, which provokes a southeastward displacement of the equatorial warm water masses. It weakens the upwelling intensity and results in warm temperature anomalies at the surface along the Peruvian margin. The cold counter phase, La Niña, is characterized by an intensification of the south-easterly trades parallel to the Peruvian coast, enhancing upwelling intensity and decreasing SSTs in the EEP [*Philander*, 1983; *Cane*, 2005].

Equatorial Subsurface Water (ESSW) is characterized by high nutrient and low oxygen levels; it originates from the EUC and is transported polewards when approaching the continental shelf. The ESSW is a temperate water mass with a relatively high salinity (T=12.5°C, S=34.9; [*Silva et al.*, 2009]). The EUC originates west of the Galápagos Islands in 100–250 m water depth [*Kessler*, 2006]; highly saline and well oxygenated waters of this water mass can be tracked all the way to the coasts of Ecuador and Peru (Fig. 5-1; [*Toggweiler et al.*, 1991]). The pronounced seasonal cycle of the EUC results in strongest flows between Jan-June (austral summer and fall) and weakest flows between July-Nov (austral winter and stronger upwelling season; [*Lukas*, 1986]). The EUC is split by the Galápagos Islands; its northern branch ultimately feeds the ESSW. The southern branch of the EUC hits the coastline at ~5°S, turning into the Peru Chile Undercurrent (PCUC). This water mass transports low oxygen waters southwards and exposes temperatures of 13-16°C [*Brink et al.*, 1983]. The PCUC is the source water for the coastal upwelling and flows southward along the shelf in depths of ~50-150 m [*Penven et al.*, 2005; *Karstensen and Ulloa*, 2008; *Czeschel et al.*, 2011]; the PCUC deepens down to ~700 m when travelling further south [*Czeschel et al.*, 2011]. The Southern Equatorial Current (SEC) flows westwards close to the equator and is the counter current of the EUC [*Wyrtki*, 1966; *Kessler*, 2006].

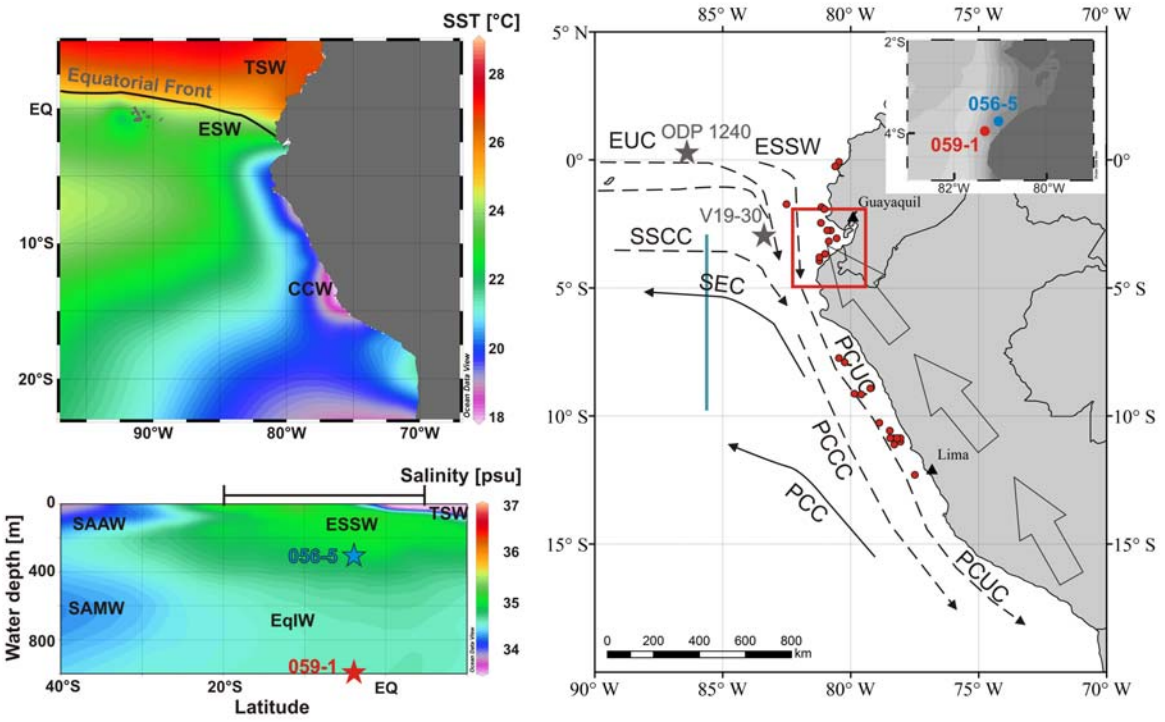

Figure 5-1: Hydrography of the study area and core sites/ reference sites

Left map in upper panel shows surface temperatures (annual mean; [*Locarnini et al.*, 2010]) in study area offshore Peru. Depicted are the EF and prominent surface water masses: Tropical Surface Water (TSW), Equatorial Surface Water (ESW) and Cold Coastal Water (CCW). Right map shows the sediment core location (red rectangular) offshore Ecuador. Red dots indicate MUC surface samples. Gray stars indicate reference sites ODP 1240 [*Pena et al.*, 2008a] and V19-30 [*Koutavas and Sachs*, 2008]. Open block arrows show main wind direction [*Kessler*, 2006]. Blue line is track P19C from WOCE (Fig. 5-2; [*Rubin et al.*, 1998]). Arrows indicate the main oceanographic currents offshore Ecuador and Peru according to [*Wyrtki*, 1967; *Brink et al.*, 1983; *P. T. Strub et al.*, 1998; *Fiedler and Talley*, 2006; *Kessler*, 2006; *Ayón et al.*, 2008; *Silva et al.*, 2009; *Bostock et al.*, 2010]. Surface currents (solid lines): SEC (South Equatorial Current), PCC (Peru Chile Current); subsurface currents (dashed lines): EUC (Equatorial Under Current), ESSW (Equatorial Subsurface Water), SSCC (Southern Subsurface Counter Current), PCUC (Peru Chile Under Current), and PCCC (Peru Chile Counter Current). Inlet provides detailed view of the two study sites, core 056-5 and 059-1; data source for both upper maps is ESRI®. Left lower panel shows salinity section from 40°S to 10°N along the South American coast (annual mean; [*Antonov et al.*, 2010]). Black bar across section indicates latitudinal range from right map. Stars indicate core locations 056 and 059. Water masses indicated are Subantarctic Water (SAAW), Subantarctic Mode Water (SAMW), EqIW (Equatorial Intermediate Water), ESSW and TSW. Ocean Data View was used to generate the two left maps [*Schlitzer*, 2010].

The Southern Subsurface Counter Current (SSCC) flows eastwards at subsurface depths and turns southward when approaching the continental shelf. Roughly 75% of the SSCC reaches the Peruvian coast, feeds the PCUC and consequently supports the Peruvian upwelling [*Montes et al.*, 2010]. About 100 to 300 km offshore, the Peru Chile Counter Current (PCCC) develops at ~7°S and flows southward as far as 35-40°S, as the southward extension of the SSCC [*Strub et al.*, 1995].

Northward flowing currents like the Peru Chile Current (PCC), which can be found ~100-300 km offshore, originate in subantarctic regions [*Penven et al.*, 2005; *Karstensen and Ulloa*, 2008]. This current belongs to the HC system, which maintains the high levels of PP in the EEP. The subantarctic water (SAAW) is characterized by temperatures of 11.5°C and a salinity of 33.8; it is transported from the south into the EEP, here it is subducted towards the equator to a depth of ~100-200 m [*Silva et al.*, 2009].

5.3: Material & Methods

5.3.1: Sediment Surface Samples

A core top study accomplished to validate our proxy signals was performed with samples from 47 stations recovered by multicorer during RV Meteor cruises M77-1 and -2. Samples were analyzed for their foraminiferal contents with respect to two planktonic species, *Neogloboquadrina dutertrei* and *Globigerinoides ruber* (white). The sediment surface samples cover a wide depth range from 60 to 2,000 m and a latitudinal range from the equator to 17°S. On average, the top 0-1 cm, or if foraminiferal content was very low, the top 0-2 cm were sampled. *N. dutertrei* and *G. ruber* were analyzed for their δ^{18}O and Mg/Ca ratio at the same station if foraminiferal content was sufficient. Each multicorer station was accompanied by a CTD cast, providing information about the vertical structure of the water column.

5.3.2: Sediment Cores

Our study focuses on two sediment cores retrieved offshore the border between Ecuador and Peru during Meteor cruise M77, Leg 2 in December 2008 at the northern rim of today's OMZ [*Pfannkuche et al.*, 2011]. Selection of the core locations was accomplished by extensive bathymetric surveying and sediment-echosounder profiling. Piston core M772-056-5 (03°44.99' S; 81°07.48' W, recovery 10.58 m; referred to as 056 in the following) was retrieved from 355 m water depth. Approximately 16 nautical miles further offshore, piston core M772-059-1 (03°57.01' S; 81°19.23' W, recovery 13.59 m; referred to as 059 in the following) was retrieved from 997 m water depth. Sediments at both locations

show a similar lithology: Dark olive to gray clays and silts dominate the sediment composition, containing varying amounts of foraminifers and shell fragments.

5.3.3: Stratigraphy

The stratigraphy of both cores is based on a combination of benthic stable oxygen isotope records ($\delta^{18}O$) and accelerator mass spectrometry radiocarbon datings (AMS^{14}C) of planktonic foraminifers. The age models were constrained using 11 (056) and 10 (059) AMS^{14}C ages, respectively [*Mollier-Vogel et al.*, 2013]. The $\delta^{18}O$ measurements were performed on 2-3 specimens of the endobenthic species *Uvigerina peregrina*; individuals were selected from the 250-355 µm size fraction to minimize a size-related bias of the benthic isotope signal [*Lutze et al.*, 1979]. *U. peregrina* $\delta^{18}O$ values appear to be in equilibrium with seawater $\delta^{18}O$ [*Shackleton and Hall*, 1984]. $\delta^{18}O$ measurements were performed at a ThermoScientific MAT 253 mass spectrometer equipped with an automated CARBO Kiel IV carbonate preparation device (GEOMAR, Germany). The isotope values are calibrated *versus* NBS 19 (National Bureau of Standards) and the in-house standard used is the "Standard Bremen" (Solnhofen limestone). Isotope values are reported in per mil (‰) relative to the VPDB (Vienna Pee Dee Belemnite) scale. The long term precision of the in-house standard is ±0.09‰ for $\delta^{18}O$ (2 σ).

From Early to Late Holocene, the benthic $\delta^{18}O$ values range from 2.8 to 1.8‰ in core 056 and from 4.2 to 3‰ in core 059 (Fig. 5-S1), and are in good agreement with the reference stack NGRIP [*NGRIP Members*, 2004]. The $\delta^{18}O$ records of the planktonic species *N. dutertrei* and *G. ruber* exhibit much lower values (Fig. 5-3a, b, d, e), caused by their shallower habitat depth and thus warmer temperatures. Similar to the benthic records, the planktonic $\delta^{18}O$ data exhibit decreasing values throughout the Holocene, although being less pronounced.

5.3.4: Approximation of Ocean Temperature and Salinity

5.3.4.1: Foraminiferal Mg/Ca

Sediment was sampled for planktonic foraminifers each 5 cm down core. Samples were freeze-dried, subsequently washed over a 63 µm mesh, and dried. On average, 25 uncon-

taminated individuals of dextral coiling *N. dutertrei* were picked from the 250-355 µm size fraction. Size classes, which should be narrow in order to keep size-related intraspecific elemental variations small [*Elderfield et al.*, 2002], had to be widened for several samples due to the low number of available specimens of foraminifers (maximum to 250-400 µm). All specimens were individually picked and identified using the planktonic foraminifers species concepts by *Kennett and Srinivasan* [1983] and *Hemleben et al*. [1989].

The depth habitat of *N. dutertrei* is difficult to specify as views on its vertical occurrence deviate largely. Initial assumptions by *Hemleben et al*. [1989], *Loubere* [2001], *Dekens et al*. [2002] and *Schmuker and Schiebel* [2002] define the depth habitat to vary between ~50 and 150 m water. *N. dutertrei* lives preferably within the tropic to subtropic thermocline [*Fairbanks et al.*, 1982], and its habitat is associated with the deep chlorophyll maximum [*Fairbanks and Wiebe*, 1980; *Fairbanks et al.*, 1982]. Several studies suggest that *N. dutertrei* occurs over a wide range of vertical temperature gradients [*Hilbrecht*, 1997]. In upwelling zones the habitat can shift with the thermocline to shallower waters in case of strong upwelling [*Hilbrecht*, 1997; *Loubere*, 2001]. A core top study from the EEP indicates a calcification depth for *N. dutertrei* of ~150 m [*Faul et al.*, 2000]. Based on a combination of foraminiferal $\delta^{18}O$ values and water samples analyzing the same parameter we estimated local calcification depths for the EEP [*Böschen et al.*, in preparation]. Based on the findings from our study we assume a depth habitat of ~200 m for *N. dutertrei* at our core locations north of the Peruvian upwelling area. Today, this water depth is influenced by the EUC and the ESSW, which have temperatures of ~12-14°C at 200 m water depth [*Lukas*, 1986; *Silva et al.*, 2009].

The annual temperature range for *N. dutertrei* at 200 m water depth is 13.6-13.9°C (Station 21835; WOA 2009 [*Locarnini et al.*, 2010]). The core tops of multi corers located next to our cores sites indicate temperatures of 15.9°C (056) and 17.1°C (059), respectively. These results support the notion of *Faul et al.* [2000], who found the depth habitat of *N. dutertrei* to be along the 15°C isotherm off Peru. The offset of ~1°C between the annual temperature range at 200 m water depth and our core top samples is within the standard error for Mg/Ca derived temperatures [*Regenberg et al.*, 2009], consequently seasonal effects on the Mg/Ca signal of *N. dutertrei* are considered negligible.

For Mg/Ca analysis of the planktonic foraminifer *G. ruber* (white) ~30 specimens were selected from the 250-355 µm size fraction. Due to low *G. ruber* abundances in some

parts of the cores, the size fraction was widened (maximum to 125-400 µm) to gain enough material for the analyses. *G. ruber* is a surface dweller [*Deuser et al.*, 1981; *Dekens et al.*, 2002], hence it is considered as an appropriate proxy to record the temperature of the top ~30 m of the water column. These findings are consistent with the results of *Faul et al*. [2000], who report *G. ruber* as an algae symbiont-bearing species being restricted to the upper water column where light levels, and not necessarily nutrients or chlorophyll levels, are highest. Species selection was restricted to the morphotype sensu stricto (s.s.), as *Wang* [2000] and *Steinke et al*. [2005] revealed measurable differences in both, Mg/Ca and $\delta^{18}O$, among different morphotypes of *G. ruber*.

Mg/Ca data of *G. ruber* from four multicorer core top samples in the study area provide a mean temperature estimate of 23.3°C, close to mean austral summer season value in the modern setting (23.5°C; Jan-Mar) and noticeable warmer than the annual mean (21.3°C; both from 0 m water depth; Station 21835, WOA 2009 [*Locarnini et al.*, 2010]). Although *G. ruber* is often regarded as a recorder of annual mean temperatures [*Hemleben et al.*, 1989; *Lin et al.*, 1997; *Lea et al.*, 2003], we assume that the Mg/Ca signal of *G. ruber* in our multicorer surface samples reflects austral summer SSTs. The good accordance between modern alkenone- and Mg/Ca-based surface temperature records indicates today a similar habitat and seasonality of both proxy carriers.

Picked foraminiferal samples were homogenized and split for stable isotope analyses (~$^1/_3$) and for Mg/Ca analyses (~$^2/_3$) and transferred into acid-cleaned vials. Samples for stable carbon and oxygen analyses were rinsed three times with ultrapure water and twice with ethanol including ultrasonic treatment in between. Samples for Mg/Ca measurements were cleaned following the protocol of *Barker et al*. [2003], but adding the reductive step with hydrazine. After cleaning, samples were transferred into new vials and a final leaching with 0.001 molar HNO_3 followed. Samples were dissolved prior to measurement in 0.075 molar HNO_3 (thermally distilled, “supra acid”). *N. dutertrei* samples of core 059 and *G. ruber* samples of both cores were dissolved in 0.075 molar HNO_3 and diluted with 2.5 ml yttrium water (concentration 1 ppm). Adding yttrium was performed to detect possible drifts of the ICP during the analyses.

Mg/Ca analyses of core 056 (*N. dutertrei*) and of surface samples (*N. dutertrei*) were carried out with the SPECTRO *Ciros^{CCD} SOP* ICP-AES (provided with a radial plasma) at Kiel University, Germany. All remaining samples were analyzed with an ICP-OES Varian 720,

equipped with axial plasma, at GEOMAR. A quality standard (ECRM 752-1) was run on both machines to track possible offsets; average values for Mg/Ca were 3.86 ±0.09 mmol mol^{-1} (Kiel University) and 3.80 ±0.06 mmol mol^{-1} (GEOMAR), respectively. Relative standard deviation for the ECRM standard with respect to Mg/Ca was 0.1 mmol mol^{-1} (2 σ). All analyzed samples were standardized with respect to the ECRM standard. To exclude clay contamination and post-depositional Mn-rich carbonate coatings, which can have strong control on Mg/Ca ratios [*Rosenthal et al.*, 2000], we checked Fe/Ca, Al/Ca and Mn/Ca ratios in our samples. Al/Ca and Mn/Ca ratios were below the detection limit within our data set. Previous studies have shown that Mn is already reduced in the water column offshore Peru and thus only minor amounts of particulate-bound Mn are available at the seafloor [*Böning et al.*, 2004; *Scholz et al.*, 2011; *Glock et al.*, 2012]. Fe/Ca ratios were on average 4.08 mmol mol^{-1}. No correlation between high Fe/Ca ratios and outliers within the Mg/Ca data set was present. We hence conclude that the measured high Fe/Ca ratios did not affect the Mg/Ca signal.

Mg/Ca ratios of planktonic *N. dutertrei* were converted into temperatures by using the 'warm water' multispecies calibration (1) of *Regenberg et al.* [2009]:

$$Mg/Ca = 0.22 * \exp(0.113 * T_c) \quad (1)$$

Mg/Ca ratios of planktonic *G. ruber* were converted into temperatures by using the 'species specific' calibration (2) for *G. ruber* of *Regenberg et al.* [2009]:

$$Mg/Ca = 0.4 * \exp(0.094 * T_c) \quad (2)$$

All Mg/Ca ratios (own data and reference data sets) were transferred into temperatures using the equations described above. This was done to exclude differences between transfer function. The application of the transfer functions by *Regenberg et al.* [2009] resulted in the best fit between core top values from our data set and annual mean temperatures [*Locarnini et al.*, 2010], hence indicating that this transfer function provides the most precise approach for Mg/Ca-based temperature reconstructions in the EEP. Dissolution of foraminiferal calcite, which might lower the analyzed Mg/Ca ratios, is discussed in the supplementary. The term $SST_{Mg/Ca}$ in the manuscript is always based on Mg/Ca ratios of *G. ruber*, while $subSST_{Mg/Ca}$ always refers to the Mg/Ca ratios of *N. dutertrei*.

5.3.4.2: The Oxygen Isotope Signature of Seawater

Regional variations of salinity were approximated from the $\delta^{18}O$ of seawater ($\delta^{18}O_{sw}$) [*Nürnberg*, 2000], which was calculated by combining the temperatures derived from foraminiferal Mg/Ca (Fig. 5-3f-i) and the corresponding $\delta^{18}O$ value of the same species (Fig. 5-3a, b, d, e). As $\delta^{18}O_{sw}$ comprises both, ice-volume-controlled changes and local variation in $\delta^{18}O_{sw}$ due to regional hydrological changes, the temperature signature from the initial $\delta^{18}O_{G.ruber}$ and $\delta^{18}O_{N.dutertrei}$ records were removed by using the equation (3) from *Thunell et al*. [1999]:

$$T = 14.9 - 4.80\ (\delta^{18}O_{calcite} - \delta^{18}O_{sw}) \quad (3)$$

To generate the regional ice volume free ($\delta^{18}O_{sw}$) record ($\delta^{18}O_{ivf\text{-}sw}$), we accounted for changes in global $\delta^{18}O_{sw}$ due to continental ice volume variability using the relative sea level curve of *Waelbroeck et al*. [2002] (Fig. 5-3).

5.3.4.3: Alkenone Temperatures

Sea surface temperatures (SSTs) were also derived from the alkenone unsaturation index ($U^{K'}_{37}$). Alkenones were extracted from 0.5 g freeze-dried and homogenized bulk sediment samples using an accelerator solvent extraction method (Dionex ASE). Samples were measured prior to C_{37} group analysis using a double column multidimensional gas chromatograph (Agilent 6890N) system [*Blanz et al.*, 2005] at Kiel University. Temperatures were calculated from the $U^{K'}_{37}$ index by applying the global core top equation of *Müller et al*. [1998]. SSTs based on $U^{K'}_{37}$ analyses will be referred to as $SST_{UK'37}$ within the following. Coccolithophorid production, and hence alkenone production, is most likely not taking place during the upwelling season, but later during the austral summer. $SST_{UK'37}$ seems to be a faithful recorder of the top 10 m in the water column, since alkenone producing coccolithophorids as photosynthesizing organisms are restricted to high light levels with the main habitat in this water depth [*Müller et al.*, 1998]. The $SST_{UK'37}$ value of 22.9°C from the MUC core top sample located nearby core 059 exceeds the modern mean annual SST of 21.3°C (0 m water depth; Station 21835 at 81.5°W, 3.5°S; WOA, 2009 [*Locarnini et al.*, 2010]), but matches the modern austral summer (Jan-Mar) SST of 23.5.3°C at the same WOA station; hence, indicating that in the area the $SST_{UK'37}$ most likely records austral

summer season. Such pattern was already recognized by *Prahl et al.* [2010] in the Peruvian upwelling between ~11°S and ~15°S, who postulated that at low latitudes the $SST_{UK'37}$ signal is skewed seasonally towards the austral summer season, when surface waters are warmest. During this season, the surface ocean is highly stratified, nutrients are depleted, and coccolithophorids dominate over diatom production. Such notion is supported by studies in the Gulf of California, showing that the coccolithophorid and thus alkenone flux is not highest during winter times when upwelling is most intense and primary production is highest, but during summer times when the system is less productive [*Goñi et al.*, 2001].

5.3.5: Paleoproductivity Proxies

The total organic carbon and total nitrogen contents were measured in bulk sediment to assess changes in paleoproductivity. The total organic carbon content (TOC, wt. %) for core 056 was determined by a LECO C-S analyzer with a precision of ±0.5% (2 σ; University of Bordeaux, France). The total nitrogen (TN, wt %) of the sediment samples from core 056 was measured with a CARLO ERBA CN analyzer 2500 at University of Bordeaux, France (precision ±0.5%, 2 σ). The TOC, TN and total carbon (TC, wt %) for sediment samples of core 059 were analyzed by CARLO ERBA Model NA 1500 Elemental Analyzer at GEOMAR, Kiel (Germany), where precision for an internal standard was 0.15% for TN and TC, and 0.2% for TOC (2 σ). The TC and TN were measured in bulk sediment samples, whereas the TOC was measured in decalcified samples. To assess the sources for TOC and furthermore to be able to distinguish between terrigenous and marine sources the ratio atomic organic carbon versus atomic total nitrogen was calculated (C/N ratio).

C/N ratios of bulk sediment are an indicator of the source of organic matter in the sediment. A plot of TOC versus TN revealed a tight linear correlation between the two proxies (R^2 = 0.94; data not shown), with the % TN intercept indicating a certain amount of the total nitrogen to be of inorganic origin [*Müller*, 1977]. To correct the effect of the inorganic ammonium, the % TN intercept was subtracted from all % TN values [*Goñi et al.*, 1998]. C/N ratios increased slightly through this correction, an incorporation of inorganic material can be excluded. Consequently, the ratio of atomic organic carbon to atomic organic nitrogen was calculated, referred to as C/N ratio hereafter.

Additionally, the split halves of both cores were analyzed in a non-destructive way with the Avaatech XRF Core Scanner (University of Kiel). The cores were scanned with a spatial resolution of 1 cm applying a basic voltage of 10 kV. Data quality was ensured by monitoring the "dead time", which was constantly below the critical value of 40% [*Tjallingii*, 2006]. The element intensities are given in counts per second (cps) and are used to estimate elemental concentrations.

5.4: Results

5.4.1: Temperature Changes in Subsurface Waters

The $subSST_{Mg/Ca}$ of core 059 scatters between 15 and 17°C during deglacial times and the Early Holocene (Fig. 5-4i), markedly interrupted by drops during the cold periods of Heinrich 1 (H1; 14.2-16.8 ka BP; [*Bond et al.*, 1992; *Bond et al.*, 1993; *Hemming*, 2004]) and the Younger Dryas (YD; 11.7-12.9 ka BP; [*Blockley et al.*, 2012]) and a warming during the Bølling/Allerød (B/A; 14.7-12.9 ka BP; [*Blockley et al.*, 2012]). The $subSST_{Mg/Ca}$ record of core 056 shows warmer and relatively constant temperatures of ~18°C during the YD and the Early Holocene (max. 19°C) and experiences a pronounced temperature drop of ~2°C at ~9.5 ka BP (Fig. 5-4h). During the Middle and Late Holocene, $subSST_{Mg/Ca}$ in this core continues to cool constantly and reaches temperatures of ~15°C in the youngest sections. Temperatures in core 059 cool more gradually compared to core 056, starting at ~11 ka BP (Fig. 5-4i) and decrease markedly after 4.5 ka BP. In total, the entire Holocene magnitude of subsurface cooling amounts to ~4°C and ~2°C in core 056 and 059, respectively. Core 056, located closer to the coast, thus experiences a more pronounced decline in $subSST_{Mg/Ca}$ during the Holocene with the temperatures approaching those of the core 059 during the Late Holocene since ~2-3 ka BP (Fig. 5-4h and i).

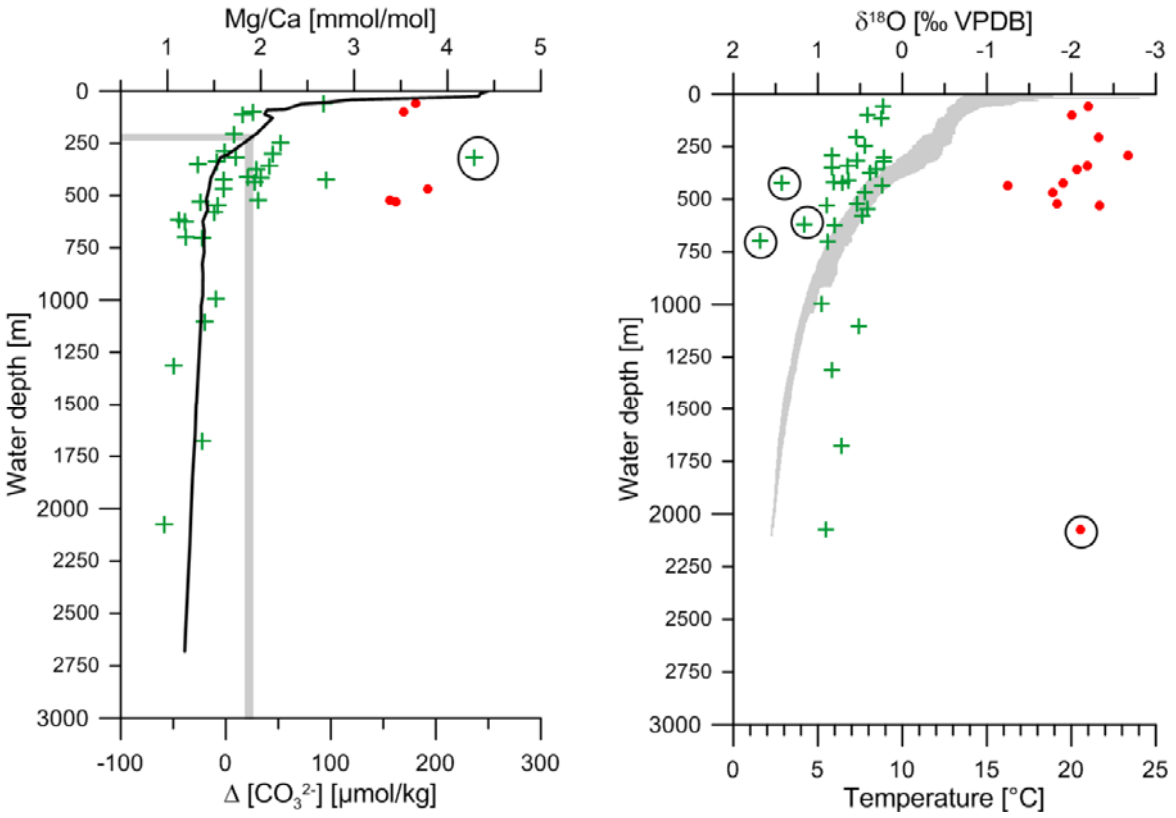

Figure 5-2: Mg/Ca and $\delta^{18}O$ of *G. ruber* and *N. dutertrei* for MUC surface samples

Left: Mg/Ca of *N. dutertrei* (crosses) and *G. ruber* (dots) from sediment surface samples *versus* water depth. $Mg/Ca_{N.\ dutertrei}$ values decrease with increasing water depth, while *G. ruber* values are more positive and remain relatively constant. The black line represents the calcite saturation index $\Delta[CO_3^{2-}]$ *versus* water depth, calculated after *Lewis and Wallace* [1998] and *Jansen et al.* [2002] on the base of WOCE line P19C, stations 359 and 361 [*Rubin et al.*, 1998]. Gray bars indicate $\Delta[CO_3^{2-}]$ thresholds of 18-26 µmol/kg critical for selective Mg-removal [*Regenberg et al.*, 2006], which are reached in ~200 m water depth.

Right: $\delta^{18}O$ values of the same samples *versus* water depth. The $\delta^{18}O$ signals for both species remain more or less constant over the wide range of water depths, with values of *G. ruber* being more negative than those of *N. dutertrei*. The gray area marks the averaged range of CTD-derived temperatures observed during M77-1 and M77-2 between the Equator and 17.5°S [*Pfannkuche et al.*, 2011]. Circled data points in both plots indicate outliers, which were excluded from further considerations.

The cooling of the water column in subsurface depths is accompanied by freshening trends. Subsurface $\delta^{18}O_{ivf\text{-}sw}$ values in core 059 (Fig. 5-4m) scatter around ~1.3‰ during the deglaciation and shift to fresher values during the Middle and Late Holocene; maximum values are 0.5‰ for the Late Holocene. The $\delta^{18}O_{ivf\text{-}sw}$ values in core 056 are stable (~1.7‰; Fig. 5-4n) until ~9.5 ka BP; then a continuous freshening starts resulting in $\delta^{18}O_{ivf\text{-}sw}$ values approaching those of core 059 for the Late Holocene.

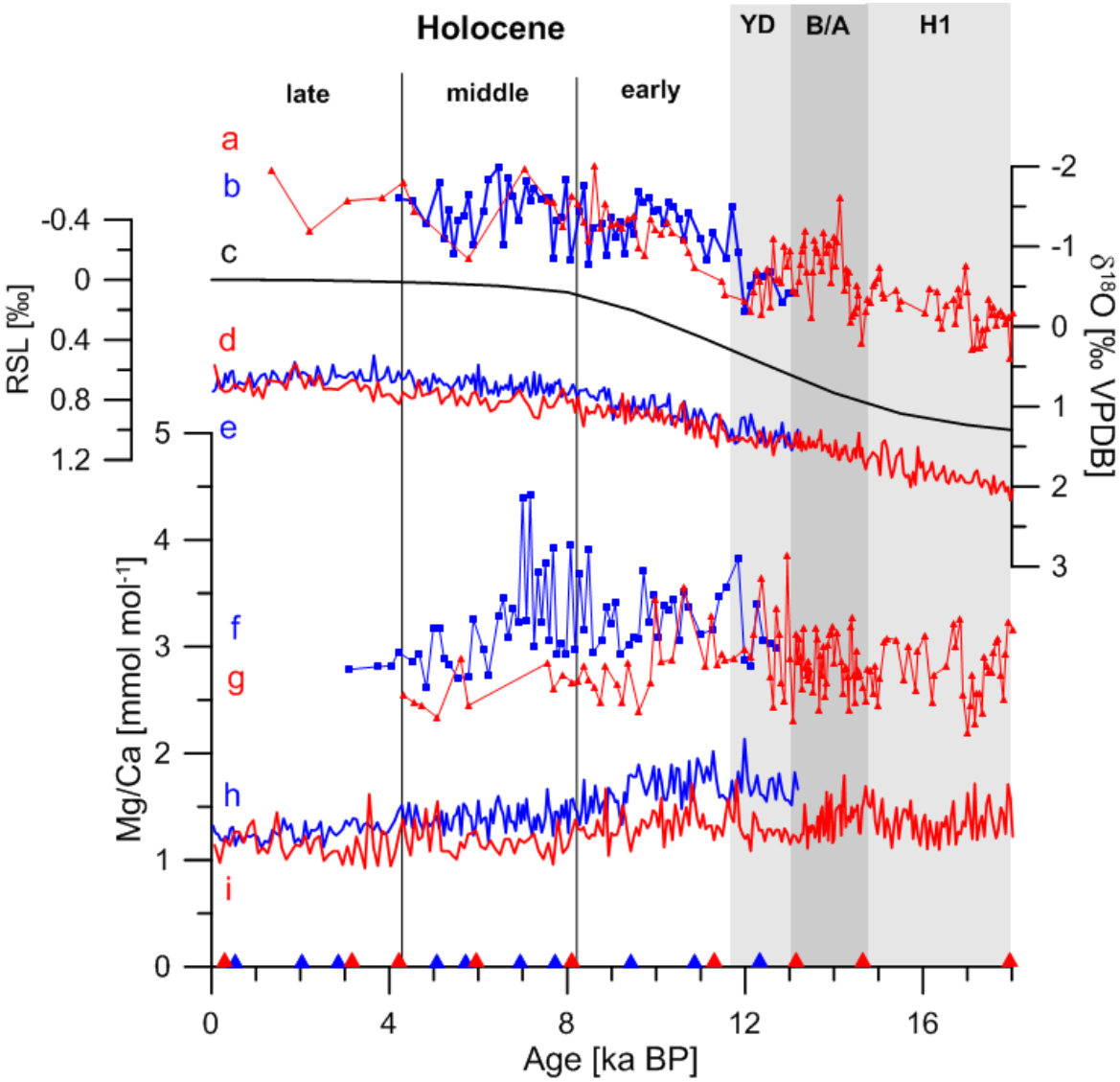

Figure 5-3: Down core Mg/Ca and $\delta^{18}O$ raw data for *G. ruber* and *N. dutertrei*

$\delta^{18}O$ values of planktonic species *G. ruber* and *N. dutertrei* are depicted in the upper panel: (a) and (b) are the $\delta^{18}O$ records of *G. ruber* for cores 059 and 056, respectively. (c) is the RSL curve by *Waelbroeck et al.* [2002], which was used to generate the regional ice volume free ($\delta^{18}O_{sw}$) record ($\delta^{18}O_{ivf\text{-}sw}$; Fig. 5-4). (d) and (e) are the $\delta^{18}O$ records of *N. dutertrei* for cores 059 and 056, respectively. Lower panel shows Mg/Ca ratios for both species: (f) and (g) are the Mg/Ca ratios for *G. ruber* for cores 056 and 059, respectively. (h) and (i) are the Mg/Ca ratios for *N. dutertrei* for cores 056 and 059, respectively. Reductive cleaning was applied to all samples. Triangles at the x-axis mark AMS^{14}C datings for core 059 (red) and 056 (blue).

5.4.2: Temperature Changes in Surface Waters

The $SST_{UK'37}$ record of core 059 varies between 19 and 21.5°C during the deglaciation and experiences a pronounced and abrupt warming of ~2°C during the YD (Fig. 5-4e). The $SST_{UK'37}$ record remains relatively stable during the Holocene and rises to ~22.5°C in the Late Holocene.

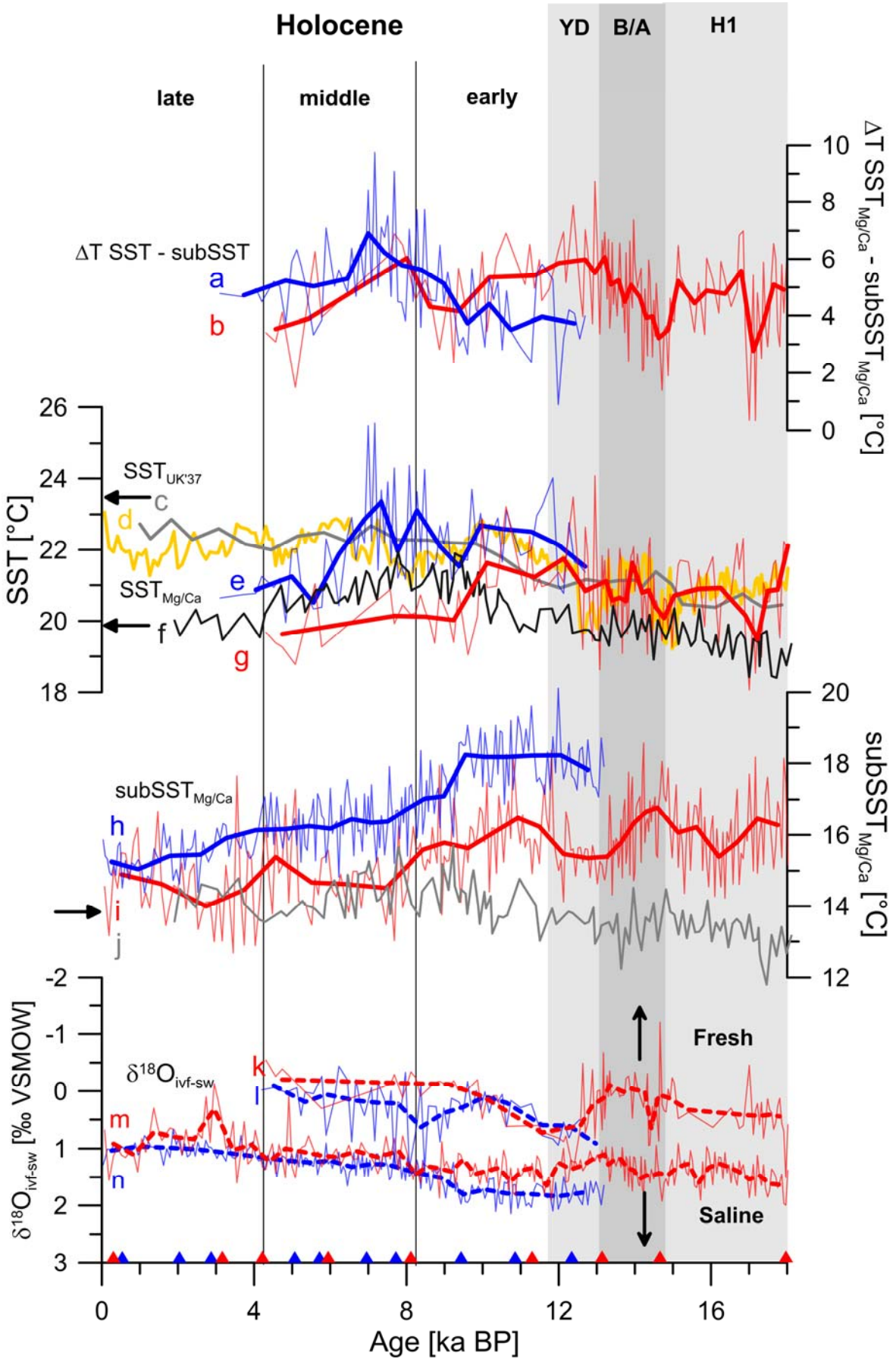

Figure 5-4: Temperature and salinity reconstructions over the last ~18 kyrs

Temperature and salinity reconstructions over the last ~18 kyrs for distinct water depth levels offshore Peru at 3.5°S. Blue lines refer to core 056 (355 m water depth) and red lines to 059 (1,000 m water depth). (a) and (b) are the ΔT records for cores 056 and 059, indicating the evolution of the thermocline; (c) is the reference record for $SST_{UK'37}$ from Site V19-30 to the west of our core location [*Koutavas and Sachs*, 2008], (d, yellow curve) is the $SST_{UK'37}$ record of core 059; (e) is the $SST_{Mg/Ca}$ record of core 056, (f) is the reference record for $SST_{Mg/Ca}$ of ODP Site 1240 to the north of our core location ([*Pena et al.*, 2008a]; Fig. 5-1), (g) is the $SST_{Mg/Ca}$ record of core and 059; running 5-point averages are included to smooth the records (thick lines). Thermocline temperatures ($subSST_{Mg/Ca}$) are derived from *N. dutertrei*; running 10-point averages are included to smooth the records (thick lines). (h) refers to $subSST_{Mg/Ca}$ in core 056 and (i) to the same proxy in core 059. (j) is the $subSST_{Mg/Ca}$ record of ODP Site 1240 [*Pena et al.*, 2008a]. Regional variations of salinity were approximated from the ice-volume corrected $\delta^{18}O$ of seawater ($\delta^{18}O_{ivf\text{-}sw}$; lower panel). (k) and (l) are the surface $\delta^{18}O_{ivf\text{-}sw}$ records of cores 059 and 056, respectively. (m) and (n) are the subsurface $\delta^{18}O_{ivf\text{-}sw}$ records of cores 059 and 056, respectively; dashed lines represent running 5-point averages. Arrows on the left of the graph indicate annual temperature range for SST's and annual mean temperature for subSST [*Locarnini et al.*, 2010]. Triangles at the x-axis mark AMS^{14}C datings for core 059 (red) and 056 (blue). All depicted Mg/Ca ratios were transferred into temperatures using the 'species specific' equation for *G. ruber* and the 'warm water multispecies' equation for *N. dutertrei* [*Regenberg et al.*, 2009]. Reductive cleaning was applied to all depicted Mg/Ca data sets.

The $SST_{Mg/Ca}$ record of core 059 scatters around 21°C during the Deglaciation (Fig. 5-4g), interrupted by a drop of ~1°C during the H1. During the Early Holocene at ~10 ka BP, $SST_{Mg/Ca}$ in core 059 experiences a cooling by ~2°C. The $SST_{Mg/Ca}$ record of core 056 shows relatively constant temperatures of ~22.5°C during the Early Holocene and scatters between ~21.5 and 22.5°C at the transition between Early and Middle Holocene (Fig. 5-4f). At ~8.5 ka BP, $SST_{Mg/Ca}$ of core 056 drops to ~20.5°C and remains at this temperature level. The $SST_{Mg/Ca}$ records of both cores end at ~4 ka BP.

The Holocene cooling trends in $SST_{Mg/Ca}$ are accompanied by the $\delta^{18}O_{ivf\text{-}sw}$ reconstructions based on *G. ruber* (Fig. 5-4k and l). Prior to 11 ka BP, both cores show relatively uniform $\delta^{18}O_{ivf\text{-}sw}$ values ranging from 0.5 to 0‰. The shift towards more negative values implying freshening starts at ~11 ka BP in core 059, whose $\delta^{18}O_{ivf\text{-}sw}$ values increase until 0.4‰ for the Late Holocene. Changes towards fresher conditions start delayed at ~8.5 ka BP at the 056 location and continue to rise up to 0‰ for the Late Holocene.

5.4.3: Changes in Marine Productivity

C/N ratios of bulk sediment indicate the source of organic matter in the sediment. Typically, marine organic matter exhibits C/N ratios of 5-8 close to the Redfield ratio of marine phytoplankton [*Redfield et al.*, 1966], while terrestrial organic matter shows ratios be-

tween 20 and 200 [*Hedges et al.*, 1986]. The C/N ratios in the lower part of core 059 show ratios of ~15-20 (Fig. 5-5b), indicating a mixture between marine and terrestrial organic matter. The values converge with the C/N ratios of core 056 (Fig. 5-5a) and values of both cores lower from ~15 at the onset of the Holocene to ~12 for the Late Holocene.

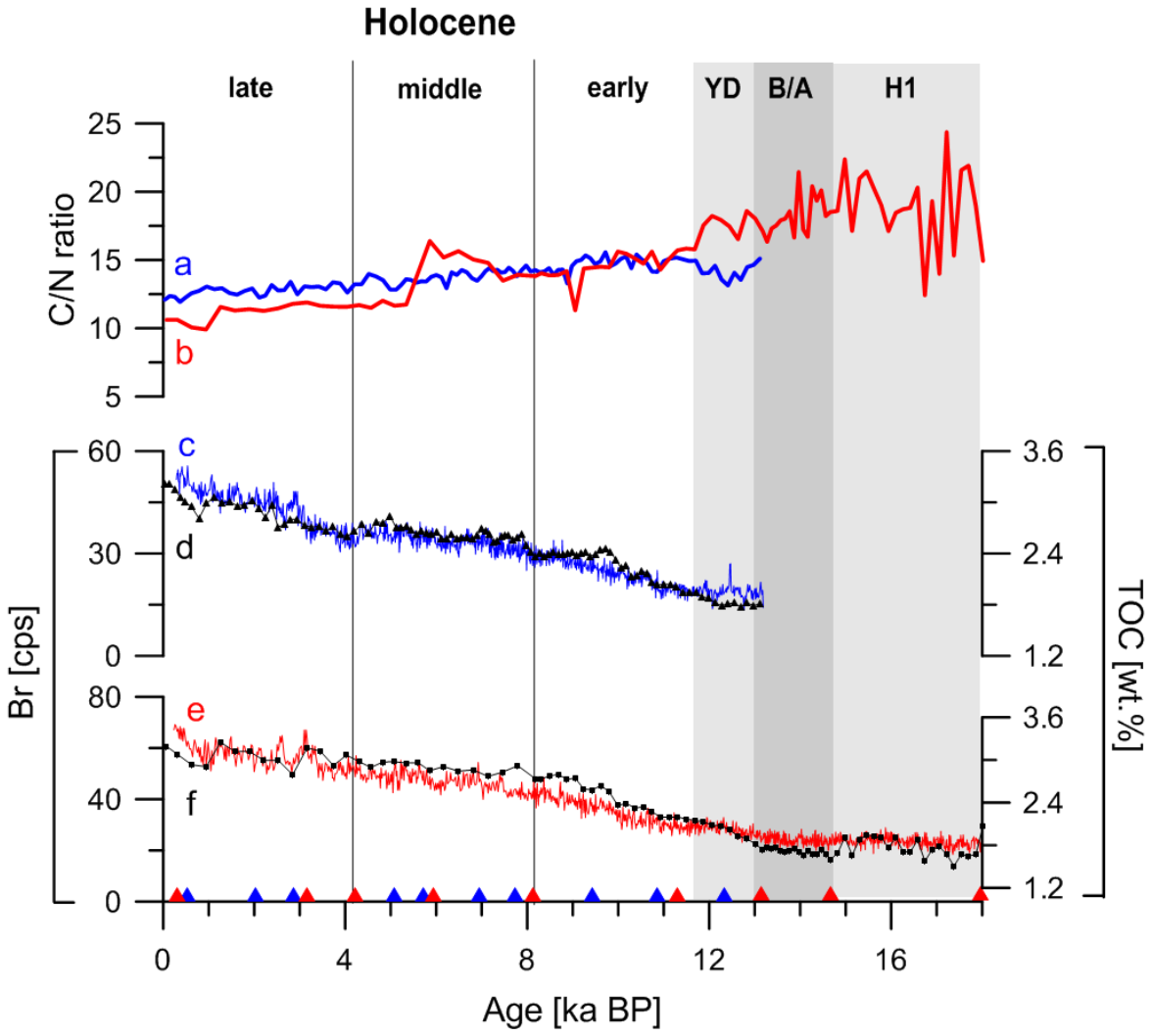

Figure 5-5: Proxies indicating marine productivity and mixture between marine and terrigenous input

Blue lines refer to core 056 (355 m water depth) and red lines to 059 (1,000 m water depth). Different proxies are plotted to indicate local changes in marine productivity as well as the varying mixture between marine and terrigenous input. (a) and (b) are the C/N ratios of core 056 and 059, respectively; the % TN intercept was subtracted from all % TN values to exclude an incorporation of inorganic material (ammonium). The close correlation between total organic carbon in the bulk sediment and XRF-scanned bromine further emphasizes an increase in marine productivity: (c) and (d) are the bromine and TOC records for core 056, (e) and (f) are the same proxy records for core 059. Triangles at the x-axis mark AMS^{14}C datings for core 059 (red) and 056 (blue).

Paleoproductivity can be reconstructed from the comparison of XRF-scanned Bromine (Br) values and TOC contents from bulk sediment (Fig. 5-5c-f). Br values increase from 20

to 70 cps in the further offshore core 059 (Fig. 5-5e) and from 15 to 50 cps in the shallower core 056 (Fig. 5-5c). Corresponding TOC values rise from 1.8 to 3.0% (core 059; Fig. 5-5f) and from 1.8 to 3.3% (core 056; Fig. 5-5d), respectively. Both cores support the tight correlation between XRF-scanned Br values and TOC from bulk sediment, which has been reported previously [*Ziegler et al.*, 2008].

5.5: Discussion

5.5.1: Subsurface Variability of Temperature and Salinity

The $subSST_{Mg/Ca}$ amplitude of ~4°C (Fig. 5-4h and i) observed in both cores mirrors hydrographic changes at ~200 m depth and is accompanied by freshening trends at both core locations (Fig. 5-4l and m). The distinctive temperature and salinity developments imply changes in the local water masses at 3.5°S in the EEP. Prevailing water masses are nowadays the southward flowing EUC and ESSW, which have temperatures of ~12.5-14°C at 200 m water depth [*Lukas*, 1986; *Silva et al.*, 2009]. The ESSW dominates the study area in the modern setting, with temperatures being slightly cooler (12.5°C; [*Silva et al.*, 2009]) than core top values at our study sites indicate (14.6-15.8°C). An increased influence of ESSW during the Holocene might explain the observed temperature developments. Another mechanism might be provided by the EUC itself, which meets the South American coastline between 2°N and 2°S at depths between 30 and 300 m [*Lukas*, 1986]. The temperatures of the EUC (T= 13-14°C [*Lukas*, 1986]) match our core tops well (14.6-15.8°C), hence enabling this water mass to influence our study sites noticeably. It seems likely that a varying mixture between cooler subsurface (EUC/ ESSW) and warmer tropical water masses (TSW) is present at our core locations: Higher proportions of tropical water masses during the deglaciation and a continuously growing contribution of cooler EUC (-sourced) waters during the Holocene.

The subsurface Mg/Ca record of the deep ODP Site 1240 (2,921 m; *N. dutertrei*; Figs. 5-1 and 5-4j; [*Pena et al.*, 2005; *Pena et al.*, 2008a]) shows slightly different trends than our $subSST_{Mg/Ca}$ records. The ODP record implies slightly cooler temperatures of ~13-14°C during the deglaciation, while our record of core 059 scatters around ~16°C (Fig. 5-4j and i). With the onset of the Holocene the ODP site experiences a slight warming while both of our records cool markedly, approaching temperatures of the equatorial ODP Site 1240

for the Middle Holocene. We propose that the records mirror changes in the admixture of the EUC into the EEP: ODP Site 1240 was continuously influenced by the EUC, while our cores indicate a shift from warmer (tropical) to cooler water masses (EUC). The convergence of all three records during the Middle Holocene points towards similar water masses at all three study sites nowadays.

Our hypothesis of an enhanced admixture of the EUC and a related cooling of the subsurface water masses in the EEP during the Holocene is not in agreement with recent interpretations of a Nd isotope data set obtained at the equatorial ODP Site 1240 (Fig. 5-1) by *Pena et al.* [2013]. These authors suggest a reduced Holocene contribution of Southern Ocean Intermediate Waters (SOIW) at their study site deduced from ε_{Nd} signatures extracted from cleaned shells of *N. dutertrei*. Recently obtained water column data from essentially the same location indicate, however, identical ε_{Nd} values for both intermediate and bottom waters of -1.6 [*Grasse et al.*, 2012]. It can thus not unambiguously be concluded that the ε_{Nd} record of *Pena et al.* [2013] truly reflects varying SOIW contributions into the EUC via 'ocean tunneling'. Alternatively, the ε_{Nd} recorded in the cleaned foraminiferal shells may represent bottom water values as for example suggested by *Roberts et al.* [2010].

An enhanced influence of the EUC seems the most likely mechanism to explain the observed temperature developments. Thus, we rule out a direct influence of southern component water masses supported by the following arguments: Our core locations close to the Gulf of Guayaquil are relatively sheltered, caused by the headland south of the Gulf, making it difficult for water masses from the South to penetrate the area. Consequently, water masses from a southern source region are unlikely to have influenced our core sites noticeably, since ADCP-profiles indicate that most subsurface currents in the study area originate from a northern to western direction [*Pfannkuche et al.*, 2011]. This points primarily towards the EUC as the main source water for subsurface depths at our study sites in the Gulf of Guayaquil. Additionally, southern water masses are either subducted further south (Subantarctic Water, SAAW) and/ or they are located to deep to influence water depths of 200 m noticeable (Subantarctic Mode Water, SAMW [*Sloyan et al.*, 2010] and Antarctic Intermediate Water, AAIW [*Silva et al.*, 2009]). CCW is a cooler water mass being located south of our core sites [*Ayón et al.*, 2008], but it remains a surface feature and is thus unlikely to have influenced our core sites noticeably.

5.5.2: Surface Variability of Temperature and Salinity

The $SST_{UK'37}$ pattern in core 059 is similar to the record of core V19-30 from further offshore ([*Koutavas and Sachs*, 2008]; Figs. 5-1 and 5-4d), indicating that surface waters at both sites were exposed to similar water masses. The core 059 $SST_{UK'37}$ and $SST_{Mg/Ca}$ records are *quasi* identical in absolute temperature and amplitude until the onset of the Holocene (Fig. 5-4e and g). Moreover, since ~11.5 ka BP, $SST_{Mg/Ca}$ values are on average lower than alkenone temperature estimates, superimposed by a pronounced cooling trend of ~2°C in the *G. ruber* signal since ~11.5 ka BP. Delayed by ~3 kyrs, the $SST_{Mg/Ca}$ values in the near-shore core 056 also decline towards the late Holocene. The Holocene cooling revealed in $SST_{Mg/Ca}$ records of *G. ruber* contrasts the alkenone signal for Holocene warming. The modern setting at 3.5°S in the EEP is characterized by almost identical SSTs being recorded in alkenones and Mg/Ca of *G. ruber* (Chapter *5.3.4.1.*), hence indicating that both proxies inhabit similar seasons/ habitat depths nowadays. However, this relation likely has changed during the past 18 kyrs, which affords consideration.

To our notion, the absolute difference between $SST_{UK'37}$ and $SST_{Mg/Ca}$ during the Early and Middle Holocene (ΔT of up to 2°C) might be explained by a different habitat depth of alkenone-producing coccolithophorids in the surface ocean (~0-10 m water depth) and slightly deeper dwelling *G. ruber* s.s. (~10-30 m water depth). A strengthened seasonality starting at the onset of the Holocene might be a further mechanism to account for the offset between $SST_{UK'37}$ and $SST_{Mg/Ca}$. The Early Holocene has been associated previously with stronger ENSO conditions [*Ehlert et al.*, 2013] and intensified coastal upwelling [*Vargas et al.*, 2006] in the EEP, which might strengthen the seasons. Additionally, and in accordance with strengthened ENSO conditions, the clear offset between $SST_{UK'37}$ and $SST_{Mg/Ca}$ strongly implies a seasonal bias between both proxies for the Early and Middle Holocene. The close correlation between $SST_{UK'37}$ and $SST_{Mg/Ca}$ prior to 11.5 ka BP indicates the recording of the same season, very likely annual mean temperatures. The $SST_{UK'37}$ might have shifted to austral summer conditions at ~11.5 ka BP, possibly caused by intensified upwelling which prevents the formation of a stratified water column needed by the coccolithophorids, while $SST_{Mg/Ca}$ continues to represent annual mean temperatures. The amount of *G. ruber* individuals found in both cores reduces continu-

ously during the Holocene and the species almost disappears at ~4 ka BP, probably indicating strengthened upwelling conditions.

The $SST_{Mg/Ca}$ record of *G. ruber* at core location 056 implies generally higher temperatures, on average by ~1°C, compared to the core 059 (Fig. 5-4f and g) for the entire period covered until 4 ka BP. This offset might be due to the more sheltered location of core 056 in the Gulf of Guayaquil, which is e.g. less exposed to coastal upwelling processes. The nearby EF is located nowadays on an annual mean clearly north of the core locations (Fig. 5-1; [*Palacios*, 2004]) and is thus unlikely to cause a temperature gradient between our study sites. However, smaller frontal systems, which can develop on short spatial and temporal scales, might have caused the temperature gradient between cores 056 and 059. The SST development in the *G. ruber* records of ODP Site 1240 (Fig. 5-4f; [*Pena et al.*, 2008a]) is similar to the development of our *G. ruber* records (Fig. 5-4e and g). While being ~1°C cooler than the $SST_{Mg/Ca}$ record of core 059 during the deglaciation, the ODP Site 1240 record shows temperatures ranging between our core sites from the Early Holocene. The Holocene cooling trends observed in our $SST_{Mg/Ca}$ records are also mirrored in the record by *Pena et al.* [2008a], implying that surface water masses at the study sites were similar.

Our $SST_{Mg/Ca}$ records end at ~4 ka BP, as numbers of *G. ruber* specimens in younger sections were sufficient only for the analyses of $\delta^{18}O$. The diminishing abundances of *G. ruber* after ~4 ka BP probably suggest a considerable change towards unfavorable environmental conditions for this species. *Thiede* [1975; 1983] and *Ibaraki* [1990] noted that *G. ruber* is rarely found in upwelling areas. Even though our core locations are located north of the main Peruvian upwelling center, we suspect that the expansion and strengthening of winter upwelling might have influenced our nearby core locations since ~4 ka BP. Coastal upwelling is relatively shallow in the area (max. 75-100 m deep; [*Huyer*, 1980; *Huyer et al.*, 1987]) and thus influencing the habitat of *G. ruber*.

The freshening trends in our cores, which are more pronounced in the *G. ruber* records, indicate an increasing proportion of a water mass with a lower salinity. Shifts in the mean ITCZ position and the associated rainfall belt are mirrored in varying discharges of the Guayas River [*Mollier-Vogel et al.*, 2013]. The variations in river discharge are not reflected in our marine productivity records (Fig. 5-5), but the varying rainfall intensity might have influenced the salinity concentration in surface depths. It is thus speculated

that the freshening trends in surface depths mirror dilution processes through varying rainfall intensities and thus changes in the Guayas discharge. The offset between Guayas discharge and marine productivity implies that the primary source for nutrients in the area is apparently not the river, but most nutrients are transported into the area via the EUC.

Evidence for enhanced SSTs along the coasts of northern Peru prior to the Holocene is given by geoarcheological investigations, showing that temperatures were higher by ~3-4°C compared to nowadays [*Sandweiss et al.*, 1996; *Andrus et al.*, 2002; *Sandweiss*, 2003]. Warm, tropical water masses penetrated the EEP as far as 10°S during the Early and Middle Holocene. Our findings from $SST_{Mg/Ca}$ and $subSST_{Mg/Ca}$ also indicate a warmer surface ocean at 3.5°S prior to 10 ka BP, which cooled by ~2°C during the Holocene. The $SST_{Mg/Ca}$ records lag the cooling trends observed in the $subSST_{Mg/Ca}$ records by ~2 kyrs (core 056) and ~1 kyr (core 059), respectively; hence, pointing towards a remote control of the subsurface towards the surface ocean in the EEP.

5.5.3: Marine Productivity and ENSO Conditions

Our subsurface records indicate a pronounced cooling during the Holocene, concomitant with a shoaling of the thermocline. Cooling of the mixed-layer and the thermocline during the past 7 kyrs has been reported to control the development of ENSO [*Loubere et al.*, 2003]. ENSO seems to be sensitive to changes in the thermocline structure, since this thermal gradient exhibits significant control on the interaction between ocean and atmosphere in the tropics. A warmer equatorial thermocline, as observed in our records prior to ~10 ka BP, results in a deeper mixed-layer zone which reduces the amount of upwelling [*Liu et al.*, 2000]. This weakens the coupling between the tropical ocean and the atmospheric heat exchange, consequently reducing the amplitude of ENSO.

Mechanisms, which ultimately control the thermocline dynamics in the EEP, are sourced in the southern high latitudes, which act as a source for waters feeding the EUC. This stream originates in the south-western subantarctic Pacific [*Toggweiler et al.*, 1991] and travels along the equator into the EEP. The formation ob Subantarctic Mode Water (SAMW) offshore Chile [*Sloyan et al.*, 2010] further contributes to the EUC, possibly transferred into the EEP via 'ocean tunneling' [*Pena et al.*, 2008a]. The relatively high nutrient

contents of the source water masses for the EUC ultimately controls the amount of biological productivity; this is mirrored in the modern setting by a very high marine productivity in the EEP as can be seen in our marine productivity records, which continuously rise during the Holocene (Fig. 5-5). Other studies also show a TOC increase for the last ~20 kyrs, but TOC values for the Late Holocene differ between sites. They reach ~2.5% at 24°S [*Mohtadi et al.*, 2004], ~1.5% at ~33°S [*Hebbeln et al.*, 2002] and ~2.5% at ~40°S [*Robinson et al.*, 2007] and thus remain lower than Late Holocene TOC values for our study sites of 3% (core 059) and 3.3% (core 056), respectively.

Southern hemisphere boreal winter warming during the Middle Holocene resulted in warmer subsurface waters with relatively lower nutrient contents entering the EEP, diminishing biological productivity during this time [*Liu et al.*, 2000; *Andrus et al.*, 2002]. Our records of different proxies confirm these finding generally, but the shift towards cooler subsurface and surface waters, also exhibiting control on the nutrient contents, was timed differently. Pronounced cooling events in our subsurface records are apparent during H1 and YD (core 059) and from ~10 ka BP onwards in both cores; surface records of *G. ruber* follow these cooling impulses at ~10 ka BP (core 059) and ~8 ka BP (core 059). Paleoproductivity proxies steadily increase in our cores (TOC and Br; Fig. 5-5c-f) or indicate shifts towards more marine productivity (Fig. 5-5a and b); this indicates a gradual shift towards cooler and higher nutrient water masses, probably originating in subantarctic regions and being transported into the EEP via the EUC. It remains unclear if modulations in the strength of the southeast trade winds along the coasts of Ecuador and Peru additionally influence the system, besides a subantarctic-sourced cooling/ warming of the subsurface in the EEP. The diminution of the southeast trades lags the development of positive SST anomalies along the South-American coast [*Rasmusson and Carpenter*, 1982], implying that SST development is shaping the intensity of the trade winds.

The onset of modern ENSO conditions has been reported previously for the coast of Peru, starting between ~7 ka BP [*Loubere et al.*, 2003] and ~5 ka BP [*Rodbell et al.*, 1999; *Vargas et al.*, 2006; *Ehlert et al.*, 2013]. The disappearance of *G. ruber* from ~4 ka BP onwards points to an intensification of winter upwelling, thus probably also pointing towards enhanced ENSO conditions in the EEP during the Holocene. The gradient between surface and subsurface Mg/Ca records further emphasizes the development of the thermocline (Fig. 5-4a+b), in close correlation with strengthened upwelling activity. The abrupt in-

crease in ΔT during the B/A in core 059 implies a severe cooling in the subsurface, while the surface warmed slightly simultaneously. An abrupt increase in ΔT in core 056 can be observed during the Early Holocene, implying that subsurface cooling and surface warming were delayed at the near-shore site. On average, both cores show trends from lower towards higher ΔT and thus point towards a shoaling of the thermocline.

5.6: Conclusions

Our high resolution Mg/Ca records propose a gradual cooling in surface and subsurface depths starting at ~10-11 ka BP; the surface cooling lags the subsurface temperatures by ~1-2 kyrs, implying that the subsurface is the key control for (surface) hydrography in the EEP. The deglaciation was characterized through warmer temperatures than today and a rather deep thermocline, these conditions changed drastically between ~10-11 ka BP. The gradient between $SST_{UK'37}$ and $subSST_{Mg/Ca}$ increased from ~5°C during the deglaciation to ~8°C during the Late Holocene, consequently showing the successive shoaling of the thermocline in the EEP. The cooling trends are accompanied by freshening trends; together with the temperature decline they point towards an enhanced admixture of the EUC and strengthened upwelling activity during the Holocene in the EEP. Marine productivity increased during the Holocene, probably related to the rising nutrient delivery of EUC source waters from subantarctic regions fueling the PP. Thermocline temperatures in the EEP are known to influence the exchange processes between atmosphere and ocean, and thus actively shaping ENSO conditions. The onset of modern ENSO conditions seems to start at the study location at ~10 ka BP. Whether the cooling of the thermocline caused the onset of modern ENSO conditions or if strengthened trade winds fueled coastal upwelling and consequently ENSO can not be answered satisfactorily with the records investigated within this study.

Acknowledgements

This work is a contribution of the DFG Collaborative Research Project “Climate – Biogeochemistry interactions in the Tropical Ocean” (SFB 754). Mg/Ca ratios were partly measured at the ICP-AES at Kiel University. We thank Dieter Garbe-Schönberg for kind support. SEM images were accomplished at Kiel University; we thank Ute Schuldt. We acknowledged technical support from N. Gehre, L. Haxhiaj (GEOMAR) and Bianca Willié (Kiel University). AMS^{14}C-measurements were kindly provided by the Leibniz Laboratory for Radiometric Dating and Isotope Research, Kiel University.

Supplementary information

Stratigraphy and Sedimentation Rates

The age models for both cores are primarily based on AMS^{14}C datings of the planktonic foraminifer *N. dutertrei* [*Mollier-Vogel et al.*, 2013], supported by benthic δ^{18}O records. Results of benthic δ^{18}O analyses show a similar course as the NGRIP δ^{18}O record (Fig. 5-S1; [*NGRIP Members*, 2004]), supporting the reliability of our age models. Linear sedimentation rates and accumulation rates for bulk sediment are also depicted in the respective figure. Linear sedimentation rates (LSR, cm kyr^{-1}) were calculated between age control points as the thickness of a sediment interval divided by the time interval of its deposition. LSR for core 059 peak during the B/A (max. 150 cm kyr^{-1}) and are much lower before and after this episode (LSR ~80-90 cm kyr^{-1}). The LSR for the shallower core 056 are on average higher (~90-110 cm kyr^{-1}), and decrease during Middle and Late Holocene towards ~60-80 cm kyr^{-1}. Towards the Late Holocene LSR for core 059 also decrease down to values of ~50 cm kyr^{-1}. Core 056 has an average temporal resolution of ~60 years for the geochemical analyses and up to 10 years for the XRF-scanned data. The temporal resolution of core 059 is slightly lower, averaging ~80 years (geochemical analyses) and ~25 years (XRF-scanned data), respectively.

The paleo-flux of bulk sediment as well as sediment components is expressed by accumulation rates (AR, in g cm^{-2} kyr^{-1}). ARs were computed following the approach of *van Andel et al*. [1975]: AR_{bulk} = LSR * D_{bulk}, where LSR is the linear sedimentation rate (cm kyr^{-1}) and D_{bulk} is the dry bulk density (g cm^{-3}). In general, the shallower core 056 has higher AR (85 to 60 g cm^{-2} kyr^{-1}) than the deeper core 059 further offshore (~50 to <30 g cm^{-2} kyr^{-1}; Fig. 5-S1). Both cores show relatively high ARs, thus providing an excellent temporal resolution.

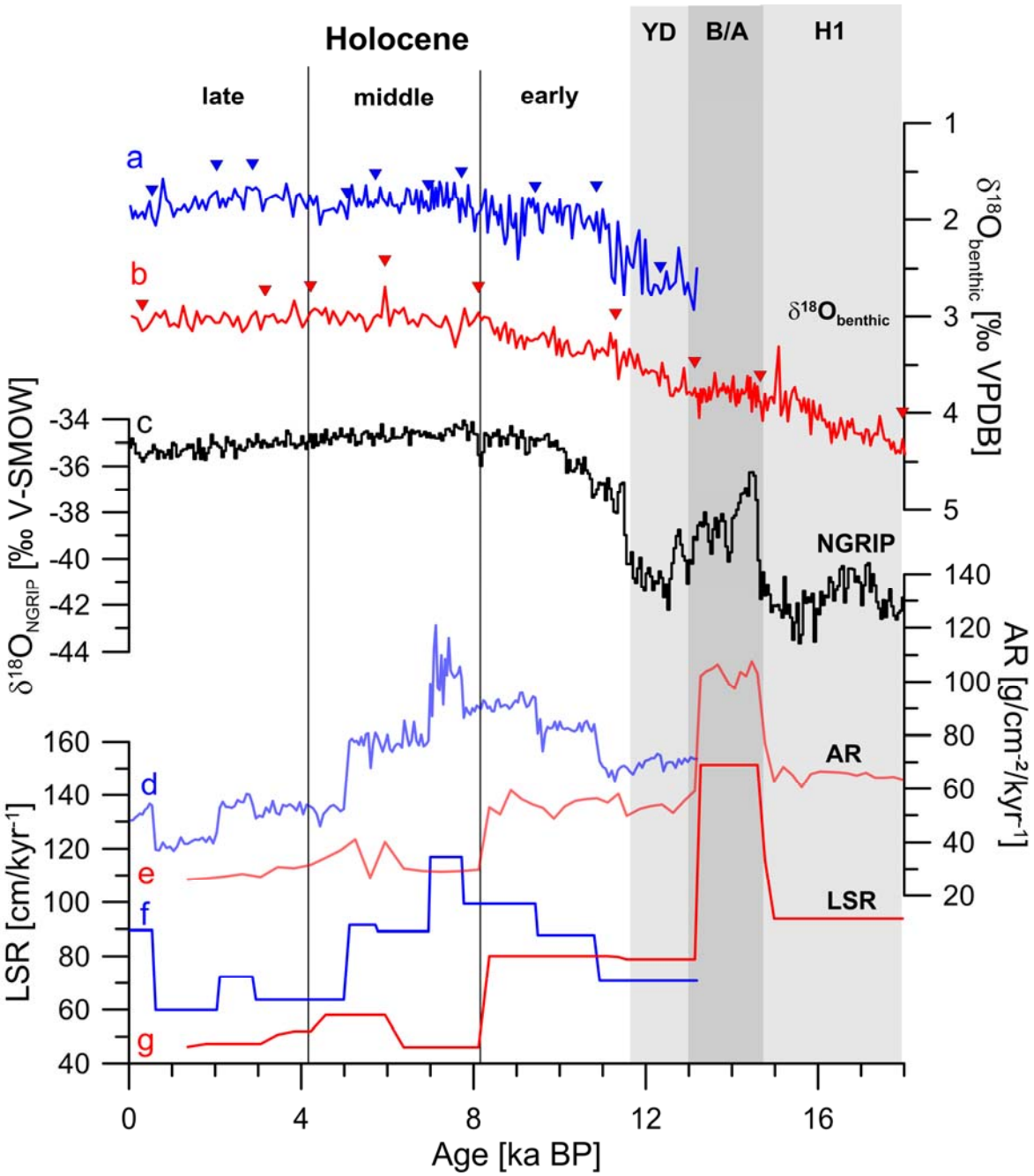

Figure 5-S1: Benthic $\delta^{18}O$, NGRIP and AR as well as LSR for cores 056 and 059

Blue lines refer to core 056 (355 m water depth) and red lines to 059 (1,000 m water depth). Stable oxygen isotopes ($\delta^{18}O$) for cores 056 (a) and 059 (b) are compared with the NGRIP record (c; [*NGRIP Members*, 2004]). Colored triangles on top of the respective curves indicate depths, which were sampled for AMS^{14}C analyses. Lower panel depicts linear sedimentation rates (LSR; solid lines) and bulk sediment accumulation rates (AR; transparent lines) for cores 056 (d and f) and 059 (e and g). LSR and AR peak during the B/A interval in core 059, closely following the course of the NGRIP record. In core 056 LSR and AR are highest during the Middle Holocene. LSR values average to ~70-90 cm kyr^{-1} for core 059 and to ~80-100 cm kyr^{-1} for the shallower core 056, respectively.

Dissolution Effect on Planktonic Foraminiferal Mg/Ca

Secondary (diagenetic) effects such as the preferential removal of Mg^{2+} during calcite dissolution [e.g. *Regenberg et al*., 2006 and references therein] may lower foraminiferal Mg/Ca and reconstructed temperatures may appear too low. Several attempts have been made to correct for Mg^{2+} loss in different ocean basins, either correcting for water depth [*Dekens et al.*, 2002; *Regenberg et al.*, 2006] or for the degree of under-saturation with respect to calcite ion concentration [*Regenberg et al.*, 2006]. Such approaches only account for modern dissolution processes, but do not consider changes of dissolution through time, which is further complicating the use of such a correction function. However, the Pacific in general and the EEP in particular are known for their lack of calcite preservation and thus this issue affords consideration.

We analyzed $\delta^{18}O$ and Mg/Ca ratios of *N. dutertrei* and *G. ruber* from core top samples (Fig. 5-2). The $Mg/Ca_{N.dutertrei}$ ratios show a large scatter of ~1.8 mmol mol^{-1} with a characteristic decrease in Mg/Ca of ~0.8–1.0 mmol mol^{-1} per kilometer water depth (Fig. 5-2). Such change is similar to what *Regenberg et al*. [2006] deduced from their Caribbean core top study (decrease of ~0.5–0.8 mmol mol^{-1} per kilometer water depth). In *G. ruber*, Mg/Ca ratios range from 3.4 to 3.8 mmol mol^{-1} with the higher values reflecting the much shallower and warmer habitat depth of this species compared to *N. dutertrei*. With respect to calcite dissolution it has been shown that *N. dutertrei* is relatively stable, while *G. ruber* is more prone to dissolution [*Berger*, 1970; *Parker and Berger*, 1971; *Bé et al.*, 1975].

Today, calcite dissolution indeed matters in the EEP. A difference between the *in situ* carbonate ion concentration [CO_3^{2-}] and [CO_3^{2-}] at saturation of about 18-26 µmol kg^{-1} is considered to be critical for selective Mg-removal [*Regenberg et al.*, 2006]. Such $\Delta[CO_3^{2-}]$ values are already reached at ~250 m water depth off Peru (Fig. 5-2) based on data from WOCE Line 19C (stations 359 and 361, located at 4°S/85°W and 3°S/85°W, respectively; [*Rubin et al.*, 1998], and calculated after *Lewis and Wallace* [1998] and *Jansen et al.* [2002]). The slight increase of carbonate under saturation with depth (Fig. 5-2) does not seem to affect the Mg/Ca ratios below the critical depth noticeably. Ratios scatter between 1 and 1.5 mmol mol^{-1} and do not show any trend with increasing water depth. The two multicorer core tops from stations 056 and 059 show Mg/Ca ratios of 1.32 and 1.52

mmol mol^{-1}, respectively. The higher ratio from the deeper (1,000 m) station is a clear indication against a severe dissolution problem.

To evaluate more precisely the dissolution effect on foraminiferal calcite, we compared down core Mg/Ca ratios of *N. dutertrei* from core 056 with scanning electron microscope (SEM) images of test cross-sections (Fig. 5-S2 A). SEM images provide visual information about possible dissolution of foraminiferal calcite. $Mg/Ca_{N.\ dutertrei}$ ratios of core 056 undergo a strong decrease (~1.8 to 1.4 mmol mol^{-1}) from Early to Late Holocene. SEM images of *N. dutertrei* test cross-sections show a constant ratio between primary and secondary calcite throughout the core (Fig. 5-S2 A). The primary calcite, which contains higher amounts of Mg, is more prone to dissolution than the more compact secondary calcite [*Eggins et al.*, 2003; *Sadekov et al.*, 2005; *Pena et al.*, 2008b; *Jonkers et al.*, 2012]. Consequently, a constant ratio between primary and secondary calcite argues clearly against a severe dissolution problem. Furthermore, SEM images of the test surfaces show relatively sharp-edged calcite crystals, further supporting a neglecting dissolution problem at our study site since dissolution tends to smoothen the calcite crystals and the test surfaces.

Species *G. ruber* was less frequently within our samples, possibly pointing towards a dissolution issue. Arguing against this is the presence of spines in *G. ruber* shells (Fig. 5-S2 B), which could be found in several depths within both cores and in case of a dissolution problem, would be dissolved preferably. The disappearance of *G. ruber* in both cores at ~4 ka BP was probably caused by enhanced upwelling intensity, resulting in environmental conditions being too unfavorable for this species [*Thiede*, 1975; 1983; *Ibaraki*, 1990]. The shells of *G. ruber* are more prone to dissolution than those of species *N. dutertrei* [*Berger*, 1970; *Parker and Berger*, 1971; *Bé et al.*, 1975]. In the following we resign from correcting the foraminiferal Mg/Ca ratios for potential dissolution effects since we evaluate the dissolution issue based on our investigations to be negligible. Any correction attempt lead to Mg/Ca-temperatures being clearly above the intra-annual range of modern WOA 2009 temperatures [*Locarnini et al.*, 2010].

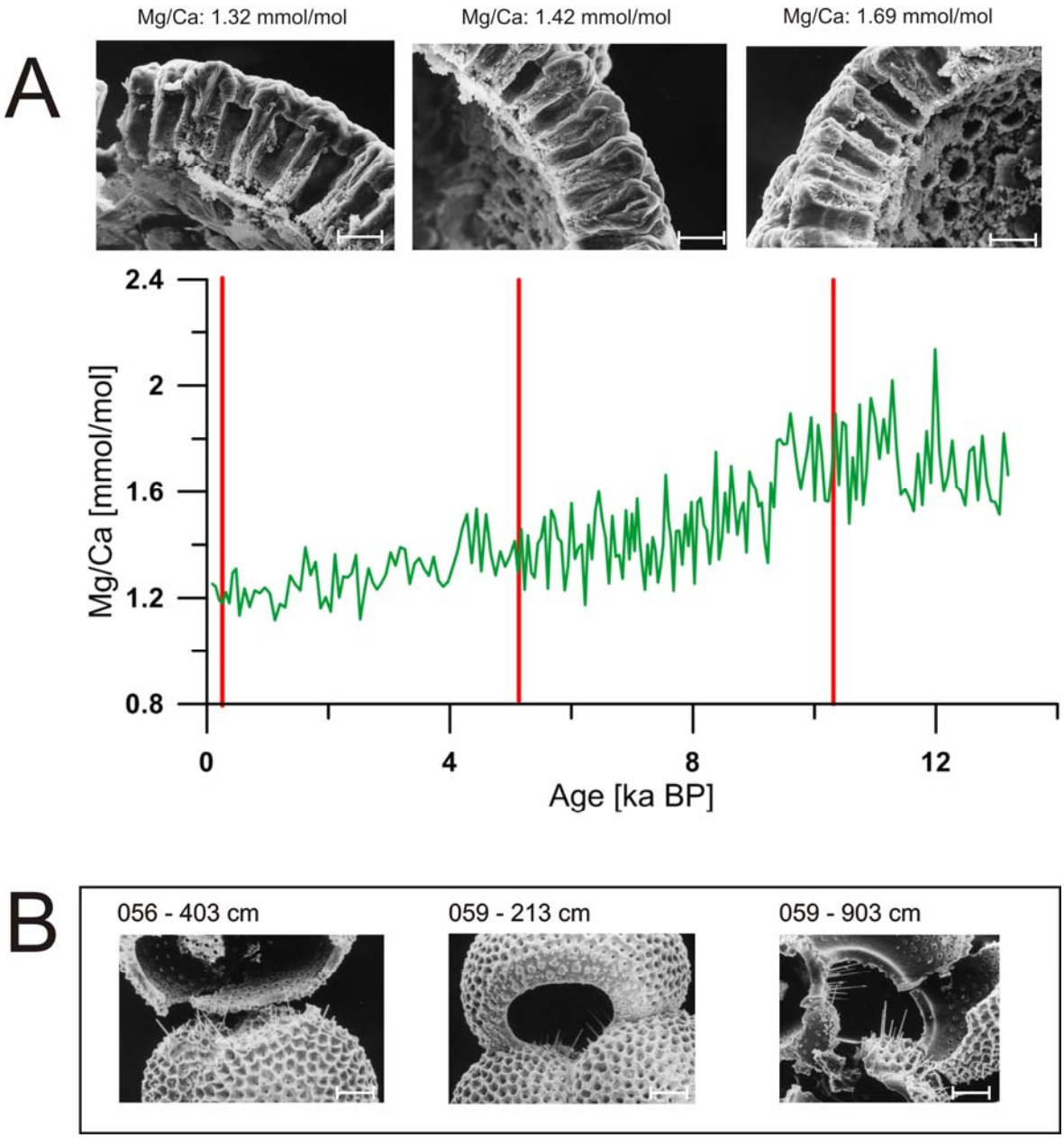

Figure 5-S2: Mg/Ca ratios of *N. dutertrei* for core 056 in comparison to SEM images of foraminiferal test walls; SEM images of *G. ruber* for cores 056 and 059

(A) Mg/Ca ratios of *N. dutertrei* for core 056 *versus* age in comparison to SEM imagery of foraminiferal test walls. SEM images reveal the existence of primary and secondary calcite within the foram tests throughout the core. In particular the primary calcite, which contains higher amounts of Mg and is thus more prone to dissolution [*Eggins et al.*, 2003; *Sadekov et al.*, 2005; *Jonkers et al.*, 2012], is well-preserved. The calcite crystals in the test surfaces remain relatively sharp-edged in our core, supporting our notion of a negligible influence on the calcite-dissolution onto our samples. Scale bars on upper SEM images correspond to 10 µm.

(B) SEM images of *G. ruber* for cores 056 and 059 from core depths as indicated on top of images. Spines in tests of *G. ruber* are present in both cores, further supporting a negligible dissolution issue at our core locations. Scale bars on lower SEM images correspond to 30 µm.

Chapter 6:

A New Mg/Ca Temperature Calibration Based on the Endobenthic Species *Uvigerina peregrina* from the Eastern Equatorial Pacific

Tebke Böschen[1*], Dirk Nürnberg[1] and Kristin Doering[2]

[1] Helmholtz Centre for Ocean Research Kiel (GEOMAR)

Wischhofstrasse 1-3, 24148 Kiel, Germany

[2] Institute of Geosciences

University of Kiel

Ludewig-Meyn-Str. 10, 24118 Kiel, Germany

Keywords: Mg/Ca, *Uvigerina peregrina*, Eastern Equatorial Pacific, bottom water temperature

Abstract

The ratio of magnesium to calcium (Mg/Ca) in the tests of benthic foraminifers is an essential and powerful tool to reconstruct past bottom water temperatures (BWT). Mg/Ca ratios represent an outstanding possibility to gain knowledge about past ocean temperatures in great water depths. The habitat depth of benthic foraminiferal species can vary from epifaunal to infaunal; corresponding BWTs are similar, but reconstructed temperatures based on Mg/Ca transfer functions may deviate largely due to species-specific recording of the Mg/Ca signal in the foraminifers tests. We present in this study a new Mg/Ca transfer function for the endobenthic species *Uvigerina peregrinea*. This function is a compilation of literature data and data from surface samples from the Eastern Equatorial Pacific (EEP). These samples cover a wide range of water depths from 114 down to 2,607 m and display measured temperatures varying between 2.2 and 13.4°C. A distinct relation for species *U. peregrina* was observed in our data set between temperatures and increasing water depth in both proxies, Mg/Ca and stable oxygen isotopes (δ^{18}O). Dissolution effects resulting in a lowering of our Mg/Ca ratios can be ruled out, since we did not observe any fragmentation with regard to our benthic proxy carrier. Here, we present a newly evolved linear transfer function for the endobenthic species *U. peregrina*, which markedly improves down core reconstructions in the EEP. Our transfer function covers a temperature range from 5 to 19.9°C and estimates Mg/Ca-based temperatures with a precision of ±1.6°C.

6.1: Introduction

6.1.1: Background Information

Physical properties like water temperatures are key mechanisms to evaluate changes in ocean circulation. The reconstruction of past BWTs is a prerequisite to monitor intermediate to deep water formation and circulation. The tight correlation between water temperatures and Mg/Ca ratios in benthic foraminifers is a common approach to investigate this issue [*Rosenthal et al.*, 1997; *Sosdian and Rosenthal*, 2009; *Elderfield et al.*, 2010]. Benthic foraminifers incorporate Mg into their tests depending on the surrounding water temperature and thus can be used to reconstruct BWTs. Benthic Mg/Ca calibrations are based on core top data and show sensitivities between 6 and 15% per °C [*Elderfield et al.*, 2006; *Bryan and Marchitto*, 2008]. Besides the temperature-dependent incorporation of Mg ions into the foraminifers tests, other influences like the carbonate ion saturation $\Delta[CO_3^{2-}]$ of bottom waters need to be considered. It has been shown for other trace metals (Cd, Ba, Li, Zn, Sr, B) that the $\Delta[CO_3^{2-}]$ can significantly influence the incorporation of these metals into the tests [*Rosenthal et al.*, 2006; *Yu and Elderfield*, 2007].

An important influence when reconstructing BWTs is the habitat of the benthic species. The estimated temperatures represent either bottom water or pore water conditions, depending on the habitat depth (epifaunal to infaunal). Most approaches focus on epifaunal species like *Cibicides wuellerstorfi*, which is known to live either on the sediment or shallow infaunal in soft sediments [*McCorkle et al.*, 1997; *Jorissen*, 1999]. A transfer function from the EEP is based on *C. wuellerstorfi* and aims to reconstruct deep water formation [*Martin et al.*, 2002]. Several approaches use the endobenthic species *Uvigerina spp.* from regions worldwide [*Elderfield et al.*, 2006; *Bryan and Marchitto*, 2008; *Yu and Elderfield*, 2008; *Elderfield et al.*, 2010]. Besides benthic foraminifers, intermediate to deep water temperatures might also be reconstructed by using stable strontium isotopes in cold water corals [*Rüggeberg et al.*, 2008] or Mg/Li ratios in the same proxy carrier [*Raddatz et al.*, 2013].

There is still a comprehensive approach missing to transfer Mg/Ca ratios of *U. peregrina* from intermediate to shallow water depths into BWTs in the tropic Pacific. Applying commonly used transfer functions to a data set from the EEP [*Doering*, 2012] revealed apparent offsets between core top BWTs and reference data sets. Hence, we present in

this study a newly evolved transfer function to calculate Mg/Ca-based temperatures for species *U. peregrina*. Base for this recently established transfer function are core top samples from the EEP, which were analyzed for their Mg/Ca and their $\delta^{18}O$ ratio. The samples from the EEP were taken offshore Peru and Ecuador between the equator and 17°S, covering a depth range of 60 to 2,600 meters. The combination of our data set with literature data results in a new linear transfer function for benthic species *U. peregrina*, which improves the estimation for Mg/Ca-based temperature reconstructions in the study area noticeable.

6.1.2: Habitat of U. peregrina

The preferred habitat of *U. peregrina* are the uppermost centimeters of the sediment, although the species may migrate up to 10 cm into the sediment [*McCorkle et al.*, 1997]. The habitat depth changes in dependence of bottom water oxygen concentrations, consequently it is shallower if oxygen concentrations are low and *vice versa* [*Sen Gupta and Machain-Castillo*, 1993; *Loubere et al.*, 1995]. *U. peregrina* is widely used for $\delta^{18}O$ analyses since *Shackleton* [1974] described the species to be a reliable recorder of the bottom water $\delta^{18}O$ signature. Although the species lives infaunal, its Mg/Ca ratios reflect BWTs reliably [*Elderfield et al.*, 2010].

Within the sediment the habitat depth for *U. peregrina* varies between different locations, indicating that its habitat depth might be limited by the oxic-anoxic boundary of the sediment. A recent study from the Peruvian OMZ [*Mallon*, 2011] indicates that the presence of *U. peregrina* is restricted by bottom water oxygen concentrations. Between 10°S and 15°S, where the OMZ is most pronounced, *U. peregrina* was not found in stations shallower than 520 m. The species was partly present in the OMZ but its main occurrence was below the OMZ, where oxygen concentrations exceed 4.8 µmol kg^{-1}. Within the OMZ in the EEP, up to 50 % of benthic foraminifers can be attributed to species *U. peregrina* when oxygen concentrations of the bottom water exceed ~4.8 µmol kg^{-1} [*Mallon*, 2011].

6.1.3: Regional Setting

The EEP is a region known for its extremely steep continental slope and a corresponding large temperature gradient down-slope. Furthermore, the area is characterized by up-

welling of subsurface waters, varying on an annual scale [*Kessler*, 2006]. Benthic habitats might be influenced by upwelling, when they are located in relatively shallow water depths. The upwelling fuels primary production which, in combination with resulting degradation processes, consumes great amounts of oxygen from the water column. These processes result in the formation of the world's largest Oxygen Minimum Zone (OMZ), which stretches along the coasts of Ecuador, Peru and Chile [*Karstensen and Ulloa*, 2008; *Fuenzalida et al.*, 2009]. The expansion and intensity of this OMZ also influences the spreading of benthic and planktonic foraminifers, whose numbers decline sharply if oxygen concentrations are too low.

The hydrographic setting in the EEP (Fig. 6-1) is extremely complex and has been described in several works, e.g. *Kessler* [2006], *Fiedler and Talley* [2006] and *Montes et al*. [2010]. Persistent easterly trade winds result in an offshore *Ekman* [1905] transport of surface waters, which is balanced by equatorial upwelling [*Kessler*, 2006], allowing colder, nutritious water masses from subsurface depths to stream into the area. Currents in the EEP are in general not very pronounced and thus short-term influences like wind events and eddies substantially influence the movement of water masses [*Czeschel et al.*, 2011]. The Equatorial Front (EF) is a sharp hydrographic barrier in the area, which separates warm and saline surface waters from north of the equator and cooler, fresher water masses south of the equator. The EF as well as the Intertropical Convergence Zone (ITCZ) are insolation-driven and thus change their position on an annual course. Subsurface depths are dominated by the Equatorial Under Current (EUC), which originates west of the Galápagos Islands and transports highly oxygenated and saline waters [*Toggweiler et al.*, 1991] into the OMZ offshore Peru.

Source of low salinity water in 500 to 1000 m water depth in the study area can be either Antarctic Intermediate Water (AAIW) or North Pacific Intermediate Water (NPIW; [*Bostock et al.*, 2010]). The AAIW in this region is subducted Antarctic Mode Water (AAMW), which has been formed in the southeast Pacific from the deep winter mixed layer north of the Subantarctic Front [*Hanawa and Talley*, 2001]. The AAIW bottom waters enter the Peru basin from the south through the Chile basin; they are characterized through low salinities (~34.5 practical salinity units, psu) and temperatures of 3.5 to 10°C [*Tsuchiya and Talley*, 1996]. Oxygen content is higher and nutrients are lower in these abyssal water masses compared to the overlying deep waters; changes of these parame-

ters from south to north indicate an aging of the bottom water masses [*Fiedler and Talley*, 2006]. The AAIW can be found in water depths of 600 to 1,300 m offshore Chile [*Bostock et al.*, 2010]. The NPIW is entering the area offshore Peru from the central North Pacific; north of the equator it can be found in depths of 400 to 800 m. Salinity (~34) and oxygen concentration are low in this water mass. Both water masses, AAIW as well as NPIW, can not be found undiluted in the study area because they mix and form another water mass, the Equatorial Pacific Intermediate Waters (EqPIW, Fig. 6-1; [*Bostock et al.*, 2010]). This water mass is characterized through relatively low salinity and oxygen concentrations as well as cool temperatures; offshore Peru it is located in water depths of roughly 300-700 m.

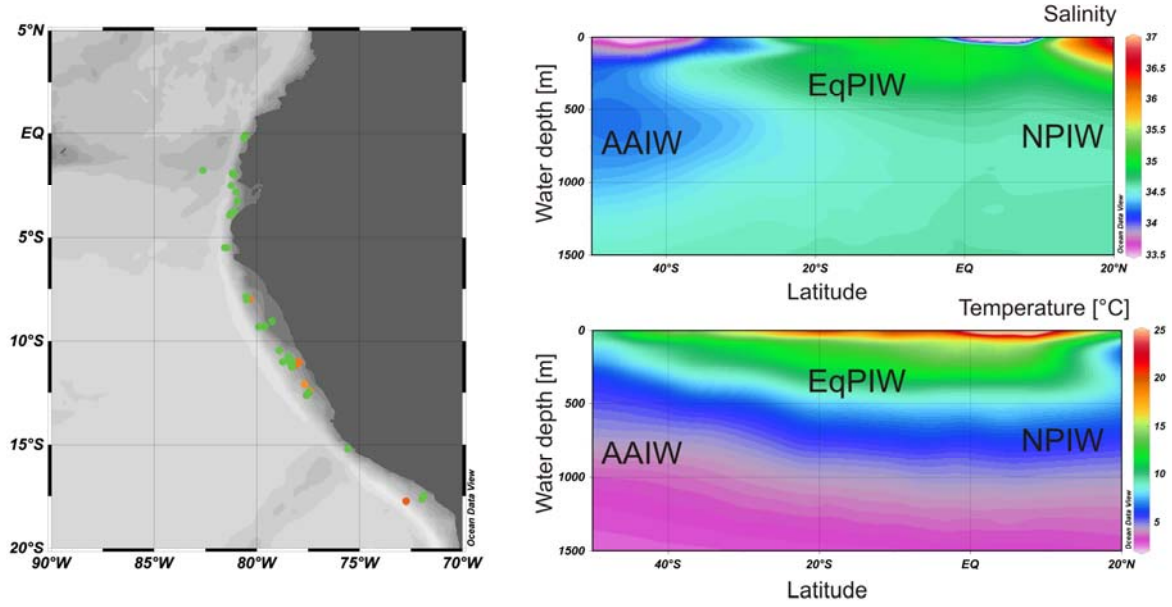

Figure 6-1: Samples locations off Ecuador and Peru; WOA 2009 T- and S-plots

Left map indicates MUC surface sample locations offshore Peru and Ecuador; gray scale in the background indicates the steepness of the continental slope. Green dots mark stations of analyzed benthic Mg/Ca ratios and $\delta^{18}O$; orange dots indicate stations for which only $\delta^{18}O$ analyses were performed. Right map shows salinity and temperature profiles ranging from 20°N to 50°S along the Central and South American coastline. Important water masses in the study area are indicated as following in the maps: Antarctic Intermediate Water (AAIW), North Pacific Intermediate Water (NPIW) and Equatorial Pacific Intermediate Waters (EqPIW). Salinity [*Antonov et al.*, 2010] and temperature data [*Locarnini et al.*, 2010] are annual mean values from WOA 2009.

6.2: Material & Methods

6.2.1: Sample Selection

All analyzed samples were taken in the EEP offshore Peru and Ecuador during Meteor cruise 77 (legs 1 and 2) from October to December 2008. Surface samples of the sediment were taken with a multicorer (MUC); these samples cover a wide range of depths from 110 to 2,607 m and a latitudinal range from the equator to 17°S. For our approach we analyzed the topmost 0-1 cm of the sediment, or if foraminifer content was too low this range was widened to 0-2 cm. A map depicting all sample locations is given (Fig. 6-1). Overall, we analyzed the benthic foraminifer *U. peregrina's* Mg/Ca ratios at 34 stations and $\delta^{18}O$ at 42 stations. Mg/Ca analyses could not be performed for all stations, because the foraminiferal content was not always sufficient. This was particularly the case directly within the OMZ.

6.2.2: Analysis of Stable Oxygen Isotopes and Mg/Ca Ratios

MUC surface samples were washed over a 63 µm wide sieve and subsequently dried at ~50°C. The samples were sieved into six different size classes (63–125, 125–250, 250-315, 315-355, 355-400 and >400 µm). Approximately 20 well preserved and clean looking specimens of *U. peregrina* were picked from the 250-355 µm size fractions. The species content was sparse in some samples, thus it was necessary to sample a larger size range at these stations (maximum 125-400 µm). Prior to cleaning, the foraminiferal samples were carefully crushed between two glass plates in order to open all chambers. The samples were homogenized and split for $\delta^{18}O$ analyses (~$^1/_3$) and for Mg/Ca analyses (~$^2/_3$ of total sample) and transferred into acid-cleaned vials.

The samples for $\delta^{18}O$ analyses were rinsed three times with ultrapure water and twice with methanol and in between treated with ultrasound. The $\delta^{18}O$ measurements were performed at a ThermoScientific MAT 253 mass spectrometer equipped with an automated CARBO Kiel IV carbonate preparation device (GEOMAR, Germany). The isotope values were calibrated versus NBS 19 (National Bureau of Standards) and the in-house standard used was the "Standard Bremen" (Solnhofen limestone). Isotope values are re-

ported in ‰ relative to the VPDB (Vienna Pee Dee Belemnite) scale. The long term precision of the in-house standard is ±0.090 ‰ for $\delta^{18}O$ (2 σ value).

The samples for Mg/Ca measurements were cleaned following the protocol of *Barker et al*. [2003], but adding the reductive step with hydrazine. After cleaning, all samples were transferred into new vials and finally leached with 0.001 molar HNO_3. Prior to measurement the samples were dissolved in 0.075 molar HNO_3 (thermally distilled, "supra acid"). Mg/Ca analyses were carried out with the SPECTRO *Ciros^{CCD} SOP* ICP-AES (provided with an axial plasma) at Kiel University, Germany. Mg/Ca ratios are reported in mmol mol^{-1}. Relative standard deviation for the calibration standard ECRM 752-1 with respect to Mg/Ca ratios was 0.1 mmol mol^{-1} (2 σ). Fe/Ca, Al/Ca and Mn/Ca ratios were monitored continuously to detect insufficient cleaning; ratios of Fe/Ca were on average 0.10 mmol mol^{-1} and 0.44 mmol mol^{-1} at maximum. Al/Ca were on average 0.15 mmol mol^{-1} and 0.67 mmol mol^{-1} at maximum. Corresponding Mn/Ca ratios were 0.01 mmol mol^{-1} on average and 0.05 mmol mol^{-1} at peak. We did not find a correlation between the increased Fe/Ca, Al/Ca and Mn/Ca ratios and outliers within our Mg/Ca data set and thus concluded that the trace metal concentrations within our data set did not noticeably affect our Mg/Ca ratios.

6.2.3: Dissolution of Benthic Foraminifers

Calcite dissolution matters in the EEP today since the local waters are under saturated with respect to carbonate ions. A difference between the *in situ* carbonate ion concentration [CO_3^{2-}] and [CO_3^{2-}] at a saturation of about 18-26 µmol kg^{-1} is considered to be critical for selective Mg-removal [*Regenberg et al.*, 2006]. Such Δ[CO_3^{2-}] values are already reached at ~250 m water depth off Peru (Fig. 6-2), based on data from WOCE Line 19C (stations 359 and 361, located at 4°S/85°W and 3°S/85°W, respectively; [*Rubin et al.*, 1998]), and calculated after *Lewis and Wallace* [1998] and *Jansen et al.* [2002]. The slight increase of carbonate under saturation with growing depth (Fig. 6-2) does not seem to noticeably affect the Mg/Ca ratios of our samples below the critical depth. Mg/Ca ratios are scattered between ~0.7 and ~2.2 mmol mol^{-1}. The decreasing Mg/Ca ratios in greater water depths are likely caused by colder temperatures and not by dissolution processes,

since *U. peregrina* is a species which is relatively resistant against dissolution through low $\Delta[CO_3^{2-}]$ values [*Elderfield et al.*, 2010].

6.3: Results and Discussion

6.3.1: Dissolution Effects on Foraminiferal Calcite

Benthic Mg/Ca ratios are stable throughout our data set and remain unaffected by dissolution processes. The distribution of the data was very likely caused by the different water depths and the corresponding habitats of the foraminifers (Fig. 6-2). This assumption is supported by the $\delta^{18}O$ data set displayed in Figure 6-2, which also indicates a clear temperature trend in the *U. peregrina* samples. We find no indication of a dissolution problem with respect to our benthic proxy carrier. It has been reported for other benthic species, e.g. in species *C. wuellerstorfi* [*Yu and Elderfield*, 2008], that the effect of the $\Delta[CO_3^{2-}]$ in bottom waters can distort the genuine Mg/Ca temperature effect. However, *Sosdian and Rosenthal* [2010] found the Mg/Ca ratios of *U. peregrina* in the North Atlantic to be barely influenced by changing $[CO_3^{2-}]$ concentrations. They concluded an increased uncertainty of BWT estimates based on *U. peregrina* Mg/Ca ratios in those cases where dissolution might be a problem. Still, they concluded that the general trend of the data should be trustable. *Elderfield et al.* [2006] evaluated *U. peregrina* as a shallow infaunal species to show only weak or absent sensitivity to carbonate ion concentrations. Other studies [*Elderfield et al.*, 2010] have shown that *Uvigerina sp*. seems to be a species which is allegedly free of $[CO_3^{2-}]$ dissolution effects. We calculated $\Delta[CO_3^{2-}]$ values and plotted them *versus* Mg/Ca ratios (Fig. 6-3A). The comparison with the data set by *Elderfield et al*. [2010] shows a range in Mg/Ca ratios comparable to our data set, although our samples were exposed to more negative $\Delta[CO_3^{2-}]$ values. The large range of our Mg/Ca ratios exposed to similar $\Delta[CO_3^{2-}]$ values in different water depths (Fig. 6-2) supports the assumption of stable test ratios and weakens the possibility of dissolution effects. The Mg/Ca ratios do not seem to be effected by the decrease of $\Delta[CO_3^{2-}]$ values with rising water depth. Consequently, Mg/Ca ratios of *U. peregrina* seem to be a robust proxy to record BWTs in the EEP.

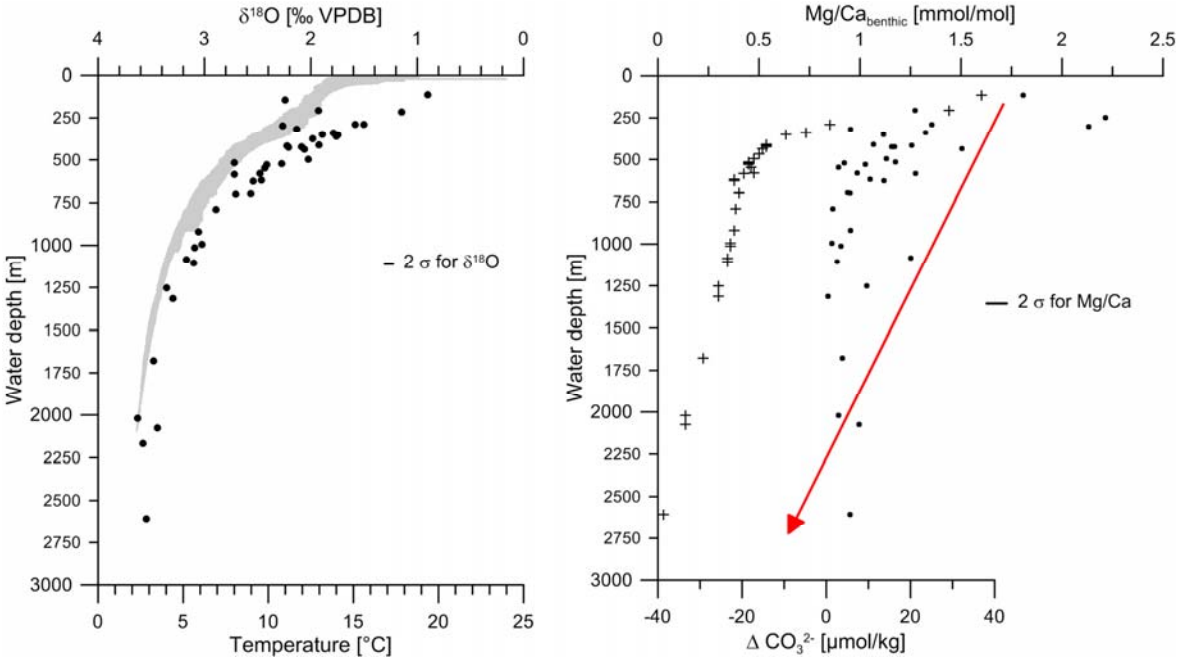

Figure 6-2: $\delta^{18}O$ and Mg/Ca of *U. peregrina* versus temperature and $\Delta[CO_3^{2-}]$

Left panel shows $\delta^{18}O$ values for species *U. peregrina* (black dots) from our data set from 42 surface stations *versus* water depth. Values increase in accordance with water depth, thus indicating a correlation between water temperatures and the $\delta^{18}O$ signature of benthic foraminifers. Gray area in the background is the temperature record from the study area (compilation of all CTD casts from M77-1 and -2). Right panel shows the Mg/Ca ratios measured at 34 surface stations in species *U. peregrina* (black dots). Mg/Ca ratios decline with increasing water depth, indicating a temperature trend within the data set. The crosses represent the calcite saturation index $\Delta[CO_3^{2-}]$ *versus* water depth, calculated after *Lewis and Wallace* [1998] and *Jansen et al.* [2002] on the base of WOCE line P19C, stations 359 and 361 [*Rubin et al.*, 1998]. For each MUC station the $\Delta[CO_3^{2-}]$ value from the respective depth was plotted. 2 σ standard deviations for $\delta^{18}O$ and Mg/Ca are indicated in the prevailing plots.

6.3.2: Stable Oxygen Isotopes and Mg/Ca Ratios

The $\delta^{18}O$ and Mg/Ca ratios measured in *U. peregrina* are depicted in Figure 6-2. The $\delta^{18}O$ values increase in accordance with water depth, consequently indicating a tight correlation between water temperature and the foraminifers $\delta^{18}O$ signature. The CTD temperature data set supports the theory of the close relation between $\delta^{18}O$ of *U. peregrina* and BWTs. The $\delta^{18}O$ ratios of *U. peregrina* decrease exponentially with increasing water depth ($y = \exp(0.989 * x) * 50.006$; $R^2 = 0.86$); these results strongly suggest a tight relation between the $\delta^{18}O$ ratios and the temperatures. The $\delta^{18}O$ values range from 0.901‰ at the shallowest station to 3.629‰ at the deepest station. CTD temperature compilation data ranges from 2.3 to 24°C.

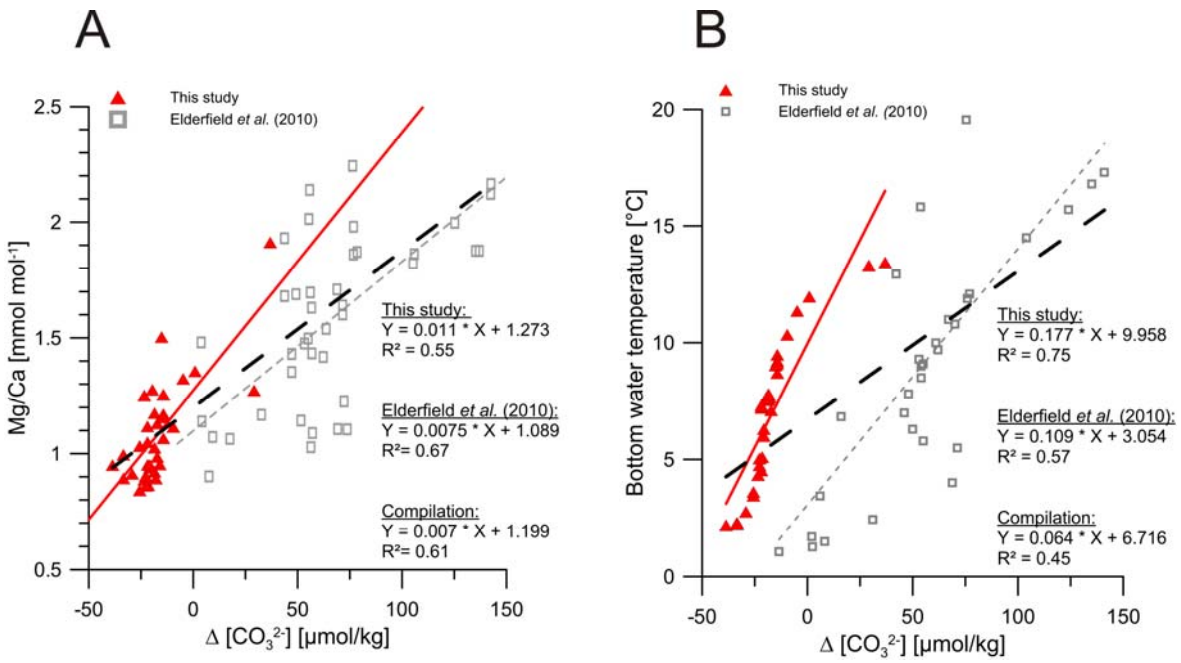

Figure 6-3: Mg/Ca and CTD-derived BWTs *versus* $\Delta[CO_3^{2-}]$ in comparison to *Elderfield et al*. [2010]

Core top Mg/Ca and CTD-derived BWTs *versus* carbonate ion saturation ($\Delta[CO_3^{2-}] = [CO_3^{2-}]_{measured} - [CO_3^{2-}]_{saturation}$) in comparison to the data compilation of *Elderfield et al*. [2010]. (A) shows benthic Mg/Ca ratios of *U. peregrina versus* $\Delta[CO_3^{2-}]$ from this study and reference data set [*Elderfield et al.*, 2010]. The range of $Mg/Ca_{U.peregrina}$ ratios of this study corresponds to the *Elderfield et al*. [2010] data range, although being at more negative $\Delta[CO_3^{2-}]$ values. The effect of bottom water $\Delta[CO_3^{2-}]$ on Mg/Ca in *U. peregrina* is apparently small. (B) depicts CTD-derived bottom water temperatures from M77-1 and -2 from this study *versus* $\Delta[CO_3^{2-}]$, again in comparison with the data set by *Elderfield et al.* [2010]. The relation between both variables is apparently closer in our data set, revealed by the markedly larger R^2 (0.75), compared to the reference data set (0.57). Our own data set and the reference data set differ markedly, especially when compared to the left plot (A). Fits for this study, for reference data set and for the compilation of both sets, are indicated in the prevailing plots.

The benthic foraminiferal Mg/Ca ratios (Fig. 6-2) remain stable across the wide range of water depths, with the variability of ~1 mmol mol^{-1} being very likely caused by the different temperatures of the foraminifers habitats. The ratios show a comparable trend of $\delta^{18}O$ values, thus also indicating a lowering of ratios with increasing water depth. Lower Mg/Ca ratios are in general associated with cooler temperatures; thus the decreasing values show a trend towards lower temperatures in greater water depths. Dissolution processes need to be considered when using Mg/Ca ratios in foraminifers to calculate temperatures; we evaluated this aspect (Chapter 3.1.). Besides Mg/Ca ratios of *U. peregrina* we also plotted $\Delta[CO_3^{2-}]$ values (WOCE, line P19C, stations 359 and 361) from water depths corresponding to the sample depth of the foraminiferal sample (Fig. 6-2). $\Delta[CO_3^{2-}]$ values decline with increasing water depth since under saturation with carbonate ions is

dependent on the water depth; thus deeper and older water masses exhibit a more pronounced under saturation. $\Delta[CO_3^{2-}]$ values as well as Mg/Ca ratios in our data set show clear trends of having been caused by the different water depths from which we collected the foraminiferal samples. We conclude from our plots (Fig. 6-2) and from previous works [*Elderfield et al.*, 2010; *Sosdian and Rosenthal*, 2010] that our samples were not affected by dissolution processes or diagenetic alteration and thus are reliable proxy recorders to reconstruct BWTs in the EEP.

6.3.3: BWT Transfer Functions: State of the Art

Since the first efforts of *Shackleton* [1974] to estimate seawater temperatures through the $\delta^{18}O$ signature in the foraminifers tests, various attempts have been made to find reliable methods to trace past ocean temperatures. Amongst others these include Mg/Ca ratios of benthic foraminifers, which are a reliable and more accurate proxy to trace changes in water temperatures than e.g. $\delta^{18}O$. Several prior studies described calibrations for converting Mg/Ca ratios of benthic foraminifer tests into temperatures (Table 6-1; [*Elderfield et al.*, 2006; *Bryan and Marchitto*, 2008; *Yu and Elderfield*, 2008; *Elderfield et al.*, 2010]). However, a linear transfer function based on species *U. peregrina* for intermediate water depths in the Pacific, and in particular for the EEP, does still not exist. Applying existing transfer functions resulted in a mismatch between the results of our surface data set from the EEP with modern BWTs.

Table 6-1: Compilation of Mg/Ca transfer functions for benthic species *U. peregrina*

Abbreviations for cleaning methods refer to the following: O (oxidative cleaning, according to *Barker et al.*, 2003), R (reductive cleaning method, including oxidative and reductive step). Samples obtained only by oxidative cleaning were adjusted by -0.2 mmol mol^{-1} [*Elderfield et al.*, 2006].

Species	Location	Mg/Ca =	Temp. range (°C)	Cleaning	Reference
U. peregrina spp.	Arabian Sea	0.075 * T + 0.87	1.7 - 20	O	*Elderfield et al.* (2006)
U. peregrina	off Somalia	0.065 * T + 0.91	1.5 – 11.8	O	*Elderfield et al.* (2006)
U. peregrina spp.	Multiple areas	0.067 * T + 1.09	1.06 – 19.56	O/ R	*Yu& Elderfield* (2008)
U. peregrina	Florida Straits	0.079 * T + 0.77	5.8 – 17.2	R	*Bryan& Marchitto* (2008)
U. peregrina spp.	Multiple areas	0.074 * T + 0.81	1.0 – 19.6	O/ R	*Elderfield et al.* (2010)
U. peregrina	off Peru/ Ecuador	0.056 * T + 0.7	2.2 – 13.4	R	This study/ CTD data
U. peregrina	off Peru/ Ecuador	0.054 * T + 0.71	2.0 – 14.4	R	This study/ WOA data
U. peregrina spp.	Multiple areas	0.097 * T + 0.52	5.0 – 19.9	O/ R	This study/ data compilation

An attempt to calculate bottom water temperatures for the Eastern Pacific was made by *Martin et al.* [2002], who evolved an exponential equation (1).

$$Mg/Ca = 1.22(\pm 0.08) \times \exp^{0.109(\pm 0.007) \times BWT} \quad (1)$$

Even though the transfer function by *Martin et al.* [2002] was evolved for application in the EEP, we failed to create a match with modern BWTs when we applied the equation to our down core data set. We suspect this offset to be caused by two different reasons: First, the equation by *Martin et al.* [2002] is based on Mg/Ca ratios of a different species (*C. wuellerstorfi*) than the species we analyzed. It has been previously reported that different foraminiferal species in the same water mass differ profoundly with respect to their Mg/Ca ratios [*Rosenthal et al.*, 1997; *Lear et al.*, 2002]. Second, the Mg/Ca-based temperature equation by *Martin et al.* [2002] was derived from samples exceeding a water depth of 1,500 m with most of them originating from depths below 3,000 m. In these abyssal depths strong temperature changes are unlikely, because these water masses are rather uniform. Consequently, the transfer function by *Martin et al.* [2002] is based on samples with a temperature range from 0.4 to 2.8°C. In contrast, our data set covers a wider range of temperatures (2.0 to 14.4°C). Therefore, the relation between Mg/Ca ratios and water temperatures of the foraminifers habitat was very likely different in our data set compared to the settings used by *Martin et al.* [2002].

6.3.4: Developing the Transfer Function

A recent work [*Doering*, 2012] from our study area, based on a piston core being recovered at the Peruvian margin from 997 m water depth (core M772-059-1), analyzed Mg/Ca ratios of *U. peregrina*. The Late Holocene mean value (0-4 ka BP) of Mg/Ca ratios for this core is 0.97 mmol mol^{-1}. When applying different transfer functions to the Mg/Ca ratios of the Late Holocene [*Bryan and Marchitto*, 2008; *Elderfield et al.*, 2010], the resulting temperatures vary markedly from the modern values (Fig. 6-6). The transfer function by *Elderfield et al.* [2010] results in too low temperatures for core 059 (~1.6°C), whereas modern data sets suggest 4.7 ±0.1°C (WOA 2009). The approach by *Elderfield et al.* [2010] does not result in satisfactory temperature estimates for the study area and thus is not suitable for down core application in the EEP. The transfer function by *Bryan and Marchitto* [2008] results in slightly higher temperatures for the Late Holocene (3.3°C), which matches the

modern data relatively well. However, this transfer function produces unrealistically large BWT variations down core. The need to develop a new transfer function, which matches modern values in the EEP more satisfactorily than existing approaches, is thus confirmed.

We present in this study an approach investigating Mg/Ca ratios of the benthic species *U. peregrina* based on data from 34 sediment surface samples from the EEP. The data set was matched with WOA 2009 data (annual mean; [*Locarnini et al.*, 2010]) as well as with CTD data measured at the same stations where the multi corers were sampled. The shown WOA 2009 data is always from the station closest to our sampling site; the plotted temperatures are those from matching water depth of the respective foraminiferal sample. Corresponding CTD values were measured during the same cruise where the sediment samples were taken; consequently the CTD temperatures represent (austral) spring to early summer conditions. The direct comparison between CTD- and WOA-based temperatures shows the close relation between both data sets (Fig. 6-4A). The plots Mg/Ca *versus* CTD-derived and WOA-based temperatures (Fig. 6-4B) do not differ considerably, implying that the lack of spatial coverage (WOA data) and the lack of seasonality (CTD data) result in similar fits (Fig. 6-4B). In the following we preferably used the CTD-casted temperature data for calculations since their greater proximity to the foraminiferal stations seemed desirable.

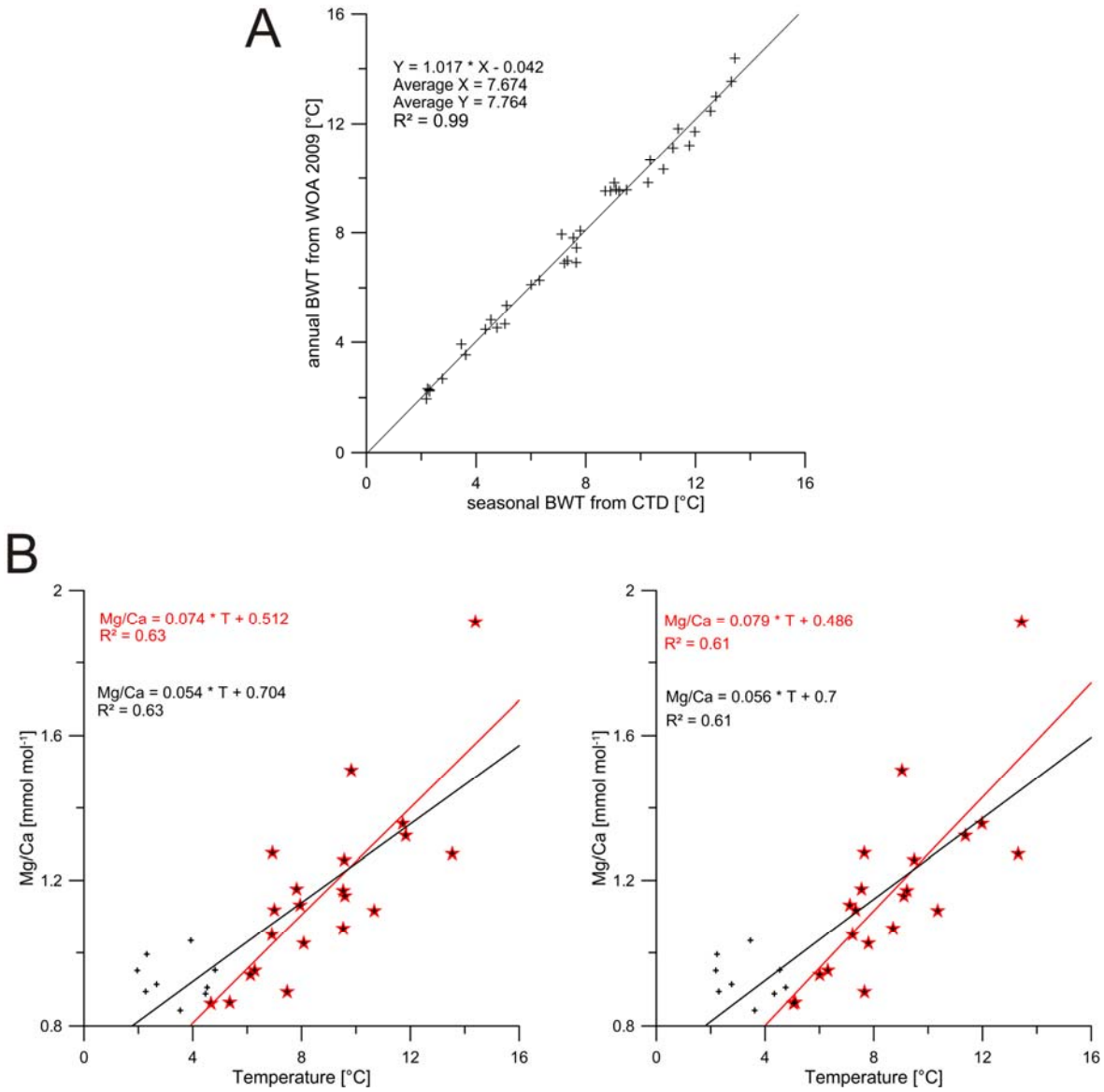

Figure 6-4: Compilation of temperatures from the study area and Mg/Ca ratios of species *U. peregrina*

(A) Shows CTD-derived temperatures *versus* annual mean values from WOA 2009 data set, indicating the tight correlation between both data sets.

(B) Compilation of Mg/Ca ratios *versus* temperatures for species *U. peregrina* from the EEP. Black crosses in both plots indicate the complete data set, whereas red stars indicate data points with temperatures above 5°C. Left panel shows Mg/Ca ratios of *U. peregrina* from our data set offshore Peru and Ecuador *versus* temperatures (annual mean) from WOA 2009 [*Locarnini et al.*, 2010]. WOA stations located closest to foraminiferal sampling stations and corresponding water depths were selected. Right panel shows Mg/Ca ratios of *U. peregrina* from our data set offshore Peru and Ecuador *versus* temperatures from CTD casts taken during the same cruise (Meteor 77-1 and 2; Oct-Dec 2008). All samples were obtained by reductive cleaning. Resulting transfer functions for both data sets are remarkably similar, only differing slightly in the y-intercept and the coefficient of determination (R^2).

Our data set for *U. peregrina* from the EEP (Fig. 6-2) was plotted *versus* CTD-sampled temperature data from the same cruise (M77-1 and -2; [*Pfannkuche et al.*, 2011]) and *versus* annual mean temperatures from the WOA 2009 data set [*Locarnini et al.*, 2010]. The tight correlation between CTD and WOA data set (Fig. 6-4A) indicates that they might both be used to evolve a new benthic transfer function. The resulting fits are remarkably similar (Fig. 6-4B), no matter if the Mg/Ca ratios of *U. peregrina* ratios were plotted *versus* WOA 2009 data or *versus* CTD data. The coefficient of determination is almost identical in both plots (R^2 = 0.63 and 0.61, respectively). Both plots in Figure 6-4B show fits for the complete data set as well as for BWT data exceeding 5°C. The data set with BWTs exceeding 5°C was used preferably since the greater temperature scatter above ~5°C is likely to be super-imposed on the calibration curve by other factors than temperatures [*Lear et al.*, 2002]. The resulting transfer functions for BWTs above 5°C are (2) for the fit *versus* CTD-based temperature data and (3) for the fit *versus* WOA 2009:

$$Mg/Ca = 0.056 * T + 0.7 \quad (2)$$

$$Mg/Ca = 0.054 * T + 0.704 \quad (3)$$

Apparently, the great physical proximity of our foraminiferal samples and CTD-sampled temperature data counteracts the fact that this temperature data is highly seasonal. By comparison, the lack of physical proximity between our foraminiferal and the WOA data set seems to be balanced by the fact that this temperature record displays an annual mean. Consequently, both data sets are applicable. The use of equations (2) and (3) for the paleo-record from the EEP [*Doering*, 2012] results in a reliable match between Late Holocene values (0-4 ka BP) and modern temperatures from the WOA 2009. Both transfer functions indicate a temperature of 6.2°C for the Late Holocene (Fig. 6-4) and match the modern temperature of 4.7 ±0.1°C from the nearest WOA station fairly well (Fig. 6-6). Application of both transfer functions to the data set [*Doering*, 2012] further supports their extremely good utilization for samples from the EEP. The evolved transfer functions (Fig. 6-4, Table 6-1) provide powerful tools to estimate BWTs, but they remain restricted to the EEP and to the species *U. peregrina*. Due to this limitation there is a need to combine this data set with others and develop a transfer function for a wider (global) approach.

The temperature-sensitive slope (a) of our linear Mg/Ca versus temperature regressions (a = 0.49-0.51; calibrated *versus* CTD and WOA data) is low compared to the *Elderfield et al*. [2010] calibration (a = 0.81), and causes large BWT amplitude variations when applied to the down core samples (Fig. 6-6). Thus, when the linear equation by *Elderfield et al.* [2010] is applied for samples from the EEP the conversion of down-core Mg/Ca values results in temperatures, which are too high for the time of their formation and consequently temperatures would be overestimated. We assume this apparent offset in the temperature-slope to be caused at least partly by the different settings from which the analyzed foraminifers were sampled. Since our study area in the EEP is characterized by an extremely complex hydrography, we suspect an appropriate Mg/Ca transfer function for this area will only work when it is based exclusively on foraminiferal samples from the area. Any offset in the tight correlation between Mg/Ca ratios in the foraminiferal tests and the *in-situ* temperatures (in which they grow) will consequently result in larger mismatches when these transfer functions are applied down core.

Relatively large down core variations are still problematic when equations (2) and (3) are applied (Fig. 6-6). Depicted are the 5-point running averages for core M772-059-1; Mg/Ca ratios were transferred into temperatures by using different transfer functions. The approach by *Elderfield et al.* [2010], as described previously, shows an unlikely high variability down core. Our newly evolved equation (2) results in a reliable match between averaged Late Holocene temperatures and modern data, but still shows a relatively large temperature range down core. This implies that an approach combining our data set from the EEP and existing reference data sets might be helpful to find a transfer function which minimizes the effect of down core variations.

The compilation of our data from the EEP and existing data sets from various regions results in another linear transfer function (Fig. 6-5), which covers a temperature range of 5 to 19.9°C. The conversion of Mg/Ca ratios of the benthic foraminiferal species *U. peregrina* into BWTs is based on an algorithm (4) derived from the data of our core top study in combination with several already existing data sets (Fig. 6-5):

$$T = (Mg/Ca - 0.524)/ 0.097 \quad (4)$$

This algorithm (R^2 = 0.77) is based on the compilation of Mg/Ca ratios from 21 benthic foraminiferal samples from species *U. peregrina* and literature data [*Elderfield et al.*, 2006; *Bryan and Marchitto*, 2008; *Yu and Elderfield*, 2008]. The Mg/Ca ratios from sam-

pled stations located at temperatures below 5°C were excluded from the algorithm. *Lear et al.* [2002] observed a great scatter in Mg/Ca ratios below temperatures of ~5°C, which is likely to be super-imposed on the calibration curve by other factors than temperatures. Samples obtained only by oxidative cleaning were adjusted by -0.2 mmol mol^{-1} to account for the lowering of Mg during the reductive cleaning step [*Elderfield et al.*, 2006]. The algorithm based on our surface data set and literature data (Fig. 6-5) displays a higher temperature-sensitive slope (a) than the other transfer functions (0.097). At similar temperatures, our core top *U. peregrina* data from the EEP exhibit significantly lower Mg/Ca ratios than the remaining data compilation. Dissolution effects lowering $Mg/Ca_{U.peregrina}$ are not likely, as the overall range of our $Mg/Ca_{U.peregrina}$ data is comparable to those of the *Elderfield et al*. [2010] compilation although at much lower carbonate ion saturation ($\Delta[CO_3^{2-}]$; see [*Brown and Elderfield*, 1996], Fig. 6-3, Chapter 6.3.1.).

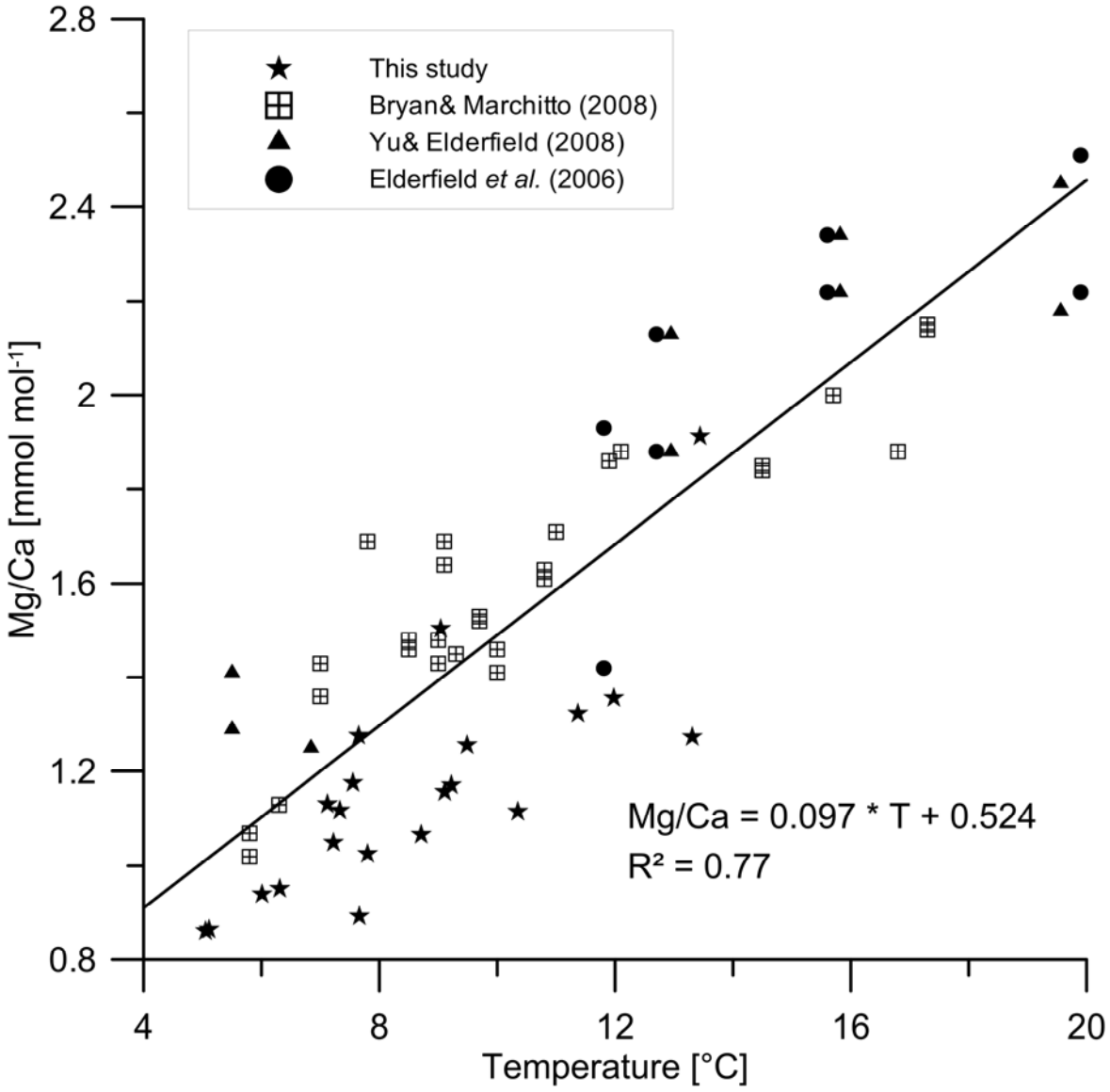

Figure 6-5: Data compilation of our Mg/Ca data set from the EEP and reference sites

Data compilation of our surface data set from the EEP (stars) plotted versus temperature data sampled during the same cruise by CTD casts. Additionally, we added *U. peregrina* data from the Arabian Sea, Florida Straits and multiple locations: Rectangles with crosses [*Bryan and Marchitto*, 2008], triangles [*Yu and Elderfield*, 2008] and dots [*Elderfield et al.*, 2006]. All samples only cleaned by oxidative cleaning (*Elderfield et al.*, 2006 and partly *Yu& Elderfield*, 2008) were adjusted by -0.2 mmol mol^{-1} to account for lowering of Mg during the reductive cleaning step. All samples recovered from temperature settings below 5°C were excluded from the algorithm, since the large scatter in BWT in this temperature range is likely to be superimposed on the calibration curve by other factors than temperatures [*Lear et al.*, 2002].

Our newly evolved algorithm (4) creates a good match between Late Holocene and modern temperature conditions, which was not achieved with the *Elderfield et al*. [2010] calibration (Fig. 6-6). Today, the annual mean temperature at 1,000 m water depth is 4.7 ±0.1°C [WOA 2009], which is comparable to the BWT estimate for the Late Holocene of

~4.6°C (averaged for the last 4,000 years; [*Doering*, 2012]). Overall, we conclude from the *U. peregrina* samples from the EEP that temperature trends in Mg/Ca ratios were faithfully recorded and preserved, but transferring these values into BWTs remains a challenge. Thus, our calibration based on a small data set of *U. peregrina* surface samples from the EEP represents a first attempt to create an appropriate function to transfer benthic Mg/Ca ratios into BWTs for this region. Further sampling in the area is required to enlarge the data set and create a BWT transfer function, which is based on an appropriate amount of foraminiferal samples from a number of depths and latitudinal ranges. However, the compilation of our data set and existing reference data sets so far seems to be a more precise approach to reconstruct down core Mg/Ca-based temperatures for species *U. peregrina* in the EEP than the equations based exclusively on samples from the study area.

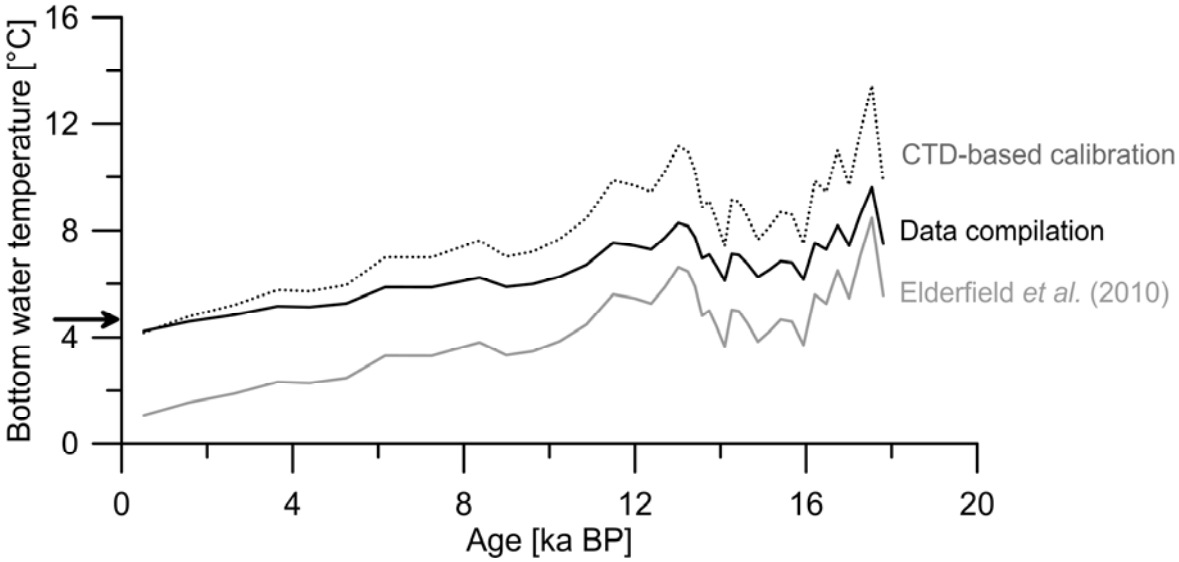

Figure 6-6: Application of different transfer functions to a down core record from the Peruvian margin

Application of three different transfer functions to a down core record from the Peruvian margin from 997 m water depth (M772-059-1; [*Doering*, 2012]). Values are 5-point running averages. The arrow on the left axis indicates modern temperatures for 1,000 m water depth from WOA 2009 [*Locarnini et al.*, 2010]. The transfer function by *Elderfield et al.* [2010] does not match the modern temperature of ~4.7°C and shows down core variability of temperatures which seems unreliable. The CTD-based calibration results in a good match with modern temperatures, but again the down core variability of temperatures is likely to be too high. The best approximation to estimate temperatures in the EEP based on Mg/Ca ratios of *U. peregrina* seems to be the combination of our own data set and reference data sets (Fig. 6-5; Equation (4)). This algorithm matches the modern temperature and shows a down core variability of ~4°C, which is markedly lower than the other approaches depicted.

6.4: Conclusions

Our Mg/Ca surface data set from the EEP, based on benthic species *U. peregrina*, proposes a tight correlation between Mg/Ca ratios recorded in the foraminifers tests and the water depths in which they lived. Further evidence for the close correlation of decreasing Mg/Ca ratios with increasing water depth is given by the $\delta^{18}O$ ratios, which also suggest a high temperature-sensitivity of species *U. peregrina*. Mg/Ca ratios and corresponding water temperatures allowed the construction of two similar algorithms, which precisely estimate BWTs from the sedimentary record in the EEP. The two functions (2) and (3) were developed solely with *U. peregrina* data from the EEP and represent a first attempt to reconstruct BWTs in the area. One remaining problem is that the resulting down core temperature variability is likely too high. Thus, we combined our Mg/Ca data set from the EEP with additional data from literature, resulting in a new transfer function (4). Our newly evolved temperature function (4) promises a higher precision for our study area, when applied to down core Mg/Ca records compared to previous approaches, and also shows less down core variability. Basis for this function is a compilation of data from the EEP and literature data, but the data set is still relatively small. There is a strong need to enlarge the benthic Mg/Ca data set for the EEP since the complex hydrography and consequently different habitat conditions need to be considered in an appropriate way.

Acknowledgements

This work is a contribution of the DFG Collaborative Research Project “Climate – Biogeochemistry interactions in the Tropical Ocean” (SFB 754). Mg/Ca ratios were measured with the ICP-AES at Kiel University; we thank Dieter Garbe-Schönberg for kind support. We acknowledged technical support from N. Gehre and L. Haxhiaj (GEOMAR).

Chapter 7: CONCLUSIONS

7.1: General Conclusions

Being part of the SFB 754 (Climate – Biogeochemistry Interactions in the Tropical Ocean), the main goal of this PhD thesis is to investigate changes in upper-ocean stratification and circulation within the OMZ offshore Ecuador and Peru. Further important aspects were the identification of past changes in hydrography and external control mechanisms actively shaping the Peruvian OMZ within the past 18,000 years. Benthic and especially planktonic foraminifers serve as a widely used tool to reconstruct past ocean conditions, hence, they were the most important proxy carriers within this thesis.

Knowledge of the exact habitat depth for planktonic species is of particular importance for the correct interpretation of paleo-data. Accordance between $\delta^{18}O_{equilibrium}$ values and $\delta^{18}O$ values measured in the foraminiferal tests was used to allocate calcification depths for surface dwelling *G. ruber* and thermocline dwelling *N. dutertrei*. Resulting ACDs indicate surface depths of 0-16 m for *G. ruber*. The results for *N. dutertrei* exhibit a pronounced north-south gradient with the ACDs being in greater depth (~200 m) in the northern than in the southern part (~70 m). These pronounced differences in habitat depth are likely caused through more intense upwelling in the southern part of the study area, resulting in steeper temperature gradients, lower oxygen concentrations and thus a shallower habitat depth for *N. dutertrei*.

Down core results indicate severe changes during the last 18,000 years, in particular during the last 10,000 years. The deglaciation in the EEP was characterized by markedly warmer and more saline conditions compared to today, both in subsurface and surface depths. With the beginning of the Holocene (~11 ka BP), a pronounced temperature drop is revealed by the subsurface Mg/Ca records from both sampling sites. In surface depth this temperature drop is less pronounced; cooling trends in both water depths are accompanied by fresher water masses, represented through $\delta^{18}O_{ivf\text{-}sw}$ values as an approximation for salinity. The $SST_{Mg/Ca}$ trends lag the development in subsurface depths by ~1-2 kyrs. The alkenone-based SST record shows a slow but steady temperature rise, which is in opposition to both foraminiferal Mg/Ca records. The growing offset between SST $U^{K'}_{37}$ and the Mg/Ca-based records is likely due to more pronounced seasonal differences:

These pushed the alkenones into the summer season, while the foraminifers continued to record annual mean temperatures. The contribution of the EUC, an important water mass for the upwelling processes in the EEP, probably changed throughout the Holocene. The observed cooling trends in subsurface and surface depths were likely caused by an enhanced admixture of EUC-sourced waters into the study area, replacing the more dominant tropical waters from the deglaciation. This resulted in a greater influence of cooler and fresher water masses in the EEP, which contained higher amounts of nutrients and thus fueled the marine productivity in the area. Even though the core locations are close together (16 nm distance) temperature effects can be observed staggered at both sides, possibly due to smaller frontal systems between both sites.

Mg/Ca ratios were also investigated in the endobenthic species *U. peregrina*, which represents a powerful tool to reconstruct BWTs. The close correlation between $\delta^{18}O$ and Mg/Ca in dependence of the water depth of the samples confirms the reliability of *U. peregrina* as a suitable recorder of bottom water temperatures. A combination of the Mg/Ca ratios and the CTD-based temperature data, supported by literature data, allowed the development of a newly established bottom water temperature calibration. An enlarged data set and particularly the greater data amount at the lower temperature scale improve the preceding algorithms. The new transfer function provides a more precise estimation of Mg/Ca-derived temperatures in the EEP for species *U. peregrina* than previous approaches. The application of this newly calibrated function for down core data from the EEP results in a reliable match between late Holocene values from sediment cores and modern temperature data from WOA 2009 data base.

7.2: Outlook

The two studied piston cores allow the observation of environmental changes with an extremely good temporal resolution (decadal to centennial). Since the two cores are located very close together and clearly north of the present OMZ and the active upwelling center, more cores from within the OMZ need to be studied to support the findings of this thesis. The gradual southward extension of cooler and fresher water masses being transported with the EUC, which is mirrored in the Mg/Ca records of sites 056 and 059, demands further investigation. More sediment cores from north of the two sites but in particular from further south of the region might help to trace the pathway of the EUC in more detail than with the core material already investigated. As the preservation of $CaCO_3$ is rather poor directly within the OMZ, foraminifera-based investigations remain a challenge.

Additionally, it still remains unclear if subsurface depths in the northern EEP are ventilated exclusively through EUC-sourced water masses from the Central Pacific. Even though recent ADCP-based observations clearly point towards the EUC being the dominant water mass at ~3.5°S, this issue affords further consideration. A possible northward extension of the CCW and related water masses originating within the vicinity of the Antarctic, travelling northwards along the South-American coast, might be proven if the spatial coverage of core material would be sufficient. Cores providing a continuous sedimentary record from further south in the EEP might solve the question, how and to what extent cooler southern component water masses might have entered the area during the past.

Additionally, the newly established transfer function to estimate benthic Mg/Ca-based temperatures demands further verification. A larger set of samples from the EEP might result in improved bottom water temperature estimations for the study area and possibly contribute towards an algorithm for *U. peregrina*, which might be applied globally.

ACKNOWLEDGEMENTS/ DANKSAGUNG

Ein großer Dank geht an Dirk Nürnberg, ohne dessen Hilfe ich diese Arbeit nicht hätte fertig stellen können. Du warst für mich der mit Abstand wichtigste Diskussionspartner, durch deine Hilfe habe ich viele gute Anregungen bekommen; danke für deine Unterstützung, deine Geduld und deine direkte Art!

Bei Ralph Schneider bedanke ich mich für Unterstützung bei der Interpretation der Daten und für die Übernahme des Zweitgutachtens.

Für Unterstützung bei den Laborarbeiten bedanke ich mich ganz besonders bei Nadine Gehre. Nadine, du bist eine Perle und ohne deine tatkräftige Hilfe hätten so mache Analysen ewig gedauert. Danke an Jutta Heinze für ihre Hilfe mit der zickigen Mrs. Murphy ☺ Außerdem ein Dank an Lulzim Haxhiaj, Anke Bleyer und Bettina Domeyer.

Martin Frank danke ich für eine kurzzeitige Finanzierung und seine hilfsbereite Art. Deine Tür stand immer für mich offen; ich danke dir sehr für deine humorvolle Art und die Zuversicht, dass auch ich es schaffen kann diese Arbeit fertig zu stellen.

Besonders bedanken möchte ich mich bei diversen Kollegen. Meinem Büro, Lisa Bohlen, Anna Noffke und Thomas Mosch. Lisa, dir ein großer Dank für deine Geduld bei den vielen mathematischen Nachfragen! Ich freue mich, dass mit dir aus einer Kollegin eine wirklich gute Freundin geworden ist. Außerdem ein Dank an Jan Riethdorf und André Bahr, die mir bei der Datenauswertung oft hilfreich zu Seite standen. Jacek Raddatz danke ich für konstruktive Rückmeldungen zu meinen Manuskripten. Außerdem danke ich Nico Glock, Jürgen Mallon, Claudia Ehlert und Patricia Grasse, insbesondere für Claudias und Patricias enorme Geduld bei meinen Nachfragen zu den Wassermassen!

Ein großer Dank geht an meine HiWis Moritz, Kristin, Maaiken, Norbert und Lisa. Danke für eure sorgfältige und zuverlässige Arbeit und Hilfe am Bino und mit Mrs. Murphy!

Elfi Mollier-Vogel danke ich für eine lehrreiche Zusammenarbeit, die teilweise von interkulturellen Unstimmigkeiten geprägt war.

Ich bedanke mich außerdem bei Christian Dullo für die Unterstützung in der Anfangsphase meiner Arbeit.

Marcus Regenberg danke ich für geduldige Erklärungen und leckeren Tee in seinem Büro, sowie für viele neue Erkenntnisse zur Anlösung von Foraminiferen.

Danke an Zhenja Kandiano für die Hilfe bei der Bestimmung von planktischen Foraminiferen.

Anne Osborne danke ich für ihre selbstlose und sehr hilfsbereite Art. Anne, in deinem Büro, das dann zu unserem wurde, habe ich in den letzten Monaten meiner Arbeit einen wunderbaren Arbeitsplatz gefunden. Ich danke dir sehr für deine Gastfreundschaft und dafür, dass du meine Launen so sang- und klanglos ertragen hast!

Svenja Papenmeier danke ich für die Bereitstellung einer ODV- und Grapher-Hotline, sowie motivierenden Antrieb in der Endphase der Arbeit. Du hast viel dazu beigetragen, dass ich diese Arbeit abschließen konnte.

Julia Hommer danke ich für ihre liebe und fürsorgliche Art, die mir besonders in der Endphase sehr geholfen hat! Außerdem warst du eine super Babysitterin für Linus ☺ Meike Dibbern danke ich für nette Gespräche und fürs Beruhigen, wenn ich mal wieder etwas durch den Wind war.

Meinem Chor „Rich-Sound“ danke ich für die Ablenkung, die ich dort trotz stressiger Zeiten immer gefunden habe. Außerdem haben mir die Wellingdorfer Zwillinge und insbesondere das Streifenhörnchen so manche Mittagspause in der Mensa versüßt.

Ich danke allen Freunden, Bekannten sowie meiner Familie, die mich beim Fertigstellen dieser Arbeit unterstützt haben.

Meiner Schwester danke ich für die sprachliche Hilfe beim Schreiben, das Korrektur lesen und die spontanen Hilfestellungen, wenn ich mal wieder ein Synonym brauchte…

Meinen Eltern danke ich für ihre Unterstützung während meines Studiums und der Promotion. Ihr habt mir viel Kraft gegeben um dieses Projekt durchzuziehen. Ein besonderer Dank geht an meine Mutter, die mich in der Endphase mit Babysitten sehr unterstützt hat!

Martin und Linus: Ihr seid ein wichtiger Teil meines Lebens und ohne euch hätte ich dieses Projekt nicht zu Ende gebracht. Linus, danke dass du ein wahres Musterkind warst und mir viel Zeit zum Arbeiten gelassen hast. Martin, ich danke dir für deine Kraft, deine Ruhe und Gelassenheit, sowie deine unglaubliche Geduld! All das hat mir sehr geholfen den Kopf nicht in den Sand zu stecken, auch wenn es mal schwierig wurde.

REFERENCES

Anand, P., H. Elderfield, and M. H. Conte (2003), Calibration of Mg/Ca thermometry in planktonic foraminifera from a sediment trap time series, *Paleoceanography*, *18*(2), 1050.

Andrus, C. F. T., D. E. Crowe, D. H. Sandweiss, E. J. Reitz, and C. S. Romanek (2002), Otolith $\delta^{18}O$ Record of Mid-Holocene Sea Surface Temperatures in Peru, *Science*, *295*(5559), 1508-1511.

Antonov, J. I., D. Seidov, T. P. Boyer, R. A. Locarnini, A. V. Mishonov, H. E. Garcia, O. K. Baranova, M. M. Zweng, and D. R. Johnson (2010), World Ocean Atlas 2009, Volume 2: Salinity, in *NOAA Atlas NESDIS 69*, edited by S. Levitus, p. 184, U.S. Government Printing Office, Washington, D.C.

Ayón, P., M. I. Criales-Hernandez, R. Schwamborn, and H.-J. Hirche (2008), Zooplankton research off Peru: A review, *Progress In Oceanography*, *79*(2-4), 238-255.

Barber, R. T., and F. P. Chavez (1983), Biological consequences of El Niño, *Science*, *222*, 1203-1210.

Barker, S., M. Greaves, and H. Elderfield (2003), A study of cleaning procedures used for foraminiferal Mg/Ca paleothermometry, *Geochemistry Geophysics Geosystems*, *4*(9), 8407.

Bé, A. W. H., J. W. Morse, and S. M. Harrison (1975), Progressive dissolution and ultrastructural breakdown of planktonic foraminifera, in *Dissolution of deep-sea carbonates*, edited by W. V. Sliter, A. W. H. Bé and W. H. Berger, pp. 27-55, Cushman Foundation for Foraminiferal Research, Washington, D.C.

Bé, A. W. H., J. K. B. Bishop, M. S. Sverdlove, and W. D. Gardner (1985), Standing stock, vertical distribution and flux of planktonic foraminifera in the Panama Basin, *Marine Micropaleontology*, *9*(4), 307-333.

Benway, H. M., and A. C. Mix (2004), Oxygen isotopes, upper-ocean salinity, and precipitation sources in the eastern tropical Pacific, *Earth and Planetary Science Letters*, *224*(3-4), 493-507.

Berger, W. H. (1970), Planktonic Foraminifera: Selective solution and the lysocline, *Marine Geology*, *8*(2), 111-138.

Blanz, T., K.-C. Emeis, and H. Siegel (2005), Controls on alkenone unsaturation ratios along the salinity gradient between the open ocean and the Baltic Sea, *Geochimica et Cosmochimica Acta*, *69*(14), 3589-3600.

Blockley, S. P. E., C. S. Lane, M. Hardiman, S. O. Rasmussen, I. K. Seierstad, J. P. Steffensen, A. Svensson, A. F. Lotter, C. S. M. Turney, and C. Bronk Ramsey (2012), Synchronisation of palaeoenvironmental records over the last 60,000 years, and an extended INTIMATE event stratigraphy to 48,000 b2k, *Quaternary Science Reviews*, *36*(0), 2-10.

Bond, G., et al. (1992), Evidence for massive discharges of icebergs into the North Atlantic ocean during the last glacial period, *Nature*, *360*, 245-249.

Bond, G., W. Broecker, S. Johnsen, J. McManus, L. Labeyrie, J. Jouzel, and G. Bonani (1993), Correlations between climate records from North Atlantic sediments and Greenland ice, *Nature*, *365*(6442), 143-147.

Böning, P., H.-J. Brumsack, M. E. Böttcher, B. Schnetger, C. Kriete, J. Kallmeyer, and S. L. Borchers (2004), Geochemistry of Peruvian near-surface sediments, *Geochimica et Cosmochimica Acta*, *68*(21), 4429-4451.

Bostock, H. C., B. N. Opdyke, and M. J. M. Williams (2010), Characterising the intermediate depth waters of the Pacific Ocean using $\delta^{13}C$ and other geochemical tracers, *Deep Sea Research Part I: Oceanographic Research Papers*, *57*(7), 847-859.

Brink, K. H., D. Halpern, A. Huyer, and R. L. Smith (1983), The physical environment of the Peruvian upwelling system, *Progress In Oceanography*, *12*(3), 285-305.

Broecker, W. S., and T. H. Peng (1974), Gas exchange rates between air and sea, *Tellus*, *26*(1-2), 21-35.

Brown, S. J., and H. Elderfield (1996), Variations in Mg/Ca and Sr/Ca Ratios of Planktonic Foraminifera Caused by Postdepositional Dissolution: Evidence of Shallow Mg-Dependent Dissolution, *Paleoceanography*, *11*(5), 543-551.

Bryan, S. P., and T. M. Marchitto (2008), Mg/Ca - temperature proxy in benthic foraminifera: New calibrations from the Florida Straits and a hypothesis regarding Mg/Li, *Paleoceanography*, *23*(2), PA2220.

Cane, M. A. (2005), The evolution of El Niño, past and future, *Earth and Planetary Science Letters*, *230*(3–4), 227-240.

Carr, M.-E., P. T. Strub, A. C. Thomas, and J. L. Blanco (2002), Evolution of 1996–1999 La Niña and El Niño conditions off the western coast of South America: A remote sensing perspective, *Journal of Geophysical Research: Oceans*, *107*(C12), 29-21-29-16.

Chavez, F. P., K. R. Buck, S. K. Service, J. Newton, and R. T. Barber (1996), Phytoplankton variability in the central and eastern tropical Pacific, *Deep Sea Research Part II: Topical Studies in Oceanography*, *43*(4-6), 835-870.

Clement, A. C., R. Seager, and M. A. Cane (2000), Suppression of El Niño during the Mid-Holocene by changes in the Earth's orbit, *Paleoceanography*, *15*(6), 731-737.

Craig, H., and L. I. Gordon (1965), Deuterium and oxygen 18 variations in the ocean and marine atmosphere, in *Stable Isotopes in Oceanographic Studies and Paleotemperatures*, edited by E. Tongiogi, pp. 9-130, Spoleto, Italy.

Czeschel, R., L. Stramma, F. U. Schwarzkopf, B. S. Giese, A. Funk, and J. Karstensen (2011), Middepth circulation of the eastern tropical South Pacific and its link to the oxygen minimum zone, *Journal of Geophysical Research - Oceans*, *116*, C01015.

Dekens, P. S., D. W. Lea, D. K. Pak, and H. J. Spero (2002), Core top calibration of Mg/Ca in tropical foraminifera: Refining paleotemperature estimation, *Geochemistry, Geophysics, Geosystems*, *3*(4), 1-29.

Deuser, W. G., E. H. Ross, C. Hemleben, and M. Spindler (1981), Seasonal changes in species composition, numbers, mass, size, and isotopic composition of planktonic foraminifera settling into the deep Sargasso Sea, *Palaeogeography, Palaeoclimatology, Palaeoecology*, *33*(1-3), 103-127.

Deuser, W. G. (1987), Seasonal variations in isotopic composition and deep-water fluxes of the tests of perennially abundant planktonic foraminifera of the Sargasso Sea; results from sediment-trap collections and their paleoceanographic significance, The Journal of Foraminiferal Research, 17(1), 14-27.

Deutsch, C., H. Brix, T. Ito, H. Frenzel, and L. Thompson (2011), Climate-Forced Variability of Ocean Hypoxia, *Science*, *333*(6040), 336-339.

Doering, K. (2012), Surface and deep-water hydrographic conditions over the last 18.000 years from the Peruvian coast based on δ^{18}O and Mg/Ca ratios of *Globigerinoides ruber* and *Uvigerina peregrina*, Diploma thesis, 83 pp, University of Kiel, Kiel.

Dubois, N., M. Kienast, C. Normandeau, and T. D. Herbert (2009), Eastern equatorial Pacific cold tongue during the Last Glacial Maximum as seen from alkenone paleothermometry, *Paleoceanography*, *24*(4), PA4207.

Duplessy, J. C., C. Lalou, and A. C. Vinot (1970), Differential Isotopic Fractionation in Benthic Foraminifera and Paleotemperatures Reassessed, *Science*, *168*(3928), 250-251.

Duplessy, J. C., P. Blanc, and A. W. H. Bè (1981), Oxygen-18 Enrichment of Planktonic Foraminifera due to Gametogenic Calcification below the Euphotic Zone, *Science*, *213*, 1247-1250.

Eggins, S., P. De Deckker, and J. Marshall (2003), Mg/Ca variation in planktonic foraminifera tests: implications for reconstructing palaeo-seawater temperature and habitat migration, *Earth and Planetary Science Letters*, *212*(3-4), 291-306.

Ehlert, C., P. Grasse, and M. Frank (2013), Changes in silicate utilisation and upwelling intensity off Peru since the Last Glacial Maximum - insights from silicon and neodymium isotopes, *Quaternary Science Reviews*.

Ekman, V. W. (1905), On the influence of the earth's rotation on ocean currents, *Arch. Math. Astron. Phys.*, *2*(11), 1-53.

Elderfield, H., and G. Ganssen (2000), Past temperature and δ^{18}O of surface ocean waters inferred from foraminiferal Mg/Ca ratios, *Nature*, *405*(6785), 442-445.

Elderfield, H., M. Vautravers, and M. Cooper (2002), The relationship between shell size and Mg/Ca, Sr/Ca, δ^{18}O, and δ^{13}C of species of planktonic foraminifera, *Geochemistry, Geophysics, Geosystems*, *3*(8), 1-13.

Elderfield, H., J. Yu, P. Anand, T. Kiefer, and B. Nyland (2006), Calibrations for benthic foraminiferal Mg/Ca paleothermometry and the carbonate ion hypothesis, *Earth and Planetary Science Letters*, *250*(3-4), 633-649.

Elderfield, H., M. Greaves, S. Barker, I. R. Hall, A. Tripati, P. Ferretti, S. Crowhurst, L. Booth, and C. Daunt (2010), A record of bottom water temperature and seawater δ^{18}O for the Southern Ocean over the past 440 kyr based on Mg/Ca of benthic foraminiferal *Uvigerina spp*, *Quaternary Science Reviews*, *29*(1-2), 160-169.

Epstein, S., R. Buchsbaum, H. A. Lowenstam, and H. C. Urey (1953), Revised carbonate-water isotopic temperature scale, *Geological Society of America Bulletin*, *64*, 1315-1325.

Erez, J., and S. Honjo (1981), Comparison of isotopic composition of planktonic foraminifera in plankton tows, sediment traps and sediments, *Palaeogeography, Palaeoclimatology, Palaeoecology*, *33*(1-3), 129-156.

Euler, C., and U. S. Ninnemann (2010), Climate and Antarctic Intermediate Water coupling during the late Holocene, *Geology*, *38*(7), 647-650.

Fairbanks, R. G., and P. H. Wiebe (1980), Foraminifera and Chlorophyll Maximum: Vertical Distribution, Seasonal Succession, and Paleoceanographic Significance, *Science*, *209*(4464), 1524-1526.

Fairbanks, R. G., M. Sverdlove, R. Free, P. H. Wiebe, and A. W. H. Be (1982), Vertical distribution and isotopic fractionation of living planktonic foraminifera from the Panama Basin, *Nature*, *298*(5877), 841-844.

Faul, K. L., A. C. Ravelo, and M. L. Delaney (2000), Reconstructions of upwelling, productivity, and photic zone depth in the Eastern Equatorial Pacific Ocean using planktonic foraminiferal stable isotopes and abundances, *Journal of Foraminiferal Research*, *30*(2), 110-125.

Fiedler, P. C., and L. D. Talley (2006), Hydrography of the eastern tropical Pacific: A review, *Progress In Oceanography*, *69*(2-4), 143-180.

Friederich, G. E., J. Ledesma, O. Ulloa, and F. P. Chavez (2008), Air–sea carbon dioxide fluxes in the coastal southeastern tropical Pacific, *Progress In Oceanography*, *79*(2–4), 156-166.

Fuenzalida, R., W. Schneider, J. Garcés-Vargas, L. Bravo, and C. Lange (2009), Vertical and horizontal extension of the oxygen minimum zone in the eastern South Pacific Ocean, *Deep Sea Research Part II: Topical Studies in Oceanography*, *56*(16), 992-1003.

Garcia, H. E., R. A. Locarnini, T. P. Boyer, J. I. Antonov, O. K. Baranova, M. M. Zweng, and D. R. Johnson (2010), World Ocean Atlas 2009, Volume 3: Dissolved Oxygen, Apparent Oxygen Utilization, and Oxygen Saturation, in *NOAA Atlas NESDIS 70*, edited by S. Levitus, p. 344 pp., Government Printing Office, Washington, D.C.

Glock, N., A. Eisenhauer, V. Liebetrau, M. Wiedenbeck, C. Hensen, and G. Nehrke (2012), EMP and SIMS studies on Mn/Ca and Fe/Ca systematics in benthic foraminifera from the Peruvian OMZ: a contribution to the identification of potential redox proxies and the impact of cleaning protocols, *Biogeosciences*, *9*, 341-359.

Goñi, M. A., K. C. Ruttenberg, and T. I. Eglinton (1998), A reassessment of the sources and importance of land-derived organic matter in surface sediments from the Gulf of Mexico, *Geochimica et Cosmochimica Acta*, *62*(18), 3055-3075.

Goñi, M. A., D. M. Hartz, R. C. Thunell, and E. Tappa (2001), Oceanographic considerations for the application of the alkenone-based paleotemperature $U^{K'37}$ index in the Gulf of California, *Geochimica et Cosmochimica Acta*, *65*(4), 545-557.

Grasse, P., T. Stichel, R. Stumpf, L. Stramma, and M. Frank (2012), The distribution of neodymium isotopes and concentrations in the Eastern Equatorial Pacific: Water mass advection versus particle exchange, *Earth and Planetary Science Letters*, *353–354*(0), 198-207.

Greaves, M., et al. (2008), Interlaboratory comparison study of calibration standards for foraminiferal Mg/Ca thermometry, *Geochemistry, Geophysics, Geosystems*, *9*(8), Q08010.

Grossman, E. L. (1984), Stable isotope fractionation in live benthic foraminifera from the southern California Borderland, *Palaeogeography, Palaeoclimatology, Palaeoecology*, *47*(3–4), 301-327.

Grossman, E. L. (1987), Stable isotopes in modern benthic foraminifera; a study of vital effect, *The Journal of Foraminiferal Research*, *17*(1), 48-61.

Gutiérrez, D., K. Aronés, F. Chang, L. Quipuzcoa, and P. Villanueva (2005), Impacto de la variación oceanográfica estacional e interanual sobre los ensambles de Microfitoplancton, mesozooplancton, ictioplancton y macrozoobentos de dos áreas costeras del norte del Peru entre 1994 y 2002, *Boletín Instituto del Mar del Perú*, *22*((1–2)), 1-60.

Hanawa, K., and L. D. Talley (2001), Mode waters, in *Ocean Circulation and Climate: Observing and Modeling the Global Ocean*, edited by G. Siedler, J. Church and J. Gould, pp. 373-386, Academic Press, New York.

Hebbeln, D., M. Marchant, and G. Wefer (2002), Paleoproductivity in the southern Peru-Chile Current through the last 33 000 yr, *Marine Geology*, *186*, 487-504.

Hedges, J. I., W. A. Clark, P. D. Quay, J. E. Richey, A. H. Devol, and U. d. M. Santos (1986), Compositions and fluxes of particulate organic material in the Amazon River, *Limnology and Oceanography*, *31*(4), 717-738.

Hemleben, C., M. Spindler, and O. R. Anderson (1989), *Modern Planktonic Foraminifera*, 363 pp., Springer-Verlag, New York, Berlin, Heidelberg, London, Paris, Tokyo.

Hemming, S. R. (2004), Heinrich events: Massive late Pleistocene detritus layers of the North Atlantic and their global climate imprint, *Reviews of Geophysics*, *42*(1), RG1005.

Hilbrecht, H. (1997), Morphologic gradiation and ecology in *Neogloboquadrina pachyderma* and *N. dutertrei* (planktic foraminifera) from core top sediments, *Marine Micropaleontology*, *31*, 31-43.

Hormazábal, S., G. Shaffer, N. Silva, and E. Navarro (2006), The Perú-Chile undercurrent and the oxigen minimum zone variability off central Chile, *Gayana (Concepción)*, *70*, 37-45.

Hut, G. (1987), Stable isotope reference samples for geochemical and hydrological investigations, in *Report of Consultants Group Meeting*, p. 42, International Atomic Energy Agency, Vienna, Austria.

Huyer, A. (1980), The Offshore Structure and Subsurface Expression of Sea Level Variations off Peru, 1976-1977, *Journal of Physical Oceanography*, *10*, 1755-1768.

Huyer, A., R. L. Smith, and T. Paluszkiewicz (1987), Coastal upwelling off Peru during normal and El Niño times, 1981–1984, *Journal of Geophysical Research: Oceans*, *92*(C13), 14297-14307.

Ibaraki, M. (1990), Eocene through Pleistocene planktonic foraminifers off Peru, Leg 112 - Biostratigraphy and Paleoceanography, *Proceedings of the Ocean Drilling Program, Scientific Results*, *112*, 239-262.

Jansen, H., R. E. Zeebe, and D. A. Wolf-Gladrow (2002), Modeling the dissolution of settling $CaCO_3$ in the ocean, *Global Biogeochemical Cycles*, *16*(2), 1027.

Jonkers, L., L. J. de Nooijer, G.-J. Reichart, R. Zahn, and G.-J. A. Brummer (2012), Encrustation and trace element composition of *Neogloboquadrina dutertrei* assessed from single chamber analyses – implications for paleotemperature estimates, *Biogeosciences*, *9*, 4851–4860.

Jorissen, F. J. (1999), Benthic foraminiferal microhabitats below the sediment-water interface, in *Modern Foraminifera*, edited by B. K. Sen Gupta, pp. 161-179, Kluwer Academic Publishers, Dordrecht, Boston, London.

Kamykowski, D., and S. J. Zentara (1986), Predicting plant nutrient concentrations from temperature and sigma-t in the upper kilometer of the world ocean, *Deep-Sea Research I*, *33*, 89-105.

Karstensen, J., and O. Ulloa (2008), Peru–Chile Current System, in *Encyclopedia of Ocean Sciences*, edited by J. H. Steele, K.K. Turekian and S.A. Thorpe, pp. 385-392, Elsevier.

Keeling, R. F., A. Körtzinger, and N. Gruber (2010), Ocean Deoxygenation in a Warming World, *Annual Review of Marine Sciences*, *2*, 199-229.

Kemle-von Mücke, S., and H. Oberhänsli (1999), The Distribution of Living Planktic Foraminifera in Relation to Southeast Atlantic Oceanography, in *Use of Proxies in Paleoceanography - Examples from the South Atlantic*, edited by G. Fischer and G. Wefer, pp. 91-115, Springer-Verlag, Berlin Heidelberg New York.

Kennett, J. P., and M. Srinivasan (1983), *Neogene planktonic foraminifera — A phylogenetic atlas*, 265 pp., Hutchinson Ross Publishing, Stroudsburg.

Kessler, W. S. (2006), The circulation of the eastern tropical Pacific: A review, *Progress In Oceanography*, *69*(2-4), 181-217.

Kienast, M., S. S. Kienast, S. E. Calvert, T. I. Eglinton, G. Mollenhauer, R. Francois, and A. C. Mix (2006), Eastern Pacific cooling and Atlantic overturning circulation during the last deglaciation, *Nature*, *443*(7113), 846-849.

Kim, S. T., and J. R. O'Neil (1997), Equilibrium and nonequilibrium oxygen isotope effects in synthetic carbonates, *Geochimica et Cosmochimica Acta*, *61*(16), 3461-3475.

Klostermann, L. (2011), Hydrography and stable isotopes (oxygen, carbon) in water masses off Peru and Ecuador, Diploma thesis, 49 pp, University of Kiel, Kiel, Germany.

Koutavas, A., P. B. de Menocal, G. C. Olive, and J. Lynch-Stieglitz (2006), Mid-Holocene El Niño–Southern Oscillation (ENSO) attenuation revealed by individual foraminifera in eastern tropical Pacific sediments, *Geology*, *34*(12), 993-996.

Koutavas, A., and J. P. Sachs (2008), Northern timing of deglaciation in the eastern equatorial Pacific from alkenone paleothermometry, *Paleoceanography*, *23*(4), PA4205.

Kroon, D., and K. Darling (1995), Size and upwelling control of the stable isotope composition of *Neogloboquadrina dutertrei* (D' Orbigny), *Globigerinoides ruber* (D' Orbigny) and *Globigerina bulloides* (D' Orbigny): examples from the Panama Basin and Arabian Sea, *Journal of Foraminiferal Research*, *25*, 39-52.

Kuroyanagi, A., and H. Kawahata (2004), Vertical distribution of living planktonic foraminifera in the seas around Japan, *Marine Micropaleontology*, *53*(1–2), 173-196.

Kuroyanagi, A., R. E. da Rocha, J. Bijma, H. J. Spero, A. D. Russell, S. M. Eggins, and H. Kawahata (2013), Effect of dissolved oxygen concentration on planktonic foraminifera through laboratory culture experiments and implications for oceanic anoxic events, *Marine Micropaleontology*, *101*(0), 28-32.

Lea, D. W., D. K. Pak, and H. J. Spero (2000), Climate Impact of Late Quaternary Equatorial Pacific Sea Surface Temperature Variations, *Science*, *289*(5485), 1719-1724.

Lea, D. W., D. K. Pak, L. C. Peterson, and K. A. Hughen (2003), Synchroneity of Tropical and High-Latitude Atlantic Temperatures over the Last Glacial Termination, *Science*, *301*(5638), 1361-1364.

Lea, D. W., D. K. Pak, C. L. Belanger, H. J. Spero, M. A. Hall, and N. J. Shackleton (2006), Paleoclimate history of Galápagos surface waters over the last 135,000 yr, *Quaternary Science Reviews*, *25*(11-12), 1152-1167.

Lear, C. H., Y. Rosenthal, and N. Slowey (2002), Benthic foraminiferal Mg/Ca-paleothermometry: a revised core-top calibration, *Geochimica et Cosmochimica Acta*, *66*(19), 3375-3387.

Leduc, G., L. Vidal, O. Cartapanis, and E. Bard (2009), Modes of eastern equatorial Pacific thermocline variability: Implications for ENSO dynamics over the last glacial period, *Paleoceanography*, *24*(PA3202).

Leutenegger, S., and H. J. Hansen (1979), Ultrastructural and radiotracer studies of pore function in foraminifera, *Mar. Biol.*, *54*(1), 11-16.

Levin, L., D. Gutiérrez, A. Rathburn, C. Neira, J. Sellanes, P. Muñoz, V. Gallardo, and M. Salamanca (2002), Benthic processes on the Peru margin: a transect across the oxygen minimum zone during the 1997–98 El Niño, *Progress In Oceanography*, *53*(1), 1-27.

Lewis, E., and D. W. R. Wallace (1998), CO_2sys — Program Developed for CO_2-System Calculations. ORNL/CDIAC-105, Carbon Dioxide Information Analysis Center, Oak Ridge, National Laboratory, U.S. Department of Energy, Oak Ridge, Tennessee.

Lin, H.-L., L. C. Peterson, J. T. Overpeck, S. E. Trumbore, and D. W. Murray (1997), Late Quaternary Climate Change From δ^{18}O Records of Multiple Species of Planktonic Foraminifera: High-Resolution Records From the Anoxic Cariaco Basin, Venezuela, *Paleoceanography*, *12*(3), 415-427.

Lisiecki, L. E., and M. E. Raymo (2005), A Pliocene-Pleistocene stack of 57 globally distributed benthic δ^{18}O records, *Paleoceanography*, *20*(1), PA1003.

Liu, Z., J. Kutzbach, and L. Wu (2000), Modeling climate shift of El Niño variability in the Holocene, *Geophysical Research Letters*, *27*(15), 2265-2268.

Locarnini, R. A., A. V. Mishonov, J. I. Antonov, T. P. Boyer, H. E. Garcia, O. K. Baranova, M. M. Zweng, and D. R. Johnson (2010), World Ocean Atlas 2009, Volume 1: Temperature, in *NOAA Atlas NESDIS 68*, edited by S. Levitus, p. 184, U.S. Government Printing Office, Washington, D.C.

Loubere, P., P. Meyers, and A. Gary (1995), Benthic foraminiferal microhabitat selection, carbon isotope values, and association with larger animals; a test with *Uvigerina peregrina*, *The Journal of Foraminiferal Research*, *25*(1), 83-95.

Loubere, P. (2001), Nutrient and oceanographic changes in the Eastern Equatorial Pacific from the last full Glacial to the Present, *Global and Planetary Change*, *29*(1-2), 77-98.

Loubere, P., M. Richaud, Z. Liu, and F. Mekik (2003), Oceanic conditions in the eastern equatorial Pacific during the onset of ENSO in the Holocene, *Quaternary Research*, *60*(2), 142-148.

Lukas, R. (1986), The termination of the Equatorial Undercurrent in the eastern Pacific, *Progress In Oceanography*, *16*(2), 63-90.

Lutze, G. F., M. Sarnthein, B. Koopmann, and U. Pflaumann (1979), Meteor core 12309: Late Pleistocene reference section for interpretation of the Neogene of site 397, *Initial Report Deep Sea Drilling Project*, *47*, 727-739.

Mallon, J. (2011), Benthic Foraminifera of the Peruvian and Ecuadorian Continental Margin, PhD thesis, 236 pp, University of Kiel, Kiel.

Martin, P. A., and D. W. Lea (2002), A simple evaluation of cleaning procedures on fossil benthic foraminiferal Mg/Ca, *Geochemistry, Geophysics, Geosystems*, *3*(10), 8401.

Martin, P. A., D. W. Lea, Y. Rosenthal, N. J. Shackleton, M. Sarnthein, and T. Papenfuss (2002), Quaternary deep sea temperature histories derived from benthic foraminiferal Mg/Ca, *Earth and Planetary Science Letters*, *198*(1-2), 193-209.

McCorkle, D. C., B. H. Corliss, and C. A. Farnham (1997), Vertical distributions and stable isotopic compositions of live (stained) benthic foraminifera from the North Carolina and California continental margins, *Deep Sea Research Part I: Oceanographic Research Papers*, *44*(6), 983-1024.

McCrea, J. M. (1950), On the isotope chemistry of carbonates and a paleotemperature scale, *Journal of Chemical Physics*, *18*, 849-857.

McPhaden, M. J., et al. (1998), The Tropical Ocean-Global Atmosphere observing system: A decade of progress, *Journal of Geophysical Research: Oceans*, *103*(C7), 14169-14240.

Mohtadi, M., O. E. Romero, and D. Hebbeln (2004), Changing marine productivity off northern Chile during the past 19,000 years: a multivariable approach, *Journal of Quaternary Science*, *19*(4), 347-360.

Mollier-Vogel, E. (2012), Peruvian Oxygen Minimum dynamics during the last 18 000 years, PhD thesis, 182 pp, University of Kiel, Kiel.

Mollier-Vogel, E., G. Leduc, T. Böschen, and R. Schneider (2013), Rainfall response to orbital and millennial forcing in northern Peru over the last 18 ka, in *Quaternary Science Reviews*.

Montes, I., F. Colas, X. Capet, and W. Schneider (2010), On the pathways of the equatorial subsurface currents in the eastern equatorial Pacific and their contributions to the Peru-Chile Undercurrent, *Journal of Geophysical Research*, *115*(C9), C09003.

Morales, C., S. Hormazábal, and J. Blanco (1999), Interannual variability in the mesoscale distribution of the depth of the upper boundary of the oxygen minimum layer off

northern Chile (18-24S): Implications for the pelagic system and biogeochemical cycling, *Journal of Marine Research*, *57*, 909-932.

Müller, P. J. (1977), C/N ratios in Pacific deep-sea sediments: Effect of inorganic ammonium and organic nitrogen compounds sorbed by clays, *Geochimica et Cosmochimica Acta*, *41*(6), 765-776.

Müller, P. J., and R. Schneider (1993), An automated leaching method for the determination of opal in sediments and particulate matter, *Deep-Sea Research I*, *40*(3), 425-444.

Müller, P. J., G. Kirst, G. Ruhland, I. von Storch, and A. Rosell-Melé (1998), Calibration of the alkenone paleotemperature index $U^{K'37}$ based on core-tops from the eastern South Atlantic and the global ocean (60°N-60°S), *Geochimica et Cosmochimica Acta*, *62*, 1757-1772.

Niebler, H.-S., H.-W. Hubberten, and R. Gersonde (1999), Oxygen Isotope Values of Planktic Foraminifera: A Tool for Reconstruction of Surface Water Stratification, in *Use of Proxies in Paleoceanography - Examples from the South Atlantic*, edited by G. Fischer and G. Wefer, pp. 165-189, Springer-Verlag, Berlin Heidelberg New York.

North Greenland Ice Core Project Members (2004), High-resolution record of Northern Hemisphere climate extending into the last interglacial period, *Nature*, 431 (7005), 147-151.

Nürnberg, D., J. Bijma, and C. Hemleben (1996), Assessing the reliability of magnesium in foraminiferal calcite as a proxy for water mass temperatures, *Geochimica et Cosmochimica Acta*, *60*(5), 803-814.

Nürnberg, D. (2000), Taking the Temperature of Past Ocean Surfaces, *Science*, *289*(5485), 1698-1699.

O'Neil, J. R., R. N. Clayton, and T. K. Mayeda (1969), Oxygen isotope fractionation in divalent metal carbonates, *Journal of Chemical Physics*, *51*(12), 5547–5558.

Ortlieb, L., G. Vargas, and J.-F. Saliège (2011), Marine radiocarbon reservoir effect along the northern Chile-southern Peru coast (14-24°S) throughout the Holocene, *Quaternary Research*, *75*(1), 91-103.

Pahnke, K., and R. Zahn (2005), Southern Hemisphere Water Mass Conversion Linked with North Atlantic Climate Variability, *Science*, *307*(5716), 1741-1746.

Pak, H., and J. R. V. Zanefeld (1974), Equatorial Front in the East Pacific Ocean, *Journal of Physical Oceanography*, *4*, 570-578.

Palacios, D. M. (2004), Seasonal patterns of sea-surface temperature and ocean color around the Galápagos: regional and local influences, *Deep Sea Research Part II: Topical Studies in Oceanography*, *51*(1–3), 43-57.

Parker, F. L., and W. H. Berger (1971), Faunal and solution patterns of planktonic Foraminifera in surface sediments of the South Pacific, *Deep Sea Research and Oceanographic Abstracts*, *18*(1), 73-107.

Pena, L. D., E. Calvo, I. Cacho, S. Eggins, and C. Pelejero (2005), Identification and removal of Mn-Mg-rich contaminant phases on foraminiferal tests: Implications for Mg/Ca past temperature reconstructions, *Geochemistry Geophysics Geosystems*, *6*(9), Q09P02.

Pena, L. D., I. Cacho, P. Ferretti, and M. A. Hall (2008a), El Niño-Southern Oscillation-like variability during glacial terminations and interlatitudinal teleconnections, *Paleoceanography*, *23*(3), PA3101.

Pena, L. D., I. Cacho, E. Calvo, C. Pelejero, S. Eggins, and A. Sadekov (2008b), Characterization of contaminant phases in foraminifera carbonates by electron microprobe mapping, *Geochemistry, Geophysics, Geosystems*, *9*(7), Q07012.

Pena, L. D., S. L. Goldstein, S. R. Hemming, K. M. Jones, E. Calvo, C. Pelejero, and I. Cacho (2013), Rapid changes in meridional advection of Southern Ocean intermediate waters to the tropical Pacific during the last 30 kyr, *Earth and Planetary Science Letters*, *368*(0), 20-32.

Pennington, J. T., K. L. Mahoney, V. S. Kuwahara, D. D. Kolber, R. Calienes, and F. P. Chavez (2006), Primary production in the eastern tropical Pacific: A review, *Progress In Oceanography*, *69*(2-4), 285-317.

Penven, P., V. Echevin, J. Pasapera, F. Colas, and J. Tam (2005), Average circulation, seasonal cycle, and mesoscale dynamics of the Peru Current System: A modeling approach, *Journal of Geophysical Research*, *110*(C10), C10021.

Pfannkuche, O., M. Frank, R. Schneider, and L. Stramma (2011), Climate- biogeochemistry interactions in the tropical ocean of the SE-American oxygen minimum zone, 200 pp, Institut für Meereskunde der Universität Hamburg, Hamburg.

Philander, S. G. H. (1983), El Niño Southern Oscillation phenomena, *Nature*, *302*(5906), 295-301.

Philander, S. G. H. (1999), A review of tropical ocean–atmosphere interactions, *Tellus B*, *51*(1), 71-90.

Prahl, F. G., J. F. Rontani, N. Zabeti, S. E. Walinsky, and M. A. Sparrow (2010), Systematic pattern in $U^{K'37}$ - Temperature residuals for surface sediments from high latitude and other oceanographic settings, *Geochimica et Cosmochimica Acta*, *74*(1), 131-143.

Raddatz, J., et al. (2013), Stable Sr-isotope, Sr/Ca, Mg/Ca, Li/Ca and Mg/Li ratios in the scleractinian cold-water coral *Lophelia pertusa*, *Chemical Geology*, *352*(0), 143-152.

Rasmusson, E. M., and T. H. Carpenter (1982), Variations in Tropical Sea Surface Temperature and Surface Wind Fields Associated with the Southern Oscillation/El Niño, *Monthly Weather Review*, *110*(5), 354-384.

Ravelo, A. C., and R. G. Fairbanks (1992), Oxygen Isotopic Composition of Multiple Species of Planktonic Foraminifera: Recorders of the Modern Photic Zone Temperature Gradient, *Paleoceanography*, *7*(6), 815-831.

Redfield, A. C., B. H. Ketchum, and F. A. Richards (1963), The influence of organisms on the composition of seawater, in *The Composition of Sea-Water - Comparative and Descriptive Oceanography*, edited by M. N. Hill, pp. 26-77, John Wiley& Sons, New York London Sydney.

Redfield, A. C., B. H. Ketchum, and F. A. Richards (1966), The influence of organisms on the composition of seawater, in *The Composition of Sea-Water - Comparative and Descriptive Oceanography*, edited by M. N. Hill, pp. 26-77, John Wiley& Sons, New York London Sydney.

Regenberg, M., D. Nürnberg, S. Steph, J. Groeneveld, D. Garbe-Schönberg, R. Tiedemann, and W. C. Dullo (2006), Assessing the effect of dissolution on planktonic foraminiferal Mg/ Ca ratios: Evidence from Caribbean core tops, *Geochemistry, Geophysics, Geosystems*, *7*(7), 1-23.

Regenberg, M., S. Steph, D. Nürnberg, R. Tiedemann, and D. Garbe-Schönberg (2009), Calibrating Mg/ Ca ratios of multiple planktonic foraminiferal species with δ^{18}O-calcification temperatures: Paleothermometry for the upper water column, *Earth and Planetary Science Letters*, *278*, 324-336.

Reimer, P. J., et al. (2009), IntCal09 and Marine09 Radiocarbon Age Calibration Curves, 0-50,000 Years cal BP, *Radiocarbon*, *51*, 1111-1150.

Rincón-Martínez, D., F. Lamy, S. Contreras, G. Leduc, E. Bard, C. Saukel, T. Blanz, A. Mackensen, and R. Tiedemann (2010), More humid interglacials in Ecuador during the past 500 kyr linked to latitudinal shifts of the equatorial front and the Intertropical Convergence Zone in the eastern tropical Pacific, *Paleoceanography*, *25*(2), PA2210.

Rincón-Martínez, D., S. Steph, F. Lamy, A. Mix, and R. Tiedemann (2011), Tracking the equatorial front in the eastern equatorial Pacific Ocean by the isotopic and faunal composition of planktonic foraminifera, *Marine Micropaleontology*, *79*(1-2), 24-40.

Roberts, N. L., A. M. Piotrowski, J. F. McManus, and L. D. Keigwin (2010), Synchronous Deglacial Overturning and Water Mass Source Changes, *Science*, *327*(5961), 75-78.

Robinson, R. S., A. Mix, and P. Martinez (2007), Southern Ocean control on the extent of denitrification in the southeast Pacific over the last 70 ka, *Quaternary Science Reviews*, *26*(1-2), 201-212.

Rodbell, D. T., G. O. Seltzer, D. M. Anderson, M. B. Abbott, D. B. Enfield, and J. H. Newman (1999), An ~15,000-Year Record of El Niño-Driven Alluviation in Southwestern Ecuador, *Science*, *283*(5401), 516-520.

Rohling, E. J., and S. Cooke (1999), Stable oxygen and carbon isotopes in foraminiferal carbonate shells, in *Modern Foraminifera*, edited by B. K. Sen Gupta, pp. 239-258, Kluwer Academic Publishers, Dordrecht, Boston, London.

Rosenthal, Y., E. A. Boyle, and N. Slowey (1997), Temperature control on the incorporation of magnesium, strontium, fluorine, and cadmium into benthic foraminiferal shells from Little Bahama Bank: Prospects for thermocline paleoceanography, *Geochimica et Cosmochimica Acta*, *61*(17), 3633-3643.

Rosenthal, Y., G. P. Lohmann, K. C. Lohmann, and R. M. Sherrell (2000), Incorporation and Preservation of Mg in *Globigerinoides sacculifer*: Implications for Reconstructing the Temperature and $^{18}O/^{16}O$ of Seawater, *Paleoceanography*, *15*(1), 135-145.

Rosenthal, Y., C. H. Lear, D. W. Oppo, and B. K. Linsley (2006), Temperature and carbonate ion effects on Mg/Ca and Sr/Ca ratios in benthic foraminifera: Aragonitic species *Hoeglundina elegans*, *Paleoceanography*, *21*(1), PA1007.

Rubin, S., J. G. Goddard, D. W. Chipman, T. Takahashi, S. C. Sutherland, J. L. Reid, J. H. Swift, L. D. Talley, and A. Kozyr (1998), Carbon Dioxide, Hydrographic, and Chemical Data Obtained in the South Pacific Ocean (WOCE Sections P16A/P17A, P17E/P19S, and P19C, R/V Knorr, October 1992-April 1993), p. 186, Carbon Dioxide Information Analysis Center, Oak Ridge National Laboratory, U.S. Department of Energy, Oak Ridge, Tennessee.

Rüggeberg, A., J. Fietzke, V. Liebetrau, A. Eisenhauer, W.-C. Dullo, and A. Freiwald (2008), Stable strontium isotopes ($\delta^{88}/^{86}Sr$) in cold-water corals — A new proxy for reconstruction of intermediate ocean water temperatures, *Earth and Planetary Science Letters*, *269*(3–4), 570-575.

Sadekov, A. Y., S. M. Eggins, and P. De Deckker (2005), Characterization of Mg/Ca distributions in planktonic foraminifera species by electron microprobe mapping, *Geochemistry, Geophysics, Geosystems*, *6*(12), Q12P06.

Sandweiss, D. H. (2003), Terminal Pleistocene through Mid-Holocene archaeological sites as paleoclimatic archives for the Peruvian coast, *Palaeogeography, Palaeoclimatology, Palaeoecology*, *194*(1-3), 23-40.

Sandweiss, D. H., J. B. Richardson, E. J. Reitz, H. B. Rollins, and K. A. Maasch (1996), Geoarchaeological Evidence from Peru for a 5000 Years B.P. Onset of El Niño, *Science*, *273*(5281), 1531-1533.

Schlitzer, R. (2010), Ocean Data View, http://odv.awi.de.

Schmidt, M. W., H. J. Spero, and D. W. Lea (2004), Links between salinity variation in the Caribbean and North Atlantic thermohaline circulation, *Nature*, *428*(6979), 160-163.

Schmuker, B., and R. Schiebel (2002), Planktic foraminifers and hydrography of the eastern and northern Caribbean Sea, *Marine Micropaleontology*, *46*(3-4), 387-403.

Scholz, F., C. Hensen, A. Noffke, A. Rohde, V. Liebetrau, and K. Wallmann (2011), Early diagenesis of redox-sensitive trace metals in the Peru upwelling area – response to ENSO-related oxygen fluctuations in the water column, *Geochimica et Cosmochimica Acta*, *75*(22), 7257-7276.

Sen Gupta, B. K., and M. L. Machain-Castillo (1993), Benthic foraminifera in oxygen-poor habitats, *Marine Micropaleontology*, *20*(3–4), 183-201.

Shackleton, N. J. (1974), Attainment of isotopic equilibrium between ocean water and the benthonic foraminifera genus *Uvigerina*: Isotopic changes in the ocean during the last glacial, *Colloques Internationaux du C.N.R.S.*, *219*, 203-209.

Shackleton, N. J., and M. A. Hall (1984), Oxygen and carbon isotope stratigraphy of Deep Sea Drilling Project Hole 552A: Plio-Pleistocene glacial history, *Initial Report Deep Sea Drilling Project*, *81*, 599-609.

Silva, N., N. Rojas, and A. Fedele (2009), Water masses in the Humboldt Current System: Properties, distribution, and the nitrate deficit as a chemical water mass tracer for

Equatorial Subsurface Water off Chile, *Deep Sea Research Part II: Topical Studies in Oceanography*, *56*(16), 1004-1020.

Sloyan, B. M., L. D. Talley, T. K. Chereskin, R. Fine, and J. Holte (2010), Antarctic Intermediate Water and Subantarctic Mode Water Formation in the Southeast Pacific: The Role of Turbulent Mixing, *Journal of Physical Oceanography*, *40*(7), 1558-1574.

Sosdian, S., and Y. Rosenthal (2009), Deep-Sea Temperature and Ice Volume Changes Across the Pliocene-Pleistocene Climate Transitions, *Science*, *325*(5938), 306-310.

Sosdian, S., and Y. Rosenthal (2010), Response to Comment on “Deep-Sea Temperature and Ice Volume Changes Across the Pliocene-Pleistocene Climate Transitions”, *Science*, *328*(5985), 1480.

Spero, H. J., and D. F. Williams (1989), Opening the Carbon Isotope "Vital Effect" Black Box 1. Seasonal Temperatures in the Euphotic Zone, *Paleoceanography*, *4*(6), 593-601.

Spero, H. J., I. Lerche, and D. F. Williams (1991), Opening the Carbon Isotope "Vital Effect" Black Box, 2, Quantitative Model for Interpreting Foraminiferal Carbon Isotope Data, *Paleoceanography*, *6*(6), 639-655.

Steinke, S., H.-Y. Chiu, P.-S. Yu, C.-C. Shen, L. Löwemark, H.-S. Mii, and M.-T. Chen (2005), Mg/Ca ratios of two Globigerinoides ruber (white) morphotypes: Implications for reconstructing past tropical/subtropical surface water conditions, *Geochemistry Geophysics Geosystems*, *6*(11), Q11005.

Stramma, L., S. Schmidtko, L. A. Levin, and G. C. Johnson (2010), Ocean oxygen minima expansions and their biological impacts, *Deep Sea Research Part I: Oceanographic Research Papers*, *57*(4), 587-595.

Strub, P. T., J. M. Mesias, and C. James (1995), Altimeter observations of the Peru-Chile Countercurrent, *Geophysical Research Letters*, *22*(3), 211-214.

Strub, P. T., J. M. Mesías, V. Montecino, J. Rutllant, and S. Salinas (1998), Coastal Ocean Circulation off Western South America, in *The Sea - Volume 11*, edited by A. R. Robinson and K. H. Brink, pp. 273-313, John Wiley & Sons, Inc., New York.

Sun, D.-Z., T. Zhang, and S.-I. Shin (2004), The Effect of Subtropical Cooling on the Amplitude of ENSO: A Numerical Study, *Journal of Climate*, *17*(19), 3786-3798.

Tedesco, K. A., and R. C. Thunell (2003), Seasonal and interannual variations in planktonic foraminiferal flux and assemblage composition in the Cariaco Basin, Venezuela, *Journal of Foraminiferal Research*, *33*(3), 192-210.

Thiede, J. (1975), Distribution of foraminifera in surface waters of a coastal upwelling area, *Nature*, *253*(5494), 712-714.

Thiede, J. (1983), Skeletal plankton and nekton in upwelling water masses off northwestern South America and Northwest Africa, in *Coastal Upwelling: Its Sediment Record, Part A. Responses of the Stratigraphy:*, edited by E. Suess and J. Thiede, pp. 263-314, Cambridge University Press, Cambridge.

Thunell, R. C., W. B. Curry, and S. Honjo (1983), Seasonal variation in the flux of planktonic foraminifera: time series sediment trap results from the Panama Basin, *Earth and Planetary Science Letters*, *64*(1), 44-55.

Thunell, R., E. Tappa, C. Pride, and E. Kincaid (1999), Sea-surface temperature anomalies associated with the 1997–1998 El Niño recorded in the oxygen isotope composition of planktonic foraminifera, *Geology*, *27*(9), 843-846.

Tjallingii, R. (2006), Application and quality of X-Ray Fluorescence core scanning in reconstructing late Pleistocene NW African continental margin sedimentation patterns and paleoclimate variations, PhD thesis, 114 pp, University of Bremen, Bremen, Germany.

Tjallingii, R., U. Röhl, M. Kölling, and T. Bickert (2007), Influence of the water content on X-ray fluorescence core-scanning measurements in soft marine sediments, *Geochemistry Geophysics Geosystems*, *8*(2), Q02004.

Tjallingii, R., K. Stattegger, A. Wetzel, and P. Van Phach (2010), Infilling and flooding of the Mekong River incised valley during deglacial sea-level rise, *Quaternary Science Reviews*, *29*(11-12), 1432-1444.

Toggweiler, J. R., K. Dixon, and W. S. Broecker (1991), The Peru Upwelling and the Ventilation of the South Pacific Thermocline, *Journal of Geophysical Research*, *96*(C11), 20467-20497.

Tsuchiya, M., and L. D. Talley (1996), Water-property distributions along an eastern Pacific hydrographic section at 135W, *Journal of Marine Research*, *54*(3), 541-564.

Twilley, R. R., W. Cárdenas, V. H. Rivera-Monroy, J. Espinoza, R. Suescum, M. M. Armijos, and L. Solórzano (2001), The Gulf of Guayaquil and the Guayas River estuary, Ecuador, in *Coastal marine ecosystems of Latin America. Ecological studies, Volume 144*, edited by U. Seelinger and B. Kjerfve, pp. 245-264.

Urey, H. C. (1947), The thermodynamic properties of isotopic substances, *Journal of the Chemical Society*, 562-581.

van Andel, T. H., G. R. Heath, and T. C. Moore (1975), *Cenozoic History and Paleoceanography of the Central Equatorial Pacific Ocean*, 74 pp., The Geological Society of America.

van Breukelen, M. R., H. B. Vonhof, J. C. Hellstrom, W. C. G. Wester, and D. Kroon (2008), Fossil dripwater in stalagmites reveals Holocene temperature and rainfall variation in Amazonia, *Earth and Planetary Science Letters*, *275*(1-2), 54-60.

Vargas, G., J. Rutllant, and L. Ortlieb (2006), ENSO tropical–extratropical climate teleconnections and mechanisms for Holocene debris flows along the hyperarid coast of western South America (17°–24°S), *Earth and Planetary Science Letters*, *249*(3–4), 467-483.

Waelbroeck, C., L. Labeyrie, E. Michel, J. C. Duplessy, J. F. McManus, K. Lambeck, E. Balbon, and M. Labracherie (2002), Sea-level and deep water temperature changes derived from benthic foraminifera isotopic records, *Quaternary Science Reviews*, *21*(1-3), 295-305.

Wang, L. (2000), Isotopic signals in two morphotypes of *Globigerinoides ruber* (white) from the South China Sea: implications for monsoon climate change during the last glacial cycle, *Palaeogeography, Palaeoclimatology, Palaeoecology*, *161*(3-4), 381-394.

Wefer, G., and W. H. Berger (1991), Isotope paleontology: growth and composition of extant calcareous species, *Marine Geology*, *100*(1–4), 207-248.

Wilke, I., T. Bickert, and F. J. C. Peeters (2006), The influence of seawater carbonate ion concentration [CO_3^{2-}] on the stable carbon isotope composition of the planktic foraminifera species *Globorotalia inflata*, *Marine Micropaleontology*, *58*(4), 243-258.

Wyrtki, K. (1966), Oceanography of the Eastern Equatorial Pacific Ocean, in *Oceanography and Marine Biology*, edited by H. Barnes, pp. 33-68, George Allen & Unwin Ltd., London.

Wyrtki, K., and G. Meyers (1976), The Trade Wind Field Over the Pacific Ocean, *Journal of Applied Meteorology*, *15*(7), 698-704.

Yu, J., and H. Elderfield (2007), Benthic foraminiferal B/Ca ratios reflect deep water carbonate saturation state, *Earth and Planetary Science Letters*, *258*(1-2), 73-86.

Yu, J., and H. Elderfield (2008), Mg/Ca in the benthic foraminifera *Cibicidoides wuellerstorfi* and *Cibicidoides mundulus*: Temperature versus carbonate ion saturation, *Earth and Planetary Science Letters*, *276*(1–2), 129-139.

Ziegler, M., T. Jilbert, G. J. de Lange, L. J. Lourens, and G.-J. Reichart (2008), Bromine counts from XRF scanning as an estimate of the marine organic carbon content of sediment cores, *Geochemistry Geophysics Geosystems*, *9*(5), Q05009.

Zuta, S., and O. Guillén (1970), Oceanografía de las aguas costeras del Perú, *Boletín del Instituto del Mar del Perú*, *5*, 157–324.

A) APPENDIX

A.1) PhD publications

Accepted

Ehlert, C., Grasse, P., Mollier-Vogel, E., **Böschen, T.**, Franz, J., de Souza, G.F., Reynolds, B.C., Stramma, L. and Frank, M., 2012. Factors controlling the silicon isotope distribution in waters and surface sediments of the Peruvian coastal upwelling. Geochimica et Cosmochimica Acta, 99, p. 128-145, http://dx.doi.org/10.1016/j.gca.2012.09.038.

Mollier-Vogel, E., Leduc, G., **Böschen, T.**, Martinez, P. and Schneider, R.R., 2013. Rainfall response to orbital and millennial forcing in northern Peru over the last 18 ka, Quaternary Science Reviews, 76, p. 29-38, http://dx.doi.org/10.1016/j.quascirev.2013.06.021.

A copy of this manuscript is added in the following section (A.2). It contains the AMS^{14}C-based age models, which rely on datings of *N. dutertrei* performed by the author of this thesis and which were used for the down core records in Chapter 5.

Submitted and in review

Böschen, T., Nürnberg, D., Mollier-Vogel, E., Doering, K., Schneider, R. and Dullo, C., 2013. Deglacial to Holocene upper ocean dynamics in the Eastern Equatorial Pacific. Paleoceanography, submitted.

Conference Contributions

2010

Böschen, T., Mollier-Vogel, E., Nürnberg, D., Schneider, R. and Dullo, C., 2010. Deglcial to Holocene changes in water temperatures as indicator for changes in the Peruvian upwelling system. 10th International Conference on Paleoceanography, San Diego, USA, Poster.

A.2) Rainfall response to orbital and millennial forcing in northern Peru over the last 18 ka

Elfi Mollier-Vogel[1*], Guillaume Leduc[1], Tebke Böschen[2], Philippe Martinez[3] and Ralph R. Schneider[1]

[1] Institute of Geosciences, University of Kiel, Germany

[2] GEOMAR Helmholtz Centre for Ocean Research Kiel, Kiel, Germany

[3] Université Bordeaux 1, UMR CNRS 5805 EPOC, avenue des facultés, 33405 Talence Cedex, France

Keywords: ITCZ, speleothem, XRF, Holocene, Deglaciation, Younger Dryas, Heinrich 1

Published as: Mollier-Vogel, E., Leduc, G., Böschen, T., Martinez, P. and Schneider, R.R., 2013. Rainfall response to orbital and millennial forcing in northern Peru over the last 18 ka, Quaternary Science Reviews, 76, p. 29-38, http://dx.doi.org/10.1016/j.quascirev.2013.06.021.

Abstract

We present a high-resolution marine record of sediment input from the Guayas River, Ecuador, that reflects changes in precipitation along western equatorial South America during the last 18ka. We log (Ti/Ca) derived from X-ray Fluorescence (XRF) to document terrigenous input from riverine runoff that integrates rainfall from the Guayas River catchment. We find that rainfall-induced riverine runoff has increased during the Holocene and decreased during the last deglaciation. Superimposed on those long-term trends, we find that rainfall was probably slightly increased during the Younger Dryas, while the Heinrich event 1 was marked by an extreme load of terrigenous input, probably reflecting one of the wettest period over the time interval studied. When compared our results to other Deglacial to Holocene rainfall records located across the tropical South American continent, different modes of variability become apparent. The records of rainfall variability imply that changes in the hydrological cycle at orbital and sub-orbital timescales were different from western to eastern South America. Orbital forcing caused an antiphase behavior in rainfall trends between eastern and western equatorial South America. In contrast, millennial-scale rainfall changes, remotely connected to the North Atlantic climate variability, led to homogenously wetter conditions over eastern and western equatorial South America during North Atlantic cold spells. These results may provide helpful diagnostics for testing the regional rainfall sensitivity in climate models and help to refine rainfall projections in South America for the next century.

A.2.1) Introduction

Seasonal and interannual rainfall variability in western equatorial South America is driven by a multitude of climatic processes, with the complex regional patterns additionally shaped by orography. On the Amazonian side of the equatorial Andes, high precipitation rates are found throughout the year, with maxima occurring at the equinoxes (Garreaud et al., 2009; Poveda et al., 2006; Figure A-2-1a). On the Pacific side, the orogenic barrier of the Andes blocks moisture transport from the Atlantic Ocean, making the Ecuadorian and Peruvian lowlands much drier than on the eastern side of the Andes. Still, there is a well defined subdivision between coastal regions located north and south of the equator which are affected by opposite seasonality in rainfall regimes (Garreaud et al., 2009; Poveda et al., 2006; Figure A-2-1a). In addition, interannual rainfall variability associated with the El Niño-Southern Oscillation (ENSO) contributes to the rainfall pattern complexity over South America (Dai and Wigley, 2000; Figure A-2-1b). Since the importance of these factors for regional rainfall patterns is difficult to assess, it remains problematic to understand the sensitivity of the hydrological cycle over South America to the climatic forcing at different timescales.

Beyond historical rainfall records, valuable information can be gained from paleoclimatic archives spanning time windows over which different forcings were at play. Past shifts in rainfall over South America since the Last Glacial Maximum (LGM) are thought to depend on, both, changes in orbital parameters and in the Atlantic Meridional Overturning Circulation (AMOC) intensity (Cruz et al., 2005; Wang et al., 2007). Changes in summer rainfall intensity are characterized by a latitudinal antiphase behaviour between northern and southern tropics (Cruz et al., 2005; Haug et al., 2001; Wang et al., 2007). At the orbital timescale, a maximum in boreal summer insolation during the early Holocene triggered intense rainfall in northern South America, followed by a progressive aridification associated with the austral summer insolation increase during the mid- to late Holocene (Haug et al., 2001). In contrast, the southern tropics experienced drier conditions during the early to mid-Holocene, followed by wet conditions during the late Holocene as recorded in speleothems from southern Brazil (Cruz et al., 2005; Wang et al., 2007) and Andean lakes (Baker et al., 2001; Bird et al., 2011).

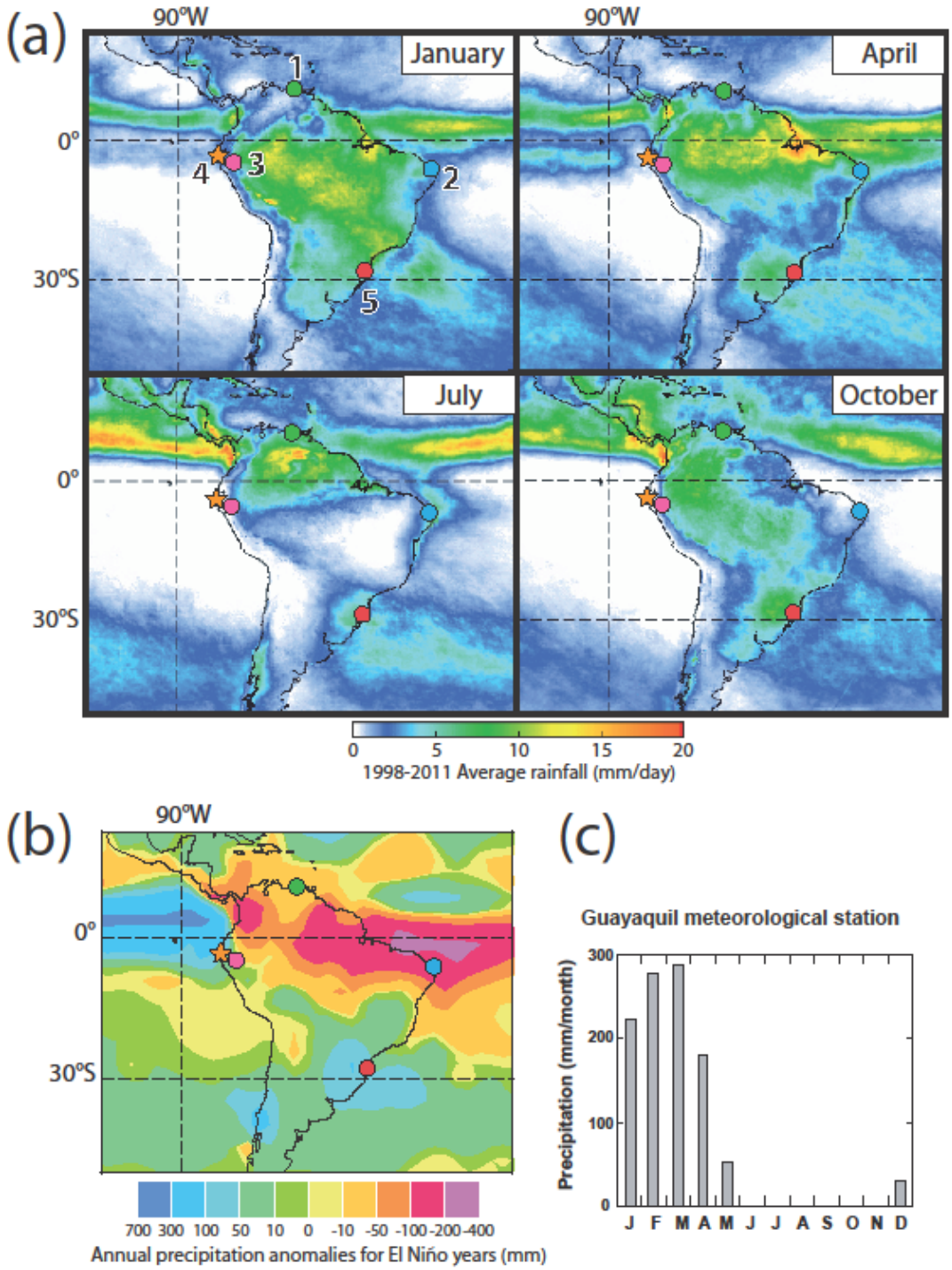

Figure A-2-1: Seasonal precipitation for South America, for El Niño and for Guayaquil

(a) Seasonal changes in mean precipitation over South America derived from the Tropical Rainfall Measuring Mission (TRMM). Data extracted from the NASA/GSFC website available at http://trmm.gsfc.nasa.gov/. Location of paleo-precipitation records displayed in Figure A-2-5 are numbered as following: (1) Haug et al. (2001); (2) Cruz et al. (2009); (3) van Breukelen et al. (2008); (4) This study; (5) Wang et al. (2007).

(b) Annual precipitation anomalies over South America for typical El Niño (modified from Dai and Wigley, 2000).

(c) Mean monthly precipitation at Guayaquil, modified from Rincón-Martínez et al. (2010).

Closer to the equator, where the sun passes twice at zenith each year, the regional pattern of rainfall variability seems to be more complex than the simple antiphase behavior observed north and south of the equator where dry and wet seasons are well defined. Speleothem records collected close to the equator at the eastern and western edges of the Amazonian Basin indicate that Holocene changes in insolation have triggered an East-West antiphase in rainfall trends (Cruz et al., 2009). During the mid Holocene in particular, Northeastern Brazil was associated with wetter conditions than nowadays South of the equator (Cruz et al., 2009), while the western equatorial South America was marked by drier conditions (van Breukelen et al., 2008).

At the millennial timescale, a slowdown in AMOC associated with North Atlantic cold spells such as the Heinrich event 1 (H1) and the Younger Dryas (YD) induced a southward shift in rainfall over northern South America (Haug et al., 2001; Leduc et al., 2007; Peterson et al., 2000). Similar to the case for orbital forcing, the southern tropical South America experienced an increase in rainfall opposite to the North. Clearly wetter conditions are revealed in speleothems from southern Brazil during the H1 and the YD (Cruz et al., 2005). The same pattern is observed for Brazilian rivers runoff situated closer to the equator in marine records (Arz et al., 1998; Jaeschke et al., 2007; Jennerjahn et al., 2004). However, no clear East-West antiphase in rainfall response to North Atlantic cold spells is apparent in existing continental speleothems records located close to the equator (Cruz et al., 2009; van Breukelen et al., 2008). The available records rather suggest a moderate increase or no changes in equatorial rainfall at the east and west of the Amazonian Basin during the H1 and the YD. Therefore climate changes at orbital and millennial timescales tend to enhance or decrease rainfall amount over tropical South America in different ways. Yet we are lacking continuous paleoprecipitation records covering the full Deglacial and Holocene time periods for the eastern equatorial Pacific (EEP) and Peruvian coastal plains to decipher whether or not the rainfall anomalies observed above the Amazonian basin are mirrored on the Pacific side of the Andes.

Here we present two continuous Ti/Ca records close to the northern Peruvian coast, south to the Gulf of Guayaquil in the EEP, covering the last 18 ka. The studied site, situated midway from the hyperhumid Colombian margin to the North and the hyperarid Peruvian desert to the South, provides the opportunity to better understand how ocean-atmosphere interactions are set up under different climatic boundary conditions and may

modulate regional rainfall regimes from oceanic areas to mountain tops. The records provide information on past changes in sediment discharge induced by regional rainfall changes with sub-centennial resolution. These Ti/Ca records compared with rainfall records from the other key regions of tropical South America (Figure A-2-1) allow an improved assessment of regional rainfall response to orbital and millennial-scale climate forcing.

A.2.2) Regional settings

At the seasonal timescale, rainfall patterns over the South American continent migrate latitudinally following the annual cycle of insolation, but over the adjacent ocean the Intertropical Convergence Zone (ITCZ) remains near 5°N because of local air-sea interactions (Figure A-2-1a). In addition, south of the equator, the Andes impede moisture transport to the Pacific Ocean, leaving the Pacific coastal plains within a rain shadow (Figure A-2-1a). Consequently, a sharp regional contrast exists between the Pacific side of the Andean Cordillera and the Amazonian Basin at the equator, the latter receiving most of its rainfall from the Atlantic Ocean (Bookhagen and Strecker, 2008). The Guayas River catchment is within a transitional region situated between the Columbian Margin to the North - which receives its rainfall from the Pacific, and the Peruvian Margin where most of the rainfall comes from moisture advected from the Atlantic and meandering through the Andes (Bookhagen and Strecker, 2008).

Rainfall patterns over the South American continent closely follow the South American Monsoon system. Rainfall maxima occur north of the equator during the boreal summer and vice-versa during the austral summer (Figure A-2-1a-c). Along the equator, a broad precipitation maximum occurs during austral summer (Figure A-2-1c). On the other hand, October rainfall is reduced and tends to be confined above the western side of the Amazonian Basin (Figure A-2-1a). These features result in a bimodal distribution of the annual cycle of rainfall, with maxima occurring at equinoxes above the Amazonian Basin (Poveda et al., 2006).

Along the Pacific coast, regional rainfall also varies from region to region because local land-ocean-atmosphere interactions regulate precipitation distribution superimposed on the dynamics of the ITCZ (Figure A-2-1a). North of the equator, the Pacific side of the Co-

lumbian Margin receives high amounts of rainfall from the low-level westerly Choco Jet, which transports moisture from the EEP to the western flank of the Andes during the boreal summer (Bookhagen and Strecker, 2008; Poveda and Mesa, 2000). South of the equator, rainfall maxima occur during austral summer when the ITCZ prevails above the eastern equatorial Pacific in the southern hemisphere (Liu and Xie, 2002; Figure A-2-1a). South of 5°S, the hyperarid Peruvian desert extends along the Pacific coastline and is sustained year-round by the cold Humboldt current and its associated upwelling system (Garreaud et al., 2009; Figure A-2-1a).

At the interannual timescale, warm ENSO anomalies in the EEP are marked by drier conditions in northern South America and along the equator above the Amazonian basin, while conditions over southeastern South America and the EEP are comparatively wetter (Dai and Wigley, 2000; Silvestri, 2004; Figure A-2-1b). Along northern Peru and Ecuadorian coastlines, El Niño events provoke important increases in precipitation as compared to normal years (Dai and Wigley, 2000; Figure A-2-1b). Little further to the South, within the northern Peruvian desert located between 5 and 10°S, significant rainfall exclusively occurs during El Niño events (Wells, 1990).

Rainfall patterns occurring within the river catchments of interest for our study area are, unlike along the Amazonian flanks of the Andes, unimodal. A rainy season from January to March occurs both in Guayaquil (1°S) and Piura (5°S), but the amount of precipitation received in Guayaquil is about an order of magnitude larger than in Piura (www.allmetsat.com).

A.2.3) Material and methods

Piston cores M772-059 (3°57.01'S, 81°19.23'W, 997 m water depth) and M772-056 (3°44.99'S, 81°07.25'W, 350 m water depth) were collected south of the Gulf of Guayaquil (Figure A-2-1). The Gulf of Guayaquil is composed of a sedimentary platform, with an outer shelf break into the continental margin situated at a water depth of ~100 m (Figure A-2-2; Witt and Bourgois, 2010). The sediments accumulating at the coring sites are dominated by terrigenous particle discharge associated with riverine runoff controlled by regional rainfall intensity, and contain as a secondary component marine biogenic carbonates. Sedimentary discharge into the Gulf of Guayaquil is mainly linked to the Guayas

River runoff, which integrates rainfall from a narrow catchment located North of Guayaquil on the western flank of the Ecuadorian Andes (Twilley et al., 2001). The Guayas River discharge closely tracks the integrated precipitation occurring on land within the basin catchment without any time lag (Twilley et al., 2001). The northern Peruvian coast is subdivided by a mosaic of small coastal river catchments, which are much more sensitive to ENSO as compared to the Guayas River (Wells, 1990).

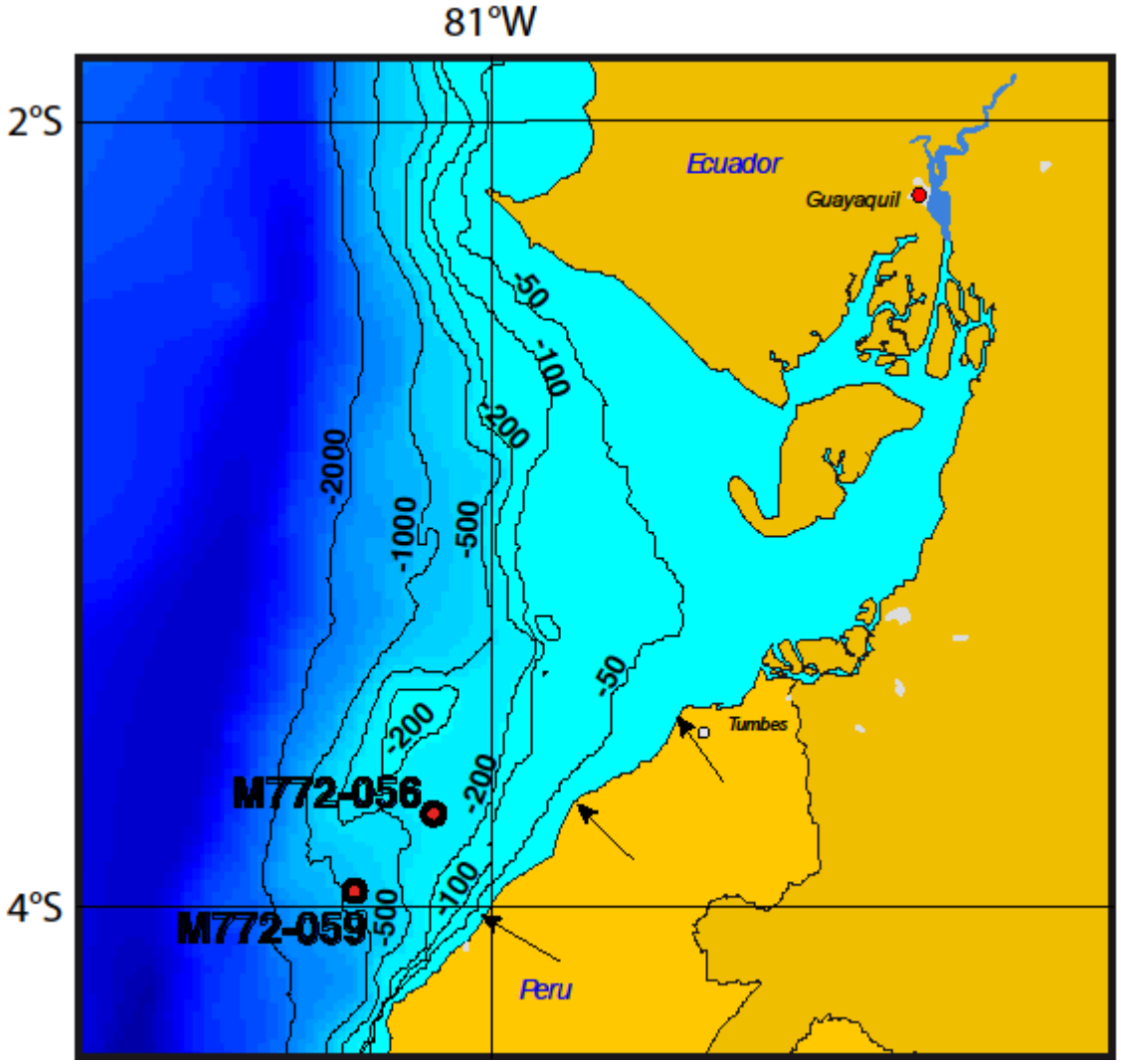

Figure A-2-2: Regional bathymetry (isobaths in meters) and sediment core locations

The Gulf of Guayaquil is typically marked by water depths shallower than 100 m. Assuming that regional relative sea level rise followed the eustatic sea level evolution, the 100 m and 50 m isobaths provide qualitative indications on how the coastline may have evolved in response to eustatic sea level, with the 100 m and 50 m isobaths representing coastlines at ~15 and 11 ka, respectively (Bard et al., 1996). The arrows locate small rivers mouths that may occasionally represent a significant source of terrigenous material to coring sites during El Niño events (Wells, 1990).

The age model of the combined full Deglacial to Late Holocene record is based on radiocarbon measurements from 10 and 11 different depth levels for cores M772-059 and M772-056, respectively (Table A-2-1; Figure A-2-3). Radiocarbon measurements were performed on the planktonic foraminifera species Neogloboquadrina dutertrei at the Leibniz Laboratory for Radiometric Dating and Stable Isotope Research, University of Kiel (CAU). Radiocarbon ages were calibrated using MARINE09 (Reimer et al., 2009), with a constant ΔR of 200 +/- 50 years based on sites with known reservoir ages situated closest to our core location in the marine Reservoir correction database (http://calib.qub.ac.uk/marine/).

Table A-2-1: AMS^{14}C data used for cores M772-059 and M772-056 age models

Conversion of radiocarbon ages to calendar ages was done using the program Calib 6.0. and the Marine09 calibration curve. A regional reservoir age offset of 200±50 years was applied. Ages were linearly interpolated between mean points of age ranges.

Depth (cm)	Radiocarbon age (yrs BP)	Age range, cal. yrs BP (2σ)	Cal. Age (yrs BP), mean value
M772-056			
2	0	0	**0**
49	1085 ± 25 BP	416 - 616	**516**
138	2575 ± 30 BP	1850 - 2153	**2001**
199	3255 ± 25 BP	2717 - 2965	**2841**
338	4960 ± 30 BP	4850 - 5225	**5037**
399	5510 ± 40 BP	5563 - 5853	**5708**
508	6620 ± 35 BP	6735 - 7088	**6911**
599	7430 ± 35 BP	7574 - 7826	**7700**
693	8220 ± 60 BP	8326 - 8678	**8502**
769	8960 ± 45 BP	9271 - 9538	**9404**
893	10085 ± 45 BP	10596 - 11060	**10828**
999	11030 ± 50 BP	12052 - 12561	**12306**
M772-059			
13	830 ± 25 BP	124 - 420	**272**
148	3490 ± 30 BP	2957 - 3303	**3130**
204	4325 ± 45 BP	3985 - 4385	**4185**
303	5725 + 50 / -45 BP	5732 - 6097	**5914**
404	7815 ± 65 BP	7922 - 8273	**8097**
658	10470 ± 50 BP	11128 - 11427	**11277**
803	11855 ± 60 BP	12916 - 13309	**13112**
804	12060 ± 130 BP	13081 - 13673	**13377**
1033	13140 ± 70 BP	14200 - 15119	**14659**
1344	15270 ± 150 BP	17251 - 18121	**17686**

For core M772-059, the resulting age model implies sedimentation rates varying between ~50 and 170 cm*kyr-1, providing a time resolution ranging from ~22 years*cm-1 during the mid-Holocene down to ~6 years*cm-1 for the Heinrich 1 time interval. For core M772-056, the resulting age model implies sedimentation rates varying between ~63 and 117 cm*kyr-1, providing a time resolution ranging from ~16 years *cm-1 during the mid-Holocene down to ~8 years*cm-1 for the early Holocene time interval.

Contents of total carbon (TC) and organic carbon (Corg) were measured on core M772-059 from bulk and decalcified sediment, respectively, using an elemental analyzer. The carbonate content was then calculated using the equation $\%CaCO_3 = (\%TC - \%C_{org})*8.33$.

The relative elemental composition of sediments was analysed using an Avaatech X-ray fluorescence (XRF) Core Scanner at 1 cm distance following the procedure described in (Tjallingii et al., 2010). We use the Ti element intensity (in counts per seconds) relative to the Ca intensity to monitor past changes in terrigenous detrital content relative to that of marine carbonates, and consider it as a proxy for riverine runoff as in previous studies (Arz et al., 1998; Haug et al., 2001; Jaeschke et al., 2007). We also check the log (Si/Al) to look for outstandingly high log (Si/Al) changes, which may indicate significant changes in biogenic opal fluxes, most likely reflecting productivity of diatoms and radiolaria.

A.2.4) Results

A.2.4.1) XRF data

We use log-ratios of Ti/Ca (log Ti/Ca), which provide unbiased estimates for the relative concentration of Ti over Ca with respect to sedimentary heterogeneities and nonlinearities between the XRF intensity and its corresponding sedimentary concentration (Weltje and Tjallingii, 2008). In marine sediments mainly composed of terrigenous material at tropical latitudes, as at our core sites, the log (Ti/Ca) can be applied to reconstruct past changes in continental detritus accumulation as a qualitative indicator for rainfall variability occurring on the adjacent continent. Such assumption relates to the fact that Ti representing the dominating detrital fraction, once normalized to marine biogenic Ca, reflects the variable input of terrigenous material at coring sites through the modulation of Ca content associated with dilution of carbonates. Variations of elemental XRF intensity of Si, Al, Ca and Fe are shown as a function of Ti intensity in Figure A-2-3. For clarity, we only

consider the core M772-059 that covers the last 18 ka and for which carbonate content data are available for validating the interpretation of XRF data. Ti is positively correlated to Si, Al and Fe with near perfection (Figure A-2-3), and shows negative correlation to Ca at a confidence level of 95% (r2=0.066, n=1327, Figure A-2-3). The positive correlation between Ti and the other terrestrial elements is expected as those elements have the same origin. The negative statistical correlation between Ti and Ca (Figure A-2-3) suggests that the amount of Ca with respect to that of Ti was mainly affected by dilution with the terrigenous phase, which is the basis of our interpretation of log (Ti/Ca). The significance of the linear regression between Ti and other terrigenous elements is probably stronger than that relying Ca and Ti. It suggests that processes other than dilution modulate the Ca XRF intensity such as changes in carbonate rain rates, but that mechanism is clearly of second-order.

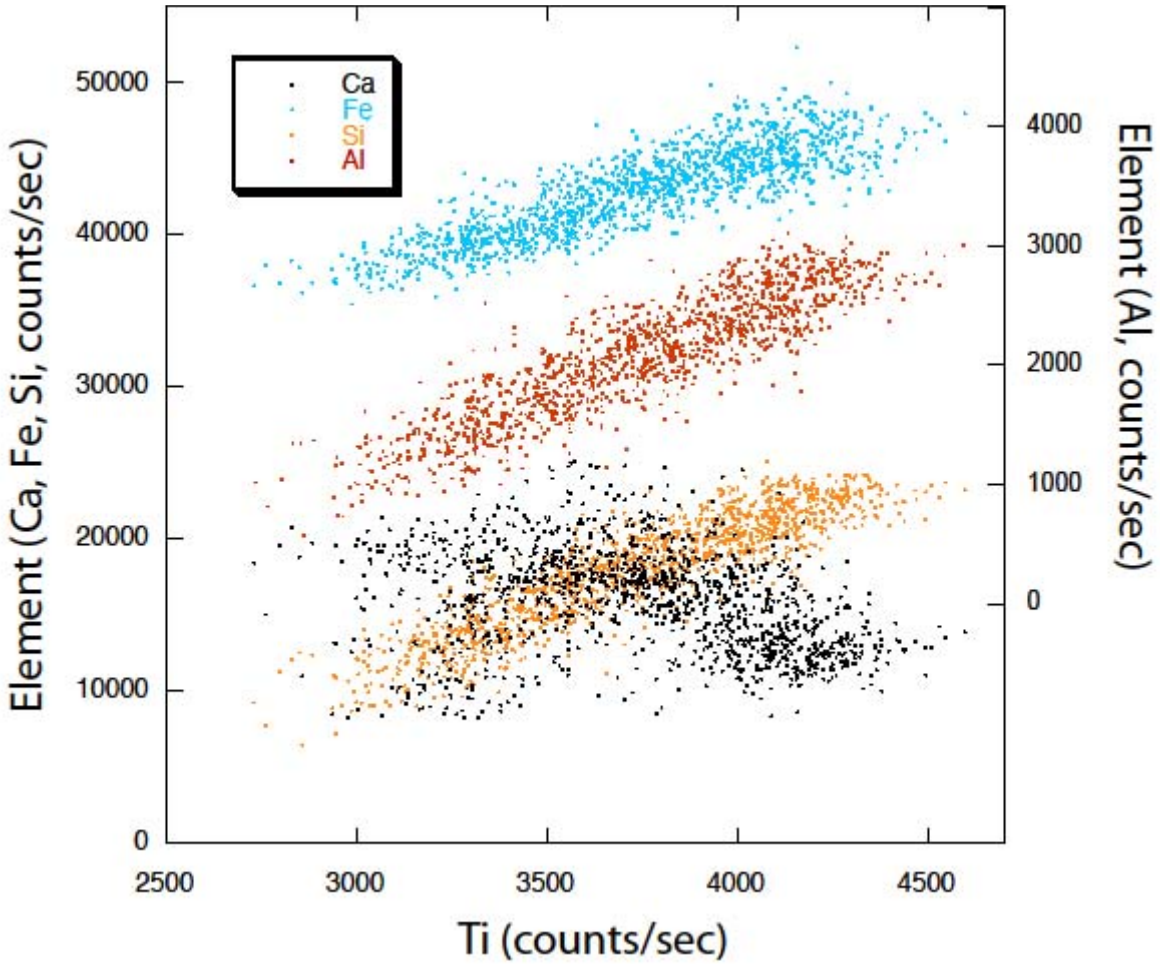

Figure A-2-3: XRF counts for Ca, Al, Si and Fe plotted as a function of Ti counts for core M772-059

The calcium carbonate content in the sediment core is only a minor component that varies between 2 and 8 % of dry bulk sediment (Figure A-2-4). Such low amount of carbonate content cannot be considered as the diluting factor for the overall terrigenous fraction indicated by changes in Ti, Al, Si and Fe. Furthermore, organic carbon content and biogenic opal content vary between 1.5% and 3% and between 0 and 4%, suggesting that the terrigenous fraction might represents ~90% of the total sedimentary fraction in our cores. The overwhelming terrigenous component, once other processes such as sedimentary compaction are accounted for, makes it impossible commenting on temporal changes of the sedimentary discharge while presenting the Ti content alone such as it has been done elsewhere (Haug et al., 2001). Rather, it is likely that coeval changes in the accumulation of the terrigenous fraction have been responsible for dilution of carbonates, but implies that the log (Ti/Ca) is a true reflection of varying terrigenous input only if a constant mass accumulation rate of carbonates and its sedimentary preservation remained constant.

Changes in marine production probably did not impact significantly the $CaCO_3$ sedimentary content for the following reasons. A low-resolution biogenic opal record measured on core M772-056 varies between 0 and 4% of dry sediment without any distinguishable features (data not shown). Such low amounts of biogenic opal are well below the analytical uncertainty associated with the opal measurement procedure (Müller and Schneider, 1993), and thus cannot be used as a reliable indicator for varying diatoms productivity. We tentatively use the log (Si/Al) to track changes in biogenic Si that can reflect variations in opal content linked to changes in productivity of diatoms and radiolaria. Downcore changes in log (Si/Al) from both M772-059 and M772-056 (Figure A-2-4) suggest little if any significant changes in biogenic Si contribution from diatoms, further corroborating our assumption that primary productivity cannot explain the observed changes in the log (Ti/Ca) at our coring sites.

Ideally, changes in lithogenic fluxes should be derived from calculation of accumulation rates using sedimentation rates and dry bulk density values (Rincón-Martìnez et al., 2010; Rühlemann et al., 1999). Taken at face value, the information contained in the computation of such fluxes would however be highly dependent on the number of age tie points (Rühlemann et al., 1999), which cannot be obtained at a resolution sufficient enough to directly date both millennial and centennial scale changes as documented by the log (Ti/Ca) records. Proxies for nutrient cycling embedded in nitrogen isotopic measurements

($\delta^{15}N$) performed on both cores provide additional information on primary productivity at coring sites, independently of sedimentary processes. Downcore measurements of $\delta^{15}N$ indicate that core M772-056 has slightly heavier $\delta^{15}N$ signature, probably because its proximity to the coastline induced higher primary productivity there (Mollier-Vogel et al., manuscript in prep). It is independently suggested by the fact that log (Ti/Ca) is found lower for M772-056 compared to core M772-059 because more carbonate accumulates closer to the coastline. However, only little - if any - changes in nutrient cycling without

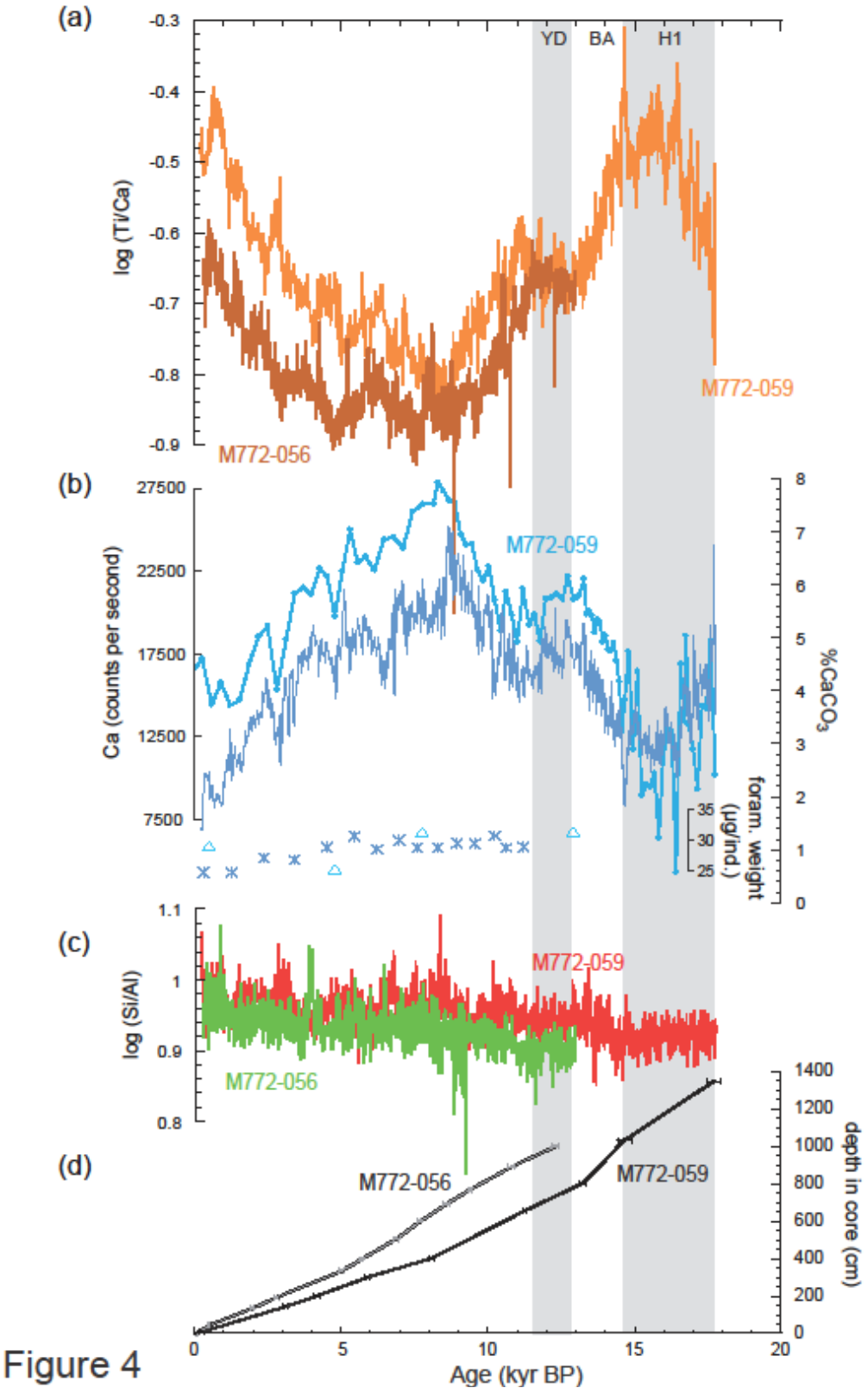

Figure A-2-4: Log (Ti/Ca), $CaCO_3$ content, Ca intensity, log (Si/Al) and age/depth relation

(a) Log (Ti/Ca) for cores M772-059 and M772-056. (b) Carbonate content, Ca intensity in counts per second in core M772-059 and weight per foraminifera: crosses and triangles for core M772-056 and M772-059, respectively. (c) Log (Si/Al) for cores M772-059 and M772-056. (d) Age / Depth relationships for cores M772-059 and M772-056, with age uncertainties (2 sigma) reported as error bar.

any distinguishable correspondence with the $CaCO_3$ content occur (Mollier-Vogel et al., manuscript in preparation). Such result unambiguously indicates that changes in primary productivity can be ruled out as a potential driver of changes in downcore carbonate content. Finally, scanning electron microscope pictures, foraminifera weights and foraminifera elemental analysis performed on N. dutertrei indicate any influence of carbonate dissolution of foraminifera tests (Böschen et al., manuscript in preparation), suggesting that the $CaCO_3$ content which varies between 2 and 8% cannot be explained at first order by any other process than dilution by the terrigenous fraction.

The advantage of XRF core scanning is to provide useful information on past changes in the proportion of elements of continental versus marine origin at very high temporal resolution. It has been successfully used to monitor rainfall variability from cores situated in the vicinity of river mouths all along the tropics (see e.g. Adegbie et al., 2003; Arz et al., 1998; Haug et al., 2001; Jaeschke et al., 2007; Jennerjahn et al., 2004; Tachikawa et al., 2011). At this stage, it is worth mentioning that in the Cariaco Basin, the sedimentary fractions of biogenic and terrigenous material are comparable and affected by equal rates of changes in dilution by each other, allowing the use of the terrigenous fraction (%Ti) only in that particular environment (Haug et al., 2001). As marine sediments at our coring site are almost exclusively composed of terrigenous material, the use of log (Ti/Ca) is here warranted.

A.2.4.2) Variations in terrigenous input

The log (Ti/Ca) record of M772-059 tracks changes in supply of terrigenous material at our deeper coring site back to 18 ka, of which the likely main contributor is the Guayaquil River runoff over Ecuadorian and northern Peruvian Andes, in association with regional response of precipitation to long and short term climate changes (Figure A-2-4). The oldest part of the core is marked by a rapid increase in log (Ti/Ca) between ~18 and 17 ka, followed by a broad maximum of log (Ti/Ca) recorded between ~17 and 15 ka, corresponding to the H1 cold event. A sharp decrease in log (Ti/Ca) which, according to our age model, corresponds to the Boelling/Alleroed time period, indicates a rapid and substantial decrease in terrigenous input immediately following the H1. At the onset of the Younger Dryas chronozone, the log (Ti/Ca) is marked by a moderate increase, which reversed the

deglacial decreasing trend in riverine runoff. The log (Ti/Ca) decreasing trend of the deglacial time interval resumes after the YD and reaches a minimum at ~8 ka BP. There is a lag of the log (Ti/Ca) decreasewith respect to the YD chronozone in core M772-059, probably due to age model uncertainties. We note that the end of the YD in core M772-056 - which has one radiocarbon data point within the YD chronozone - is associated with the same log (Ti/Ca) reversal but with a perfect phasing with the YD chronozone (Figure A-2-4). The mid- to late Holocene part of the sequence is marked at first order by an increasing trend in lithogenic fluxes over the last 8 ka, on which rapid multi-centennial scale changes are superimposed.

We note that the mid- to late Holocene log (Ti/Ca) increase is not associated with an increase in sedimentation rate. Given the data we have in hands, we cannot provide any satisfactory information for such feature. Because of the matrix effect, probable is that the Ca fluorescence is affected more than Ti within the upper part of the core. Where chlorine (Cl) counts are increasing, such as in the sedimentary interval corresponding to the mid- to late-Holocene, the water content is probably responsible for a matrix effect which absorbs more the fluorescence of light elements, such as Al, than the heavier ones such as Ti. For example, computing the log of two light elements such as log (Al/Ca), reduces the magnitude of the estimated changes in sediment delivery, indicating that porewater content induces a matrix effect that may slightly overestimate the sedimentary load of terrigenous material depicted in log (Ti/Ca). It however cannot modify the sign of change observed in log (Ti/Ca) so that we are confident in the interpretation of the log (Ti/Ca) trends we make for the Holocene period. Possible is that the age model is affected by major shifts in radiocarbon reservoir ages occurring during the Holocene. Radiocarbon reservoir ages from environments as dynamic as the southwestern American margin have to be interpreted with caution. A major decrease in marine radiocarbon reservoir of several centuries was detected between the early and the late Holocene (Ortlieb et al., 2011), probably contributing to overestimate the calibrated radiocarbon age of the early Holocene and/or underestimate the ones from the late Holocene. Whether that characteristic had repercussions at our sites is undetermined and requires further investigations. We however note that this artifact might obscure the computed sedimentation rates, in a way that correcting our age models using trends in marine reservoir ages reconstructed

from the Chilean margin (Ortlieb et al., 2011), will eventually contribute to detect an increase in the sedimentation rate over the Holocene once this artifact is accounted for.

A.2.5) Discussion

A.2.5.1) Sedimentary patterns

Despite the relative proximity of cores M772-059 and M772-056 to the Guayas River estuary, sediment delivery at the two core sites may have been affected also by oceanic transport processes. Core M772-056 is situated closer to the edge of the shelf platform of the Gulf of Guayaquil while core M772-059 was retrieved from the upper Peruvian slope (Figure A-2-2). Any change in subsurface to intermediate water mass movements could have modified the sedimentary pattern; however, these are not expected to alter the sedimentary signals in a similar way at the respective water depths. Therefore, the observation that cores M772-059 and M772-056 share similar changes at the multi-centennial and multi-millennial timescales suggests that mainly changes in regional rainfall and its associated river runoff with terrigenous delivery control the log (Ti/Ca) variability at our core sites.

The log (Ti/Ca) record of M772-056 covers the last 13 ka only, but the main patterns described for core M772-059 remain valid (Figure A-2-4). Small contrasts in the timing of submillennial-scale variations superimposed on the long-term trends in both cores indicate that adjustments in the age model may be needed to improve the one-to-one coupling of these events (Figure A-2-4).

For the earlier part of the deglaciation, which is only recorded in M772-059, we cannot dismiss an impact of sea level rise on the log (Ti/Ca). However, the earliest sharp increase in log (Ti/Ca) recorded between ~18 to 16.5 ka corresponding to the onset of the H1 climatic chronozone occurred when the deglaciation and sea level rise already began (Bard et al., 1996), moving depositional accommodation space shoreward. Therefore the high sedimentary input at M772-059 site during the H1 was linked to a change in sediment delivery caused by increased riverine runoff and associated regional rainfall. Similar reasoning can be applied to the YD chronozone, during which the slight but significant increase in log (Ti/Ca) cannot be attributed to the retraction of the shoreline linked to sea level rise. We thus assume that the H1 and, to a lesser extent the YD, were influenced by

increased sedimentary delivery from the surrounding hinterland during wetter conditions as compared to the time interval bracketing those events. On the other hand we cannot rule out that sea level rise contributed to the overall magnitude of the decreases in log (Ti/Ca), recorded between 14.5 and 13 ka as well as between 11 and 9 ka BP.

A.2.5.2) Review of precipitation changes around equatorial South America during the last 18 ka

Overall, our record confirms the equatorial East-West antiphasing in precipitation trends as previously found at the orbital timescale for the last 18 ka in speleothem records collected in equatorial South America (Figure A-2-5). Modeling experiments successfully reproduce the implied zonal antiphasing in precipitation trends recorded along the equator during the Holocene when they are forced by changes in orbital parameters, e.g. Cruz et al., (2009). This feature can be explained by an atmospheric response to latent heat release in the upper troposphere, which caused stronger subsidence over northeastern Brazil to accommodate the enhanced convection and upward motion during times of enhanced austral summer insolation and its associated increase in austral summer monsoon (Cruz et al., 2009).

The rainfall increase recorded at our studied site during H1 stands out as a prominent wet phase and co-occurred with wet conditions on the eastern side of the Amazonian Basin (Arz et al., 1998; Cruz et al., 2009; Jaeschke et al., 2007; Jennerjahn et al., 2004). This strongly suggests in-phase rainfall anomalies at equatorial latitudes at millennial timescales (Figure A-2-5). Moreover, as indicated by the log (Ti/Ca) record, the H1 event was probably experiencing large centennial scale variance in rainfall, highlighting the internal complexity of this event (see also Álvarez-Solas et al., 2011). A recent lacustrine record in the Lake Peten Itza provides evidence for such a multi-phased H1 climate anomaly (Escobar et al., 2012). The authors assigned these centennial-scale shifts within the H1 chronozone to multiple iceberg discharges in the North Atlantic during H1 (Bard et al., 2000). A recent speleothem record from the central Peruvian Andes recorded similar high-frequency shifts in precipitation during Heinrich events 4 and 3 (Kanner et al., 2012), which mimics sea surface temperature changes from the Bermuda Rise (Sachs and Lehman, 1999). All this evidence reinforces the idea that Heinrich stadials contain complex

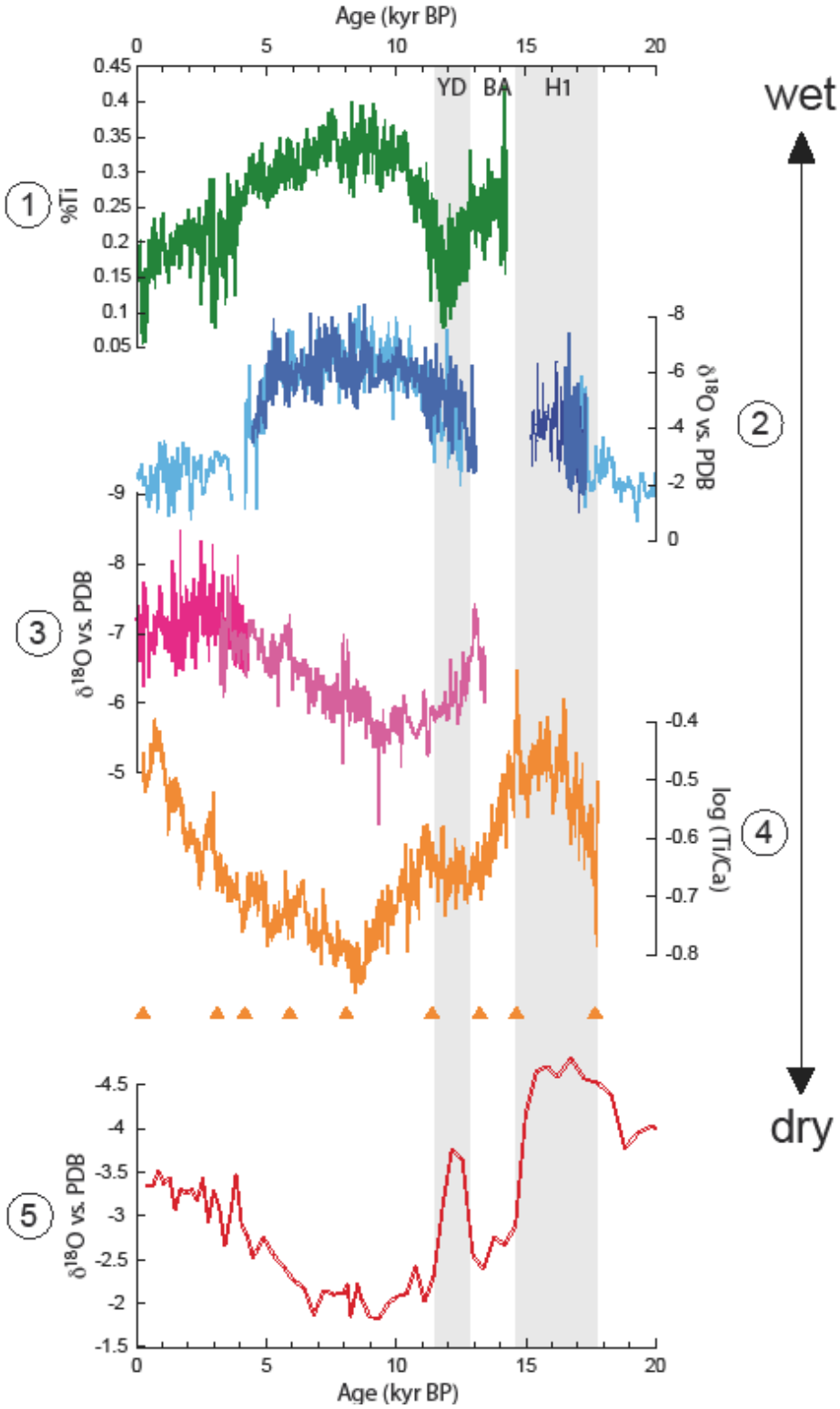

Figure A-2-5: Records for past changes in precipitation over South America

(1) Haug et al. (2001); (2) Cruz et al. (2009); (3) van Breukelen et al. (2008); (4) This study; (5) Wang et al. (2007). The Younger Dryas (YD) and Bolling/Alleroed (BA) time intervals are reported at top of the panel according to the GISP2 timescale (Grootes et al., 1993) while the timing of the Heinrich event 1 (H1) chronozone was chosen after Bard et al. (2000). Orange triangles indicate radiocarbon ages used to compute the M772-059 age model.

internal climate variability, which needs to be further studied. An overall wet H1 can be at least partly explained by a southward shift in the mean ITCZ latitudinal position over oceanic regions surrounding South America along with its associated monsoon variability over the continent in analogy to increases in precipitation recorded in speleothems from Southern Brazil (Figure A-2-5) (Cruz et al., 2005; Wang et al., 2004; Wang et al., 2007) and in the Andean altiplano by ~20°S (Blard et al., 2009).

At our studied site, the 18 to 8 ka time interval is marked by a general decrease in sediment discharge from the Ecuadorian Andes (Figure A-2-5). This suggests a long-term aridification co-occurring with the deglaciation phase from the Last Glacial to the Early Holocene, with potentially some superimposed sea level imprint (Figure A-2-5). Such a feature is in contrast with sites located north of the equator where the last deglaciation is marked by an overall increase in precipitation (Pahnke et al., 2007). Interestingly, a marine site located at the equator close to the northern Ecuadorian margin was also marked by pronounced increases in riverine runoff over the last five terminations (Rincón-MartÌnez et al., 2010). However, the temporal resolution of these records is not resolving millennial scale variations superimposed on the deglacial trend. Although our record is not covering the full glacial period, from the oldest part of the record it is apparent that the start of H1 was associated with a strong increase in the log (Ti/Ca), which decreased back toward the deglacial values observed before the H1. Overall, our riverine runoff record from northern Peru suggests that rainfall changes occurring during the deglaciation and the H1 were of opposite sign as compared to those recorded at marine and continental sites located in the northern tropics (Leduc et al., 2007; Escobar et al., 2012).

The only moderate increase in precipitation along the equator during the YD compared to the H1 probably reflects differences in the magnitude of these cold spells and/or in the regional climate response to AMOC perturbation under glacial and interglacial boundary conditions (Roche et al., 2011). A muted YD anomaly compared to that associated with H1 was also recorded in Lake Peten Itza (Escobar et al., 2012), suggesting that these two events did not affect tropical rainfall with the same intensity.

For the mid- to late Holocene rapid rainfall fluctuations are detected, superimposed on the first-order increasing trend in precipitation. Analogous fluctuations occurring at multicentennial times scales are analogous to other climatic features from sedimentary archives collected around Latin America that have connections with the ITCZ dynamics of

ENSO. These records include precipitation changes in the southern tropics (Stríkis et al., 2011) and at the equator (Moy et al., 2002), as well as ENSO-induced changes in SST along Baja California (Marchitto et al., 2010). The phasing of these changes however cannot be satisfactorily resolved given the limitation in the existing age model of our sedimentary sequence. Thus it remains speculative to associate these centennial changes in regional rainfall to shorter Holocene fluctuations in AMOC (Bond et al., 2001).

A.2.5.3) Processes controlling equatorial rainfall variability at different timescales

The M772-059 log (Ti/Ca) record, while compared to the speleothem record from north-eastern Brazil and Peru, suggests that East-West in-phase increases in precipitation may have occurred along the equator during the H1 and the YD (Figure A-2-5). This observation was recently confirmed by newly obtained speleothem records from the western Amazonian Basin (Cheng et al., 2013).

At orbital timescale, an anti-phase behavior is apparent in rainfall trends with the western South Americas becoming dry in the Early Holocene as compared to the H1 and the Late Holocene, and vice versa for the Northeastern Brazil (Figure A-2-5). Such trend is recorded virtually everywhere from 5°N to 17°S in all the precipitation records from the western South America at sites situated close to the Andes (see Figure 8 in Bird et al., 2011). Our new record compared to the Cariaco Basin supports the view of a North-South antiphase at millennial and orbital timescales in response to a bi-polar precipitation see-saw. Our log (Ti/Ca) record is also supported by the trends recorded in speleothems from southern Brazil and from Northeast Peru (Figure A-2-5), even though the speleothem record suggests a late Holocene rainfall decrease, seen in the □18O, which trends back toward heavier values (Figure A-2-5). It is unclear whether such feature reveals different rainfall trends for those two localities, or if isotopic values are an artifact associated with large-scale atmospheric circulation as it has recently been identified into the northern hemisphere (Leduc et al., 2013). This pattern corresponds to the assumption that at millennial and orbital timescales latitudinal shifts of the ITCZ across the equator control the position of the rainfall belt. At the millennial timescale, the southward ITCZ movements are probably triggered by the reduction of the AMOC that induces a low-latitude southward shift in maximum SST. At the orbital timescale, modifications of seasonal insolation

occurring during the wet season of both hemispheres induce a North-South antiphase in the intensity of rainfall. This is apparent in our record by drier conditions in the Early to mid Holocene compared to wet conditions in Cariaco Basin (Figure A-2-5). The speleothem from Northeastern Brazil however indicates an antiphase response of rainfall with our record, even though both records are located at the same latitude (Figure A-2-5). This result is robust because the same rainfall evolution is recorded on the eastern flank of the Andes, a region under the influence of the South American monsoon (Figure A-2-5). According to Cruz et al. (2009), this feature can be due to convective heating over tropical South America, and its and associated adjustments in large-scale atmospheric subsidence over northeast Brazil (Cruz et al., 2009).

Our cores were collected in an area where precipitation occurs both during the austral summer and during El Niño events (Figure A-2-1). Therefore, the Mid to Late Holocene long-term precipitation increase may be assigned partly to an increase in austral summer insolation and its associated rainfall increase within the southern tropical band as a whole (Braconnot et al., 2007) or, as a sizable amount of publications suggests, to an increase in ENSO activity in the course of the Holocene (Koutavas et al., 2006; Moy et al., 2002). Similar reasoning could be applied to the H1 and YD time intervals, assigning rainfall increase to a southward shift in the ITCZ (Leduc et al., 2009a; Leduc et al., 2009b) or to an increase of an ENSO type-Walker circulation state (Stott et al., 2002). A more recent study from the Cortes Sea also suggests that neither changes in the seasonal dynamics of the ITCZ nor in the ENSO activity may be reliable analogues for describing the suite of climatic events that marked the last deglaciation in the tropical East Pacific (McClymont et al., 2012). To solve this controversy, a more detailed comparison of high resolution records from regions sensitive to the modern ENSO phenomenon is needed. Such comparison should be including areas where different regional precipitation sensitivity to ENSO and to the seasonal cycle of the ITCZ is found in comparison with the EEP. Those conditions are found in northeastern Australia and southeastern Africa, where austral winters are associated with positive rainfall anomalies such as in Ecuador, but where El Niño events are associated with drier conditions than during normal years (Dai and Wigley, 2000). Considering the record by Schefuss et al., (2011) from Southeast Africa, showing the same first order pattern as our XRF record, would argue against the ENSO being a primary driver of precipitation changes over the last 18 ka BP.

Increases in rainfall along the equator and in the southern tropics are successfully captured by climate models applying water hosing experiments to simulate Heinrich events (Stouffer et al., 2006). In these model experiments, freshwater releases in the northern North Atlantic induce sea surface warming south of the equator, and southward ITCZ migration because of deep atmospheric convection closely following the regions of maximum surface temperature (Stouffer et al., 2006). Similarly, precipitation changes orchestrated by changes in orbital parameters likely responded with an asymmetric behavior across the equator in the tropics (Braconnot et al., 2007; Tachikawa et al., 2011). Nonetheless, considerable regional heterogeneity is observed between different models (Braconnot et al., 2007; Stouffer et al., 2006). It highlights the difficulty that models have to capture regional scale atmospheric changes in areas where orography and local wind regimes play a key role in shaping past rainfall changes around the Andes (Kim et al., 2008). Here more rainfall proxy records like presented in this study may help to verify model results at the regional scale.

A.2.6) Conclusions

We report a new, high-resolution record of riverine runoff covering the last 18 ka from the northern Peruvian margin at 3.5°S. We detect periods of high runoff during the H1, the YD and the late Holocene, while conditions of reduced runoff occurred during the Early and mid Holocene. These changes in runoff are considered as the expression of rainfall variability during the wet season at the western flanks of the Andes. Our record mimics rainfall variability reported from speleothem records of precipitation in southern Brazil, suggesting that both the southern tropical America and the Pacific coast situated much closer to the equator were affected in similar ways by orbital and millennial-scale climate forcing. This however contrasts with another speleothem record located in northeastern Brazil very close to the equator, which shows wetter conditions during the early Holocene and the H1.

The comparison of our record with other available high-resolution records from South America implies that shifts in rainfall pattern above South America were influenced in different ways by climate forcing at different timescale. The sediment cores as well as the speleothems records show a North-South antiphase of the rainfall maxima occurring at

both orbital and millennial timescales, likely triggered by changes in insolation and in AMOC intensity, respectively. This antiphase is observed all around the South American continent, except in a speleothem from northeastern Brazil which is located in the southern hemisphere, but where the trend in rainfall changes at the orbital timescale is in phase with the rainfall trends recorded in other archives from the northern hemisphere. Such feature was explained so far by a remote forcing of the South American monsoon triggered by changes in orbital parameters. Such mechanism is fully consistent with our new XRF results that testify to an interhemispheric seesaw in monsoon-driven precipitation changes above the South America continent at the orbital timescale.

Regardless whether changes in the annual cycle of rainfall and/or in the ENSO were also at play in shaping those rainfall trends, our results may help to better understand how regional rainfall may change over South America under anthropogenic climate forcing. However, given the complexity of the tropical South America rainfall response to climate changes that have occurred over the last 18 ka, further mapping efforts with high resolution time series are needed to draw a clearer picture of the spatial extent of regional rainfall shifts associated with ITCZ movements and monsoonal moist air transport onto the South American continent. Reductions of model-proxy data mismatches at the regional scale may be achieved when using modeling studies integrating a better spatial resolution of the Andean topography. This may contribute also to reduce the regional uncertainties on the future evolution of rainfall patterns associated with anthropogenic climate change.

Acknowledgments

We thank Rik Tjallingii for his help with XRF measurements and Francisco Cruz and Jeroen van der Lubbe for fruitful discussion. Two anonymous reviewers are thanked for their constructive comments on an earlier version of the manuscript that significantly improved its quality.

References

Adegbie, A. T., Schneider, R. R., Röhl, U., and Wefer, G. (2003). Glacial millennial-scale fluctuations in central African precipitation recorded in terrigenous sediment supply and freshwater signals offshore Cameroon. Palaeogeography, Palaeoclimatology, Palaeoecology 197, 323-333.

Álvarez-Solas, J., Montoya, M., Ritz, C., Ramstein, G., Charbit, S., Dumas, C., Nisancioglu, K., Dokken, T., and Ganopolski, A. (2011). Heinrich event 1: an example of dynamical ice-sheet reaction to oceanic changes. Clim. Past 7, 1297 - 1306.

Arz, H. W., Pätzold, J., and Wefer, G. (1998). Correlated Millennial-Scale Changes in Surface Hydrography and Terrigenous Sediment Yield Inferred from Last-Glacial Marine Deposits off Northeastern Brazil. Quaternary Research 50, 157-166.

Baker, P. A., Seltzer, G. O., Fritz, S. C., Dunbar, R. B., Grove, M. J., Tapia, P. M., Cross, S. L., Rowe, H. D., and Broda, J. P. (2001). The History of South American Tropical Precipitation for the Past 25,000 Years. Science 291, 640-643.

Bard, E., Hamelin, B., Arnold, M., Montaggioni, L., Cabioch, G., Faure, G., and Rougerie, F. (1996). Deglacial sea-level record from Tahiti corals and the timing of global meltwater discharge. Nature 382, 241-244.

Bard, E., Rostek, F., Turon, J.-L., and Gendreau, S. (2000). Hydrological Impact of Heinrich Events in the Subtropical Northeast Atlantic. Science 289, 1321-1324.

Bird, B. W., Abbott, M. B., Rodbell, D. T., and Vuille, M. (2011). Holocene tropical South American hydroclimate revealed from a decadally resolved lake sediment δ18O record. Earth and Planetary Science Letters 310, 192-202.

Blard, P. H., Lavé, J., Farley, K. A., Fornari, M., Jiménez, N., and Ramirez, V. (2009). Late local glacial maximum in the Central Altiplano triggered by cold and locally-wet conditions during the paleolake Tauca episode (17-15 ka, Heinrich 1). Quaternary Science Reviews 28, 3414-3427.

Böschen, T., Nürnberg, D., Mollier-Vogel, E., Doering, K., Schneider, R., Dullo, C. (Manuscript in perparation). Deglacial to Holocene changes in thermocline depth reflecting migration of the Equatorial Front off Peru.

Bond, G., Kromer, B., Beer, J., Muscheler, R., Evans, M. N., Showers, W., Hoffmann, S., Lotti-Bond, R., Hajdas, I., and Bonani, G. (2001). Persistent Solar Influence on North Atlantic Climate During the Holocene. Science 294, 2130-2136.

Bookhagen, B., and Strecker, M. R. (2008). Orographic barriers, high-resolution TRMM rainfall, and relief variations along the eastern Andes. Geophys. Res. Lett. 35, L06403.

Braconnot, P., Otto-Bliesner, B., Harrison, S., Joussaume, S., Peterchmitt, J.-Y., Abe-Ouchi, A., Crucifix, M., Driesschaert, E., Fichefet, T., Hewitt, C. D., Kageyama, M., Kitoh, A., Loutre, M.-F., Marti, O., Merkel, U., Ramstein, G., Valdes, P., Weber, L., Yu, Y., and Zhao, Y. (2007). Results of PMIP2 coupled simulations of the Mid-Holocene and Last Glacial Maximum -

Part 2: feedbacks with emphasis on the location of the ITCZ and mid- and high latitudes heat budget. Clim. Past 3, 279 - 296.

Cheng, H., A. Sinha, F.W. Cruz, X. Wang, R.L. Edwards, F.M. d'Horta, C.C. Ribas, M. Vuille, L.D. Stott and A.S. Auler (2013). Climate change patterns in Amazonia and biodiversity. Nature Communications, 4, 1411.

Cruz, F. W., Burns, S. J., Karmann, I., Sharp, W. D., Vuille, M., Cardoso, A. O., Ferrari, J. A., Silva Dias, P. L., and Viana, O. (2005). Insolation-driven changes in atmospheric circulation over the past 116,000 years in subtropical Brazil. Nature 434, 63-66.

Cruz, F. W., Vuille, M., Burns, S. J., Wang, X., Cheng, H., Werner, M., Lawrence Edwards, R., Karmann, I., Auler, A. S., and Nguyen, H. (2009). Orbitally driven east-west antiphasing of South American precipitation. Nature Geosci 2, 210-214.

Dai, A., and Wigley, T. M. L. (2000). Global patterns of ENSO-induced precipitation. Geophys. Res. Lett. 27, 1283-1286.

Escobar, J., Hodell, D. A., Brenner, M., Curtis, J. H., Gilli, A., Mueller, A. D., Anselmetti, F. S., Ariztegui, D., Grzesik, D. A., Pérez, L., Schwalb, A., and Guilderson, T. P. (2012). A ,~43 ka record of paleoenvironmental change in the Central American lowlands inferred from stable isotopes of lacustrine ostracods. Quaternary Science Reviews.

Garreaud, R. D., Vuille, M., Compagnucci, R., and Marengo, J. (2009). Present-day South American climate. Palaeogeography, Palaeoclimatology, Palaeoecology 281, 180-195.

Haug, G. H., Hughen, K. A., Sigman, D. M., Peterson, L. C., and Röhl, U. (2001). Southward Migration of the Intertropical Convergence Zone Through the Holocene. Science 293, 1304-1308.

Jaeschke, A., Rühlemann, C., Arz, H., Heil, G., and Lohmann, G. (2007). Coupling of millennial-scale changes in sea surface temperature and precipitation off northeastern Brazil with high-latitude climate shifts during the last glacial period. Paleoceanography 22, PA4206.

Jennerjahn, T. C., Ittekkot, V., Arz, H. W., Behling, H., Pätzold, J. r., and Wefer, G. (2004). Asynchronous Terrestrial and Marine Signals of Climate Change During Heinrich Events. Science 306, 2236-2239.

Kanner, L. C., Burns, S. J., Cheng, H., and Edwards, R. L. (2012). High-Latitude Forcing of the South American Summer Monsoon During the Last Glacial. Science 335, 570-573.

Kim, S.-J., Crowley, T., Erickson, D., Govindasamy, B., Duffy, P., and Lee, B. (2008). High-resolution climate simulation of the last glacial maximum. Climate Dynamics 31, 1-16.

Koutavas, A., deMenocal, P. B., Olive, G. C., and Lynch-Stieglitz, J. (2006). Mid-Holocene El Niño-Southern Oscillation (ENSO) attenuation revealed by individual foraminifera in eastern tropical Pacific sediments. Geology 34, 993-996.

Leduc, G., Vidal, L., Tachikawa, K., Rostek, F., Sonzogni, C., Beaufort, L., and Bard, E. (2007). Moisture transport across Central America as a positive feedback on abrupt climatic changes. Nature 445, 908-911.

Leduc, G., Vidal, L., Cartapanis, O., and Bard, E. (2009a). Modes of eastern equatorial Pacific thermocline variability: Implications for ENSO dynamics over the last glacial period. Paleoceanography 24, PA3202.

Leduc, G., Vidal, L., Tachikawa, K., and Bard, E. (2009b). ITCZ rather than ENSO signature for abrupt climate changes across the tropical Pacific? Quaternary Research 72, 123-131.

Leduc G., Sachs J.P., Kawka O.E., Schneider R.R. (2013). Holocene changes in eastern equatorial Atlantic salinity as estimated by water isotopologues. Earth and Planetary Science Letters, 362, 151-162.

Liu, W. T., and Xie, X. (2002). Double intertropical convergence zones-a new look using scatterometer. Geophys. Res. Lett. 29, 2072.

Marchitto, T. M., Muscheler, R., Ortiz, J. D., Carriquiry, J. D., and van Geen, A. (2010). Dynamical Response of the Tropical Pacific Ocean to Solar Forcing During the Early Holocene. Science 330, 1378-1381.

McClymont, E. L., Ganeshram, R. S., Pichevin, L. E., Talbot, H. M., van Dongen, B. E., Thunell, R. C., Haywood, A. M., Singarayer, J. S., and Valdes, P. J. (2012). Sea-surface temperature records of Termination 1 in the Gulf of California: Challenges for seasonal and interannual analogues of tropical Pacific climate change. Paleoceanography 27, PA2202.

Mollier-Vogel, E., Martinez, P., Schneider, R., (manuscript in perparation). Mid-Holocene collapse of the Peruvian oxygen minimum zone.

Moy, C. M., Seltzer, G. O., Rodbell, D. T., and Anderson, D. M. (2002). Variability of El Niño/Southern Oscillation activity at millennial timescales during the Holocene epoch. Nature 420, 162-165.

Müller, P. J., and Schneider, R. (1993). An automated leaching method for the determination of opal in sediments and particulate matter. Deep Sea Research Part I: Oceanographic Research Papers 40, 425-444.

Ortlieb, L., Vargas, G., and Saliège, J. F. (2011). Marine radiocarbon reservoir effect along the northern Chile-southern Peru coast (14-24 degrees S) throughout the Holocene. Quaternary Research 75, 91-103.

Pahnke, K., Sachs, J. P., Keigwin, L., Timmermann, A., and Xie, S.-P. (2007). Eastern tropical Pacific hydrologic changes during the past 27,000 years from D/H ratios in alkenones. Paleoceanography 22, PA4214.

Peterson, L. C., Haug, G. H., Hughen, K. A., and Röhl, U. (2000). Rapid Changes in the Hydrologic Cycle of the Tropical Atlantic During the Last Glacial. Science 290, 1947-1951.

Poveda, G., and Mesa, O. J. (2000). On the existence of Lloró (the rainiest locality on Earth): Enhanced ocean-land-atmosphere interaction by a low-level jet. Geophys. Res. Lett. 27, 1675-1678.

Poveda, G. n., Waylen, P. R., and Pulwarty, R. S. (2006). Annual and inter-annual variability of the present climate in northern South America and southern Mesoamerica. Palaeogeography, Palaeoclimatology, Palaeoecology 234, 3-27.

Reimer, P. J., Baillie, M. G. L., Bard, E., Bayliss, A., Beck, J. W., Blackwell, P. G., Ramsey, C. B., Buck, C. E., Burr, G. S., Edwards, R. L., Friedrich, M., Grootes, P. M., Guilderson, T. P., Hajdas, I., Heaton, T. J., Hogg, A. G., Hughen, K. A., Kaiser, K. F., Kromer, B., McCormac, F. G., Manning, S. W., Reimer, R. W., Richards, D. A., Southon, J. R., Talamo, S., Turney, C. S. M., van der Plicht, J., and Weyhenmeyer, C. E. (2009). IntCal09 and Marine09 radiocarbon age calibration curves, 0-50,000yeats cal BP. RADIOCARBON 51, 1111-1150.

Rincón-MartÌnez, D., Lamy, F., Contreras, S., Leduc, G., Bard, E., Saukel, C., Blanz, T., Mackensen, A., and Tiedemann, R. (2010). More humid interglacials in Ecuador during the past 500 kyr linked to latitudinal shifts of the equatorial front and the Intertropical Convergence Zone in the eastern tropical Pacific. Paleoceanography 25, PA2210.

Roche, D. M., Renssen, H., Paillard, D., and Levavasseur, G. (2011). Deciphering the spatio-temporal complexity of climate change of the last deglaciation: a model analysis. Clim. Past 7, 591-602.

Rühlemann, C., Müller, P.J., and Schneider, R.R., (1999), Organic carbon and carbonate as paleoproductivity proxies: Examples from high and low productivity areas of the tropical Atlantic, in: Fischer, G., and Wefer, G. (eds), Use in proxies of paleoceanography: Examples from the South Atlantic. Springer-Verlag Berlin Heidelberg, pp 315-344.

Sachs, J. P., and Lehman, S. J. (1999). Subtropical North Atlantic Temperatures 60,000 to 30,000 Years Ago. Science 286, 756-759.

Schefuss, E., Kuhlmann, H., Mollenhauer, G., Prange, M., and Patzold, J. (2011). Forcing of wet phases in southeast Africa over the past 17,000 years. Nature 480, 509-512.

Silvestri, G. E. (2004). El Niño signal variability in the precipitation over southeastern South America during austral summer. Geophys. Res. Lett. 31, L18206.

Stott, L., Poulsen, C., Lund, S., and Thunell, R. (2002). Super ENSO and Global Climate Oscillations at Millennial Time Scales. Science 297, 222-226.

Stouffer, R. J., Yin, J., Gregory, J. M., Dixon, K. W., Spelman, M. J., Hurlin, W., Weaver, A. J., Eby, M., Flato, G. M., Hasumi, H., Hu, A., Jungclaus, J. H., Kamenkovich, I. V., Levermann, A., Montoya, M., Murakami, S., Nawrath, S., Oka, A., Peltier, W. R., Robitaille, D. Y., Sokolov, A., Vettoretti, G., and Weber, S. L. (2006). Investigating the Causes of the Response of the Thermohaline Circulation to Past and Future Climate Changes. Journal of Climate 19, 1365-1387.

Stríkis, N. M., Francisco W. Cruz, Hai Cheng, Ivo Karmann, R. Lawrence Edwards, Mathias Vuille, X. W., Marcos S. de Paula, Valdir F. Novello, and Auler, A. S. (2011). Abrupt variations in South American monsoon rainfall during the Holocene based on a speleothem record from central-eastern Brazil. Geology In Press.

Tachikawa, K., Cartapanis, O., Vidal, L., Beaufort, L., Barlyaeva, T., and Bard, E. (2011). The precession phase of hydrological variability in the Western Pacific Warm Pool during the past 400 ka. Quaternary Science Reviews 30, 3716-3727.

Tjallingii, R., Stattegger, K., Wetzel, A., and Van Phach, P. (2010). Infilling and flooding of the Mekong River incised valley during deglacial sea-level rise. Quaternary Science Reviews 29, 1432-1444.

Twilley, R.R., Cárdenas, W., Rivera-Monroy, V.H., Espinoza, J., Suescum, R., Armijos, M.M., and Solórzano, L. (2001), The Gulf of Guayaquil and the Guayas River estuary, Ecuador, in: Seelinger, U., and Kjerfve, B., (eds), Coastal marine ecosystems in Latin America. Ecological studies 144, p. 245-264.

van Breukelen, M. R., Vonhof, H. B., Hellstrom, J. C., Wester, W. C. G., and Kroon, D. (2008). Fossil dripwater in stalagmites reveals Holocene temperature and rainfall variation in Amazonia. Earth and Planetary Science Letters 275, 54-60.

Wang, X., Auler, A. S., Edwards, R. L., Cheng, H., Cristalli, P. S., Smart, P. L., Richards, D. A., and Shen, C.-C. (2004). Wet periods in northeastern Brazil over the past 210 kyr linked to distant climate anomalies. Nature 432, 740-743.

Wang, X., Edwards, R.L., Auler, A.S., Cheng, H., and Ito, E., (2007), Millennial-Scale Interhemispheric Asymmetry of Low-Latitude Precipitation: Speleothem Evidence and Possible High-Latitude Forcing, in: Ocean Circulation: Mechanisms and Impacts. AGU Geophysical Monograph 173, p. 279-294, 10.1029/173GM18.

Wells, L. E. (1990). Holocene history of the El Niño phenomenon as recorded in flood sediments of northern coastal Peru. Geology 18, 1134-1137.

Weltje, G. J., and Tjallingii, R. (2008). Calibration of XRF core scanners for quantitative geochemical logging of sediment cores: Theory and application. Earth and Planetary Science Letters 274, 423-438.

Witt, C. s., and Bourgois, J. (2010). Forearc basin formation in the tectonic wake of a collision-driven, coastwise migrating crustal block: The example of the North Andean block and the extensional Gulf of Guayaquil-Tumbes Basin (Ecuador-Peru border area). Geological Society of America Bulletin 122, 89-108.

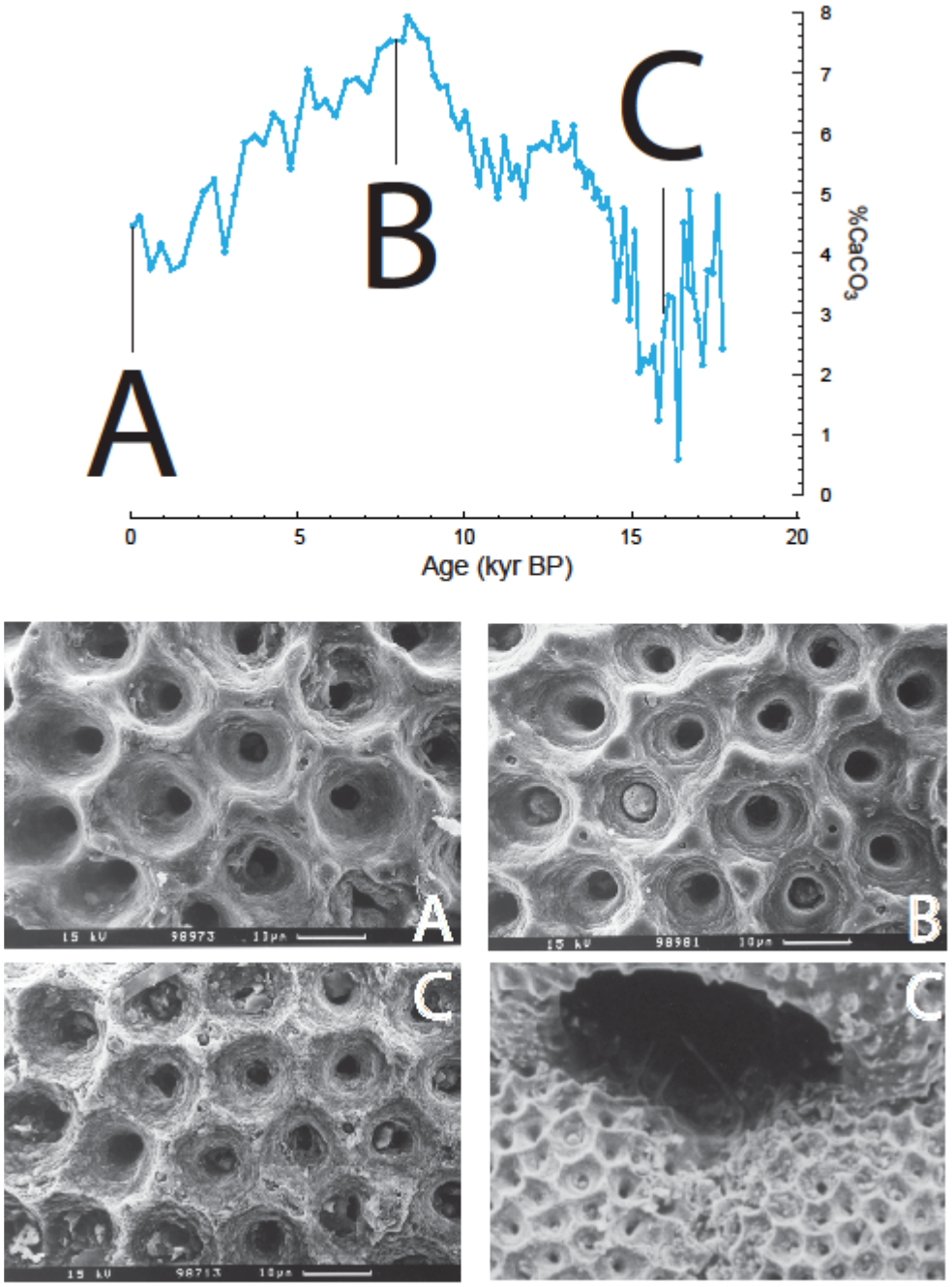

Supplementary figure: Down core $CaCO_3$ content with accompanying SEM images

Upper panel: Down core carbonate content of core M772-059, with A, B and C that locates horizons where foraminifera were picked for images.

Lower panel: Scanning Electron Microscope images taken from *G. ruber* test at different depth horizons. A), B) and C) correspond to intermediate (A), high (B) and low (C) carbonate content at 3 cm, 403 cm and 1158 cm sediment depths, respectively. Preservation of pores architecture at all depths, as well as observation of spines within the aperture observed at depth where lowest carbonate content was measured, indicates that no dissolution took place at coring site.